ADVANCED SIMULATION OF PARTICLE PROCESSING: THE ROLES OF COHESION, MASS AND HEAT TRANSFER IN GAS-SOLID FLOWS

by

Deliang Shi

B.S., Beijing Technology and Business University, China, 1999

M.S., Tianjin University, China, 2002

Submitted to the Graduate Faculty of

the Swanson School of Engineering in partial fulfillment

of the requirements for the degree of

Doctor of Philosophy

University of Pittsburgh

2008

UNIVERSITY OF PITTSBURGH

SWANSON SCHOOL OF ENGINEERING

This dissertation was presented

by

Deliang Shi

It was defended on

January 4, 2008

and approved by

Joseph J. McCarthy, Ph.D., Associate Professor, Chemical and Petroleum Engineering

Robert S. Parker, Ph.D., Associate Professor, Chemical and Petroleum Engineering

J. Karl Johnson, Ph.D., Professor, Chemical and Petroleum Engineering

C. Fred Higgs, III, Ph.D., Assistant Professor, Mechanical Engineering, Carnegie Mellon University

Dissertation Director: Joseph J. McCarthy, Ph.D., Associate Professor, Chemical and Petroleum Engineering

ADVANCED SIMULATION OF PARTICLE PROCESSING: THE ROLES OF COHESION, MASS AND HEAT TRANSFER IN GAS-SOLID FLOWS

Deliang Shi, PhD

University of Pittsburgh, 2008

This dissertation addresses the simulation of several important unit operations in the field of granular processing, which includes particle mixing and segregation, cohesive gas-solid flows, liquid transfer between particles, heat transfer in gas-solid flows and the drying process in gas-solid flows. Particle dynamics (PD) is employed to probe the solid flows and computational fluid dynamics (CFD) is used to simulate the gas phase.

Achieving good mixing of free-flowing particulate solids with different properties is not a trivial exercise. By introducing periodic flow inversions, we show both experimentally and computationally that forcing with a value above a critical frequency can effectively eliminate both density and size segregation.

The mechanics of cohesive flowing gas-particle systems is still poorly understood. Toward that end, we introduce a discrete characterization tool for gas-solid flow of wet (cohesive) granular material- the Granular Capillary Number (Ca_g). The utility of this tool is computationally tested over a range of cohesive strengths in two prototypical applications of gas-solid flows.

While slow granular flows have been an area of active research in recent years, heat transfer in flowing particulate systems has received relatively little attention. We employ a computational technique that couples the PD, CFD, and heat transfer calculations to simulate realistic heat transfer in a rotary kiln. Our results suggest a transition in heat transfer regime as the conductivity of the particles changes.

Liquid transfer between particles plays a central role in the operation of a variety of particle processing equipment. We introduce a dynamic liquid transfer model for use in PD of heterogeneous particle systems. As a test of this new model we present results from the simulation of a rotary drum spray-coating system.

The drying process in gas-solid flows involves complex mass, momentum and heat transfer. By incorporating mass transfer modeling into our existing gas-solid PD-based heat transfer code, the drying process is successfully simulated. Results are reported for both mono-disperse and bi-disperse cases.

Finally, we outline how to simulate amphiphilic particles, which are spheres comprised of two parts. We use the quaternion method to track the particle rotation, such that we can study the issues relating to anisotropic particles .

DESCRIPTORS

Cohesive	Drying
Gas-Solid Flows	Heat Transfer
Liquid Bridge	Mass Transfer
Particle Rotation	Quaternion

TABLE OF CONTENTS

LIST OF TABLES

LIST OF FIGURES

PREFACE

I want to express my deep gratitude to my advisor, Dr. Joseph J. McCarthy. His patience, enlightening and encouraging have accompanied me through my Ph.D. study. His talent and professionalism have guided me into this wonderful simulation world. Dr. McCarthy not only gives me direction on doing research, but also teaches me how to do it. There is no doubt what I have learned from him will benefit me in my whole life.

Using this chance, I would like to thank Dr. Robert S. Parker, Dr. J. Karl Johnson, Dr. C. Fred Higgs, III and Dr. Minking K. Chyu for their always support and help during my Ph.D. study.

I would also like to thank my colleagues at the University of Pittsburgh: Adetola Abatan, Hongming Li, Isabel Figueroa, Kunal Jain, Watson Vargas, Ann Hays, Suman Hajra, Abhishek Soni and John Harrold. From John Harrold, I learned we can help other people even when we lead very simple lives.

I want to thank all the faculty, stuff and students in Chemical Engineering Department of University of Pittsburgh for their help during these years. I also want to thank the Pitt Library for their excellent job on literature search.

Finally, I would like to dedicate this work to my parents. Thank them for the education and support in my life. I also want to dedicate this work to my wife, Xin Fan, for her help, understanding and trust. I want to thank my son, Lyndon Lida Shi, for his smile to push me to grow up.

1.0 INTRODUCTION

More than 60% of US manufactured goods rely substantially on particle science and technology. Despite the significance, our understanding of particle processing lags dramatically compared to fluid processing. This can be attributed, in part, to difficulties in experimentally probing particle agents. Particle dynamics (PD), a robust technique for simulating particle flow, can determine the trajectories of individual particles, and it has emerged as one of the most important tools in probing granular flows. In this work, we use PD to simulate particulate flows. When gas is present, Computational Fluid Dynamics (CFD) is employed to simulate the gas phase. Several important advances in the modeling of granular flows are necessary to facilitate these studies, and are outlined in this work. In addition, a further development which enables the modeling of anisotropic particles is outlined and sets the stage for more refinement of the models used herein.

Particle mixing processes are widely used in the chemical, pharmaceutical, food and coal industries and many particulate goods or their intermediate products are mixtures. Therefore, mixing processes are very important for the quality of the final products[1]. For free-flowing powders, particles of different size and density prefer to remain segregated. In order to produce mixtures with better quality, a variety of methods and equipment have been used, such as controlling cohesive forces between particles [2, 3], or using complex mixers [4]. Despite the fact that a sustained amount of work has been done in this field, particle mixing still remains an art[5].

Due to their simplicity and potential to be easily scaled-up, rotating drums are widely used in industry, as well as in therotical research. Segregation of different density and size particles in rotating drums is well observed in both experiments and simulations [6]. An

attempt to augment mixing is often made through the use of conventional baffles which are attached to the wall of a tumbler. These conventional baffles, however, have little effect on mitigating segregation [7, 8]. In contrast, through periodic flow inversions, we show that segregation can be effectively eliminated. The critical frequency of these flow perturbations is related to the inverse of the characteristic time of segregation and is shown to scale with the shear rate of the particle flow. As an application of this theory, one can achieve a dramatic increase in the asymptotic degree of mixedness for typically segregating systems, as well as in the mixing rate to achieve the asymptotic state through novel placement of baffles.

Gas-solid transport is crucial in a variety of industrially important applications. In particular, the fluidization and transport of solid particles either by gravity or by pneumatic means are used in fluidized catalytic cracking, fluid hydro-forming and solid fuel processes such as coal gasification and liquefaction [9]. The most widely used classification system for particles in gas-solid flows was introduced by Geldart [10, 11] based on the density difference between the particles and the gas ($\rho_p - \rho_g$) and the average particle diameter d_p. In this system, particles are generally considered cohesive (C), aeratable (A), sand-like (B), and spoutable (D) as particle diameter increases (Figure 1). In many instances the cohesive nature of a powder sample is a prime factor contributing to difficulties in powder flowability, for example, causing channeling and defluidization in combustion/feeder systems. Despite recent advances [12, 13, 14, 15], an understanding of the flow and characterization of cohesive gas-solid flows remains poor and manipulation/control of the flow variables is still largely done on a trial-and-error basis. While some progress has been made in our understanding of liquid-induced cohesion at the macroscopic level, in general, it is still not possible to directly connect this macroscopic understanding of cohesion with a microscopic picture of the particle properties and interaction forces. In fact, conventional theories make no attempt to distinguish between these modes of cohesion, despite clear qualitative differences (lubrication forces in wet systems or electrostatic repulsion are two good examples); however, we show that quantifying cohesion using the Granular Capillary Number (Ca_g), which is a ratio of the capillary force to the drag force, yields a collapse of data for varying surface tensions and fluidization velocities. This leads to a clear transition from free-flowing to cohesive behavior at a distinct value of Ca_g. In addition, we extend this argument from a homoge-

neous system to binary systems, where particles have different sizes, densities and/or wetting characteristics. In order to examine the impact of cohesion on particle mixing/segregation, we use this extended Granular Capillary Number to outline a predictive theory of cohesive mixing/segregation based on phase diagrams. A combined PD and CFD model is used to simulate the gas-solid flows and several points of the phase diagram are tested.

Coupled PD and CFD have been widely used for the study of fluidized beds [3, 12, 13, 14, 15, 16, 17, 18], however for rotary kilns, no such simulations exist to the best of our knowledge. For some chemical and pharmaceutical products, it is desirable to reduce the water content by thermal treatment in a kiln[19]. In metals or minerals processing and wood dehumidifying, roasting in a rotary kiln is a common routine [20, 21]. Hence, we extend previous work of gas-solid flow in fluidized beds to heat transfer in rotary kiln. To maintain simplicity, while simulating the cylindrical kiln, we use a non-uniform grid in our code. Different materials, particle sizes and rotation speeds are used to track the transition from convection-dominated heat transfer to conduction-dominated heat transfer.

Liquid transfer between particles plays the central role in a series of industrial applications such as flotation, coating, flocculation, granulation and drying. During these processes, wetting, dewetting and mixing all take place simultaneously. In each of these applications, the local liquid concentration within the bed dramatically affects the flow behavior of the system and can strongly impact performance. We develop a liquid transfer model which will help on the understanding of liquid transfer between particles. We explicitly track moisture levels on individual particles and utilize an experimentally validated rule-set for liquid transfer upon forming/breaking contacts. Thus it can aid in the control of these processes. We expect that this liquid transfer-modified PD is general and would be applicable to wide range of processing operations.

Drying of particulate materials involves a complex combination of mass (liquid transfer between particles, liquid evaporation to the gas phase and mass transfer in the gas phase), momentum (solid contacts, gas flow, inter-phase momentum transfer) and heat transfer (heat transfer on solid contacts, convective heat transfer in gas phase, inter-phase heat transfer). There is no previous model capable of addressing this topic. By combining elements of our

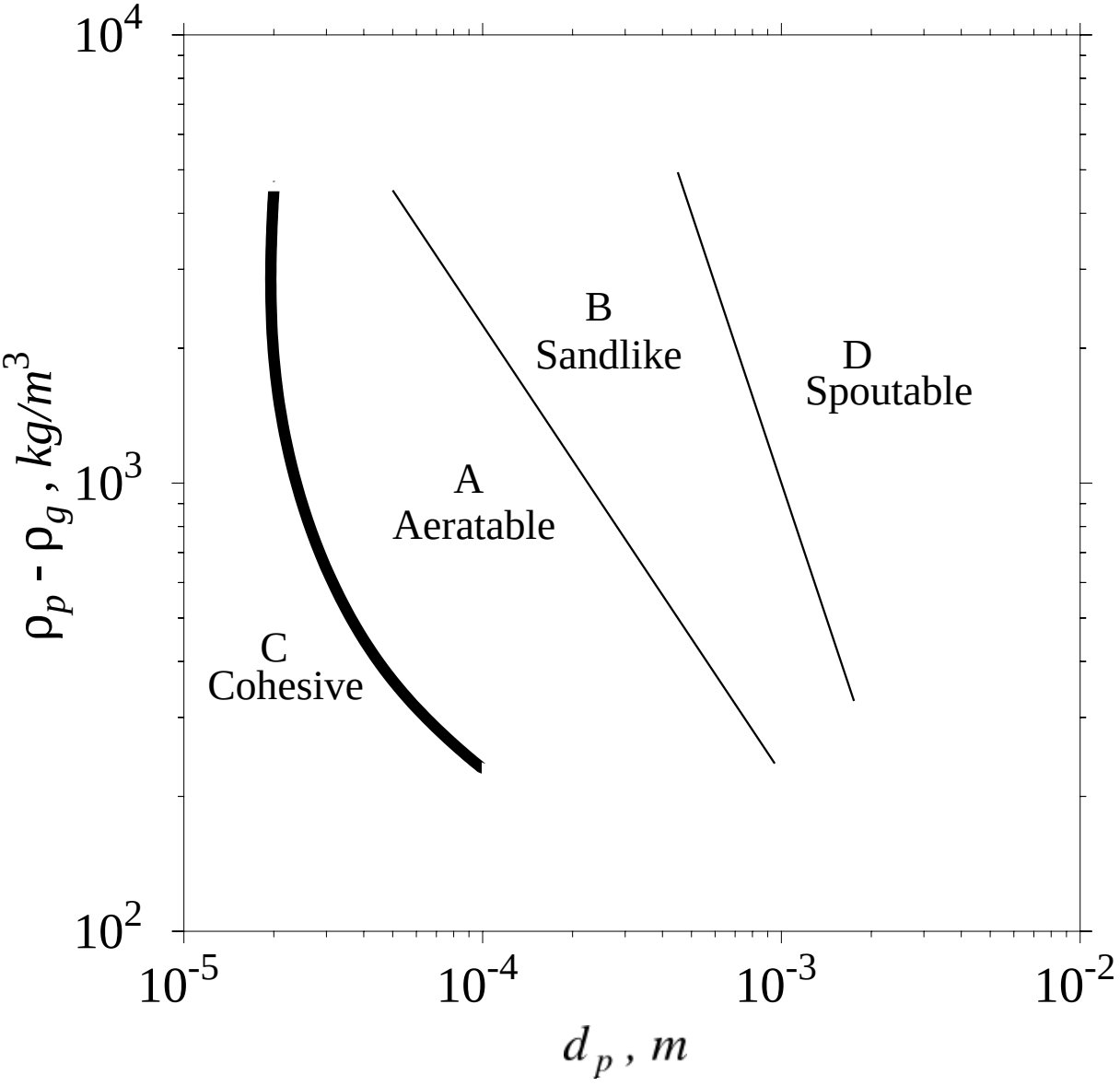

Figure 1: Geldart's classification of fluidized particles

PD/CFD heat transfer model with our liquid transfer and newly developed mass transfer (liquid evaporation from particle surface to gas phase and mass transfer in the gas phase) models, we develop a method to fully model the drying process.

Despite the degree of rigor employed in the simulations presented in this work, most current research in particle processing is focused on isotropic particles, meaning that individual particles are considered to have uniform physico-chemical properties as well as temperatures, and liquid distributions etc. While this is accurate for small particles and slow external transport, under certain conditions, it may be necessary to consider different parts of the particle to be different either in properties or temperature, concentration etc. This dissertation will discuss how to simulate anisotropic particles in PD such that we can study the issues of heat transfer inside a particle, unevenly distributed liquid on a particle surface and complex particle mixing.

This dissertation is organized as follows. Chapter II deals with the background on cohesive granular materials, particle dynamics and computational fluid dynamics. Chapter III introduces a theory for eliminating segregation in free-flowing particle flows and it is validated by experiments and simulations in chute flow and a rotary kiln. In Chapter IV, the Granular Capillary Number (Ca_g) is developed for studying wet (cohesive) gas-solid flow. The utility of this tool is computationally tested for both mono-disperse and binary systems in fluidized beds. In Chapter V, heat transfer is incorporated into the gas-solid flows, and the code is modified in order to simulate a rotary kiln. Chapter VI outlines a liquid transfer model amenable to heterogeneous particle mixtures, (i.e., particle may have different sizes and contact angles). This model is used to simulate a spraying process in a rotary drum. Chapter VII discusses our drying process model, which includes mass, momentum and heat transfer models in both solid and gas phases. Chapter VIII is the outlook section which concentrates primarily on the development and use of an anisotropic particle model.

2.0 BACKGROUND

2.1 PARTICLE DYNAMICS

Particle Dynamics has emerged as one of the most important tools in probing granular flows [3, 12, 14, 15, 16, 22, 23, 24, 25, 26, 27]. This discrete method of simulation is extremely general in that Newton's second law of motion is used to determine the trajectories of individual particles as shown in Figure 2. The time evolution of these trajectories then determines the global flow of the granular material. The equations that describe the particle motion, therefore, are:

Linear Motion:

$$m_p \frac{d\mathbf{v}_p}{dt} = -m_p \mathbf{g} + \mathbf{F}_n + \mathbf{F}_t \tag{2.1}$$

Angular Motion:

$$I_p \frac{d\omega_p}{dt} = \mathbf{F}_t \times \mathbf{r} \tag{2.2}$$

where F_n and F_t are the interparticle forces – normal and tangential, respectively – acting on the particle and are functions of contact, drag, pressure and capillary interactions.

There are two types of particle dynamics simulations, i.e. the hard sphere model and the soft sphere model. The hard sphere model assumes all collisions are binary and instantaneous. The soft sphere model takes into account the multiple collisions/contacts and the delayed force propagation. While a soft particle technique is more robust and often more accurate, the technique is quite computationally expensive. A schematic of a soft sphere model, which consists of springs and dash-pots, is shown in Figure 3. The interparticle

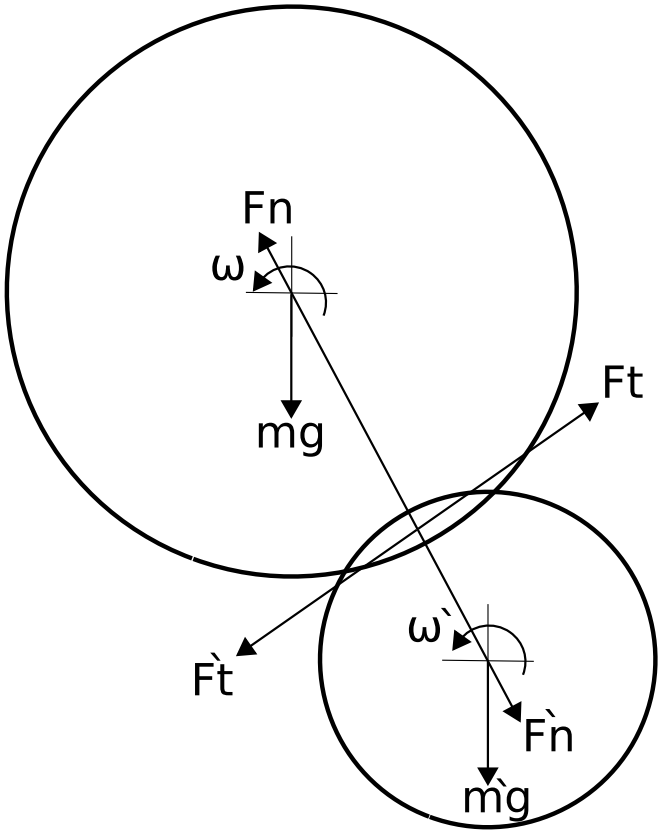

Figure 2: Forces acting on two contacting particles

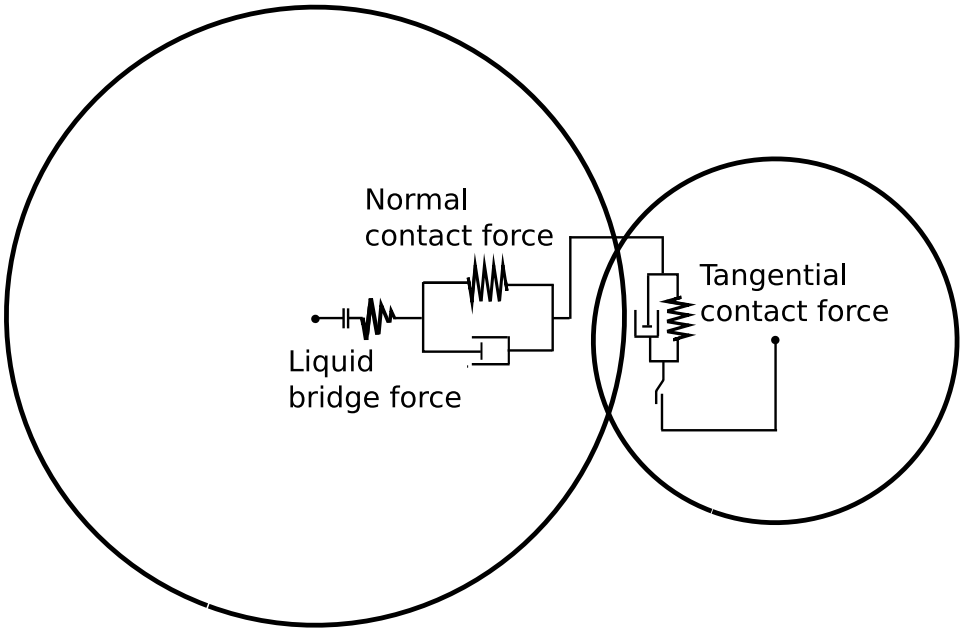

Figure 3: Forces model, including liquid bridge force, between two contacting particles

forces for cohesionless systems are typically determined from contact mechanics considerations, so that in their simplest form they include normal (often, Hertzian) repulsion [28] and some approximation of tangential friction [29].

The normal interactions are modeled as elasto-plastic contacts after the work of Thornton [30], while a single-parameter history-dependent friction is used in the tangential direction [31]. At the initial stages of loading the normal force, F_n, is given by

$$F_n = k_n \alpha^{3/2}, \tag{2.3}$$

where α is the deformation of the particles (computationally an "overlap" given by $\alpha = (R_1 + R_2) - C_{12}$ where R_i is the particle radius and C_{12} is the distance between particle centers), and k_n is the normal force constant from the Hertz theory[32]. The constant k_n is related to the particle radii, R_i, and elastic properties (Young's modulus, E_i, and Poisson ratio, ν_i) by

$$k_n = \frac{4}{3} E^* \sqrt{R^*}, \tag{2.4}$$

where R^* and E^* are

$$\frac{1}{E^*} = \frac{1-\nu_1^2}{E_1} + \frac{1-\nu_2^2}{E_2} \tag{2.5}$$

$$\frac{1}{R^*} = \frac{1}{R_1} + \frac{1}{R_2} \tag{2.6}$$

respectively. Once the normal force exceeds a yield force, F_y (essentially a fitting parameter), further loading is given by the linear expression

$$F_n = F_y + k_y(\alpha - \alpha_y). \tag{2.7}$$

In this expression, k_y is the plastic stiffness, which is related to the yield force by $k_y = (2/3)(F_y/\alpha_y)$, and α_y is the deformation at the point of yield. Unloading prior to exceeding the yield limit is purely elastic, while unloading after the yield limit is given by

$$F_n = F_{max} - k_n \sqrt{\bar{R}} (\alpha_{max} - \alpha)^{3/2}, \tag{2.8}$$

where F_{max} and α_{max} are the maximum force and deformation, respectively and $\bar{R}$ is the ratio of the new contact radius due to plastic deformation, R', to R^*,

$$\bar{R} = \frac{R'}{R^*} = \frac{F_y}{F_{max}} \left(\frac{2F_{max} + F_y}{3F_y} \right)^{3/2}. \tag{2.9}$$

The tangential or frictional force is derived from Walton and Braun [33]. A complete description of the implementation of this expression is given by Walton [34], and only the expressions themselves are shown here.

At any time-step, the new tangential force acting at a particle-particle contact, F_t, is given by the sum of the old tangential force, F_{t_o}, and the incremental change in the tangential force due to motion during the present time-step. This yields

$$F_t = F_{t_o} - k_s \Delta s, \tag{2.10}$$

where Δs is the displacement during the present time-step and is easily calculated from the component of velocity tangent to the contact surface, v_t (i.e., $\Delta s = v_t dt$ where dt is the time-step). In order to mimic an annular region of micro-slip at the edge of the contact (as described by Mindlin [29]) as well as limit the overall tangential force to the Amonton's Law limit ($F_t \leq \mu F_n$ where μ is the coefficient of sliding friction), the frictional stiffness, k_t, is given by the nonlinear expressions

$$k_t = k_{t_o} \left(1 - \frac{F_t - F_t^*}{\mu F_n - F_t^*} \right)^{\gamma}, \quad for\ increasing\ F_t \tag{2.11}$$

$$k_t = k_{t_o} \left(1 - \frac{F_t^* - F_t}{\mu F_n + F_t^*} \right)^{\gamma}, \quad for\ decreasing\ F_t. \tag{2.12}$$

The first expression is used when the direction of the incremental change in the tangent force would result in an increase in the total F_t and the second corresponds to a decrease in F_t. The quantity F_t^* refers to the value of F_t at the point in which the direction of tangential slip changes. The value γ is a constant which is typically set to (1/3) to parallel the expression from Mindlin [29] and k_{t_o} is the initial tangential stiffness and is related to the Hertzian normal stiffness by

$$k_{t_o} = \frac{k_n(1-\nu)}{1-\nu/2}. \tag{2.13}$$

2.1.1 Capillary Forces

Moisture is a common cause of cohesion in particle flows and the forces arising due to the same have been modeled using the concept of liquid bridges. The amount of moisture/liquid determines the degree of saturation which may be characterized as pendular, funicular, capillary and droplet (Figure 4). The pendular regime assumes the saturation is low enough that discrete binary bridges are present between solid surfaces. Several models for this regime based on the solution of the Young-Laplace equation are available in the literature [14, 15, 35] (Figure 5). The capillary force, F_c between particles with suitable wetting characteristics, due to both the surface tension of the bridge fluid as well as the pressure difference arising from neck curvature may be approximated (assuming a toroidal shape for the bridge profile) as:

$$F_c = 2\pi r_2 \gamma sin\beta sin(\beta+\theta) + \pi r_2^2 \Delta P sin^2\beta, \tag{2.14}$$

where r_2 is the bridge neck radius, β is the half filling angle, θ is the contact angle, γ is the fluid's surface tension and ΔP is the pressure difference across the air-liquid interface. The pressure reduction across the capillary bridge is given by the Laplace equation

$$\Delta P = \gamma \left[\frac{1}{r_1} - \frac{1}{r_2}\right], \tag{2.15}$$

where r_1 is the bridge meridional radius of curvature. Alternatively, Mikami *et al.* [15] provide an empirical fit to the numerical solution of the Laplace-Young equation not relying on the toroidal approximation, which is valid for particles with similar wetting characteristics. In dimensionless form, this is given as

$$\hat{F} = exp(A\hat{h} + B) + C \tag{2.16}$$

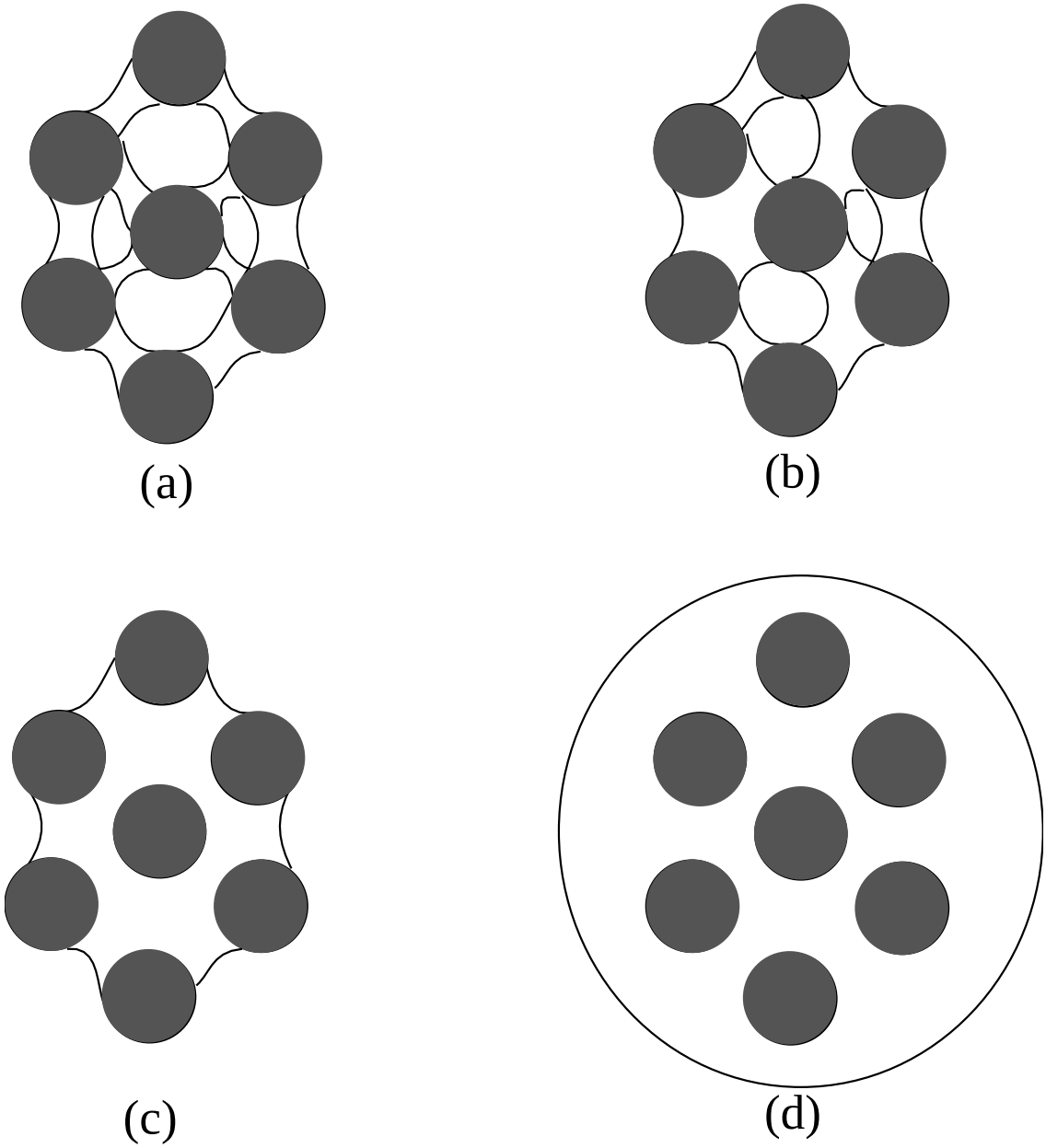

Figure 4: Degrees of liquid saturation: (a) pendular; (b) funicular; (c) capillary; (d) droplet.

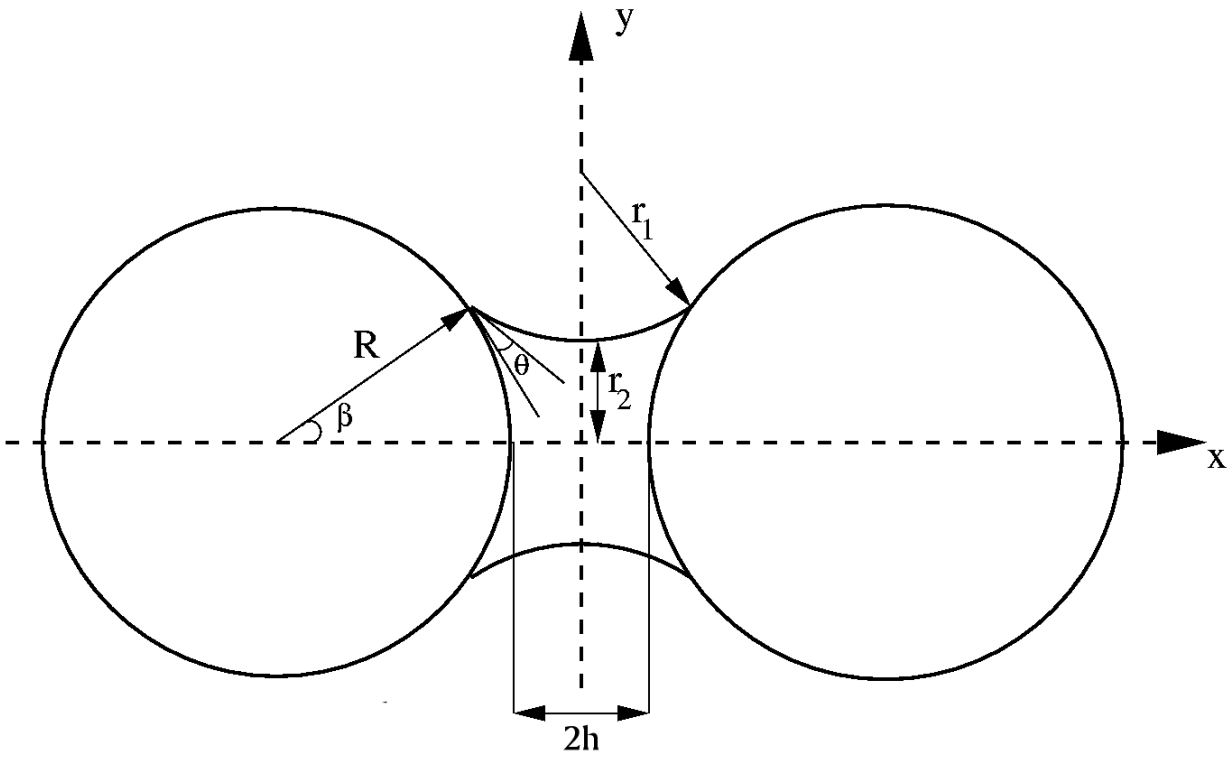

Figure 5: Schematic of a symmetric liquid bridge.

$$A = -1.1\hat{V}^{-0.53}$$

$$B = (-0.34ln\hat{V} - 0.96)\theta^2 - 0.019ln\hat{V} + 0.48 \tag{2.17}$$

$$C = 0.0042ln\hat{V} + 0.0078$$

where $\hat{F}$ is the normalized capillary force ($F_c/2\pi R\gamma$); $\hat{V}$ is the bridge volume made dimensionless by the particle radius (R); $2\hat{h}$ is the separation distance between the particle made dimensionless by the particle radius (R); and A, B and C are constants. In our simulations, the moisture content is assumed to be sufficiently low that bridges only form upon contact of the solid surfaces. These bridges remain in place, however, after solid contact has ceased, until the particles reach a critical separation (rupture) distance (h_c) given by:

$$\hat{h}_c = (0.62\theta + 0.99)\hat{V}^{0.34}. \tag{2.18}$$

In order to avoid system-size effects, no bridges are formed between the particles and confining walls.

2.1.2 Viscous Forces

Dynamic formation/breakage of liquid bridges results in a viscous force resisting motion, derived from lubrication theory (see, for example Ref. [36]). It is essential that any liquid-induced cohesion simulation include these effects as they may become large relative to the capillary force as the particle velocity increases [37]. In the limit of rigid spheres, Adams and Perchard [38, 39] derive the viscous force in the normal direction (F_{v_n}) to be

$$F_{v_n} = 6\pi\mu R v_n \frac{R}{2h}, \tag{2.19}$$

where μ is the bridge fluid's viscosity, and v_n is the relative normal velocity of the spheres. In the tangential direction (F_{v_t}), Lian *et al.* [14] suggest the use of the the solution due to Goldman *et al.* [40] for the viscous force between a sphere and a planar surface

$$F_{v_t} = \left(\frac{8}{15} ln\frac{R}{2h} + 0.9588\right) 6\pi\mu R v_t, \tag{2.20}$$

where v_t is the relative tangential velocity of the spheres.

2.2 COMPUTATIONAL FLUID DYNAMICS

2.2.1 Differential Equations

Fluid flow is described by the continuity equation

$$\frac{\partial \rho}{\partial t} + (\nabla \cdot \rho u) = 0, \tag{2.21}$$

and momentum equation (Navier-Stokes Equation) [41]

$$\frac{\partial (\rho u)}{\partial t} + (\nabla \cdot \rho u u) = -\nabla p - \nabla \cdot \tau + \rho g. \tag{2.22}$$

For a continuum particulate phase, Anderson and Jackson [42] formulated continuum equations representing mass and momentum balances using the concept of local mean variables. The point variables are averaged over regions that are large compared to the particle diameter but small with respect to the characteristic dimension of the complete system.

The resulting mass and momentum balances for the fluid-phase, dropping the averaging brackets (<>) on the variables are as follows. The continuity equation is expressed:

$$\frac{\partial (\epsilon \rho_g)}{\partial t} + (\nabla \cdot \epsilon \rho_g u) = 0. \tag{2.23}$$

The momentum equation is expressed:

$$\frac{\partial (\epsilon \rho_g u)}{\partial t} + (\nabla \cdot \epsilon \rho_g u u) = -\epsilon \nabla p - \Sigma(\epsilon F_d) - \nabla \cdot \epsilon \tau_g + \epsilon \rho_g g, \tag{2.24}$$

where $\Sigma(\epsilon F_d)$ is the summation of all particles' drag force in the control volume.

2.2.2 Discretized Equations

In our model, we use the finite volume technique for obtaining the discretized equations. The advantage of finite volume over finite differences and finite element is that conservation is enforced in the construction of the discretized equations. The finite volume scheme begins with an integration of the governing equation over a control volume. The conservation law for the transport of a property ϕ can be written as:

$$\frac{\partial}{\partial t}(\rho\phi) + \nabla \cdot (\rho u\phi) = \nabla \cdot (\tau \nabla\phi) + S_\phi \tag{2.25}$$

where u represents the velocity vector and τ represents the diffusion coefficient. The first term of the equation represents the rate of change term. The second term gives the net convective flux. The right hand side of the equation represents the net diffusive flux and the generation of property ϕ within the control volume. A formal integration over a control volume ΔV gives:

$$\int_{\Delta_V} \left(\int_t^{t+\Delta t} \frac{\partial}{\partial t}(\rho\phi)dt \right) dV + \int_t^{t+\Delta t} \left(\int_A n \cdot (\rho \mathbf{u}\phi)dA \right) dt \;=\; \int_t^{t+\Delta t} \left(\int_A n \cdot (\tau\nabla\phi)dA \right) dt + \int_t^{t+\Delta t} \int_{\Delta_V} S_\phi dV\, dt. \tag{2.26}$$

Figure 6 shows the center of a fluidized bed that has a brick shape and is subdivided into small control volumes. In order to couple with the particle dynamics, the flow domain is divided into cells of width three times the particle diameter and discretized using a finite volume method. A staggered grid as shown in Figure 7 is employed to store the variables. The scalar variables are stored at the nodes marked $(\cdot)$ and denoted by upper case letters. The vectors are defined at the cell faces in between the nodes and denoted by lower case letters. In our notation W, E, N and S denote the nodes lying west, east, north and south of node P and w, e, n and s denote the faces lying west, east, north and south of node P, respectively. Horizontal $(\rightarrow)$ arrows indicate the locations for x-velocities (u_x) and vertical$(\uparrow)$ ones denote those for y-velocities (u_y). Unrealistic oscillating pressures which might be produced by using a co-located grid are easily avoided by using a staggered grid [43, 44]. In order to derive useful forms of the discretized equation, an approximation of the diffusive and convective terms is needed.

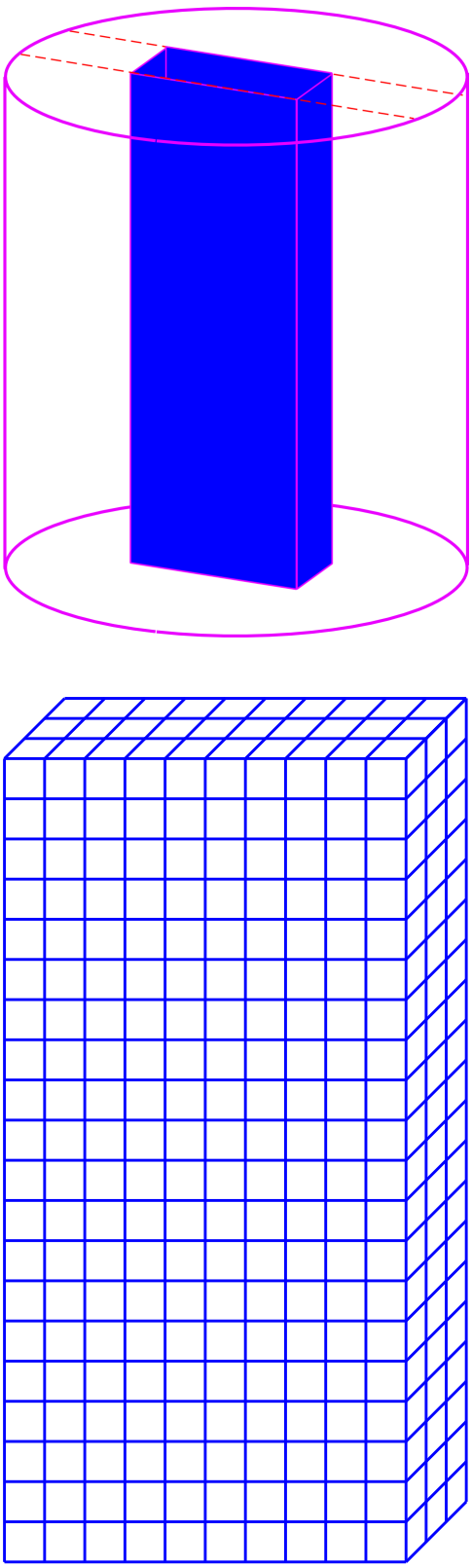

Figure 6: Mesh generation for fluidized bed.

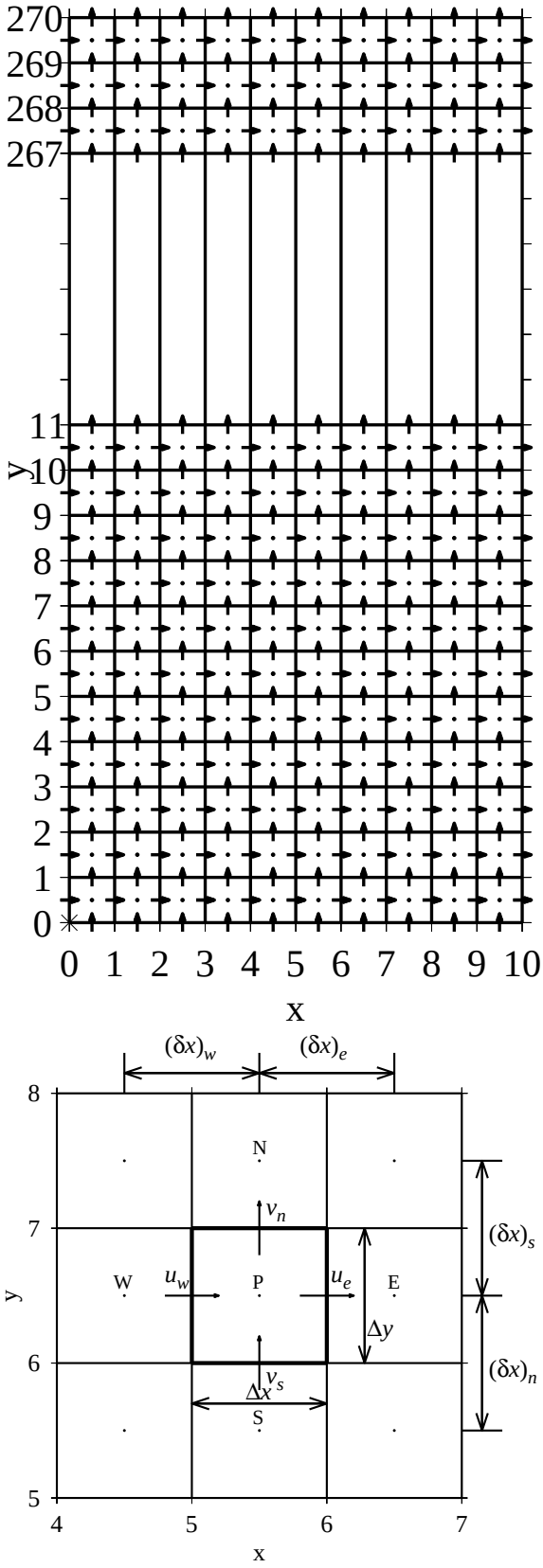

Figure 7: Staggered grid for fluid field.

The ratio of the strengths of diffusion and convection can be measured by the Péclet number, which is defined as $Pe = \frac{\rho u L}{\mu}$. The function $A(|Pe|)$ has different value based on which discretization scheme is used, as shown in Figure 8. For the upwind scheme, the value of $A(|Pe|)$ is 1.

Here the central differencing scheme is used to approximate the diffusive terms ($\tau A \frac{\partial \phi}{\partial x}$). For a uniform grid, an expression for the value of a property at a face can be written as:

$$\left(\tau A \frac{\partial \phi}{\partial x}\right)_e = \tau_e A_e \left(\frac{\phi_E - \phi_P}{\delta x_{PE}}\right) \tag{2.27}$$

$$\left(\tau A \frac{\partial \phi}{\partial x}\right)_w = \tau_w A_w \left(\frac{\phi_P - \phi_W}{\delta x_{WP}}\right) \tag{2.28}$$

where δx_{PE} and δx_{WP} represent the distances between points P and E and W and P respectively, A_e and A_w represent the face areas, τ_e and τ_w represent the diffusivity at the faces. The central differencing is a direct outcome of the Taylor-Series formulation.

For the convective terms ($\rho u \phi$), using the central differencing scheme results in the possibility of negative discretized coefficients which can lead to physically unrealistic results. One method of avoiding this difficulty is to use the upwind scheme. According to the upwind scheme, the value of ϕ at an interface is equal to the value of ϕ at the grid point on the upwind side. In other words,

$$\phi_e = \phi_P \text{ if } G_e \geq 0 \tag{2.29}$$
$$\phi_e = \phi_W \text{ if } G_e \leq 0$$

where $G_e = (\rho u_x)_e$.
The conditional statements can be rewritten as:

$$G_e \phi_e = \phi_P ||G_e, 0|| - \phi_E || - G_e, 0|| \tag{2.30}$$

where $||A, B||$ represents the maximum of A and B.

The evolution of the value of ϕ can be determined from the old value ϕ^0 and the new value ϕ^1 as

$$\phi = f\phi^0 + (1 - f)\phi^1, \tag{2.31}$$

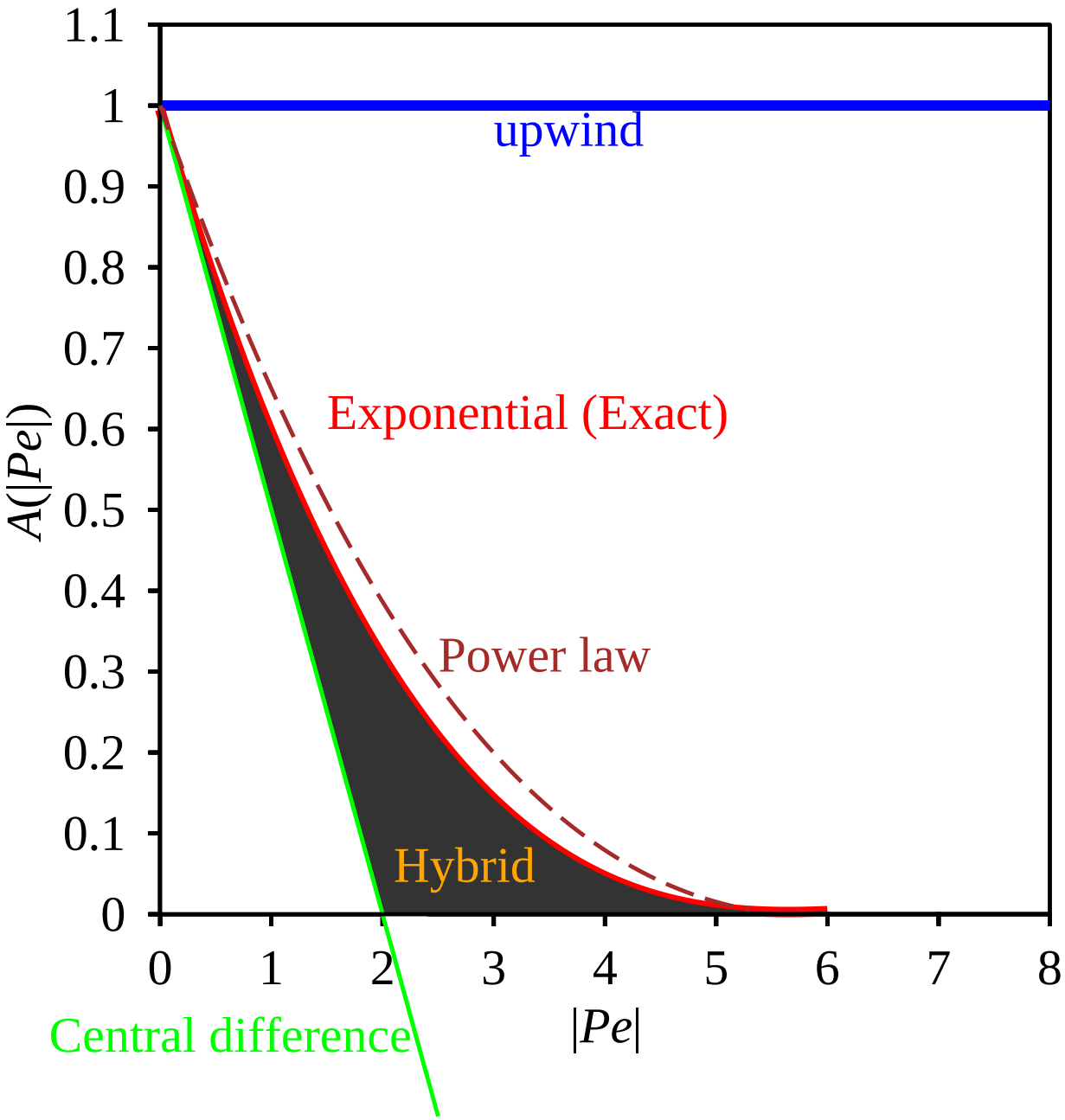

Figure 8: Function $A(|Pe|)$ for different schemes

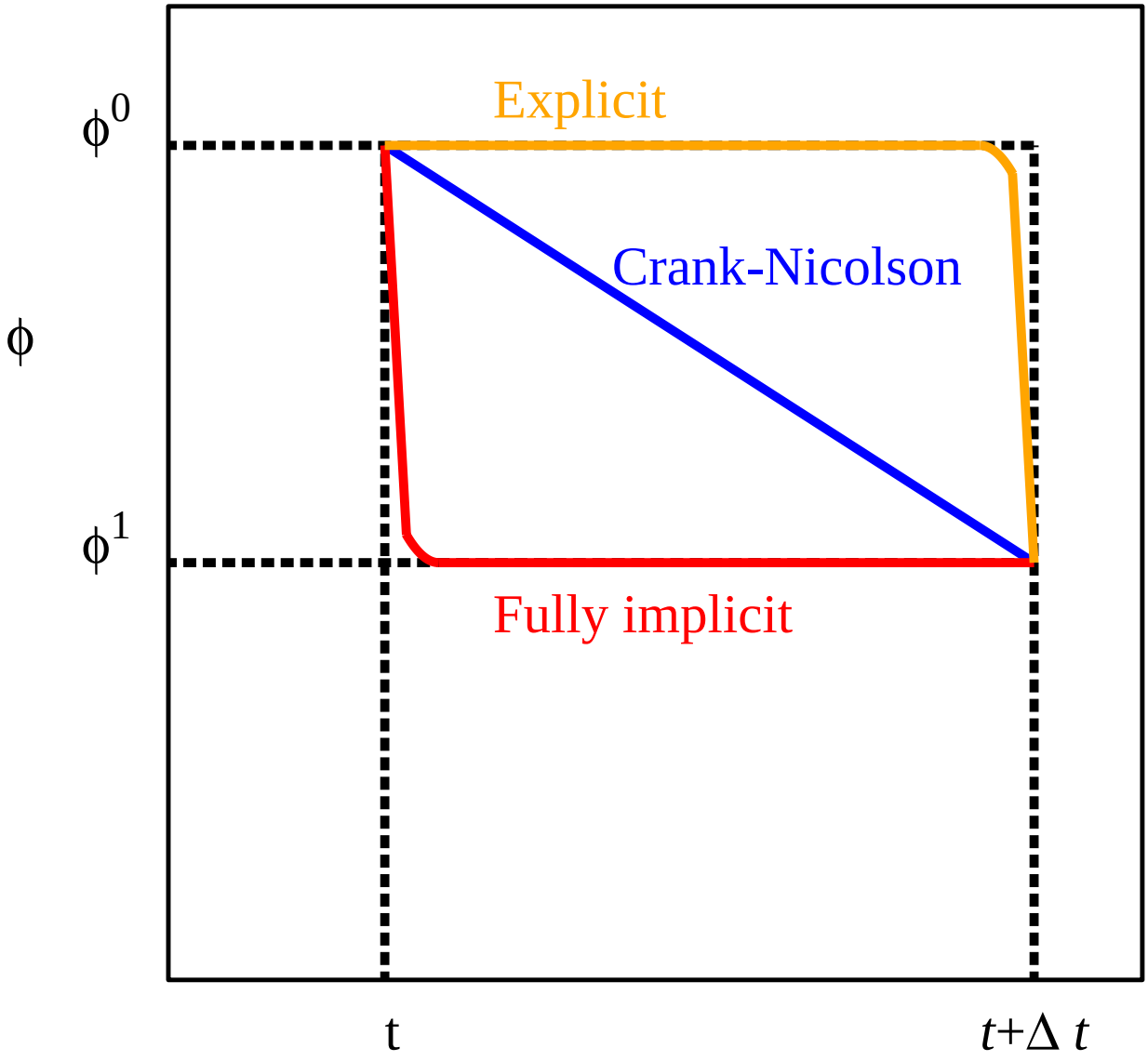

Figure 9: Variation of ϕ_p with time for different schemes

where f is a weighting factor between 0 and 1. In particular, $f = 0$ leads to an explicit time integration scheme, $f = 0.5$ to the Crank-Nicolson scheme (famous for its is unconditionally stable but causing oscillations for large time step), and $f = 1$ to the fully implicit scheme, as shown in Figure 9. If a fully implicit scheme is adopted for discretizing the temporal terms, the variable ϕ assumes the new value ϕ^1 at the beginning of the time step. With the implicit time scheme, all flux coefficients are positive making it stable and robust for any size of time step.

Any given discretized equation should have the following properties:

1. Conservativeness: To ensure conservation of ϕ for the whole solution domain, the flux of ϕ leaving a control volume across a certain face must be equal to the flux of ϕ entering the adjacent control volume through the same face. To achieve this, the flux through a common face must be represented by the same expression.
2. Boundedness: The 'boundedness' criterion states that in the absence of sources, the internal nodal values of the property ϕ should be bounded by its boundary values. To ensure this, the following should be kept in mind:
   - All coefficients of the discretized equation should have the same sign.
   - The Scarborough criterion must be satisfied:

$$\Sigma\frac{a_{nb}}{a_P}\begin{cases} \leq 1 & \text{at all nodes} \\ < 1 & \text{at one node at least} \end{cases} \tag{2.32}$$

The final two-dimensional discretized equation for a property ϕ can be written as:

$$a_p\phi_p = a_E\phi_E + a_W\phi_W + a_N\phi_N + a_S\phi_S + b, \tag{2.33}$$

where,

$$a_E = D_eA(|Pe_e|) + ||-G_e, 0|| \tag{2.34}$$

$$a_W = D_wA(|Pe_w|) + ||G_w, 0|| \tag{2.35}$$

$$a_N = D_nA(|Pe_n|) + ||-G_n, 0|| \tag{2.36}$$

$$a_S = D_sA(|Pe_s|) + ||G_s, 0|| \tag{2.37}$$

$$a_P^o = \frac{\rho_P^o\Delta x\Delta y}{\Delta t} \tag{2.38}$$

$$b = S_C + a_P^o\phi_P^o \tag{2.39}$$

$$a_P = a_E + a_W + a_N + a_S + a_P^o - S_P\Delta x\Delta y \tag{2.40}$$

and Δx and Δy represent the dimensions of the control volume. ϕ_P^0 and ρ_P^0 refer to the values at the previous time step.

Notice, the source term is

$$S = S_c + S_p\phi_p. \tag{2.41}$$

2.2.3 Solution Method

A discretized equation for pressure is needed for solving the pressure-velocity field. If the flow is compressible, the continuity equation is used as a transport equation for density; however for incompressible flows, the density is constant and not linked to the pressure. In this scenario, the continuity equation may be used to derive an equation for pressure, but it introduces a constraint on the solution of the flow field: if the correct pressure field is applied in the momentum equations the resulting velocity field should satisfy continuity. The SIMPLE (Semi-Implicit Pressure Linked Equations) algorithm [44] tackles these problems by adopting an iterative solution strategy. The pressure and velocities are resolved into two components, guessed and corrected:

$$p = p^* + p^{'} \tag{2.42}$$

$$u_x = u_x^* + u_x^{'} \tag{2.43}$$

$$u_y = u_y^* + u_y^{'} \tag{2.44}$$

where the superscript $*$ denotes the guessed part and $'$ denotes the corrected portion. The momentum equation for the x-velocity can be written by replacing ϕ with the u_x in Eq. 2.33:

$$a_e u_{x_e} = \Sigma a_{nb} u_{x_{nb}} + (p_P - p_E) A_e + b \tag{2.45}$$

where subscript nb represents the neighbor coefficients.
Similarly, the momentum equation for y-velocity can be written as:

$$a_n u_{y_n} = \Sigma a_{nb} u_{y_{nb}} + (p_P - p_N) A_n + b. \tag{2.46}$$

Using Eq. 2.42 and Eq. 2.43, the x-momentum equation can be rewritten as:

$$a_e u_{x_e}^* = \Sigma a_{nb} u_{x_{nb}}^* + (p_P^* - p_E^*) A_e + b \tag{2.47}$$

$$a_e u_{x_e}^{'} = \Sigma a_{nb} u_{x_{nb}}^{'} + (p_P^{'} - p_E^{'}) A_e, \tag{2.48}$$

and the y-momentum equation can be rewritten using Eq. 2.42 and Eq. 2.44 as:

$$a_n u^*_{y_n} = \Sigma a_{nb} u^*_{y_{nb}} + (p^*_P - p^*_N) A_n + b \tag{2.49}$$

$$a_n u^{'}_{y_n} = \Sigma a_{nb} u^{'}_{y_{nb}} + (p^{'}_P - p^{'}_N) A_n. \tag{2.50}$$

Since dropping the term $\Sigma a_{nb} u^{'}_{nb}$ in Eq. 2.48 will help to yield the converged solution which still satisfies Eq. 2.48, $\Sigma a_{nb} u^{'}_{nb}$ is dropped from the Eq. 2.48. A detailed discussion on this dropping issue can be found in Ref. [44]. Thus, the equation can be rewritten as:

$$a_e u^{'}_{x_e} = (p^{'}_P - p^{'}_E) A_e \tag{2.51}$$

Hence, the total velocity can be written as:

$$u_{x_e} = u^*_{x_e} + d_e (p^{'}_P - p^{'}_E). \tag{2.52}$$

where $d_e = \frac{A_e}{a_e}$.

A similar procedure can be applied to the y-velocities to obtain:

$$u_{y_n} = u^*_{y_n} + d_n (p^{'}_P - p^{'}_N). \tag{2.53}$$

These x and y velocities can be plugged into the continuity equation and a pressure correction equation can be obtained. The continuity equation for an incompressible flow can be written as:

$$\frac{\partial u_x}{\partial x} + \frac{\partial u_y}{\partial y} = 0. \tag{2.54}$$

The corresponding discretized equation becomes:

$$a_P P^{'}_P = a_E P^{'}_E + a_W P^{'}_W + a_N P^{'}_N + a_S P^{'}_S + b^{'} \tag{2.55}$$

where,

$$a_E = \rho_e d_e A_e \tag{2.56}$$

$$a_W = \rho_w d_w A_w \tag{2.57}$$

$$a_N = \rho_n d_n A_n \tag{2.58}$$

$$a_S = \rho_s d_s A_s \tag{2.59}$$

$$a_P = a_E + a_W + a_N + a_S; \tag{2.60}$$

$$b^{'} = [(\rho_w u^*_{x_w} A_w) - (\rho_e u^*_{x_e} A_e)] + [(\rho_s u^*_{y_s} A_s) - (\rho_s u^*_{y_n} A_n)]. \tag{2.61}$$

The SIMPLE algorithm operation sequences are:

1. Guess the pressure field p^*
2. Solve the discretization momentum equation to obtain u^*, v^*, w^*

$$a_e u^*_e = \Sigma a_{nb} u^*_{nb} + b + (p^*_P - p^*_E) A_e \tag{2.62}$$

3. Solve the $p^{'}$ equation

$$a_P p^{'}_P = a_E p^{'}_E + a_W p^{'}_W + a_N p^{'}_N + a_S p^{'}_S + a_T p^{'}_T + a_B p^{'}_B + b \tag{2.63}$$

4. Calculate corrected pressure p from equation

$$p = p^* + p^{'} \tag{2.64}$$

5. Calculate u, v, w from their velocity-correction formulas

$$u_e = u^*_e + d_e(p'_P - p'_E) \tag{2.65}$$

6. Treat the corrected pressure p as a new guessed pressure p^*, repeat from step 2 until a converged solution is obtained.

A schematic of the algorithm is shown in Figure 10. The solver used in our code is the Gauss-Seidel step-by-step method. The values of the variable are calculated by visiting each grid point sequentially. Only one set of variables are maintained in the memory. For the first iteration these represent initial guesses. For neighbors that have already been visited during the current iteration, the new values are used. When all grid points have been visited, one iteration of Gauss-Seidel is completed.

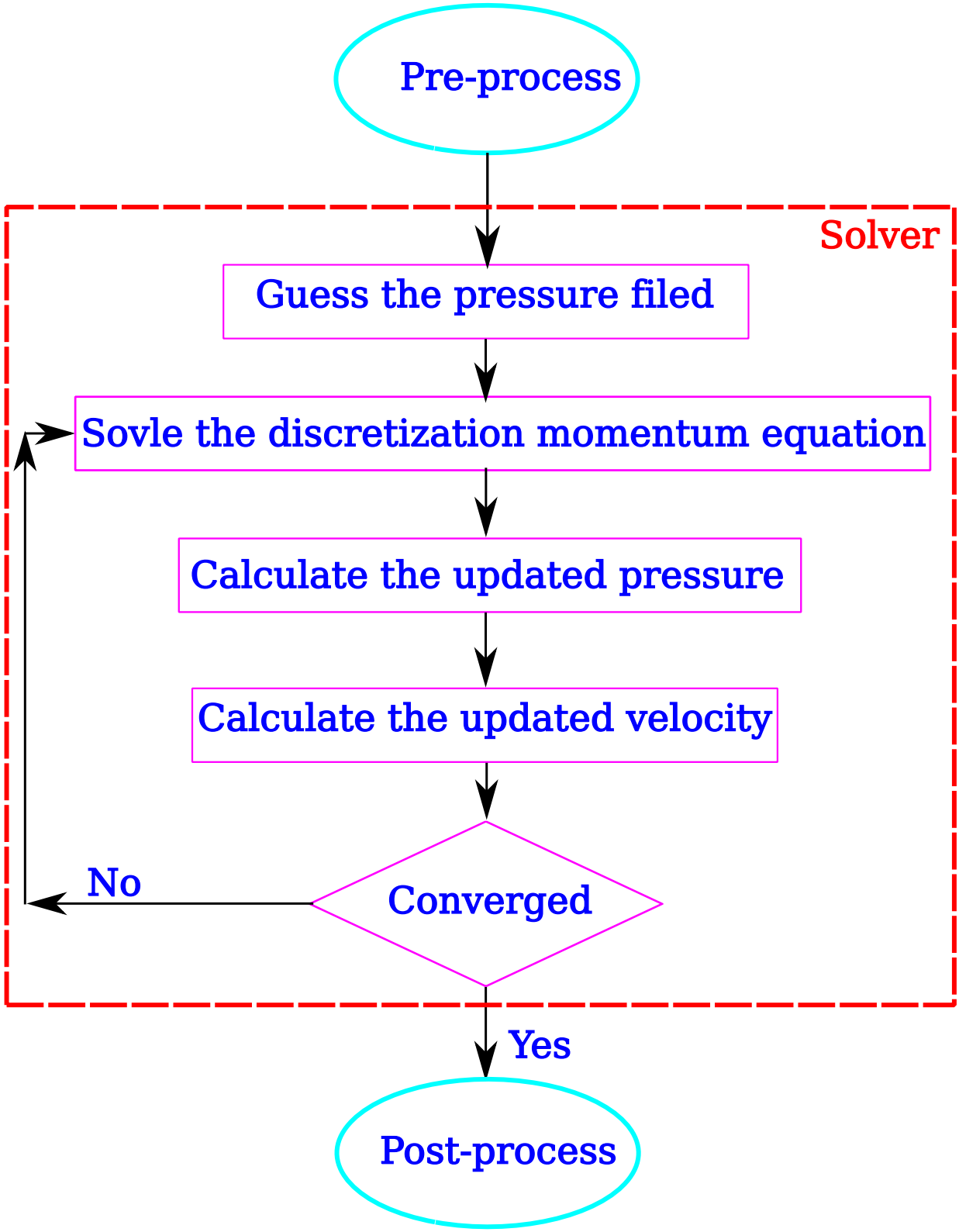

Figure 10: CFD calculation algorithm

2.3 COUPLING OF PARTICLE DYNAMICS AND COMPUTATIONAL FLUID DYNAMICS

2.3.1 Porosity

The porosity is the ratio of the void volume to the volume of a computational cell. In gas-solid flow systems, it is possible that a particle belongs to several adjacent cells. If V_i is the volume of particle i inside a computational cell, then the porosity is calculated as

$$\epsilon = 1 - \frac{\Sigma V_i}{\Delta x \Delta y \Delta z} \tag{2.66}$$

This above definition is exact in 3-D simulations; however, in a 2-D simulation, it will give porosity values not comparable with those for a 3-D simulation [45, 46]. If all the particles have similar diameter, a pseudo 3-D value can be obtained through a 2-D simulation [18] by assuming the cell thickness Δz equal to the diameter of a spherical particle. In other words, the pseudo 3-D simulation will examine only 1 layer of particles. Though the simulation may be much faster than a true 3-D simulation, the porosity may still be larger than the corresponding 3-D cases.

2.3.2 Inter-Phase Interaction

In gas-solid flows, the gas phase will exert a force on the solid phase. Based on Newton's third law of motion, the solid phase will exert an equal, yet opposite, force on the gas phase. This inter-phase interaction is the coupling term between the particle dynamics and computational fluid dynamics realizations and can be expressed as [47, 48]

$$\mathbf{f}_{fpi} = -v_{pi}\nabla p + v_{pi}\nabla \cdot \tau_f + \epsilon \mathbf{f}_{di} \tag{2.67}$$

where v_{pi} is the individual particle volume, τ_f is the stress tensor, and f_{di} is the drag force.

A general constitutive equation for the stress tensor τ_f may be written as

$$\tau_f = ((\mu_b - \frac{2}{3}\mu_s)\nabla \cdot u)\delta + \mu_s((\nabla u) + (\nabla u)^{-1}) \tag{2.68}$$

where μ_b is the bulk viscosity and μ_s is the shear viscosity, while

$$\delta = \begin{bmatrix} 1 & 0 & 0 \\ 0 & 1 & 0 \\ 0 & 0 & 1 \end{bmatrix}$$

is the identity tensor.

Drag between the gas and the particle couples the discrete simulation to the fluid flow and represents the primary mode of inter-phase momentum transfer. The drag force not only depends on the local fluid flow field but also on the presence of the neighboring particles [49]. It is extremely difficult to determine the drag force theoretically. The Ergun [50] and Wen-Yu [51] correlations are often used [52, 53, 54, 55, 56, 57, 58, 59] for evaluating drag forces in small and large porosity gas-solid flow systems, respectively. Using these correlations, the drag force is given by

$$\mathbf{f}_d = \frac{\beta V_p}{1-\epsilon}(\mathbf{u} - \mathbf{v}_p), \tag{2.69}$$

$$\beta = \begin{cases} 150\frac{(1-\epsilon)^2}{\epsilon}\frac{\mu_g}{d_p^2} + 1.75(1-\epsilon)\frac{\rho_g}{d_p}|\mathbf{u} - \mathbf{v}_p| & \epsilon < 0.8 \qquad Ergun \\ \frac{3}{4}C_d\frac{1-\epsilon}{d_p}\rho_g|\mathbf{u} - \mathbf{v}_p|\epsilon^{-2.65} & \epsilon \geq 0.8 \qquad Wen - Yu \end{cases}$$

where the drag coefficient C_d is a function of the particle Reynolds number:

$$C_d = \begin{cases} \frac{24}{Re}(1 + 0.15Re^{0.687}) & Re < 1000 \\ 0.44 & Re \geq 1000 \end{cases}$$

and the particle Reynolds number Re is based on the superficial slip velocity

$$Re = \frac{2R\rho_g\epsilon|\mathbf{u} - \mathbf{v}_p|}{\mu_g} \tag{2.70}$$

Since the Ergun and Wen-Yu correlations have a step change when ϵ is 0.8, it is unacceptable from a numerical point of view. Di Felice [60] suggests an empirical fit to a wide range of fixed and suspended-particle systems given as a single-function for the drag force

on a particle in a multi-particle system over the full practical range of particle Reynolds number. In the formulation:

$$\mathbf{f}_d = \frac{1}{2} C_d \rho_g \pi R^2 |\mathbf{u} - \mathbf{v}_p| (\mathbf{u} - \mathbf{v}_p) \epsilon^{-\chi+1}, \tag{2.71}$$

where u is the local gas velocity, v_p is the particle velocity, C_d and χ are functions of the particle Reynolds Number

$$C_d = \left[0.63 + \frac{4.8}{Re^{0.5}} \right]^2 \tag{2.72}$$

$$\chi = 3.7 - 0.65 \mathrm{e}^{-\frac{(1.5 - log_{10} Re)^2}{2}}. \tag{2.73}$$

Thus, the Di Felice correlation has no step change as in Ergun and Wen-Yu correlations at $\epsilon = 0.8$, and the Di Felice correlation is used in our simulations.

2.4 CODE VALIDATION

Coupling PD and CFD, the gas-solid flow system can be simulated and the pressure drop over the bed can be calculated (Section 4.1.2). The pressure drop at the minimum fluidization velocity is one of the few cases that can be used for verification of a model in the absence of experimental validation. A commonly accepted wisdom in fluidization studies is that the bed pressure drop at minimum fluidization should balance the weight of the bed of particles. Thus, for a fluidized bed at minimum fluidization, we can estimate the pressure drop as

$$\Delta P_{bed} = \frac{G_{bed}}{A_{bed}}, \tag{2.74}$$

where ΔP_{bed} is the pressure drop over the fluidized bed, A_{bed} is the cross sectional area of the gas inlet, and G_{bed} is the bed weight, i.e. the weight of all the particles in the fluidized bed,

$$G_{bed} = \sum_{i=1}^{n} m_i g. \tag{2.75}$$

Alternatively, if the porosity ϵ is known, the balanced pressure drop over the fluidized bed ΔP_{bed} can be calculated as

$$\Delta P_{bed} = [(1-\epsilon)\rho_p + \epsilon\rho_f]g. \tag{2.76}$$

Thus, the model can be validated by comparing the calculated value of the pressure drop to that achieved in the simulation.

2.5 MIXING INDEX

The mixing extent of the particles can be quantified based on the standard deviation σ of the composition of the mixture, or its square, the variance σ^2, which can be calculated from

$$\sigma^2 = \frac{\Sigma_{i=1}^{N}(c-\bar{c})^2}{N-1}, \tag{2.77}$$

where c and $\bar{c}$ are the particles local and average concentration, respectively, and N is the number of local concentrations. We define the local concentration to consist of each particle's 10 nearest neighbors, so that our number of measurements is the same as the number of particles in the systems.

For a binary system, values of mixture variance σ^2 lie between the completely segregated system ($\sigma_0^2 = P(1-P)$) and randomly mixed system ($\sigma_R^2 = P(1-P)/N$), where P is the proportion of one component in the whole mixture [61]. σ_R^2 is dependent on particle number. As the total number of particles in a system increases, σ_R^2 decreases, so that for large numbers of particles, σ_R^2 is negligible.

Our group has used intensity of segregation (IS), which is the standard deviation of the local concentration σ as shown below

$$IS = \sigma = \sqrt{\frac{\Sigma_{i=1}^{N}(c - \bar{c})^2}{N - 1}}, \tag{2.78}$$

for quantifying the mixing extent in fluidized beds [3] and rotary drums [26]. For a $50 : 50$ binary mixture, the value of IS is 0.5 for a completely segregated state and 0 for a randomly mixed state.

Several other mixing indices have also been developed based on the standard deviation. In pharmaceutical applications, the relative standard deviation (RSD) is used to ensure a specified percentage of all extracted samples meet the mixing protocols [1, 5]. RSD is defined to be

$$RSD = \frac{\sigma}{\bar{c}}. \tag{2.79}$$

Lacey's mixing index M is defined as [62, 63]:

$$M = \frac{\sigma_0^2 - \sigma^2}{\sigma_0^2 - \sigma_R^2}. \tag{2.80}$$

The Lacey mixing index is normalized because $M = 1$ and $M = 0$ correspond to completely random mixed and segregated states, respectively. As an example, we will calculate the Lacey's mixing index of the simulations in Section 3.4 to illustrate the working mechanism of mixing indices. Certainly, any above mentioned mixing index can be used to quantify the mixing result.

2.5.1 Mixing Extent

By letting both kinds of particles have the same volume, we make $P = 0.5$ in volumetric fraction for each component of the binary system. During the mixing processes, the Lacey mixing indices will increase from around 0 toward some asymptotic value, as shown in Figure 11 for different density particles. Figure 12 shows the evolution of the Lacey mixing index on different size particles. Typically, a tumbler achieves an asymptotic state after a couple of revolutions.

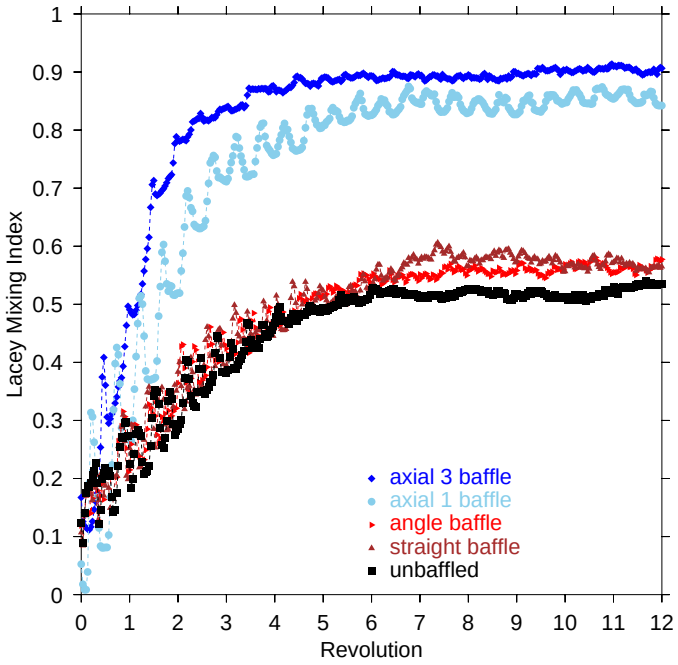

Figure 11: Lacey mixing index for different density particles

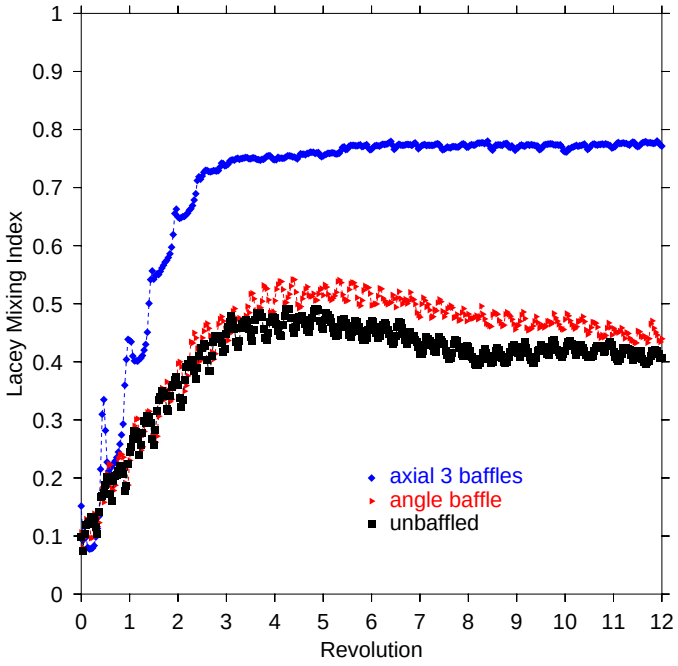

Figure 12: Lacey mixing index for different size particles

2.5.2 Mixing Rate

Often it is industrially significant to know not only the extent of mixing, but also the rate at which that asymptotic state is approached. In general, we will use the initial slope of the mixing index vs. t curves as a quantitative measure of the mixing state. Figure 11 shows that axially-baffled tumblers have resulted in a much larger slope before achieving asymptotic state than all other tumblers. Table 1 shows the times for achieving 90% of the highest mixing extent for each tumbler. We used 90% of the maximum Lacey mixing index here instead of the maximum Lacey mixing index due to the fluctuations evident in Figure 11. While the maximum Lacey mixing index is strongly affected by the fluctuations, we find that 90% of the maximum value is considerably less sensitive. As shown in Table 1, it takes 4.17s for an unbaffled mixer to achieve 90% of the highest mixing extent. For a tumbler with a single axially-located baffle, however, it takes only 3.30s to achieve that extent, or 78.7% of the time required for an unbaffled tumbler. Surprisingly, it takes even more time for a tumbler with conventional baffles to achieve that extent. For example, the time required for a tumbler with straight baffles is 41.3% higher than that for an unbaffled tumbler.

These results (see Table 1) show that both the mixing extent and mixing rate can be improved greatly by using our unconventional baffles.

Table 1: SIMULATION TIME ACHIEVING 90% MAXIMUM LACEY MIXING INDEX.

	Simulation	Max(M)	90% Max(M)	Time used to achieve 90% Max(M)	Used time relative to unbaffled tumbler
different density particles	unbaffled	54.8%	49.5%	4.17 s	100.0%
	straight baffle	60.6%	55.2%	5.93 s	141.3%
	angle baffle	59.2%	53.4%	5.77 s	137.3 %
	axial 1 baffle	87.5%	78.9%	3.30 s	78.6%
	axial 3 baffles	91.6%	82.9%	2.57 s	61.1%
different size particles	unbaffled	49.1%	44.4%	2.87 s	100.0%
	angle baffle	54.2%	49.1%	3.27 s	114.0%
	axial 3 baffles	78.0%	71.2%	2.50 s	87.2%

3.0 ELIMINATING SEGREGATION

Particle segregation has been a topic of intense research and industrial frustration for many decades [64, 65, 66, 67]. When particles differ in almost any mechanical property, processing typically leads to pattern formation [68, 69], layering [70, 71], or complete separation of the materials [72, 73, 74], and this non-homogeneity can cause dramatic revenue loss and product failure in a variety of industries. In particular, particles of different size and density may segregate quite strongly in free-surface flows; the larger (lighter) particles often rise to the top, while the smaller (denser) particles sink to the bottom. While recent efforts have made inroads in controlling segregation using cohesion [2, 75] or particle modification (to *balance* competing segregation modes) [76, 77], even these laudable efforts are not robust to changes in particle properties and/or cohesion degree and therefore are applicable to only a subset of typical industrial practice. Here, we show that periodic flow inversions either manually – in a chute – or via selective baffle placement – in a tumbler-type mixer – can serve as a general method for eliminating segregation in free-surface flows, perhaps the most common and well-studied of granular flows [78, 79, 80].

3.1 THEORY

Time-modulation in fluid mixing and other dynamical systems [81] is a common practice, but has found only limited application in granular processing [82, 83, 84]. The key to adapting this idea to free-surface segregation lies in recognizing that it takes a finite time for material to segregate and that there is always a preferred direction that particles tend to segregate. In

order to exploit these two facts, one needs to perturb the flow at a sufficiently high frequency, f, such that $f > t_s^{-1}$, where t_s is the characteristic segregation time.

A critical issue with this technique is that a full understanding of segregation kinetics – and therefore the characteristic segregation time, t_s – is still lacking. Nevertheless, using existing theoretical tools [72, 85], an estimate of the value of t_s, and therefore the critical forcing frequency, f_{crit}, may be obtained via a scaling argument, as follows. One may write a segregation flux expression as $J_s = v_s\phi$, where v_s is the segregation velocity and ϕ is the concentration of the segregating species. Taking density segregation as an example (size segregation is similar, albeit more complex [85]), the segregation velocity will take the form $v_s = K_s(1-\bar{\rho})$ [72], where $(1-\bar{\rho})$ is the dimensionless density difference and K_s will depend on the local void fraction and granular temperature, which is defined as,

$$T_g = \frac{(u_x - \bar{u}_x)^2 + (u_y - \bar{u}_y)^2 + (u_z - \bar{u}_z)^2}{3}, \tag{3.1}$$

where u_x, u_y, u_z are the instantaneous particle velocities of each individual particle, $\bar{u}_x$, $\bar{u}_y$,$\bar{u}_z$ are the local mean velocities in the shear layer. This version of granular temperature is based on the kinetic theory of gases and the analogy is clear between molecular chaos and the disordered motion of granular flows [79, 86, 87, 88]. Alternatively, the granular temperature can be defined as

$$T_g = m \cdot \frac{(u_x - \bar{u}_x)^2 + (u_y - \bar{u}_y)^2 + (u_z - \bar{u}_z)^2}{3k}, \tag{3.2}$$

so that it yields temperature units. In molecular kinetic theory, m is the mass of the molecule and k the Boltzmann constant. In the case of granular media, however, such a definition is meaningless because the mass is very large and the Boltzmann constant is small. Because of this, a temperature scale for granular flows is typically chosen such that $m/k = 1$ [79] as shown in Eq. 3.1. For a mixture of particles having different masses, the expression

$$T_g = m \cdot \frac{(u_x - \bar{u}_x)^2 + (u_y - \bar{u}_y)^2 + (u_z - \bar{u}_z)^2}{3}, \tag{3.3}$$

can be used.

The characteristic segregation time may then be written as $t_s = R/[K_s(1-\bar{\rho})]$, where R is the radius of the particles. Using this value, we can define a segregation-based Péclet

number as $Pe = \frac{K_s(1-\bar{\rho})R}{D_c}$, where D_c is the collisional diffusivity. Due to current theoretical uncertainty and the time-varying nature of our flow (as well as our granular temperature, etc.), we treat $\beta = K_s R/D_c$ as a fitting parameter that should be a decreasing function of the fluctuation energy of the flow and should be close to unity at small to moderate energies [72]. This yields $Pe = \beta(1-\bar{\rho})$, so that using the diffusivity as given by Ref. [45] ($D_c = 0.01R^2\dot{\gamma}$), we get t_s written as $t_s = \frac{t_D}{Pe} = \frac{R^2}{D_c Pe} = \frac{100}{\beta\dot{\gamma}(1-\bar{\rho})}$, where $\dot{\gamma}$ is the shear rate schematically depicted in Figure 13 and mathematically expressed as

$$\dot{\gamma} = \frac{\partial u_x}{\partial y}. \tag{3.4}$$

This suggests that the critical perturbation frequency, f_{crit}, will vary linearly with the shear rate as

$$f_{crit} = 0.01\beta\dot{\gamma}(1-\bar{\rho}). \tag{3.5}$$

A simple geometry can be used to illustrate how this might be accomplished. Consider a chute flow that "zig-zags" periodically in such a way that, at each bend, the bottom of the previous flow leg now becomes the top of the next flow leg, and so on (see Figure 14a). If the length, L, of each leg is chosen such that $L < U_{avg}t_s$. Our theoretical arguments suggest that segregation can be effectively thwarted. While this thought experiment is theoretically satisfying, physically implementing this model system, either computationally or experimentally, is cumbersome. Instead, we examine two analogues of the "zig-zag" mixer that are schematically depicted in Figure 14 (b and c).

3.2 ZIGZAG FLOW SIMULATION

Computationally, we mimic the "zig-zag" mixer using a vertically-bounded, periodic box whose sense of gravity oscillates vertically (see Figure 14b) using Particle Dynamics. In these 3D simulations, particles are initially randomly mixed, gravity is inclined at angles ranging from 22°-29° with respect to the horizontal, and particle-roughened walls are used.

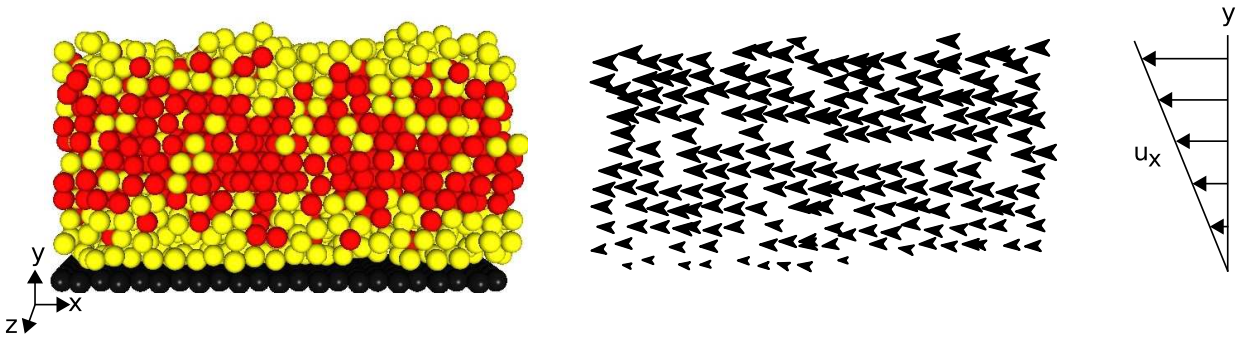

Figure 13: Shear rate calculation in granular material. The bed, which is a mixture of two kinds of particles, is shown in the left figure. The particle velocity u_x changes along y direction as shown in the middle figure. The right figure shows the velocity schematic in different layers.

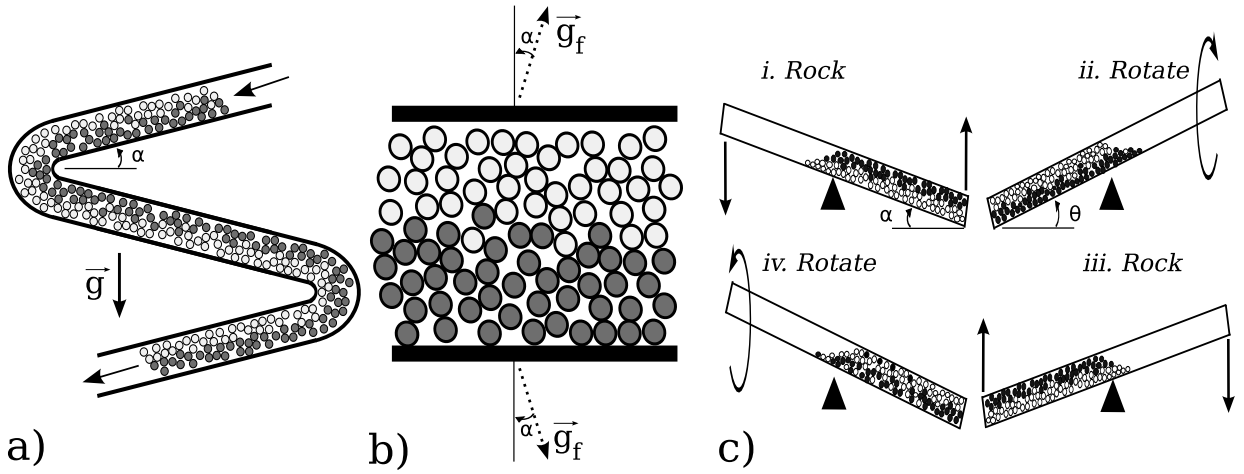

Figure 14: A schematic representation of the (a) "zig-zag" chute thought experiment, along with the (b) model simulation and (c) experiment used to approximate it. (a) In a vertical gravity field, the chute changes direction periodically so that the material becomes roughly inverted. (b) In our simulations, we use a simple model of this whereby the system is periodic in the flow direction and the inclined gravitational field, $\vec{g_f}$, has an oscillatory y-component. (c) Experimentally, in order to achieve an asymptotic concentration distribution in a modest-size system we put particles in a square tube which is first rocked, then rotated in order to alter the sense of gravity (taking advantage of particles' tendency to behave like a solid during the rotate step by angling the tube at $\theta >> \alpha$ (repose angle) during the rotate step).

Two particle bed heights, 10 and 20 particle diameters (2mm), are examined as are two density ratios, $\bar{\rho} = 0.5$ and 0.25 ($\rho_{light} = 1000\text{kg/m}^3$).

Figure 15 shows the time evolution of a zigzag flow in a simulation, where $f = 1/4$, $\bar{\rho} = 0.25$ and $\alpha = 24°$. Figure 15a depicts the simulation with oscillatory gravity in y direction. The arrows in Figure 15b shows the individual particle velocities in the bed and Figure 15c shows the average velocity values at different heights. The velocity gradient can be calculated based on these values, thus, we can get the shear rate for the system.

Figure 16 shows the evolution of IS for $\bar{\rho} = 0.25$ and $\alpha = 24°$ that are forced at different frequencies. In an average sense, we can get the following relationship of IS values, $f = 1/8, 1/6 > f = 1/4 > f = 1/2 > f = 1$. These results indicate that a larger frequency will help to eliminate segregation.

Figure 17 and 18 show the results for $\alpha = 26°$, the former having $\bar{\rho} = 0.25$ and the later having $\bar{\rho} = 0.5$. As the frequency is decreased, the fluctuations in IS values is increases.

The relationship of period and frequency is

$$T_{period} = \frac{1}{f}. \tag{3.6}$$

Thus, at 96s, all the systems in Figures 17 and 18 are at the end of their individual integral period. Both figures show that higher frequency forcing results in smaller IS value. When f is 1/8, the IS value is larger in Figure 17 than that in Figure 18, which indicates a smaller density ratio will result in larger segregation.

Using Eq. 3.5 with an empirically fit $\beta = 0.1$ (due to high fluctuational energy within the flow), we plot the "zig-zag" simulation results of density segregation as a function of the ratio of the gravitational "flipping" frequency to f_{crit} as shown in Figure 19. Since high IS values (typically greater than 0.25) imply poorly mixed systems while low values correspond to good mixing [82], the plot of our simulation results in Figure 19 should yield points with high values of IS for $f/f_{crit} < 1$ and low values of IS when $f/f_{crit} > 1$. Despite the fact that many of our simulations resulted in non-linear shear profiles – making appropriate values of $\dot{\gamma}$ problematic – our results follow this trend to a remarkable extent when we obtain $\dot{\gamma}$ from the most highly shearing portion of the flow.

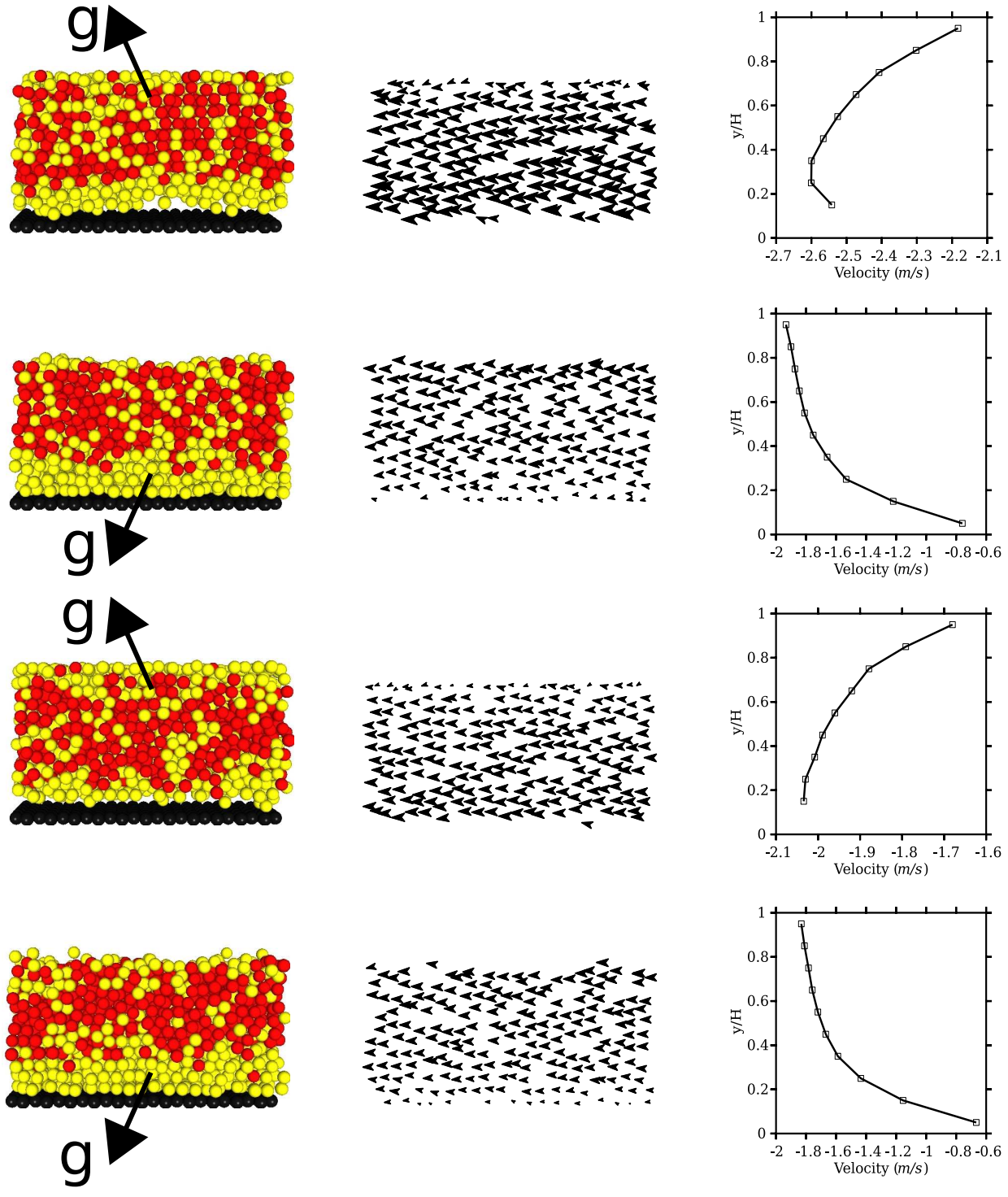

Figure 15: The time evolution of zigzag chute flow at 4s, 6s, 8s, 10s for $f = 1/4$, $\bar{\rho} = 0.25$ and $\alpha = 24°$ particle system. The left figures show the simulation having an oscillatory gravity. The arrows in the middle column figures show the vector of particle velocities. The right figures show the average particle velocity along y direction.

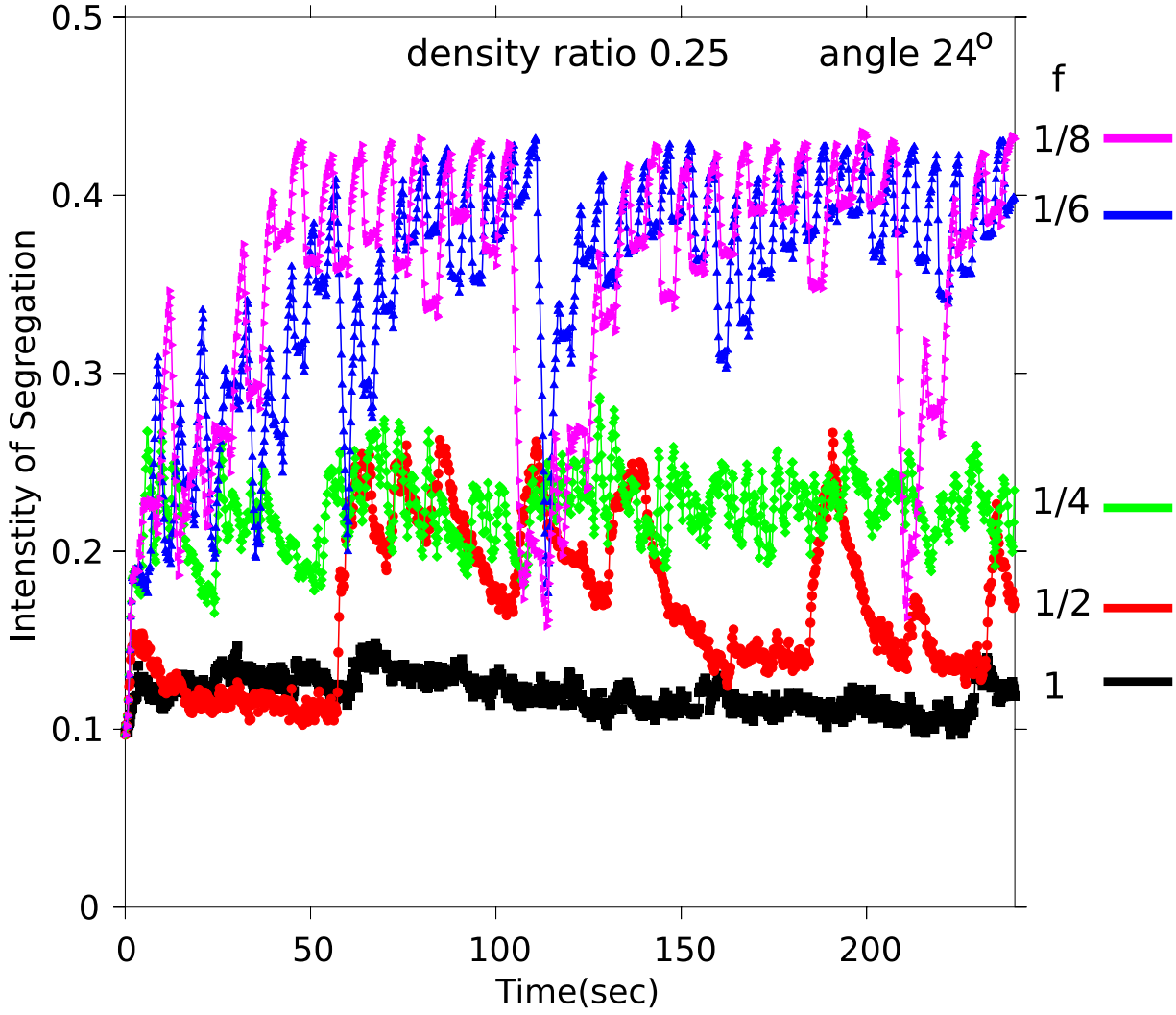

Figure 16: With the increasing of frequency, the system has decreased IS. At 240s, the number of periods are 240, 120, 60, 40, 20 for f=1, 1/2, 1/4, 1/6, 1/8, respectively. In other words, they are all in the end of their individual period. The IS are 0.12, 0.17, 0.23, 0.40, 0.43 as shown in the figure.

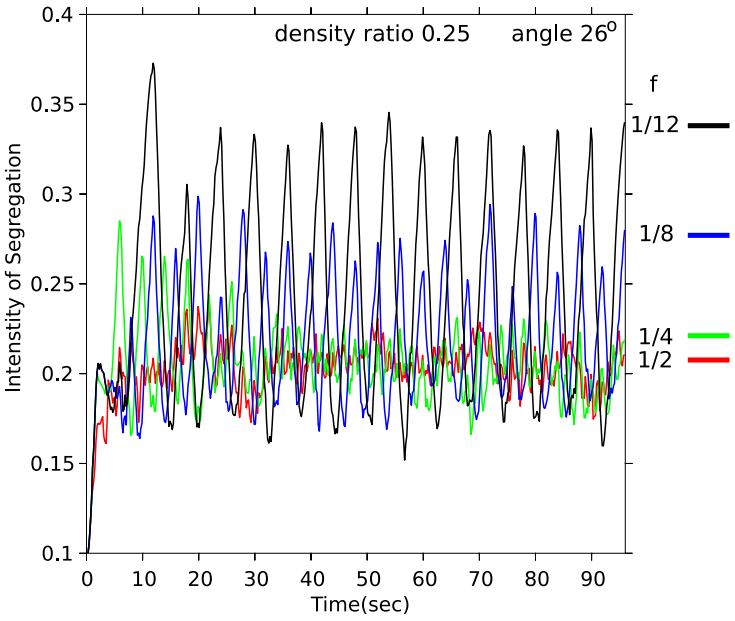

Figure 17: The IS evolution of f=1/2, 1/4, 1/8, 1/12 for chute flow with density ratio 0.25 and angle 26°. At 96s, i.e. the end of each period, the IS are 0.20, 0.22, 0.28, 0.33.

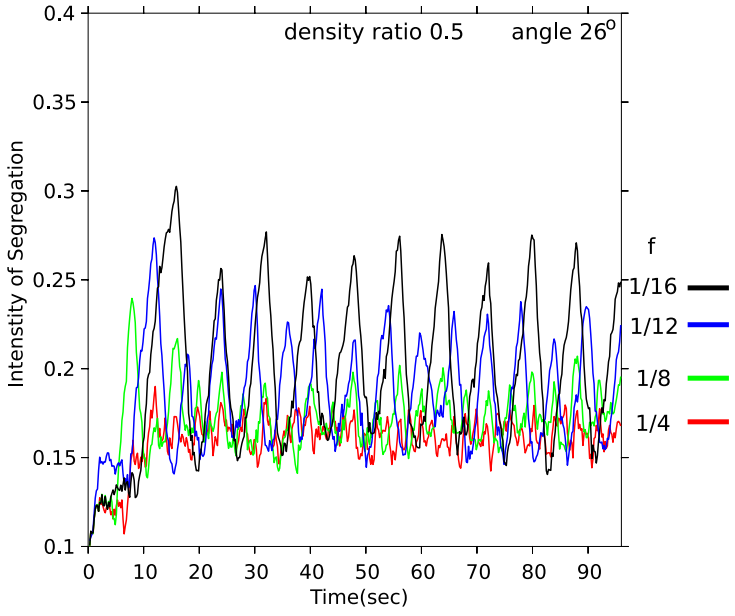

Figure 18: The IS evolution of f=1/4, 1/8, 1/12, 1/16 for chute flow with density ratio 0.5 and angle 26°. At 96s, i.e. the end of each period, the IS are 0.17, 0.20, 0.23, 0.25.

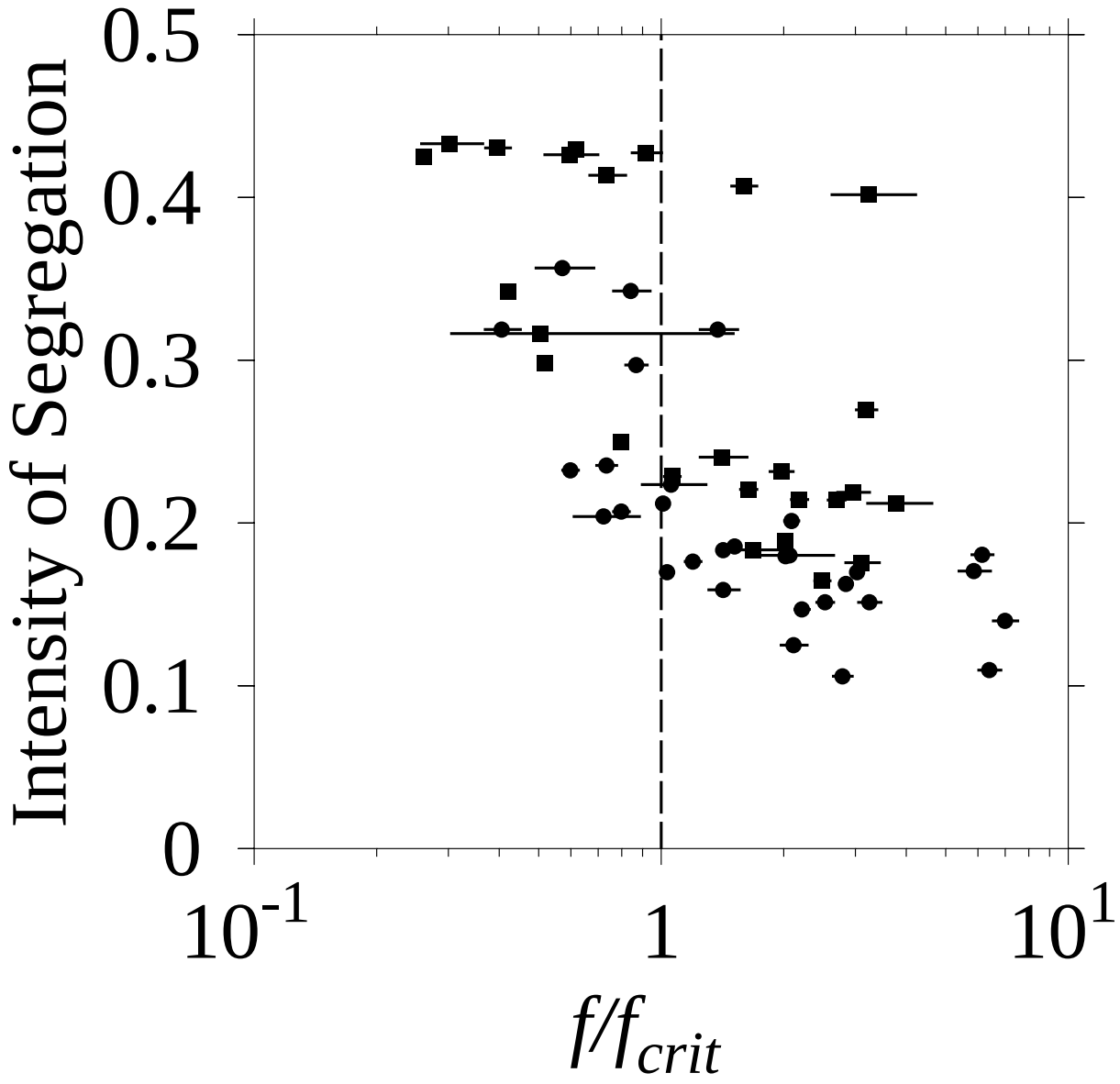

Figure 19: Computational results from our models of the "zig-zag" chute. Under a wide range of conditions, our computational results show high (low) values of IS when f/f_{crit} is less (greater) than 1. The filled circles denote simulations using a density ratio of 0.25, while the squares represent 0.5. Lines through the points show the standard deviation of the shear rate calculation.

3.3 ZIGZAG FLOW EXPERIMENT

Our experimental analogue of the "zig-zag" mixer consists of hollow square rods (which allow a flow height of $H = 1.8$cm) with lengths varying from 25cm to 205cm that are partially filled with (initially mixed) particles. In order to mimic the behavior of the "zig-zag" mixer the rods are first rocked to induce flow down the inclined plane, and then rotated to change the orientation of the particles prior to the next rocking event (see Figure 14c). This process is repeated until the particle distribution no longer changes with time. Note that the rotate step is performed with the rod held at an angle (θ) significantly larger than the particles' angle of repose (α) so that no particle rearrangement occurs during the rotation. The rods are roughened on top and bottom to minimize particle slip and have their back (conductive) wall grounded to reduce electrostatic effects as shown in Figure 20. Interestingly, in analyzing the results of these experiments, one notes that the ratio of f/f_{crit} is a function of the density ratio and aspect ratio of the tube only. This can be understood as follows. We first experimentally verified that the flow down the tube is essentially linear (see Ref. [89]) so that $\dot{\gamma} = 2U_{avg}/H$, where U_{avg} is the average stream-wise flow velocity and H is the height perpendicular to the flow direction. We then note that the effective forcing frequency is given as $f = 2U_{avg}/L$, so that (using Eq. 3.5)

$$\frac{f}{f_{crit}} = \frac{100H}{\beta L(1-\bar{\rho})}. \tag{3.7}$$

Taking $\beta = 1.06$ (due to relatively low flow energy obtained during such a short acceleration), we plot the results of experiments with mixtures of glass-acetate, acetate-steel, and glass-steel in Figure 21. The experiments are analyzed via image thresholding techniques to extract concentration profiles and IS values. For this plot, we define an experiment as yielding a mixed result if the IS value of the rocked-and-rotated particles is smaller than that of a control experiment where the rotate step is omitted, otherwise it is denoted as a segregated result. In this way, we eliminate the impact of rod length on our evaluation of mixing. Since the particles change flow direction twice in every period, another way to identify a mixed/segregated result is to compare the images from the half $t = (n + \frac{1}{2})T_{period}$ periods as

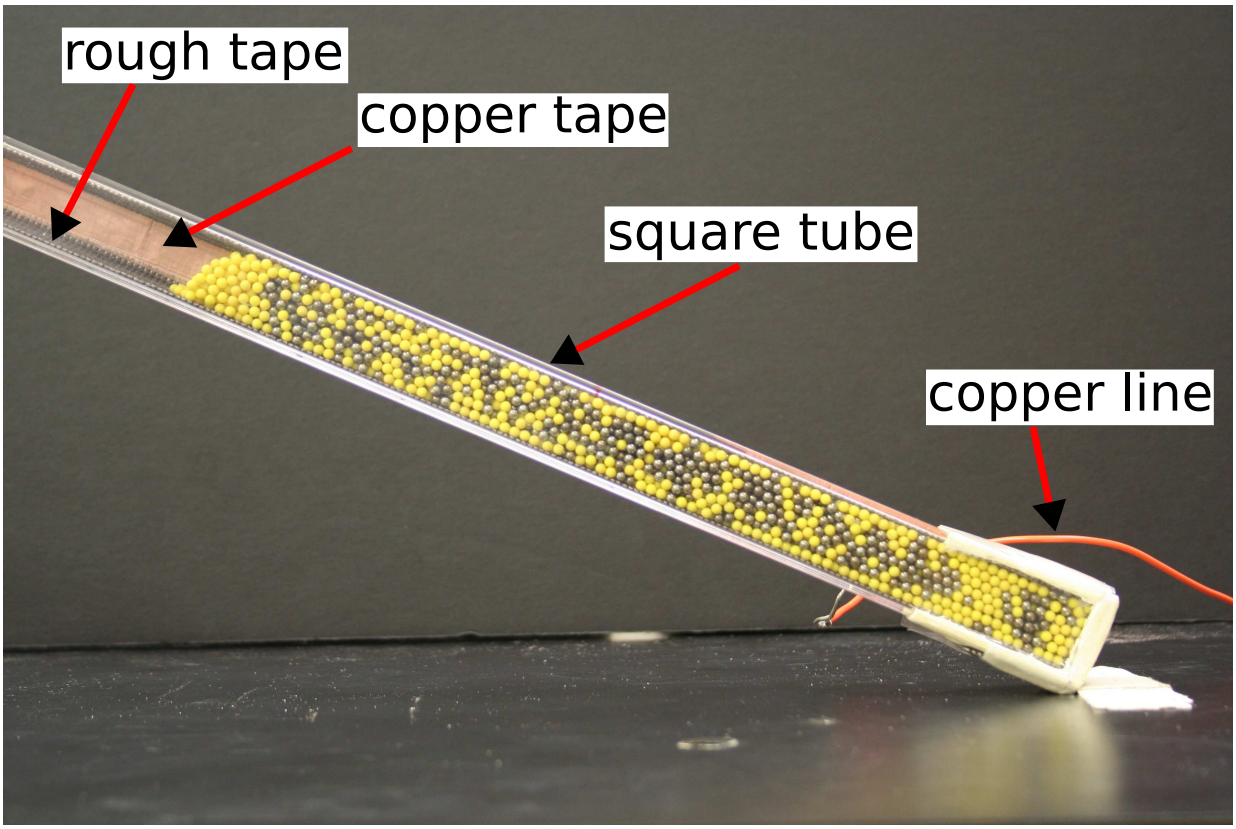

Figure 20: Zigzag experiment in a square tube. Rough tapes are applied on top and bottom of the inside wall to minimize particle slip. Conductive copper tape is applied on back wall and grounded to reduce electrostatic effects.

shown in Figure 22. If we define the characteristic flow time as t_f, we expect three results of this comparison. If $t_f \ll t_s$, the particles have essentially no time to segregate, so we have the odd and even half-periods yielding the same (mixed) image. If $t_f \gg t_s$, segregation can come to completion during the flow, so we again expect the half-period images to be the same; however, now they should both be segregated. If $t_f \sim t_s$, we could argue that some segregation occurs during one half-period only to be reversed in the next half-period so that the images differ.

3.4 TUMBLER

In order to exploit the segregation-limiting ideas, we recognize that, industrially, baffles are often used to augment mixing. As we show, these have little impact on segregation; however, a modified use of baffles is effective.

Both the (PD) simulations and the experiments use 1.5-4mm glass and acetate particles in short (6 particle diameters) 70 particle wide tumblers. Both size and density segregation involve 2:1 ratios (4mm:2mm for acetate particles and 3mm:1.5mm for glass particles). The simulated particle sizes and densities (as well as vessel size) are matched to their corresponding experiments, the particle stiffness used is reduced in order to decrease necessary simulation time (a practice shown to have essentially no impact on flow kinematics [90]). The wall is created by loading the particles along a cylindrical geometry. The inner particles are created by loading the particles in a rectangular lattice. The baffles are modeled as overlapping arrays of particles that have the same rotation angular velocity as the wall particles. All simulations have similar initial conditions in order to get values for comparison between different tumblers. In all cases, the binary system is initially completely segregated with the left-half of the bed consisting of one type (color) of particle and the right-half another. By using the same volume of particles for both kinds of materials, we make the initial state corresponding to $IS = 0.5$ based on volumetric fraction for the binary system. With the rotation of the tumbler, the particles will fall under the influence of gravity and deposit into a packed bed which then rotates with the tumbler wall.

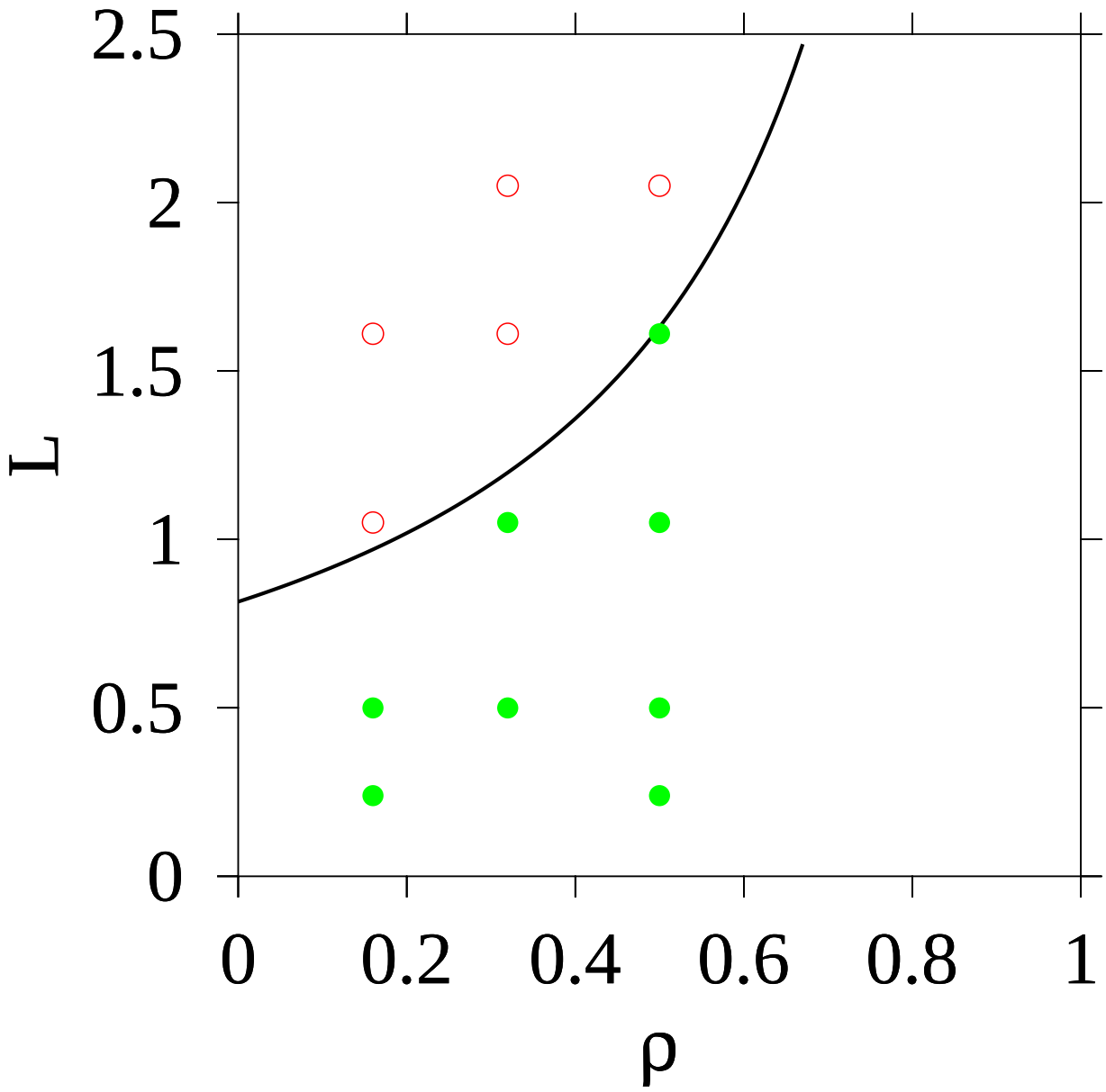

Figure 21: Experimental results from our models of the "zig-zag" chute. Plotting our experimental results as a function of tube aspect ratio versus density ratio, we obtain agreement with theory for three different density ratios. Here the line is a plot of Eq. 3.7 with $\beta = 1.06$, the solid circles denote mixed systems, and the open circles denote segregated systems.

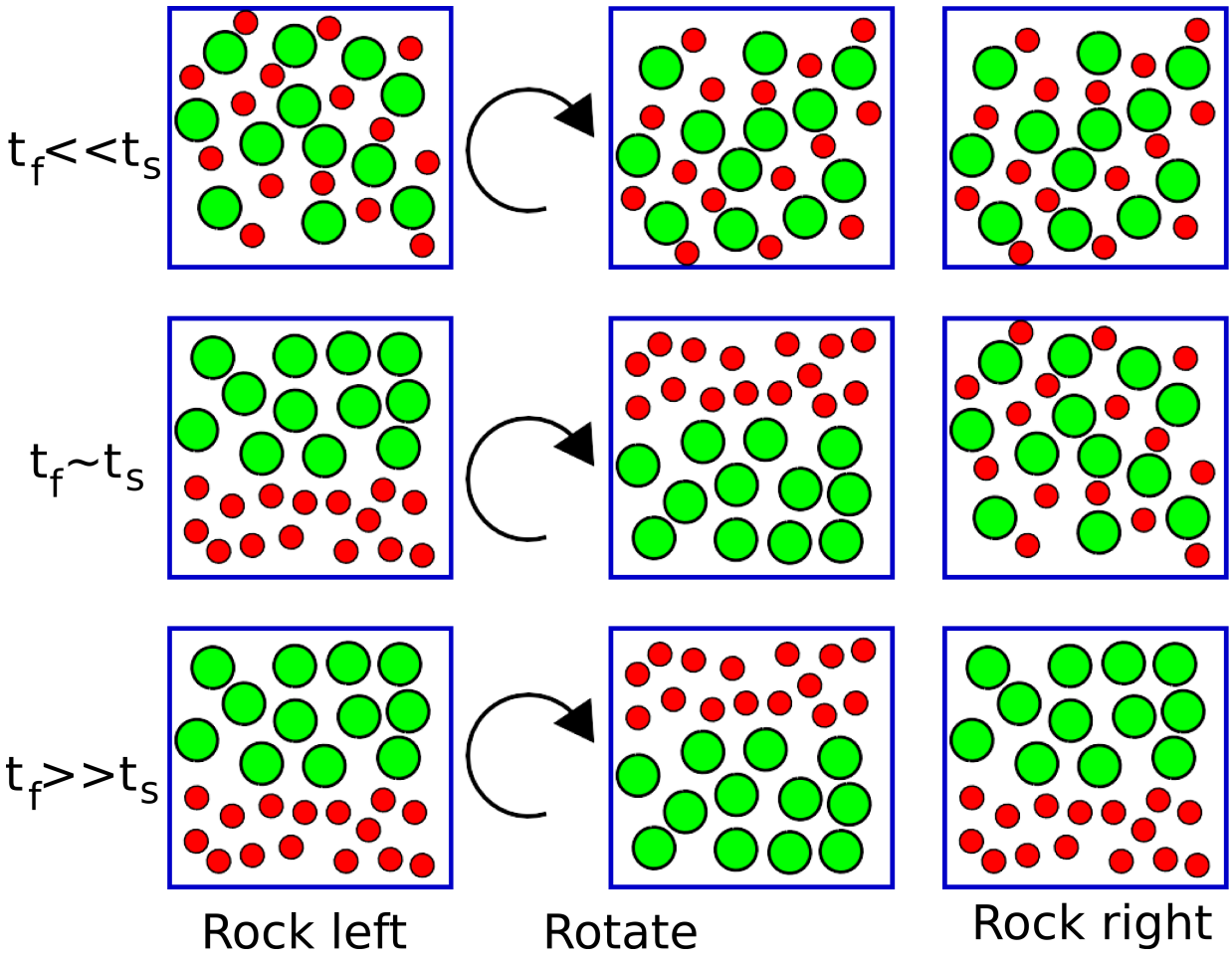

Figure 22: Rock and rotate experiments schematic

The tumblers are rotated at 6 revolutions per minute (RPM) with filling level 50%. As shown in Figure 23, we studied both the straight and angled traditional baffles. For axial baffles, the 1 baffle and 3 baffle mixers are studied . All the results are compared with the unbaffled system.

3.4.1 Shear Layer

There is always only 1 shear layer for unbaffled tumblers as shown in Figure 24. The arrow length and direction represent the magnitude and direction of the particle velocity respectively. In the shear layer, the velocities are much greater (red color) than that in the bed (blue color).

Figure 25 shows the time evolution of the shear layer in a traditional short baffle tumbler. Similar to the unbaffled tumbler, there is always only 1 shear layer. Figure 26 shows the time evolution of the shear layer in a traditional long baffle tumbler. There is still only 1 shear layer in the tumbler, but it can have a very large velocity gradient as shown in the image of $\frac{3\pi}{8}$. Figure 27 shows the time evolution of shear layers in an axially-located 1 baffle tumbler. Depending on the baffle position, there are up to 4 shear layers. When the baffle is horizontal, there are many more particles in shear layers than when the baffle is vertical. As shown in Figure 28, the IS decreases faster when the shear layer is large (when the baffle is in a horizontal position, there are more particles in the moving bed), than that when the shear layer is small (when the baffle is vertical, there are more particles in the static bed).

Similarly, Figure 29 shows the time evolution of shear layers in an axially-located 3 baffle tumbler. The mixing rate is larger when the shear layer is large (when the baffles are in a horizontal position), than that when the shear layer is small (when the baffles are vertical). Thus, the IS fluctuates periodically in the tumbler. For the sake of comparison of different tumbler systems, the average value of IS of each evolution will be used in the following analysis as shown in Figures 30 and 31.

The baffles attached at the periphery of a tumbler are ineffective in reducing segregation. This can be understood by tracking the preferred direction of segregation within these tumblers, whereby one notes that the static portion of the bed simply “stores” the material

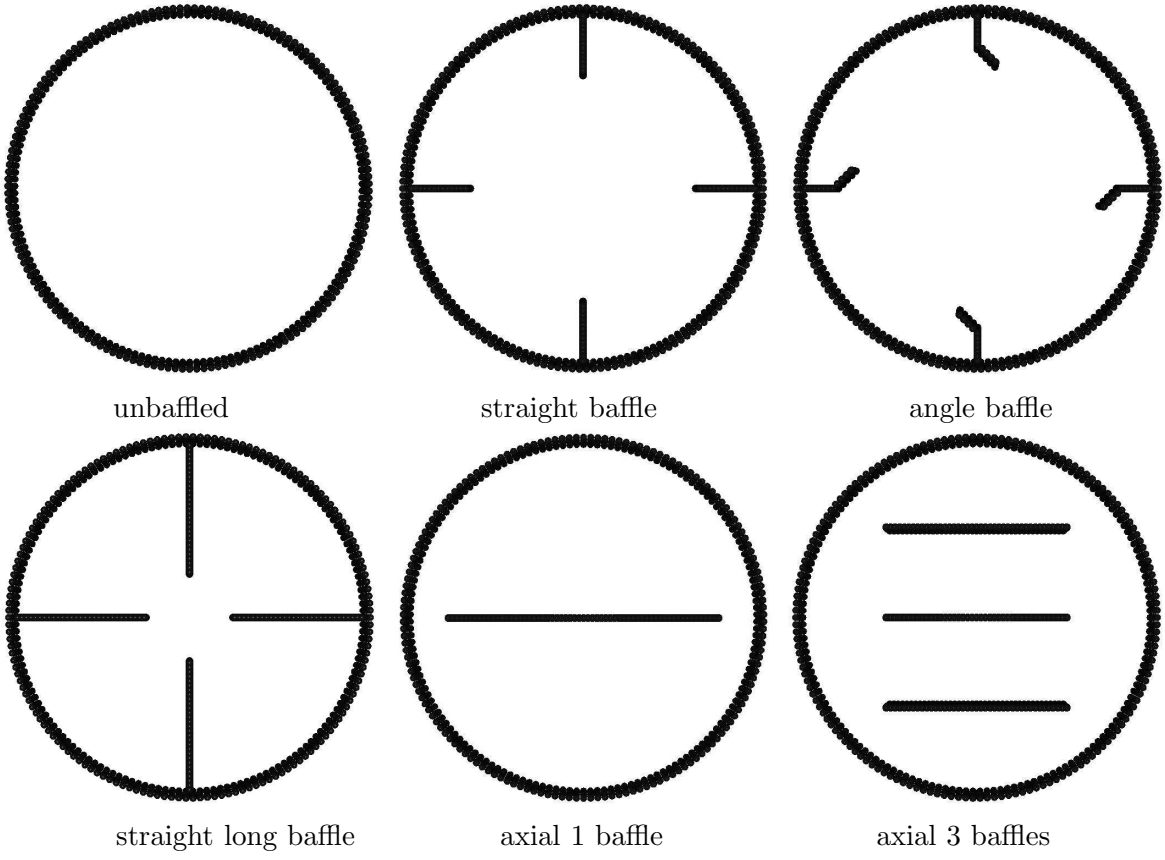

Figure 23: Tumbler geometries used in the simulation

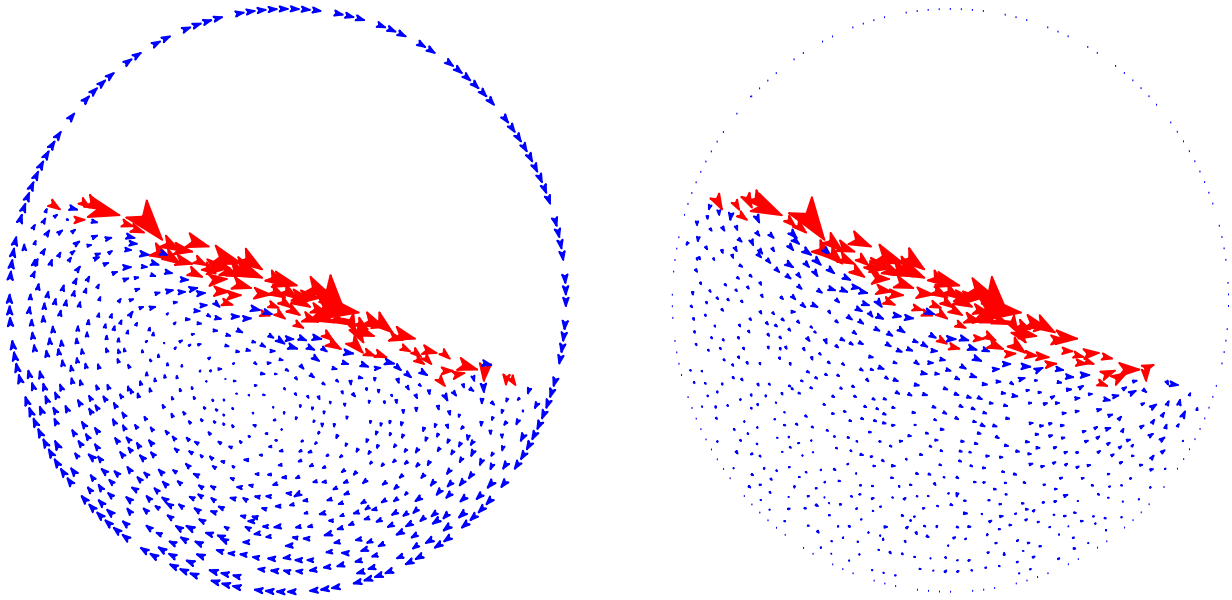

Figure 24: Shear layer of unbaffled tumbler. The particles have a much greater velocity when in the shear layer (large red arrow) than in the bed (small blue arrow). The left figure shows the velocity of the particles. The right figure shows the net velocity of the particles, which doesn't include the tumbler rotation. Both figures show a similar shear layer region. For an unbaffled tumbler, there is always only one shear layer.

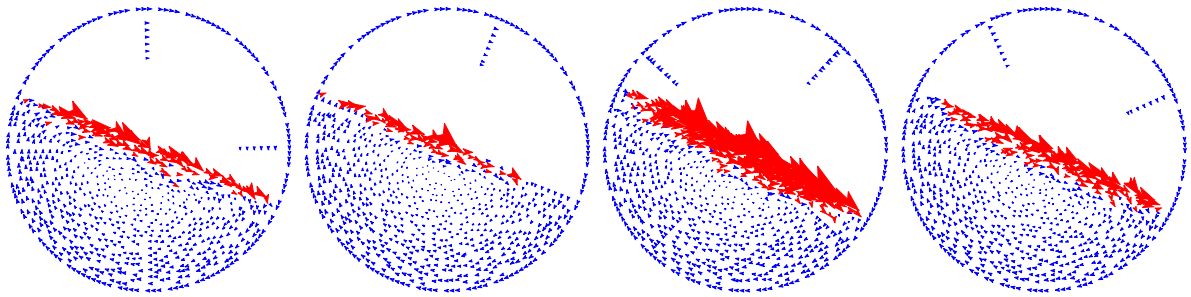

Figure 25: Shear layer of traditional short baffle tumbler. Depending on the baffle position, the particles in the shear layer may have different velocities. The 4 figures show the shear layer of the tumbler at a rotation angle of 0, $\frac{\pi}{8}$, $\frac{2\pi}{8}$, $\frac{3\pi}{8}$, respectively. For traditional short baffle tumbler, there is always only 1 shear layer.

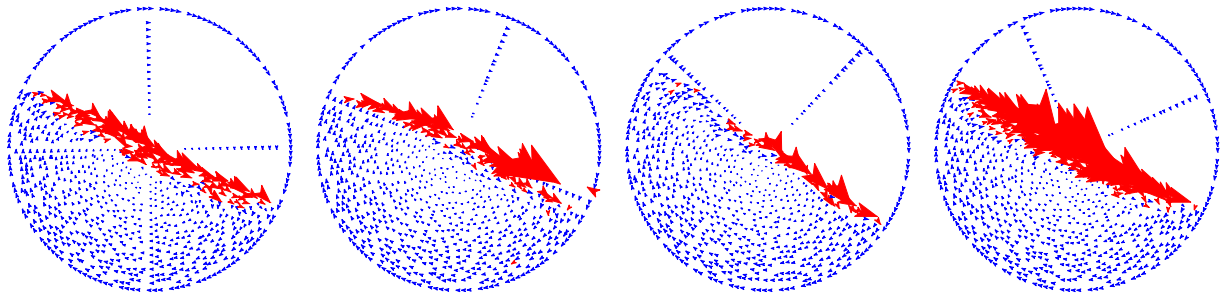

Figure 26: Shear layer of traditional long baffle tumbler. Depending on the baffle position, the particles in the shear layer may have different velocity. The 4 figures show the shear layer of the tumbler at a rotation angle of 0, $\frac{\pi}{8}$, $\frac{2\pi}{8}$, $\frac{3\pi}{8}$, respectively. For traditional long baffle tumbler, there is always only 1 shear layer, but the shear layer may have very large velocity gradients as shown in the figure of $\frac{3\pi}{8}$.

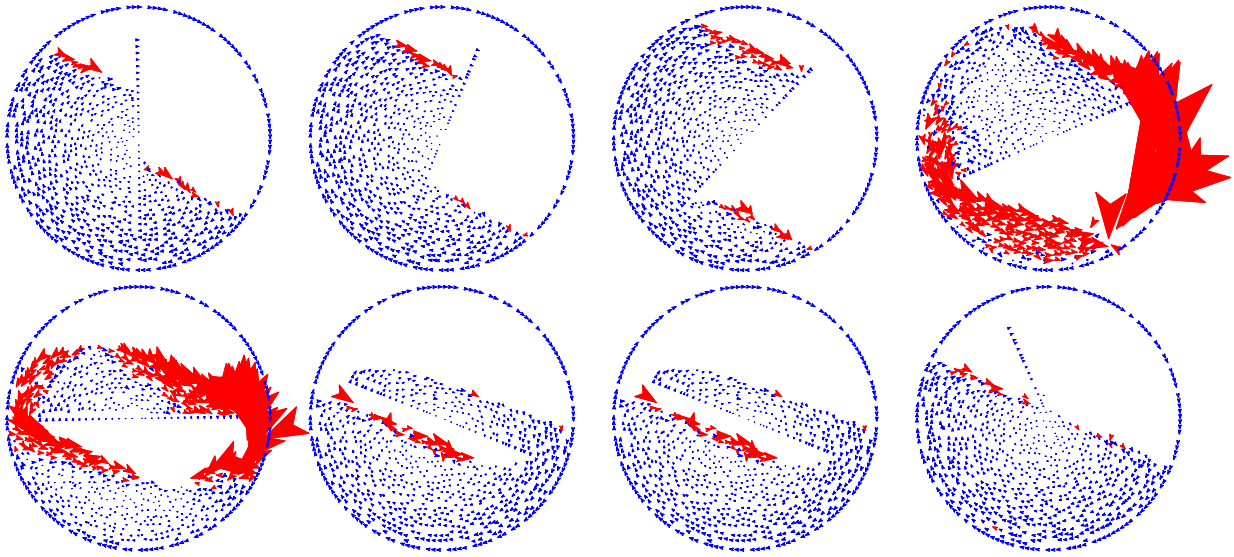

Figure 27: Shear layers of axially-located 1 baffle tumbler. The 8 figures show the shear layer of the tumbler at a rotation angle of 0, $\frac{\pi}{8}$, $\frac{2\pi}{8}$, $\frac{3\pi}{8}$, $\frac{4\pi}{8}$, $\frac{5\pi}{8}$, $\frac{6\pi}{8}$, $\frac{7\pi}{8}$, respectively. Depending on the baffle position, there are up to 4 shear layers.

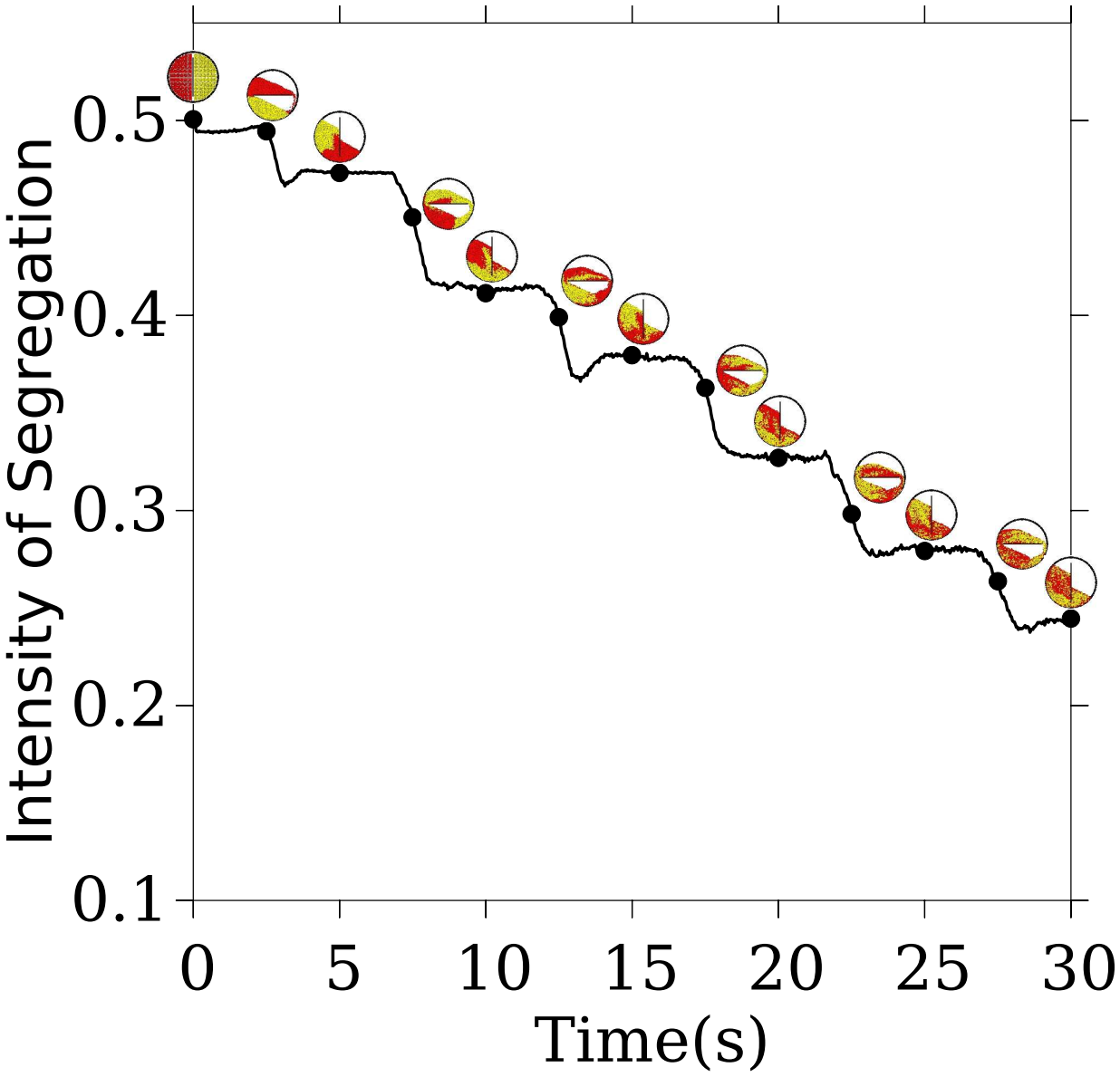

Figure 28: The periodic evolution of IS in 1 baffle tumbler. The mixing rate is larger when shear rate is large (horizontal baffle) than that when shear rate is small (vertical baffle).

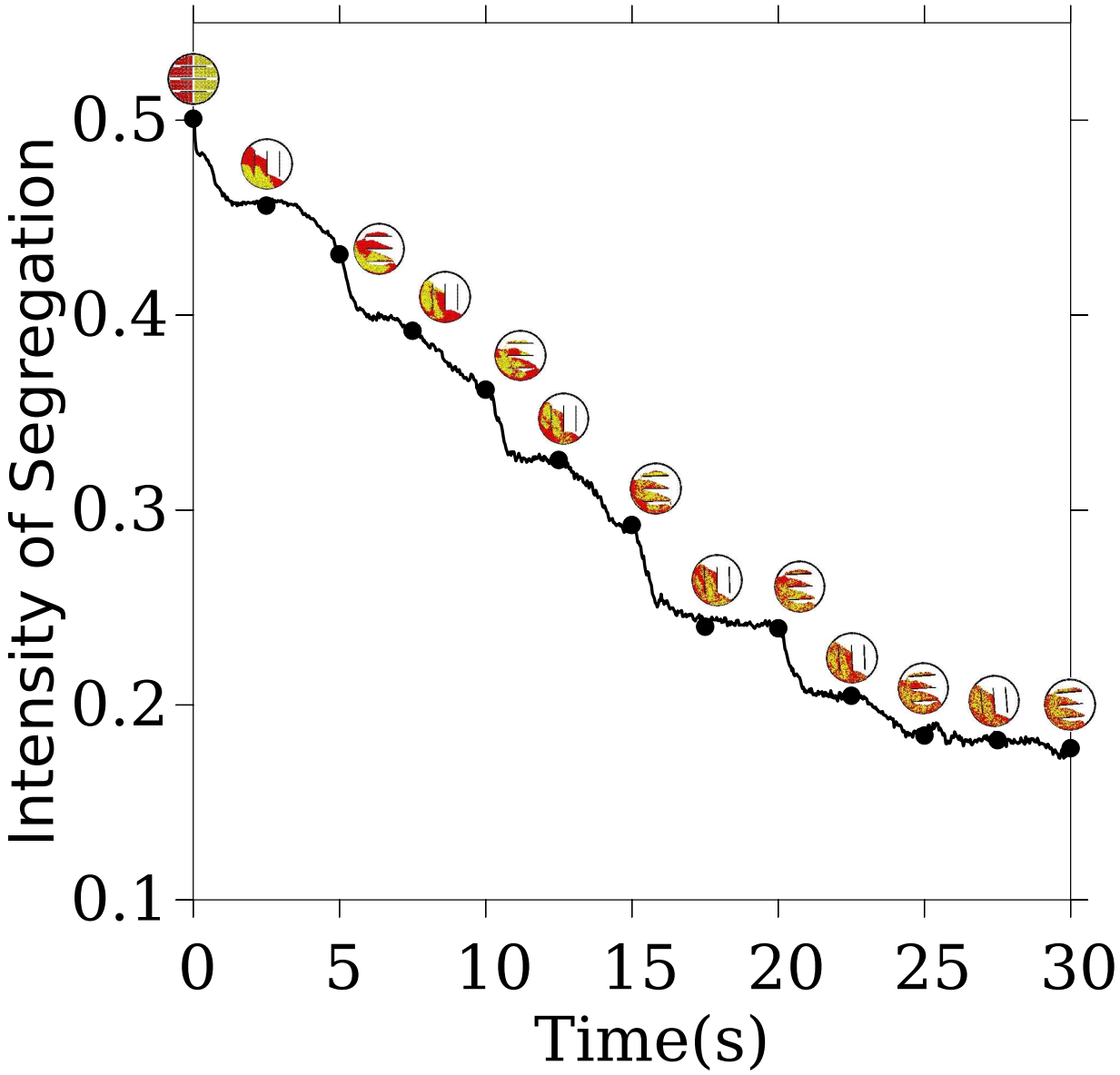

Figure 29: The periodic evolution of IS in 3 baffles tumbler. The mixing rate is larger when shear rate is large(horizontal baffle), than that when shear rate is small (vertical baffle).

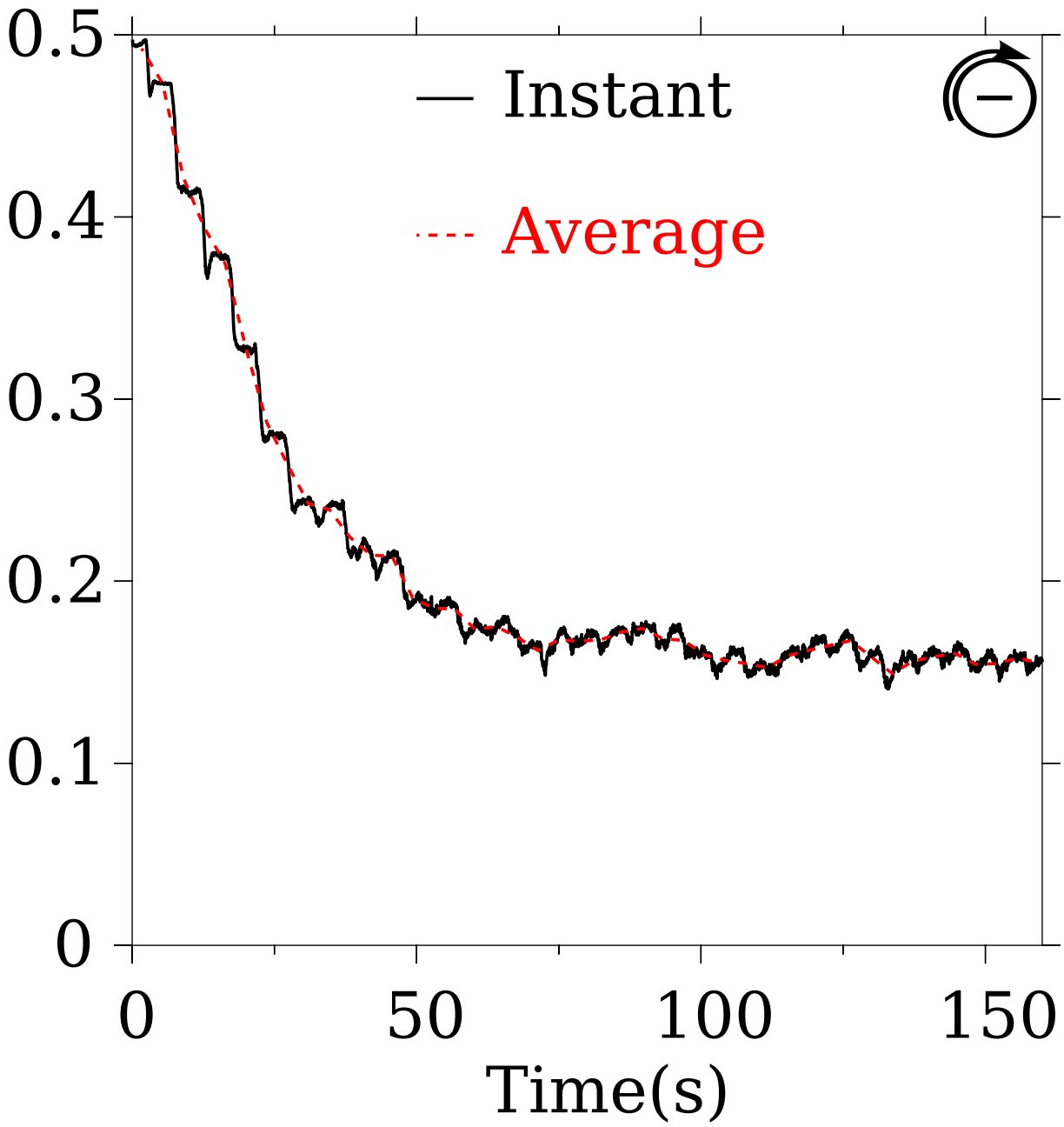

Figure 30: The instantaneous IS evolution show a periodic trend with peaks and valleys in an axially-located 1 baffle tumbler. The average value of IS, which has smoothed the peaks and valleys, will be used.

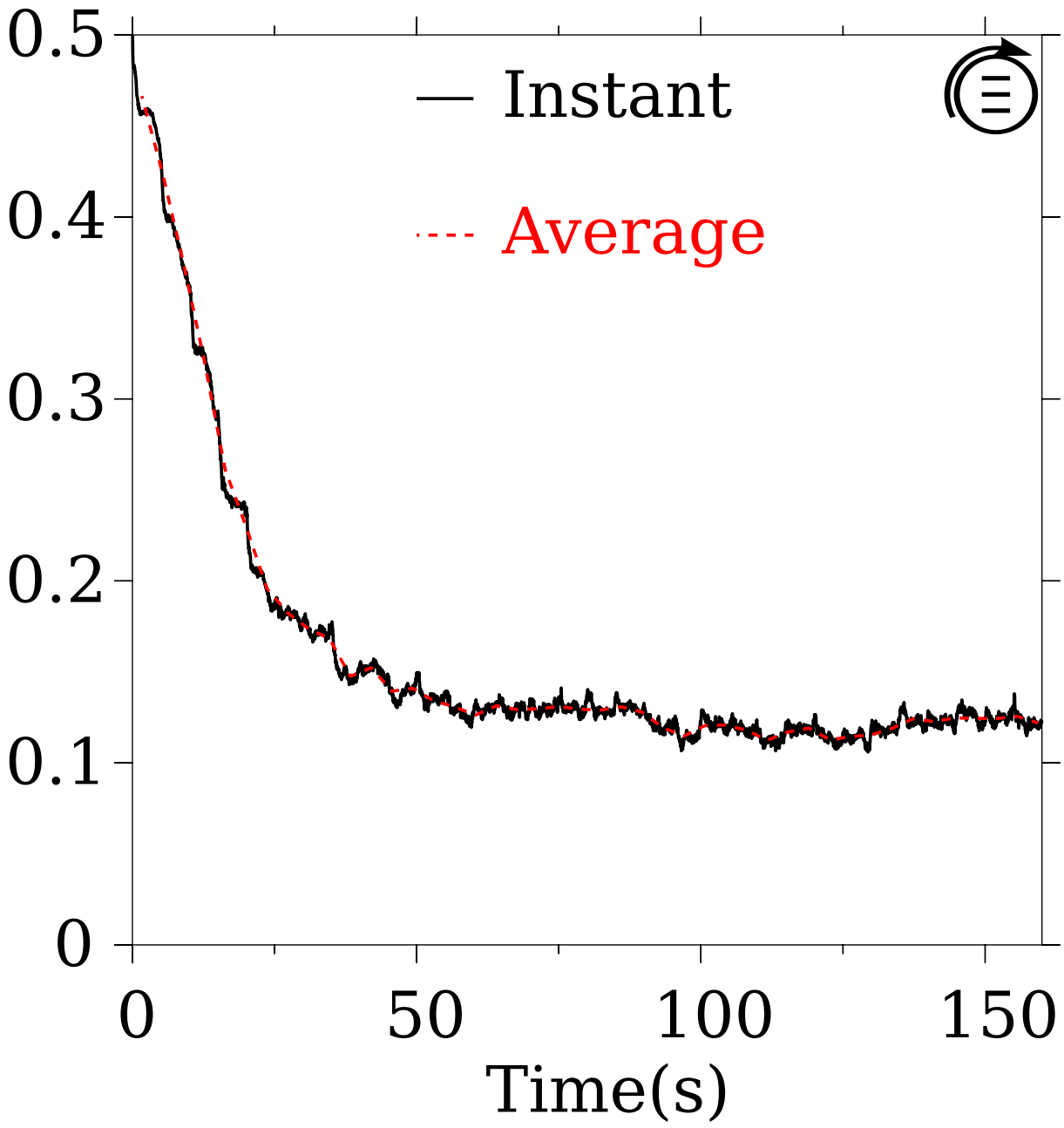

Figure 31: The instantaneous IS evolution show a periodic trend with peaks and valleys in an axially-located 3 baffles tumbler. The average value of IS has no peaks and valleys.

and returns it in almost the same orientation for its next pass through the surface layer (i.e., it undergoes a full 180° change in orientation prior to returning to the flowing layer; see Figure 32). This results in asymptotically segregated systems even for tumblers whose surface length, L, is small compared to $U_{mean}t_s$. If we instead place baffles near the axis of rotation, we periodically alter the flowing layer so that we achieve both (a) a smaller average uninterrupted flow length, L, and (b) periodic variations in the effective direction of segregation with respect to the tumbler streamlines (as the baffles rotate with the tumbler; see Figure 32). This leads to results quite similar to those seen in the "zig-zag" mixer as the static bed no longer returns the material to the flowing layer(s) in the same orientation in which it left. Another way to analyze the flow is shown in Figure 33. Recalling that a single pass through the shearing layer would re-orient particles by 180°, one notes that the segregation orientation will change during the mixing process if the particles pass through the layer, on average, in fewer than one half of a rotation. The number of rotations per layer pass is almost exactly 0.5 for an unbaffled mixer, and one with (shorter) traditional baffles; however, the distribution of rotation times broadens considerably both for long traditional baffles and for any number of axial baffles.

Some typical snapshots are shown in Figure 34 for different density particles. With the tumbler rotating, different color particles will mix with each other from an initially segregated state. However, for unbaffled and traditional short baffle tumblers, the particles remain largely segregated after 40s (IS > 0.3). In contrast, for an axially-located 1 baffle tumbler, the particles are mixed pretty well (IS $= 0.22$). For different size particles, Figure 35 shows the snapshots of unbaffled, traditional angle baffle and axially-located 3 baffle mixers. The axially-located 3 baffle mixer reduces the segregation significantly compared to the other two mixers.

Figure 36 depicts qualitative images of the asymptotic state for both experiments and simulations, for both bi-disperse density and size-related segregation. Figure 37 shows the time evolution of IS from 0.5, i.e. completely segregated state. While the (short) traditional baffles produce results similar to the non-baffled case, axially-located baffles dramatically reduce the measured asymptotic degree of segregation as do the very long traditional baffles.

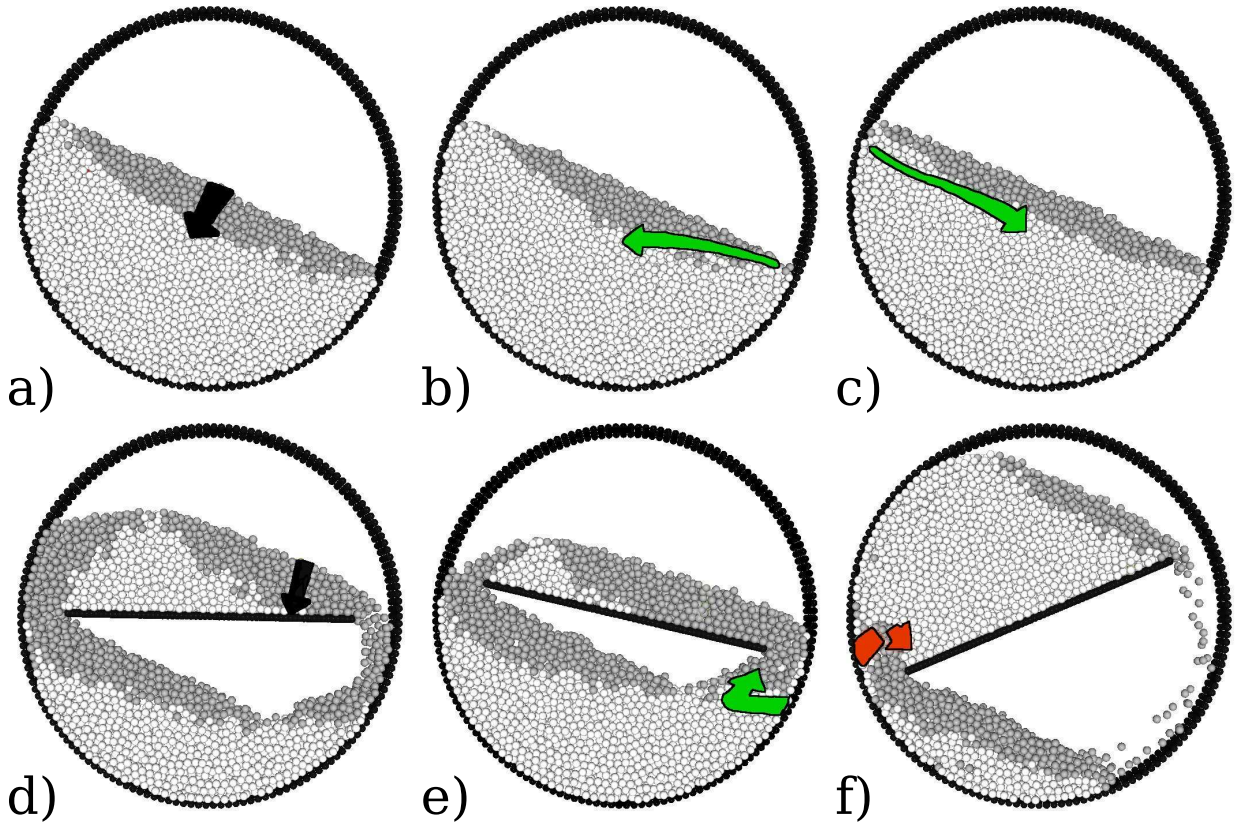

Figure 32: Images a-f show particle positions from PD simulations for an unbaffled tumbler (a-c) and a tumbler with a single axially-located baffle (d-f). The light colored particles are in the fixed bed portion of the flow (low velocity relative to the tumbler wall), while the darker gray particles are in the flowing layer. At the outset of the simulations, we "tag" a vertical line of particles within the flowing layer and denote their original orientation with a black arrow (see frames a and d). In the other frames, the green arrows denote the future average position and orientation of the initially tagged particles as they move through the bed. The broken, red arrow in frame f represents a particle orientation that has "folded" upon itself (i.e., the orientation contains a loop from a partial layer pass). Note that the orientation of the arrow in the unbaffled case both leaves and enters the flowing layer almost perfectly tangent, while the orientation of the arrow in the baffled case is rotated roughly ninety degrees.

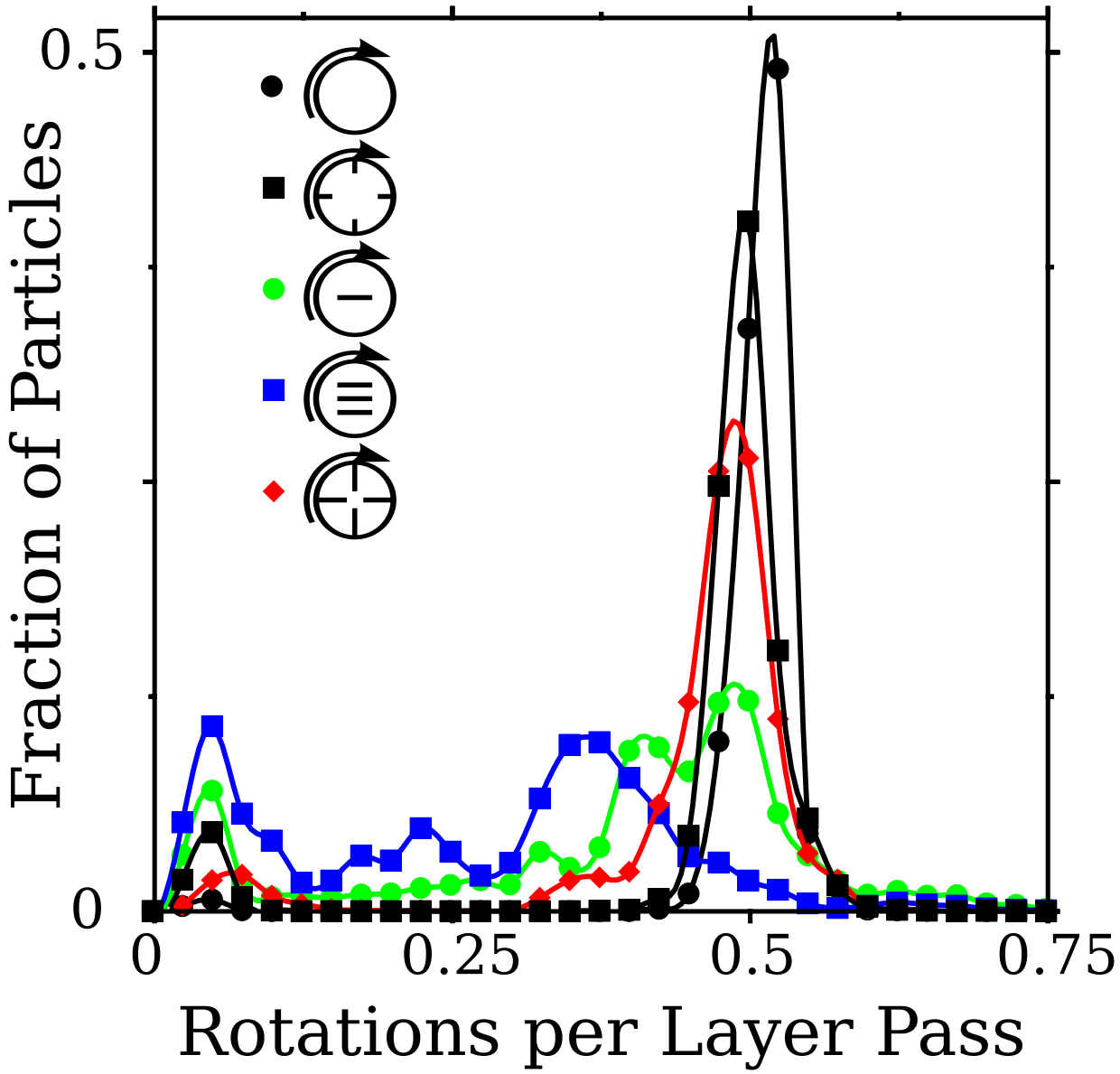

Figure 33: The plot shows the distribution of rotations between particle layer passes for various tumbler configurations. The black symbols represent the unbaffled case and a case with (short) traditional baffles, both of which have very narrow distributions centered on 0.5 rotations. In contrast the axially-located baffles (green and blue symbols) or long traditional baffles (red symbols) result in much broader distributions, suggesting that the orientation of particles in future layer passes should be almost uncorrelated with previous passes. Note that we define long traditional baffles as those that actually transversely cut a portion of the flowing layer, much like the axially oriented baffles.

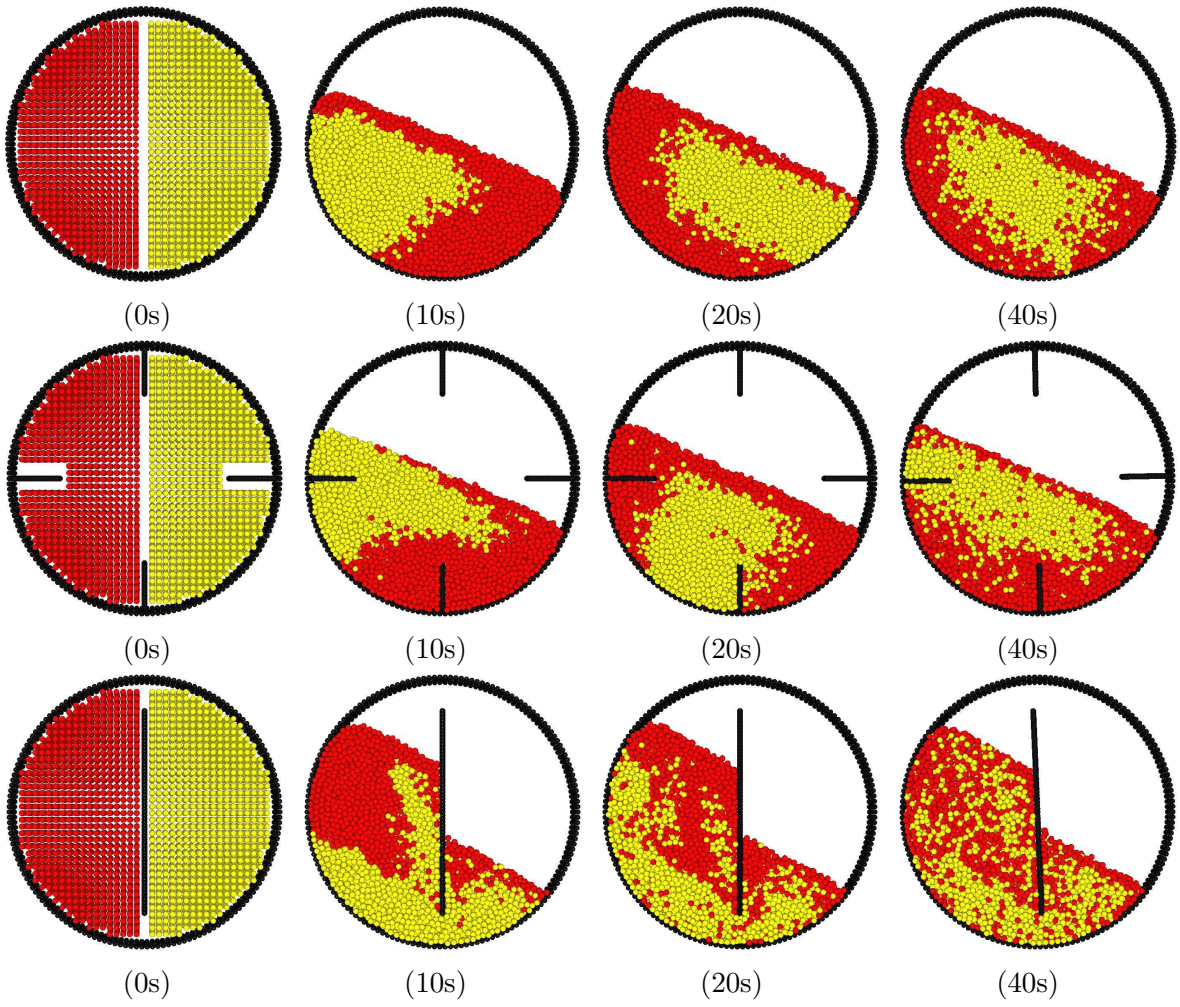

Figure 34: Snapshots for different density particles inside unbaffled tumbler, traditional short straight baffle tumbler and axially-located 1 baffle tumbler at 0s, 10s, 20s, 40s.

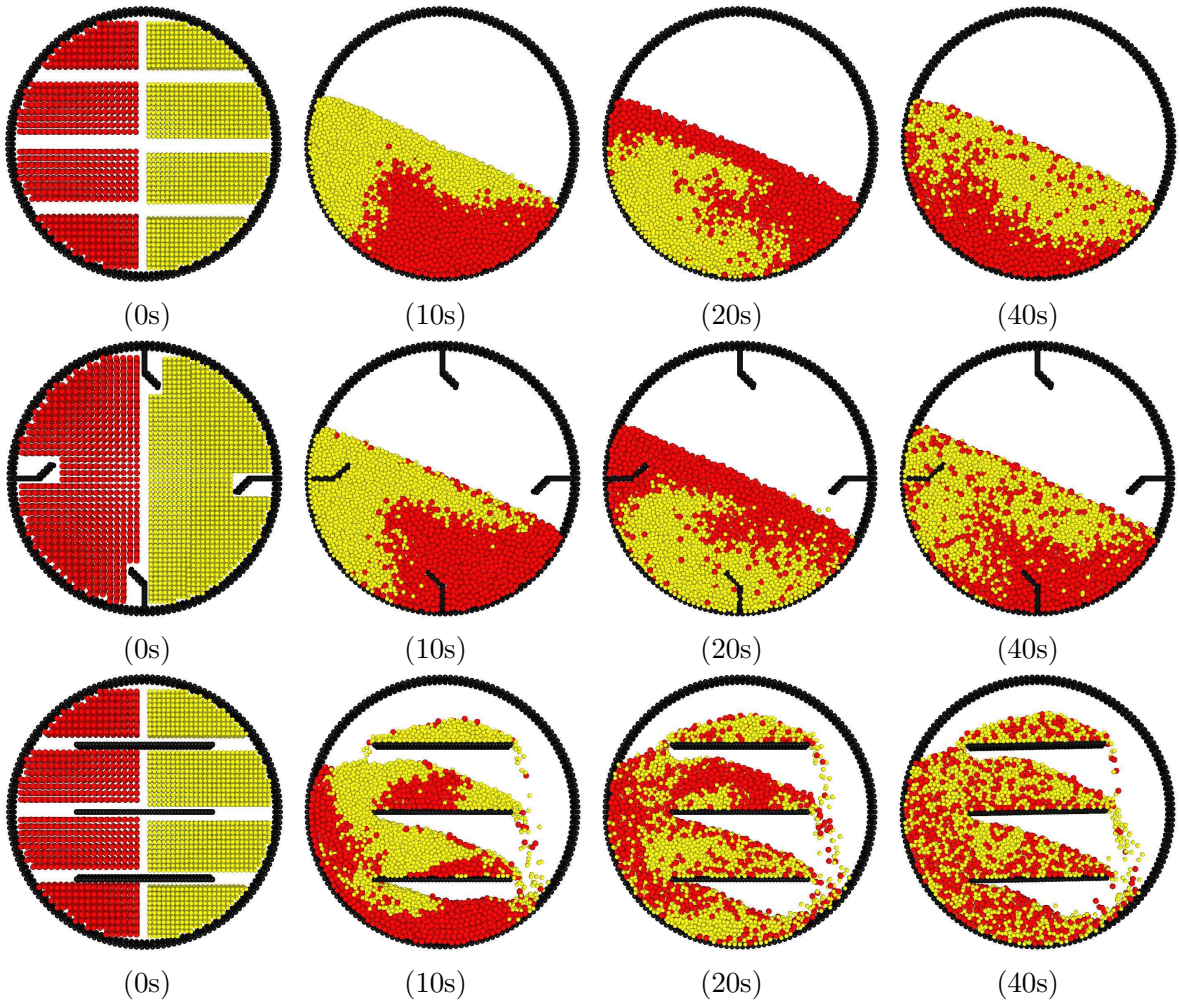

Figure 35: Snapshots for different size particles inside unbaffled tumbler, traditional short straight baffle and axially-located 1 baffle tumbler at 0s, 10s, 20s, 40s.

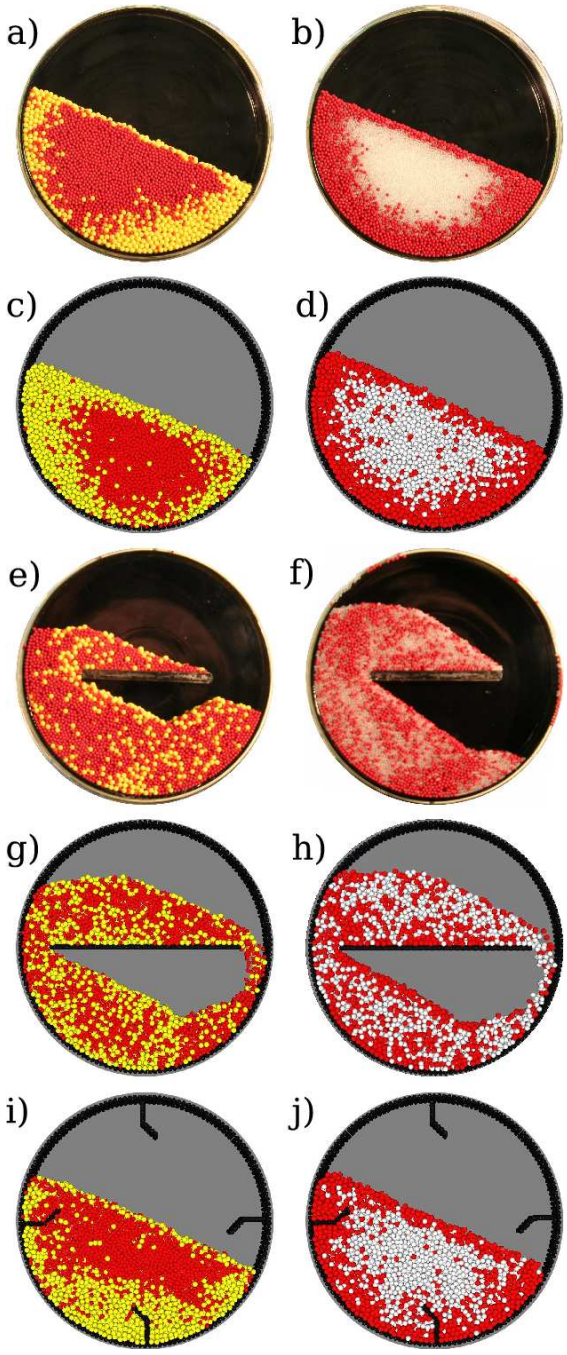

Figure 36: Asymptotic mixing results in tumbler mixers for both size (left) and density (right) segregation. Unbaffled tumblers (a and b, experiments; c and d, simulations) result in strong radial segregation. In contrast, baffles that truncate the flowing layer (shown experimentally in e and f, and computationally in g and h) dramatically reduce the degree of segregation. For comparison, computational results for a traditional baffle arrangement are shown in i and j.

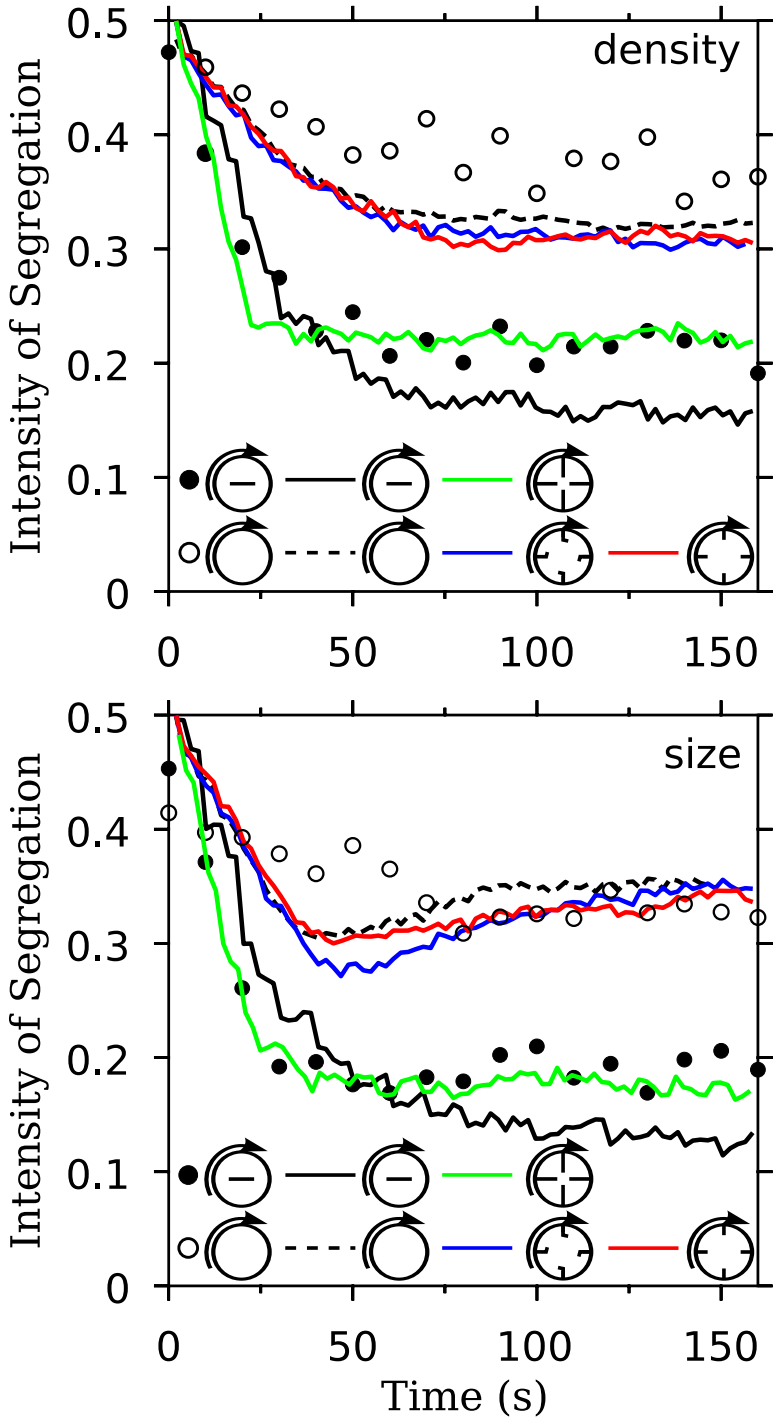

Figure 37: Quantitative mixing results in tumbler mixers for both density (top) and size (bottom) segregation. Experiments are shown as symbols and simulations as lines. Note that unbaffled mixers and mixers with short baffles behave very similarly, while axial baffles or very long traditional baffles results in significantly lower IS values (increase the degree of mixing).

Table 2 shows that the Lacey mixing index for 3 axial baffles mixer is 77.3% at 100 seconds, which is much higher than 41.5% achieved by unbaffled mixer. The value for conventional angle baffle mixer is 46.4%, which is just slightly higher than that achieved by unbaffled mixer.

Table 2: PARAMETERS AND MIXING EXTENT OF THE SIMULATION.

	Simulation	IS at 100s	Lacey Mixing Index at 100s
different density particles	unbaffled	0.350	51.0%
	straight baffle	0.326	57.5%
	angle baffle	0.332	55.9%
	axial 1 baffle	0.193	85.1%
	axial 3 baffles	0.156	90.3%
different size particles	unbaffled	0.382	41.6%
	angle baffle	0.366	46.4%
	axial 3 baffles	0.238	77.3%

3.4.2 Mixing Rate

Using the baffles that can penetrate the shear layer will not only eliminate segregation, but also achieve a higher mixing rate. For the two kinds of same density and size particles, they will always proceed to a completely mixed state which is not related to the baffle geometry or position. Figure 38 shows that the IS decreases, from a completely segregated state, toward the same asymptotic value in 150s; however, the slope of the IS curve, which is the mixing rate, is different for each system. The traditional short straight baffle mixer has a little bit larger mixing rate than the unbaffled mixer, however, the axial baffle mixer has much larger mixing rate than the short baffle mixer. As shown in Figure 39, the axial baffle and very long traditional baffle mixers have significantly larger mixing rate than the short baffle and unbaffled mixers.

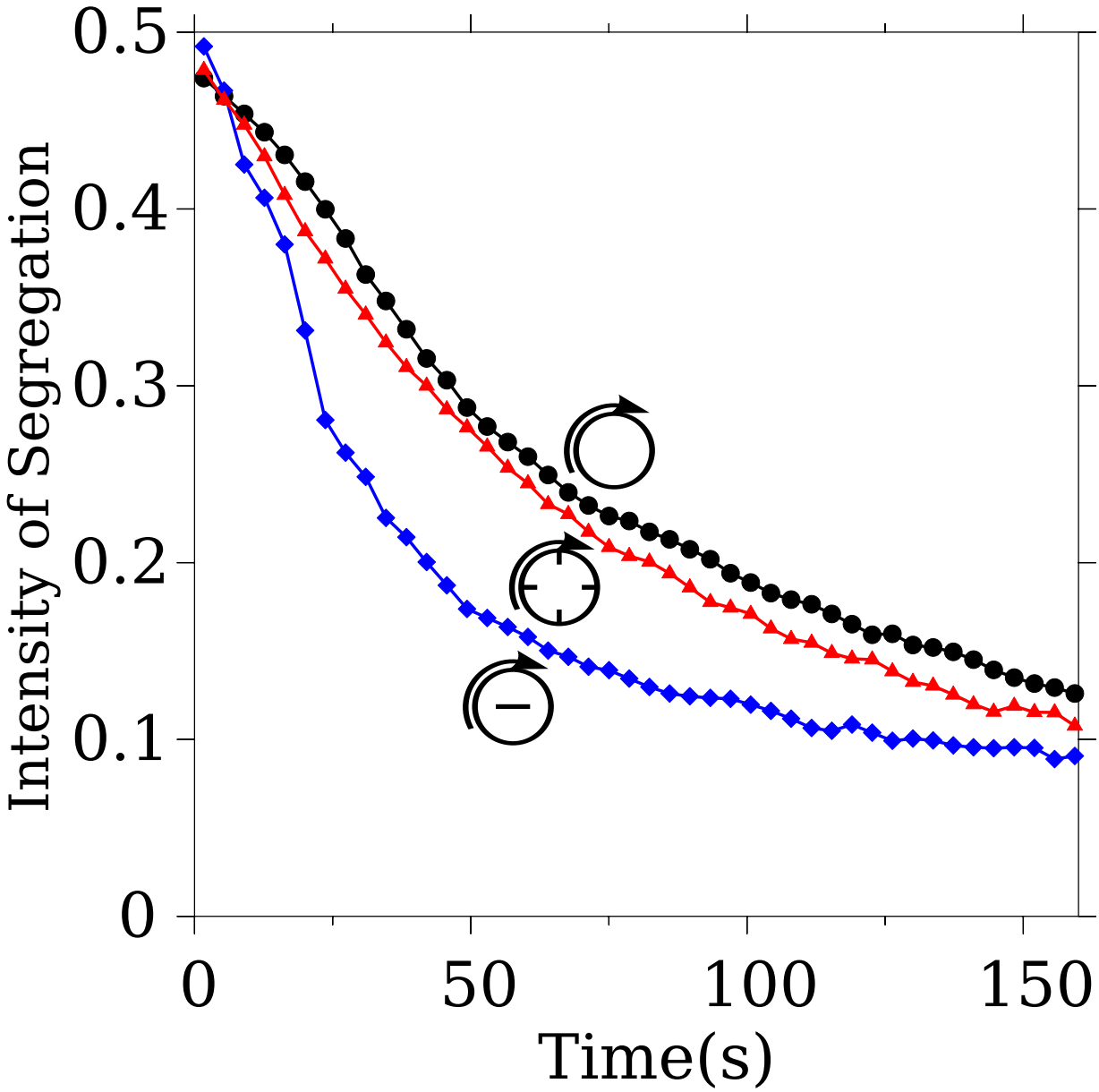

Figure 38: IS evolution for the two kinds of same density and size particles. The slopes of the IS, which is the mixing rate, are different for each system. The short baffles mixer has a little bit larger mixing rate than the unbaffled mixer, however, the axial baffles mixer has much larger mixing rate than the short baffles mixer.

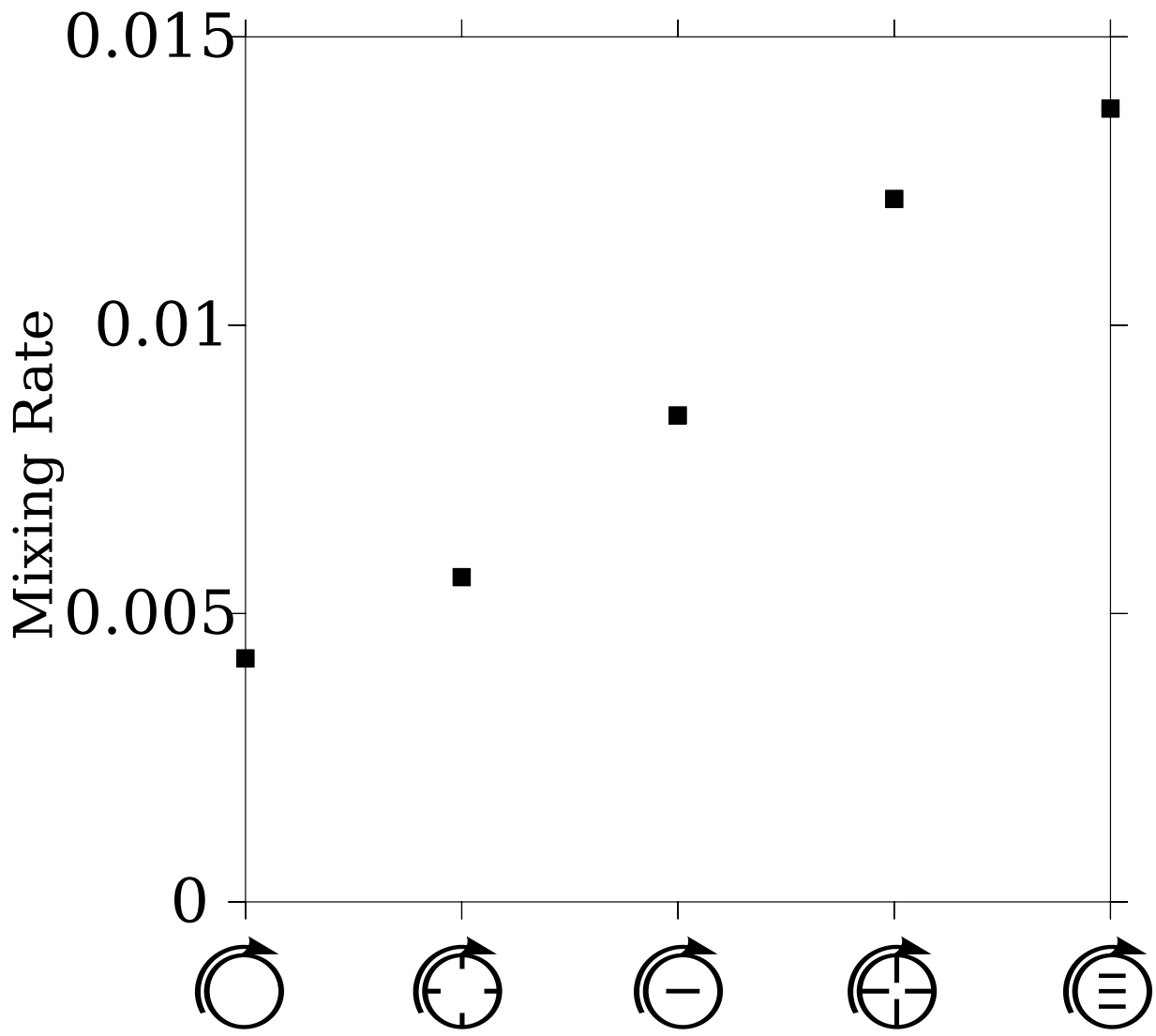

Figure 39: The average mixing rates in the first two revolutions. The axial baffles or very long traditional baffles have larger mixing rate than the short baffles and unbaffled mixers.

3.4.3 Scaling

Figure 40 shows the scaling results for an axial 1 baffle mixer. The diameter and baffle length of the double size mixer is twice as large as the normal one. The top figure shows the result for two kinds of different density particle systems. It is noticeable that both the double size and normal size mixers have almost the same IS curve. For different size particles, the double size mixer achieved even better mixing results than the normal size one.

3.5 CONCLUSIONS

The conventional baffles, some even having complicated geometry such as angled baffles, result in only little improvement on mixing extent, however, the mixing performance was greatly improved by implementing our unconventional baffles. The unconventional baffles can have a profound effect on future mixer designs.

The baffle can not only increase the mixing extent in the asymptotic state, but also reduces the time to achieve that state. While we developed the theory for the requirements necessary to eliminate segregation in the asymptotic state, the kinetics of this process still need to be determined.

While we have demonstrated two simple examples of flow modulation, the method described here is entirely general. As long as the flow perturbations alter the direction of segregation (relative to the previous particle flow history) at high enough frequencies, this technique may be used for a wide range of particle processing applications, ranging from mixing to conveying, and can have a significant impact in industries from foodstuffs to ceramics to pharmaceuticals.

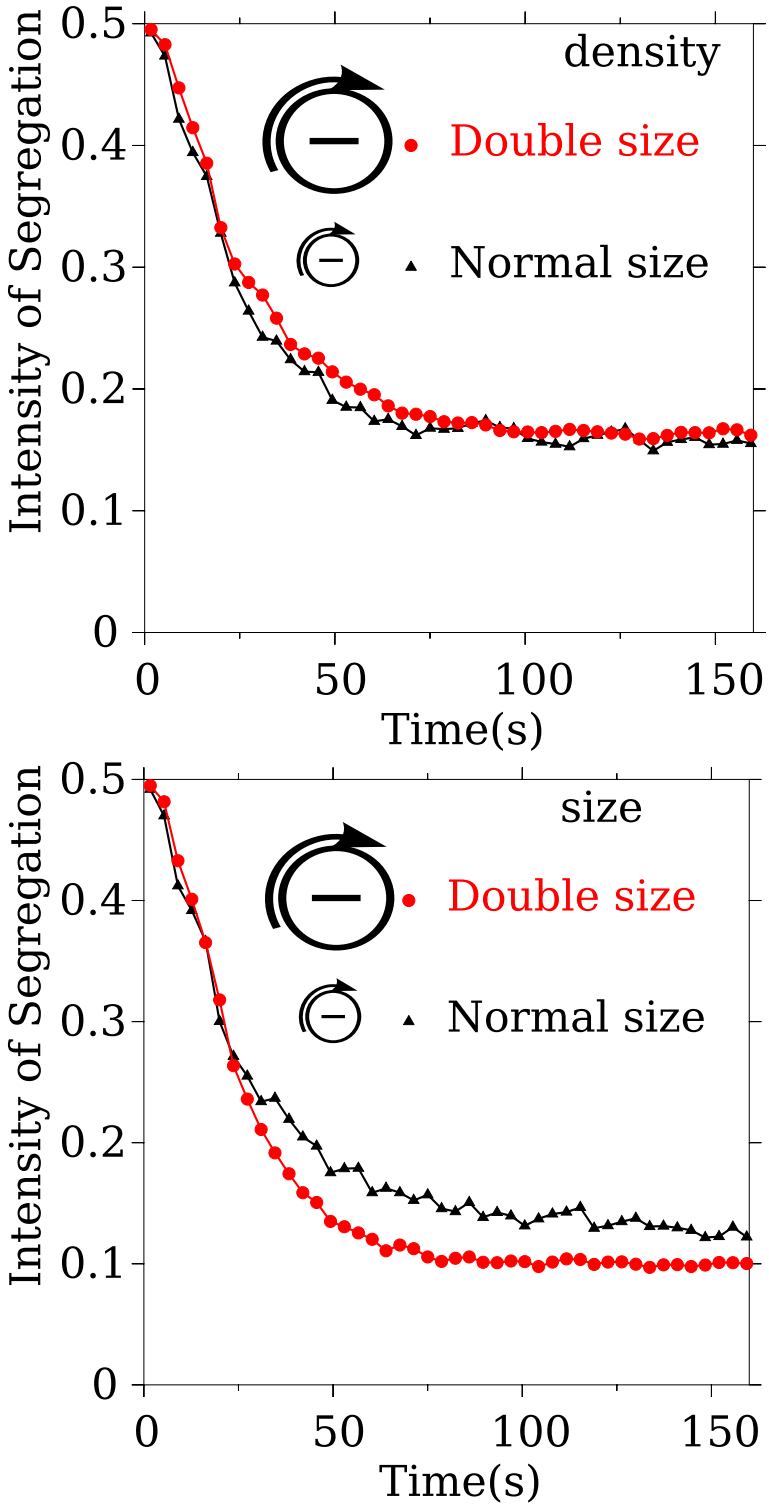

Figure 40: For density segregation, the double size mixer achieves almost the same IS as the normal size mixer. For size segregation, the double size mixer achieves even better mixing results than the normal size mixer.

4.0 COHESIVE GAS-SOLID FLOWS

Fluidized beds are one of the most widely used devices in particle processing. Tsuji [91] and Hoomans [92] have incorporated CFD into PD to study the two-dimensional gas fluidization process. The algorithm is shown in Figure 41. Yu [18, 47] and Thornton [48] were the first groups to explicitly use Newton's third law in generating their PD/CFD coupling expression, thereby making the simulation consistent with the commonly accepted wisdom- the bed pressure drop at minimum fluidization balances the weight of bed [93].

4.1 CHARACTERIZATION OF COHESION IN GAS-SOLID FLOWS

Computer simulations of fluidized beds are run using soda lime glass particles and air with properties as given in Table 7. Dimensions of the fluidized bed are 30mm (width) $\times$ 510mm (height) $\times$ 1mm (thickness). All simulations have the same initial condition in order to aid comparison between differing degrees of cohesion. The initial condition is created by loading the particles in a rectangular lattice. The degree of inter-particle cohesion is varied by changing the surface tension of the liquid bridge fluid (as might be done with surfactants, experimentally), while maintaining a constant viscosity.

As shown in Figure 42, periodic boundary conditions are employed on the left and right sides of the fluidized bed and a Dirichlet boundary condition is used at the bottom with a uniform gas inlet velocity. At the top, Neumann boundary conditions (zero gradient) are applied assuming the flow to be fully developed. The pressure is fixed to a reference value at the bottom. Figure 43 shows the simulation results of gas velocity and gas pressure.

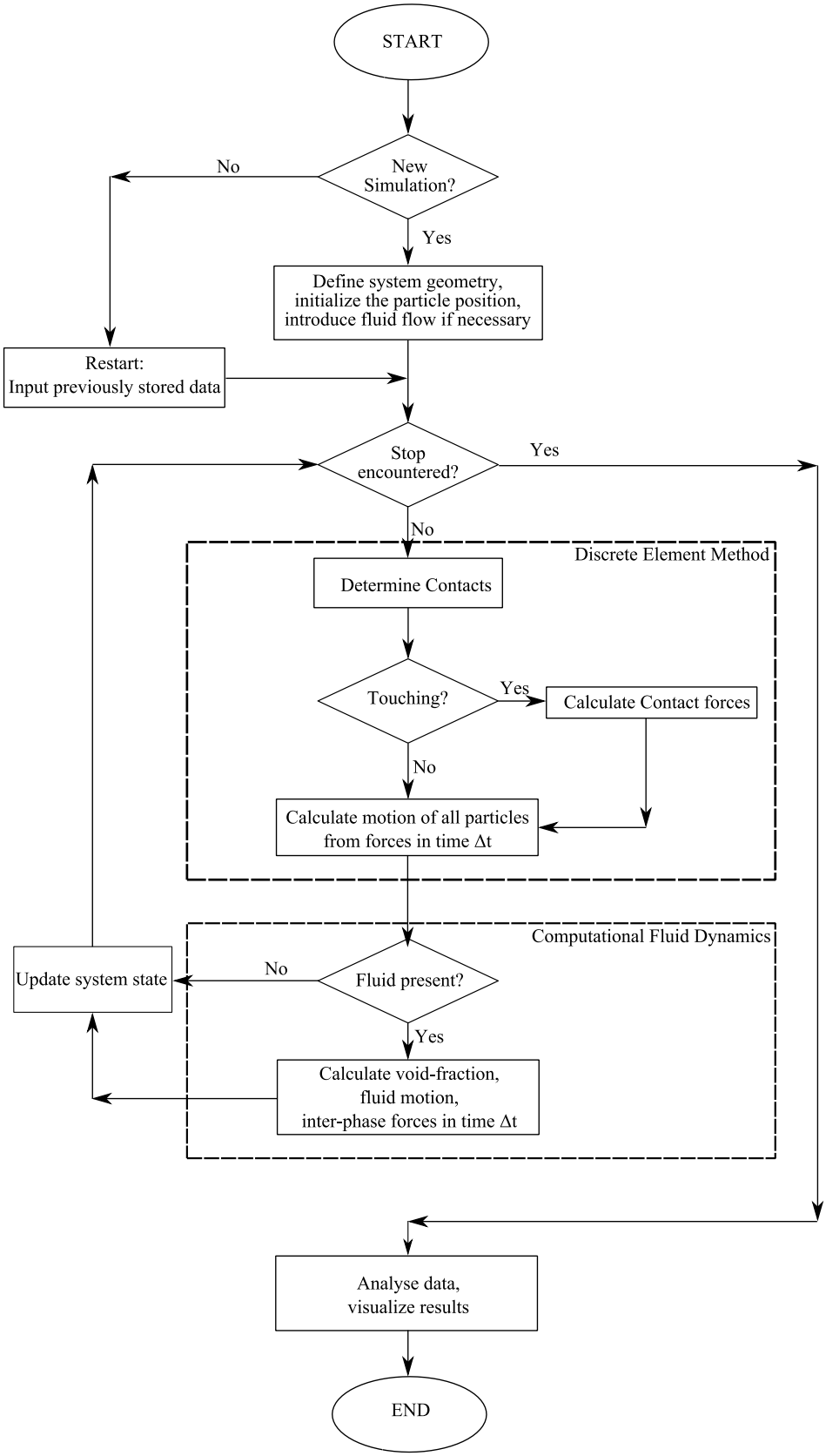

Figure 41: PD CFD calculation algorithm

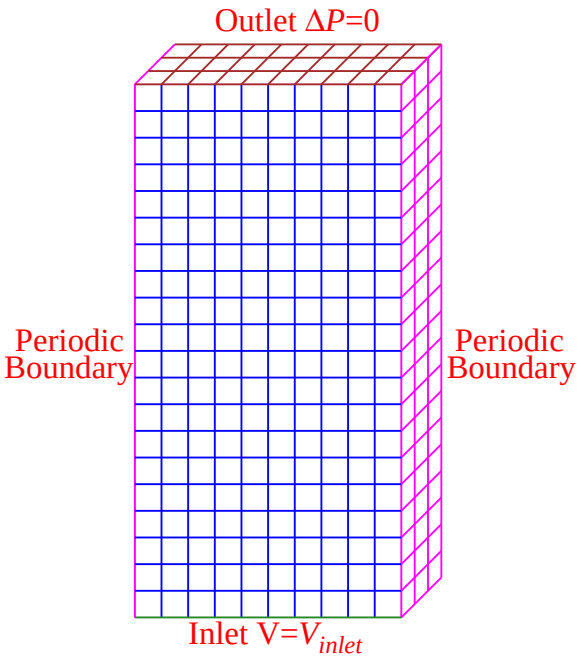

Figure 42: Fluidized bed boundary conditions.

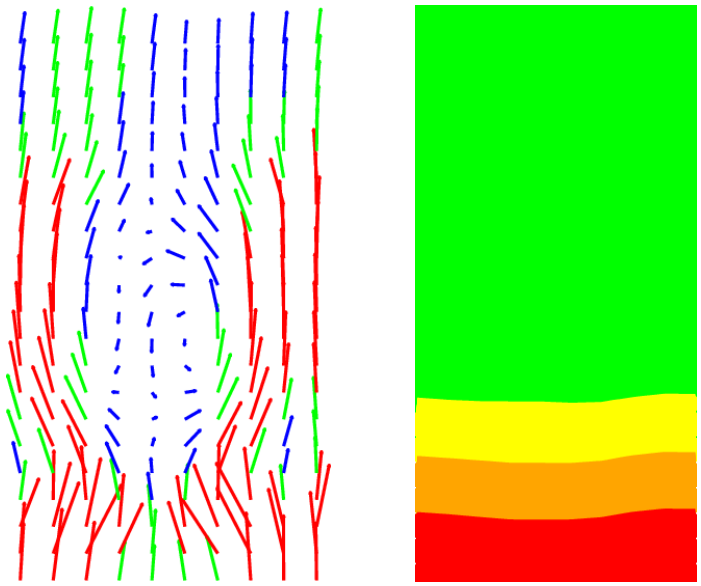

Figure 43: CFD simulation of fluidized bed. The arrows in the left figure shows the velocity magnitude and direction. Red color represents large velocity magnitude and blue color represents small velocity magnitude. The right figure shows the pressure distribution in the fluidized bed. The bottom has high (red) pressure and the top has low (blue) pressure.

4.1.1 Tools

The relevant variables that need to be considered in studying gas-solid flows include R, ρ_s, ρ_g, g, γ, $\hat{V}$, δ, μ_g, where δ is a characteristic length of any shearing regions and $\hat{V}$ is alternatively the relative velocity of the particle with respect to the fluid velocity ($\hat{V} = u - v_p$) or the relative velocity between neighboring particles ($\hat{V} = v_{p_i} - v_{p_j}$). It should be noted that, in this study, the viscosity of the liquid bridge fluid, μ, is maintained constant as the effects of dynamic viscous forces in wet media have been aptly explored by Ennis *et al.* [37, 94]

By a Buckingham Pi analysis [95], five dimensionless groups are determined:

$$\phi_1 = \frac{\delta}{R}, \phi_2 = \frac{\rho_s}{\rho_g}, \phi_3 = \frac{\gamma}{\rho_s g R^2}, \phi_4 = \frac{\hat{V}^2}{gR}, \phi_5 = \frac{\gamma}{\mu_g \hat{V}}. \tag{4.1}$$

The trivial dimensionless groups arising from the length-scale and density do not directly factor into studying cohesion and are ignored. The remaining three dimensionless groups may be thought of as combinations of forces acting in the system: the cohesive force, the force due to particle collisions, the weight of a particle, and the drag force. Previous work [23] detailed the significance of the third and fourth (using the relative interparticle velocity) group of variables for characterization of wet granular systems, so they are only briefly reviewed below.

The third group (ϕ_3), the Granular Bond Number (Bo_g) [23], represents the ratio of the maximum capillary force to the weight of a particle. This group has been shown to be dominant in characterizing the effects of cohesion in static or near-static systems [23]. The fourth group (ϕ_4) can be combined with Bo_g to yield the Collision Number (Co) [23], which represents the ratio of the maximum cohesive force and the collisional force due to Bagnold [96]. This number has been shown to be dominant in highly sheared or collisional granular flows where $Bo_g > Co > 1$[23].

It is the fifth group (ϕ_5) and its derivatives which are examined in this context for the first time and are of primary importance here. This group may be easily interpreted as a ratio of the maximum capillary force

$$F_{c_{max}} = 2\pi R\gamma \tag{4.2}$$

to the drag force

$$F_d = \frac{1}{2} C_d \rho_g \pi R^2 |u - v_p| (u - v_p) \epsilon^{-\chi+1}.$$

This yields the Granular Capillary Number (Ca_g) as

$$Ca_g = \frac{F_c}{F_d} = \frac{4\gamma}{C_d \rho_g R |u - v_p| (u - v_p) \epsilon^{-\chi+1}}. \tag{4.3}$$

4.1.2 Fluidization

As a first test of the utility of the Granular Capillary Number, we examine the onset of fluidization – the minimum fluidization velocity – in cohesive gas-solid systems. The minimum fluidization velocity is typically defined as the velocity at which the bed pressure drop goes through a maximum value. A critical component of this definition is that, while the pressure drop is ultimately determined solely by the weight of the fluidized particles, the value of the pressure drop can exceed this limit prior to fluidization. In the small fluidization systems examined here a simpler, but equivalent, definition of the minimum fluidization velocity is used. The approach used for determining the minimum fluidization velocity is similar in spirit to that followed by Thornton *et al.* [48] which is based on monitoring the state of the particle connectivity network. Figure 44 shows a plot of pressure drop versus time for different gas-velocities. For $u < u_{mf}$, the pressure drop essentially remains constant and for $u \geq u_{mf}$, the pressure drop varies with time. The amplitude and standard deviation of the pressure disturbance also increase sharply as the fluidization velocity becomes greater than the minimum fluidization velocity (Figure 44 and Figure 45). Hence, the minimum fluidization velocity can be defined as the velocity at which the fluctuations (standard deviation) of the pressure drop has a step change. This technique provides reproducible results and avoids difficulties in averaging for small systems.

We find that, using this definition of the minimum fluidization velocity, an increase in the Ca_g (surface tension) increases the velocity necessary to achieve a fluidized system relative to that of the completely dry (non-cohesive) case. Figure 46 shows a plot of the percentage increase in the minimum fluidization velocity as a function of the Ca_g. For values of surface

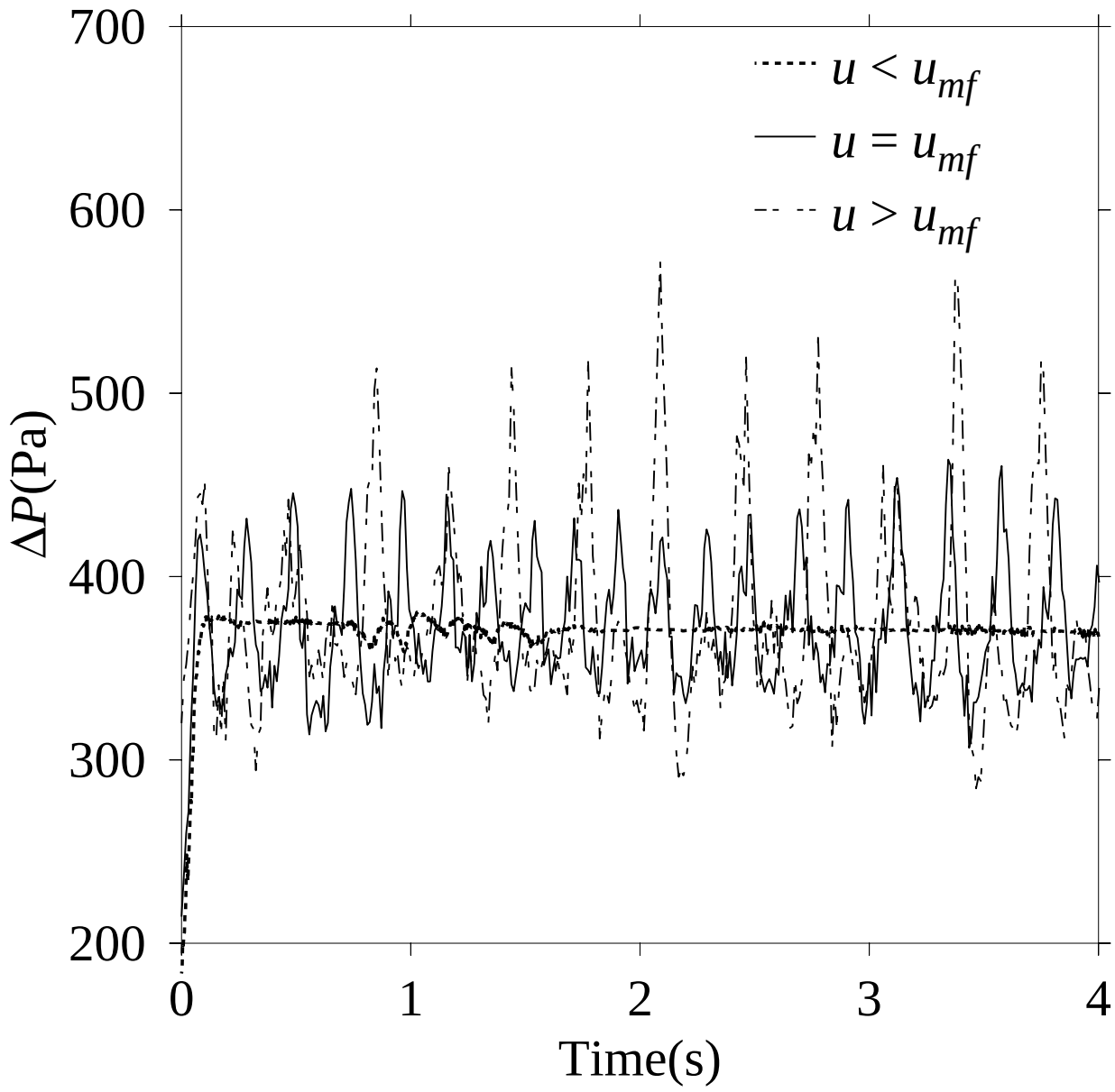

Figure 44: Pressure drop versus time for different gas velocities.

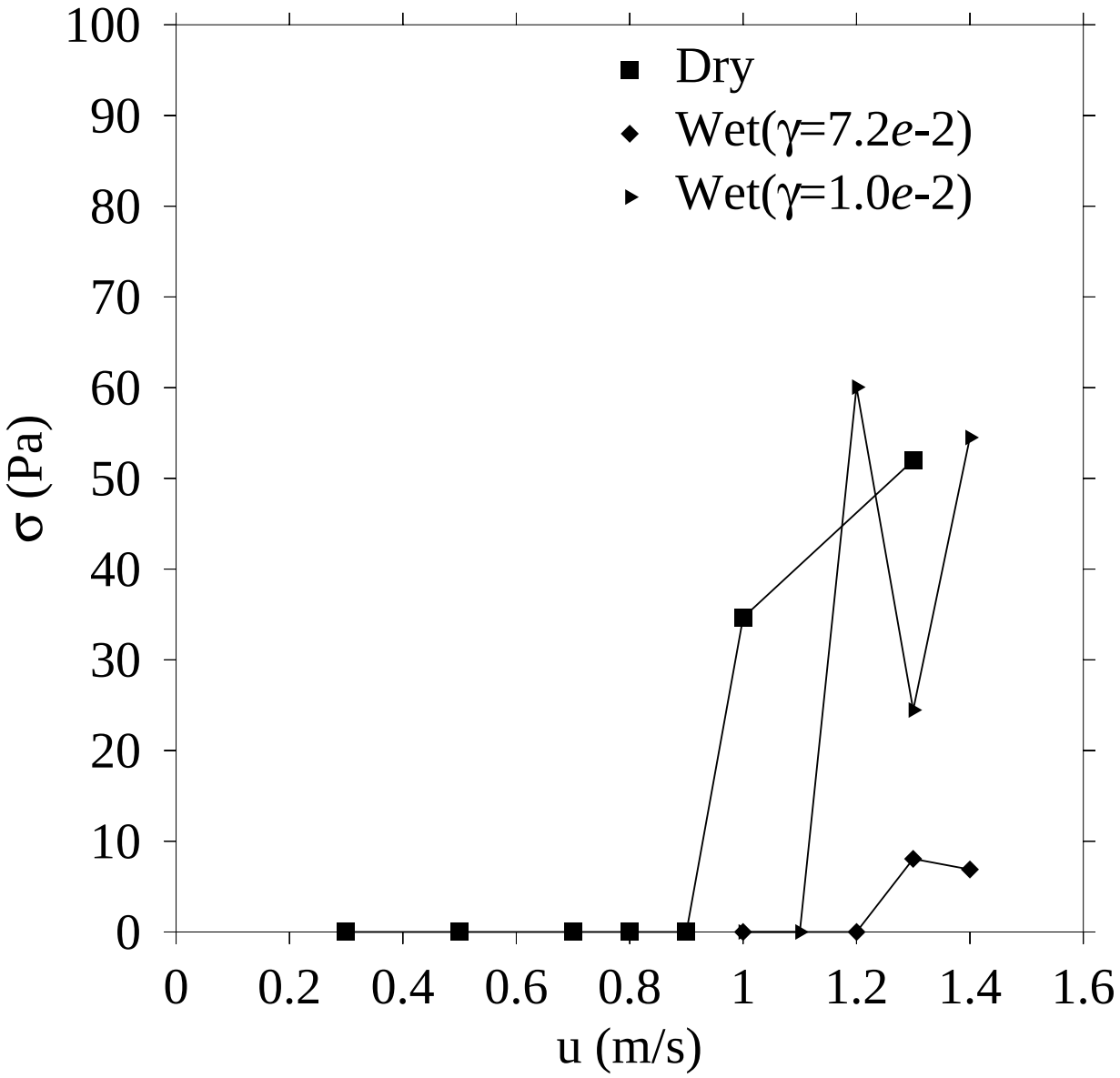

Figure 45: Standard deviation of the pressure drop versus gas-velocity for dry and wet systems.

tension where the $Ca_g < 1$, changes in the fluidization velocity from that of a completely dry granular material are essentially unmeasurable; however, for larger surface tensions, where the values of $Ca_g > 1$, the fluidization velocities increase markedly, requiring as much as a 30% increase in u_{mf} at the highest Ca_g examined.

4.1.3 Mixing

The mixing in gas-solid systems is often extremely rapid compared to mixing in surface-dominated flows [22]. In this section we examine changes of the mixing rate of mechanically identical particles with varying gas velocity as well as liquid bridge surface tension.

In all cases, the system is initially completely segregated with the right-half of the bed consisting of one type (color) of particle and the left-half another. Typical snapshots of a dry and wet simulation can be seen in Figure 47, and particle clusters exist in the cohesive material. If the IS is plotted as a function of time, the value – initially at 0.5 for completely segregated – will decrease as the system proceeds toward a mixed state. Figure 48 shows the evolution of the IS at several different gas velocities. As might be expected for steady mixing progress, the slope of the IS curves (which may be interpreted as the mixing rate) decreases with increasing fluidization velocity. Figure 49 shows similar results for a fixed gas velocity and varying liquid bridge surface tension, where the slope magnitude of the IS curves (or mixing rate) decrease with increasing liquid bridge surface tension. By fitting these data to an exponential function, a mixing rate constant can be extracted.

Examining both figures (48 and 49), it is clear that higher velocities and/or lower surface tensions result in larger (faster) mixing rates. Our definition of the Granular Capillary Number (Ca_g) then suggests that the importance of cohesion to mixing is determined by an interplay between the capillary force and the fluid drag. Plotting the resultant mixing rate constants as a function of Ca_g, in Figure 50, causes the data from the previous trials to collapse on one curve, showing that this assertion is valid. That is, mixing rates are high for small Ca_g and drop dramatically as Ca_g increases.

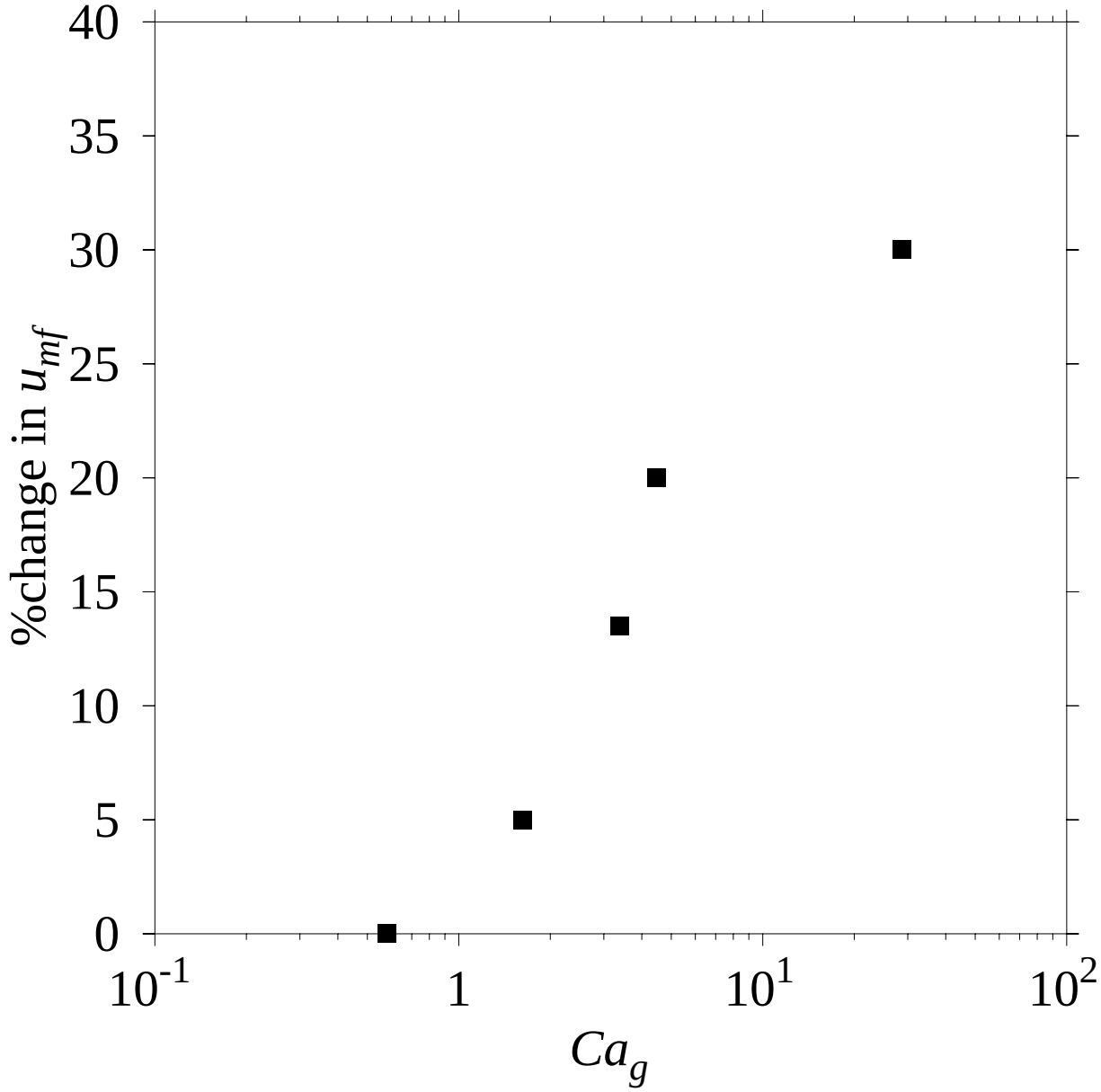

Figure 46: Increased fluidization velocity versus Granular Capillary Number.

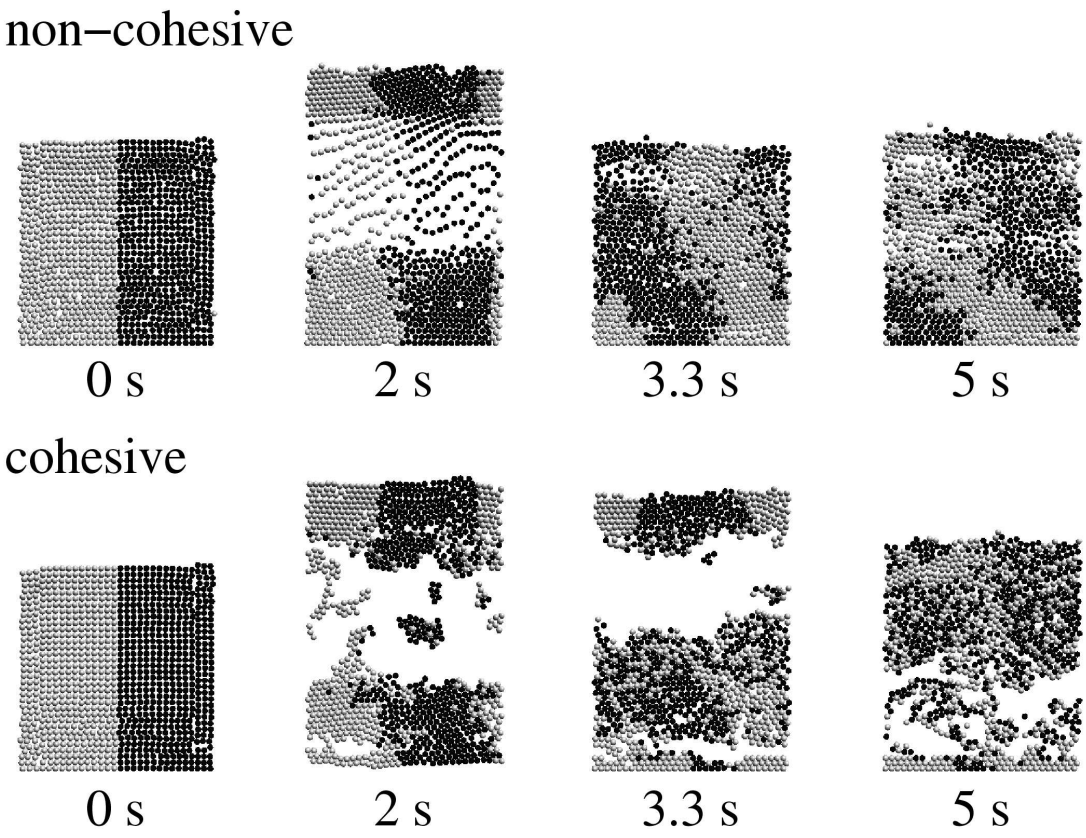

Figure 47: Mixing progress for non-cohesive/cohesive materials.

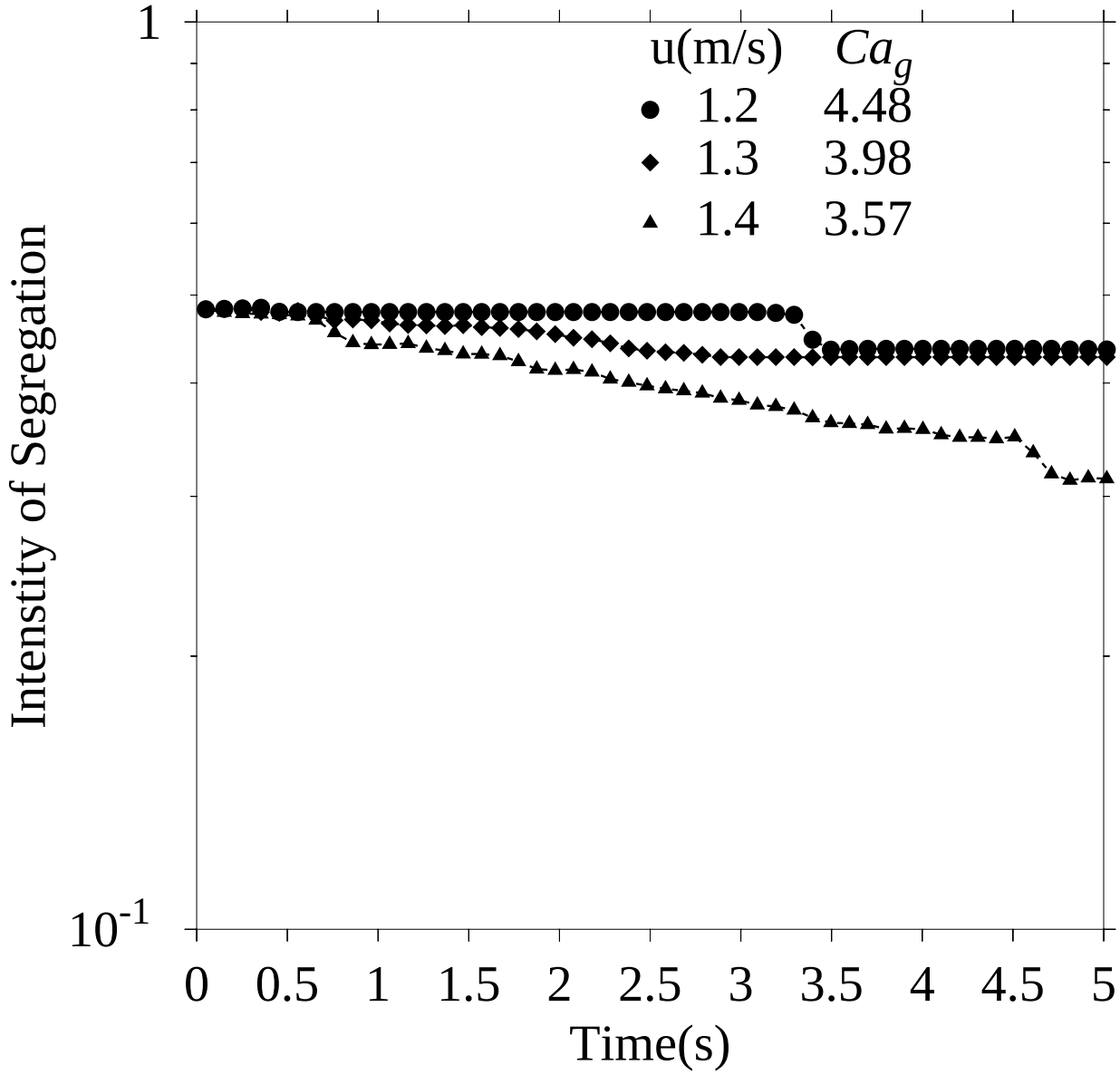

Figure 48: Mixing rates at different gas velocities.

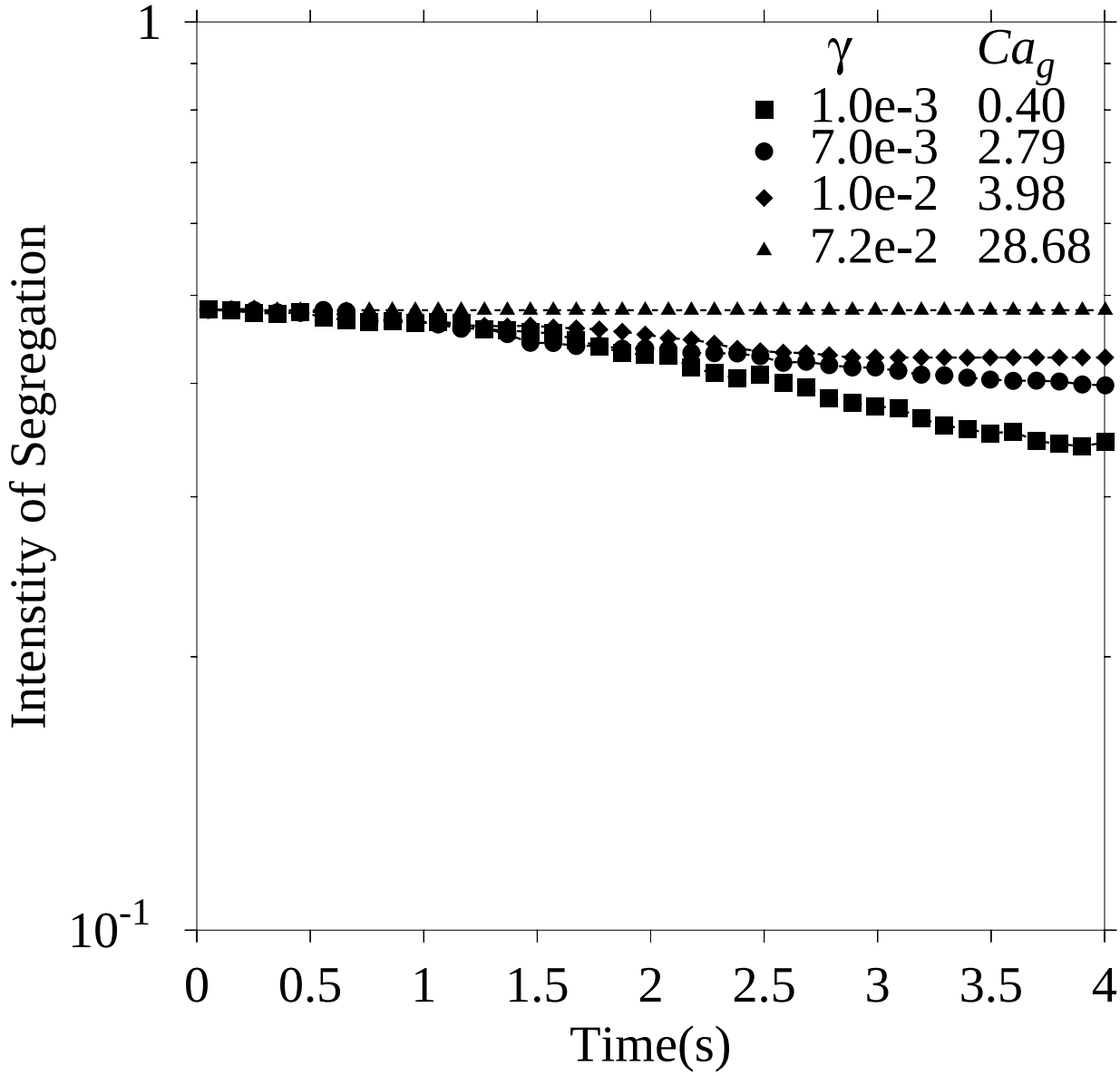

Figure 49: Mixing rates at different surface tensions.

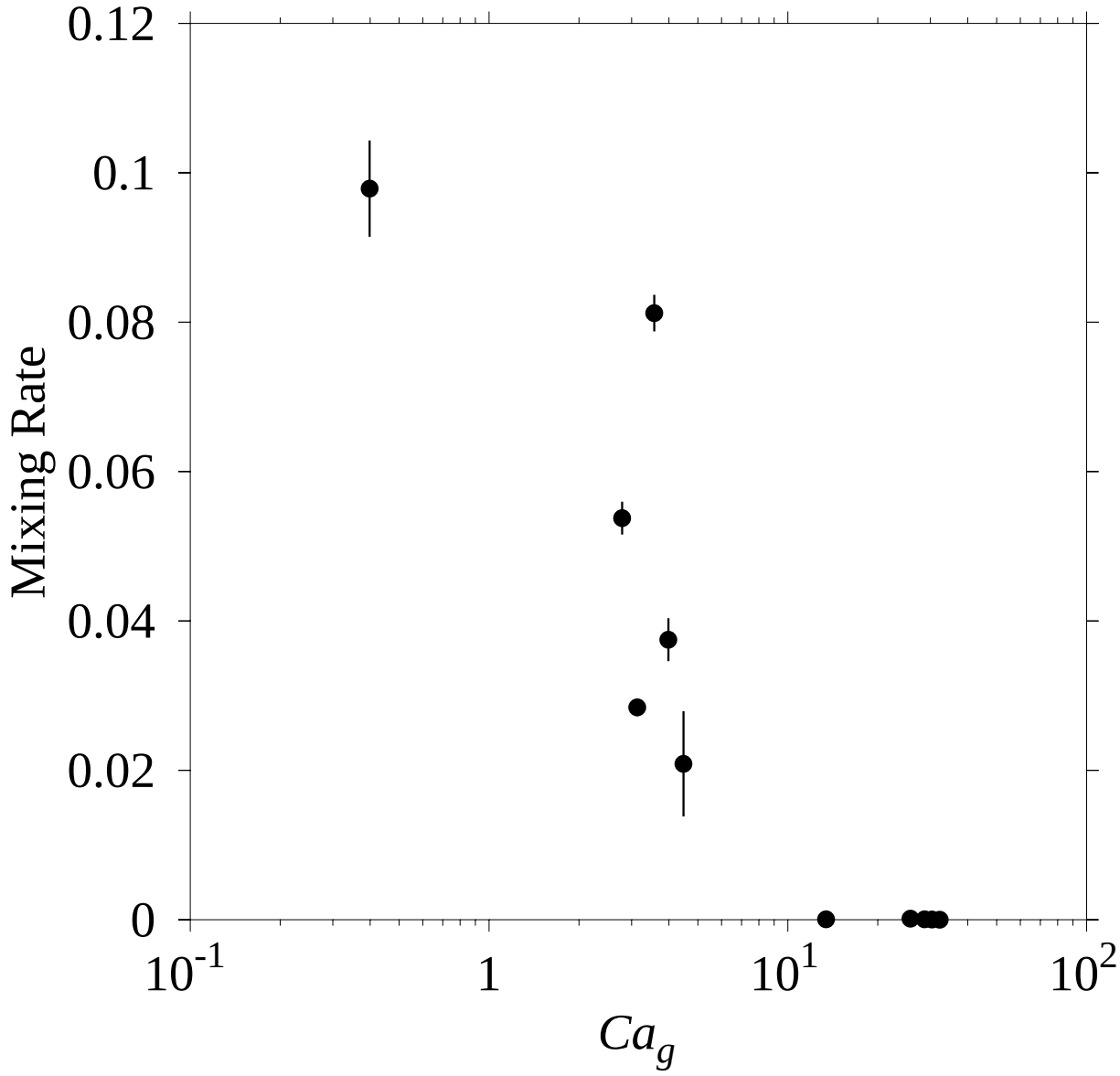

Figure 50: Mixing rate versus Granular Capillary Number.

4.2 MIXING AND SEGREGATION IN GAS-SOLID FLOWS

4.2.1 Phase Diagram for Binary System

The capillary number has been shown to predict the behavior of cohesive mono-disperse systems [3]. In order to extend the definition to binary systems, we must modify our approach in two ways. First, we use the effective radius to calculate the capillary force. In the case of binary interactions, we also must choose a particular value of the particle's drag force. In our approach, we hypothesize that the correct value of the drag for a binary interaction is that which contributes to the bigger ratio of drag force to weight, i.e.

$$Ca_{g12} = \frac{F_{c_{eff}}}{F_{d^*}} \tag{4.4}$$

$$F_{d^*} : \max(\frac{F_{d1}}{W_1}, \frac{F_{d2}}{W_2}). \tag{4.5}$$

Using this extended definition of the capillary number, we can develop a phase diagram to predict the mixing and segregation in the asymptotic state for a binary system, where particles have different sizes, densities and/or wetting characteristics. By calculating the capillary number for every potential pair of particles, we can rank $Ca_{g11}, Ca_{g22}, Ca_{g12}$. If $Ca_{g11} < Ca_{g12}$ and $Ca_{g22} < Ca_{g12}$, the cohesion between different particles is more dominant than that between the same type of particle, thus the cohesion will make the particle system more mixed than in a dry case. If $Ca_{g11} < Ca_{g12} < Ca_{g22}$ or $Ca_{g22} < Ca_{g12} < Ca_{g11}$, we can expect the cohesion to make the system more segregated than in a dry case.

Figure 51 shows the phase diagrams for a binary system. In the top diagram, both particles have the same density. In the bottom diagram, the two particles have a density ratio of 2. If a point is in the E region, a wet particle system should be more segregated than a dry case. If a point is in the M region, a wet particle system should be more mixed than a dry case.

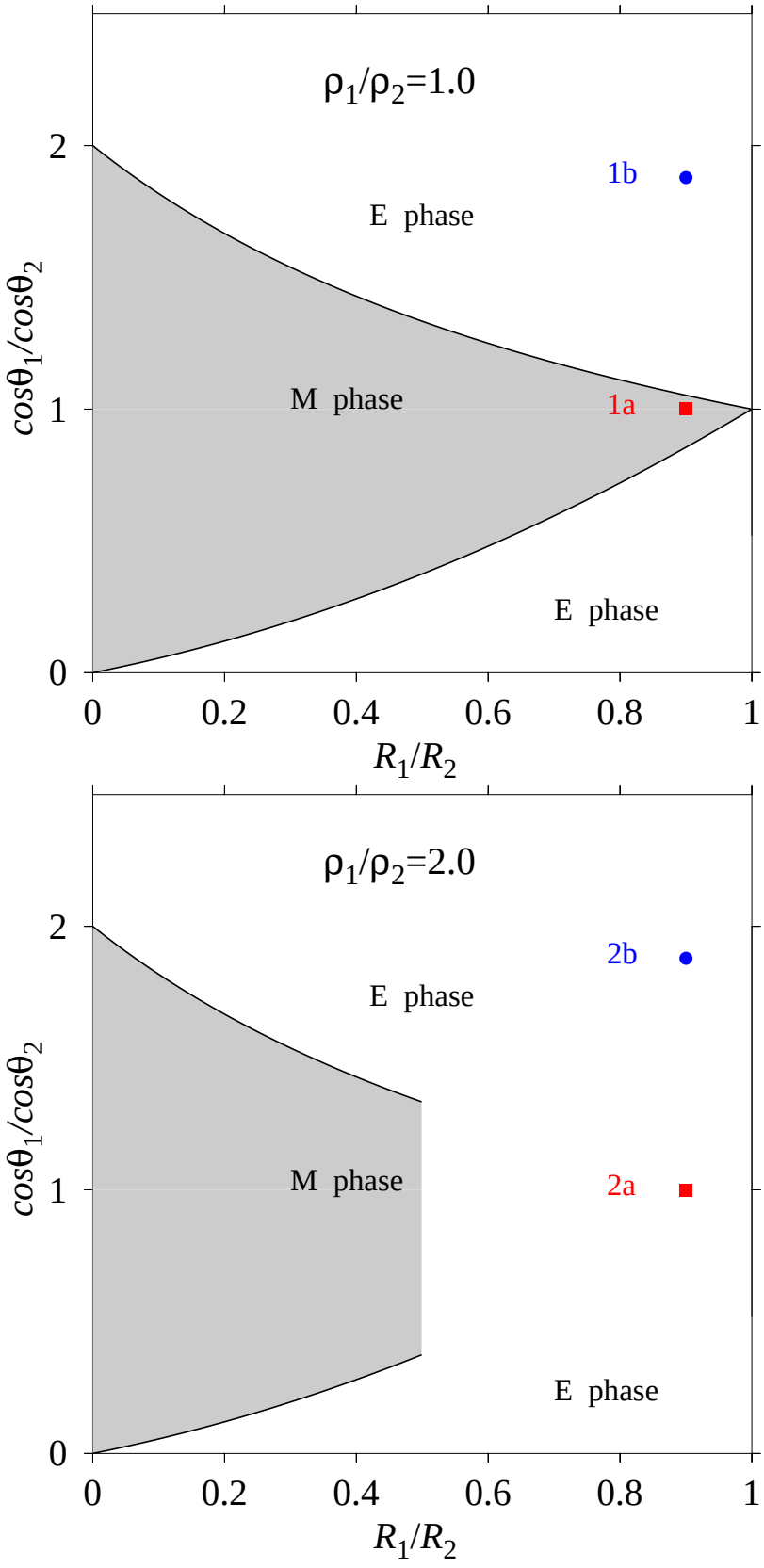

Figure 51: Phase diagram for binary system

4.2.2 Controlling Mixing and Segregation in Gas-Solid Flows

To test our theory, we perform some simulations with particles having various sizes, densities and wetting angles. For the simulation having particles of the same density ($\rho_1 = \rho_2$=2000 kg/m^3) and wetting characteristics ($\theta_1 = \theta_2 = 20°$), but differing size ($R_1 = 1.35$ mm, $R_2 = 1.5$ mm), we are examining the M phase of Figure 51 (point 1a). From Figure 52, we see that the values of IS for point 1a are below that of the dry case, corresponding to a more mixed state. Thus, point 1a is more mixed than the dry case in the asymptotic state, which is consistent with the prediction of our model.

By changing the wetting angle ($\theta_2 = 60°$) while keeping all other properties constant, we can examine the E phase of Figure 51 (point 1b). As shown in Figure 52, the IS values for point 1b are larger than that for dry case, as we expected.

Using the same approach, we can examine points 2a and 2b in Figure 51, which have different density (ρ_1=2000 kg/m^3, ρ_2=1000 kg/m^3). As shown in Figure 52, the IS curve for both points 2a and 2b overlap with that of the Dry case, which can be explained by the fact that the dry case is already very segregated (the IS values are above 0.46). In both cases it is clear that cohesion does not favorably impact mixing.

The simulations above have a gas velocity 1.8 m/s. In order to check the influence of different gas velocity on mixing and segregation, a higher gas velocity 2.0 m/s was used to repeat the simulations. The results can be seen in Figure 53. The values of IS are lower than that of the corresponding 1.8 m/s simulations. These results show that higher gas velocity can improve the mixing extent of both the dry and wet systems, a conclusion that is consistent with that of Hoomans et al. [16], where only the dry case is studied.

In Figure 53, the IS values for all three cases essentially overlap with results in 1b not necessarily supporting our predictions. This observation can be attributed to the fact that at the higher gas velocity the Ca_g values decrease, so that, at least in Case 1b ($Ca_{g22} < 1$ and $Ca_{g12} < 1$), the system will behave more like a dry system despite the presence of cohesion.

Due to the fact that $F_d \approx W$, so $Bo_g \approx Ca_g$, both Granular Bond Number and Capillary Number of the system, as well the predicted region in the phase diagram, are listed in Table 3.

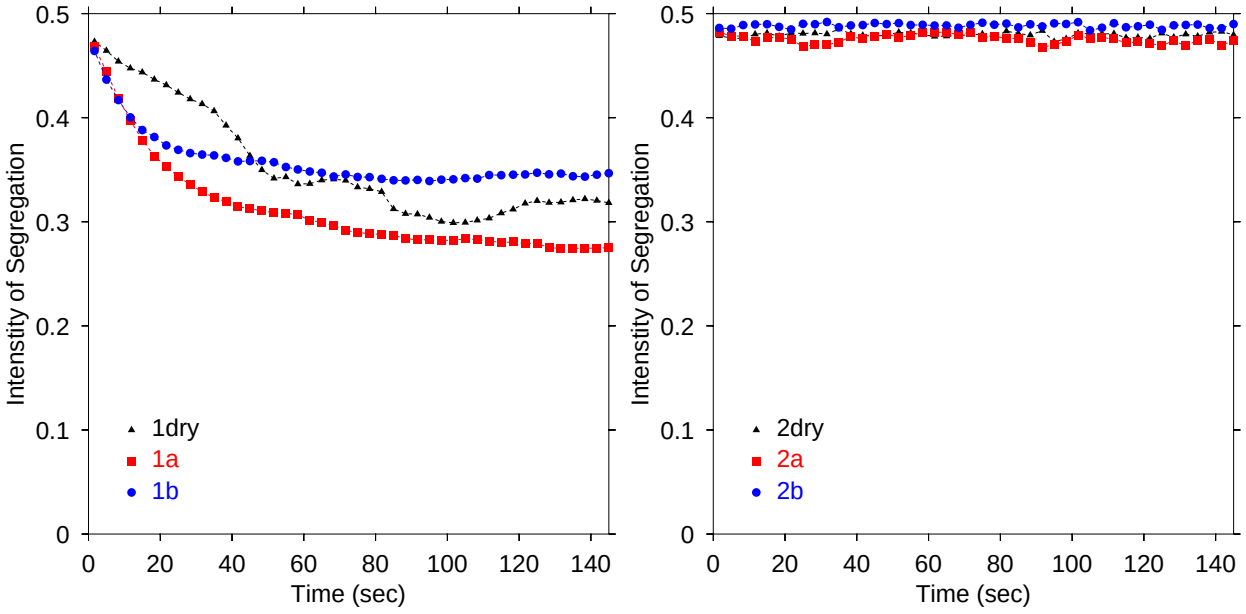

Figure 52: Simulation having gas velocity 1.8m/s

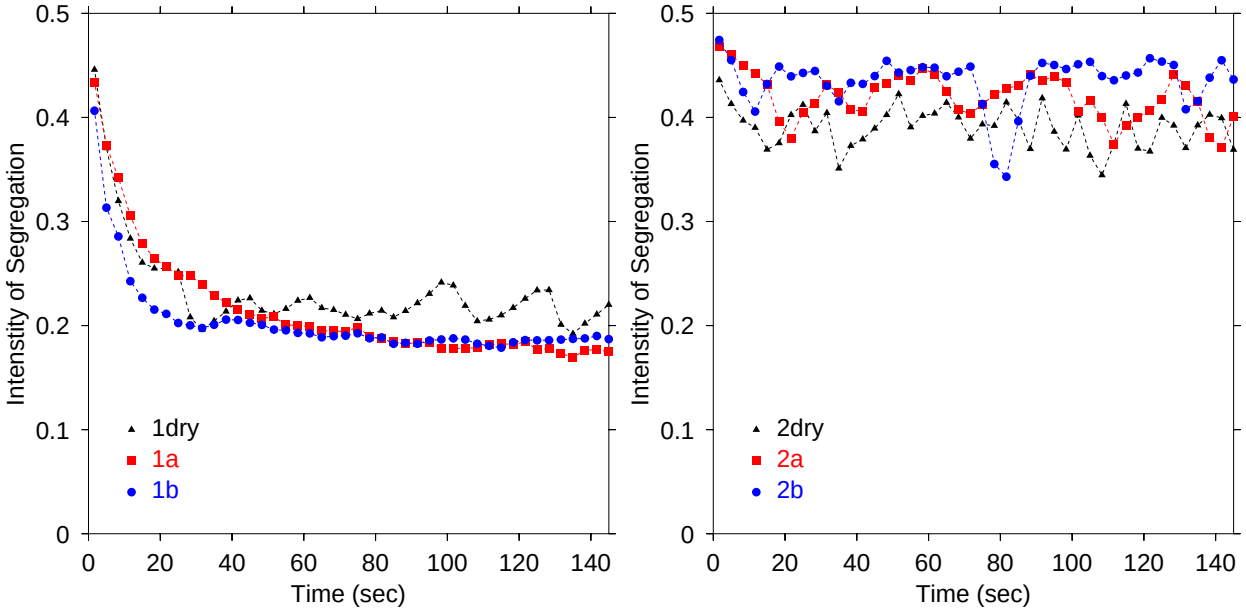

Figure 53: Simulation having gas velocity 2.0m/s

4.3 CONCLUSIONS

Here we examine the transition from free-flowing to cohesive behavior in gas-solid flows. Our group have shown in previous work [23] that discrete characterization tools are extremely useful for studying the practical applications of both static and sheared granular materials. Again, with the introduction of the Ca_g, we note that changes in the fluidization onset are aptly captured by these types of tools. While this simple approach works surprisingly well for predicting the transition point for the minimum fluidization velocity, at present it does not address the nature of the change – although there is clearly an exponential change in its value. Moreover, the mixing behavior is surprisingly sensitive to these changes as well and, in fact, the transition seems dramatically sharper for this unit operation. Ultimately, this simple characterization tool may serve as a useful *a priori* test of the fluidization character and mixing/segregation to be expected in a wet gas-solid system.

It should be noted that mixing rates in fluidized systems vary dramatically with fluidization velocity. This makes our analysis considerably more difficult than cohesive mixing studies in other devices [2, 97]. Since the minimum fluidization velocity changes with Granular Capillary Number, which has been shown in Figure 46, the effective degree of fluidization varies even from wet to dry cases in the same gas velocity system. For the above simulations, the minimum fluidization velocities changing with Granular Capillary Number are shown in Table 4. Despite all of these difficulties, the discrete number Ca_g still captures the fluidization behavior to a reasonable extent.

Table 3: LIST OF CAPILLARY NUMBER AND BOND NUMBER.

Gas Velocity	Simulation	Ca_{g11}	Ca_{g22}	Ca_{g12}	Phase	Bo_{g11}	Bo_{g22}	Bo_{g12}	Phase
1.8 m/s	1a	2.12	1.93	2.23	M	1.26	1.02	1.32	M
	1b	1.99	0.96	1.11	S	1.18	0.51	0.66	S
	2a	2.12	1.93	1.83	S	1.26	2.04	1.93	S
	2b	1.99	0.96	0.91	S	1.18	1.02	0.97	S
2.0 m/s	1a	1.73	1.58	1.83	M	1.26	1.02	1.32	M
	1b	1.63	0.79	0.91	S	1.18	0.51	0.66	S
	2a	1.73	1.58	1.49	S	1.26	2.04	1.32	S
	2b	1.63	0.79	0.75	S	1.18	1.02	0.97	S

Table 4: MINIMUM FLUIDIZATION VELOCITY FOR DRY AND WET CASES.

R_1 (mm)	ρ (kg/m^3)	Dry	$Ca_g = 1.0$	$Ca_g = 1.5$	$Ca_g = 2.0$
1.35	2000	1.64 m/s	1.66 m/s	1.70 m/s	1.75 m/s
1.50	2000	1.75 m/s	1.78 m/s	1.81 m/s	1.87 m/s
1.50	1000	1.21 m/s	1.23 m/s	1.25 m/s	1.29 m/s

5.0 HEAT TRANSFER

Heat transfer in gas-solid flows involves a complex interplay between mechanical (flow and mixing/segregation) and thermal (contact conductance, convective heat transfer) behavior and a variety of techniques have been employed in the literature to attack this difficult problem. Without considering the gas, Chaudhuri etc. [98] simulated granular flow heat transfer using particle dynamics in a rotating vessel. Assuming each particle represents a heat reservoir and exchanges heat through a thermal pipe, Shimizu [99] simulated the heat transfer process in a fixed coarse-grid fluidized bed. Louge etc. [100] used kinetic theory to simulate steady fully developed heat transfer in the pneumatic transport of a dilute system of massive particles. In this model, the heat transferred to particles in and between collisions is neglected. Li and Mason [101] developed a 2D transient model to simulate the heat transfer in a horizontal pneumatic transport pipe. They used the heat conduction analysis for impinging particles provided by Sun and Chen [102] to model the particle-particle and particle-pipe wall heat transfer, while Zhou *et al.* [103] simulated a bubbling fluidized bed using a similar strategy. According to Sun and Chen's analysis, the contribution of heat transfer due to solid contact is negligible at very small contact time; however, Schlünder [104] concluded that the mechanism of heat transfer at medium and long contact times is different to that at very short contact times. Thus, while the heat transfer by contact conductance may be considered negligible for dilute systems under rapid flow conditions like in work [101] and [103], it cannot be ignored in systems under slow flow conditions and with high particle solid fractions, where lasting contacts between particles are dominant. Molerus [105] has shown, through the evaluation of data published in the literature, that the contact resistance between particles in contact and between the heated surfaces and the particles is the factor

that primarily determines the heat transfer rate between a heated wall and particles in a dense moving bed.

In this chapter, heat transfer is combined with the PD and CFD outlined previously to simulate the heating process of a gas-solid flow system inside a rotary kiln. A simple CFD model has been developed to simulate the cylindrical geometry while maintaining a rectangular cell lattice. The heat transfer models dealing with both the solid phase and gas phases have been introduced as well. The heat transfer coefficients are calculated and the effects of conductive and convective heat transfer are compared.

5.1 MODELING

5.1.1 Fluid Dynamics

In order to cover the kiln, a square area that bounds the circle is mapped. First, an equidistant grid that divides the domain into cells of width three times the particle diameter is used, as shown in Figure 54. Then some lines are added around the sides of the square to make the kiln boundary not cross any side of the control volume as shown in Figure 55, where the kiln boundary only crosses the corner of the corresponding control volumes. The pressure, void fraction and temperature are defined at the geometry center of each control volume. The circular kiln boundary is approximated as lines that connect the corners of related control volumes.

An upwind scheme for convection, a central differencing scheme for diffusion, and a fully implicit scheme for temporal terms is used. The equations are then solved on a staggered grid as shown in Figure 56 using the SIMPLE algorithm suggested by Patankar [44] and detailed in Chapter 2. In the present application, however, the control volumes are not uniform in the whole domain. Figure 56 illustrates the process for calculating the temperature. As we stated before, the node for temperature is at the center of each control volume, which has length Δx, height Δy and thickness Δz. The distance between the node and its neighbors are $(\delta x)_w$, $(\delta x)_e$, $(\delta y)_n$, $(\delta y)_s$, $(\delta z)_t$, $(\delta z)_b$, respectively.

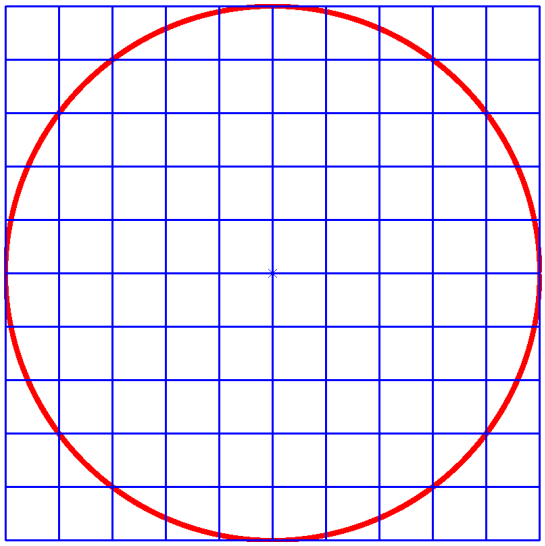

Figure 54: Uniform grids are usually used to mesh rectangular geometries, such as rectangular fluidized beds.

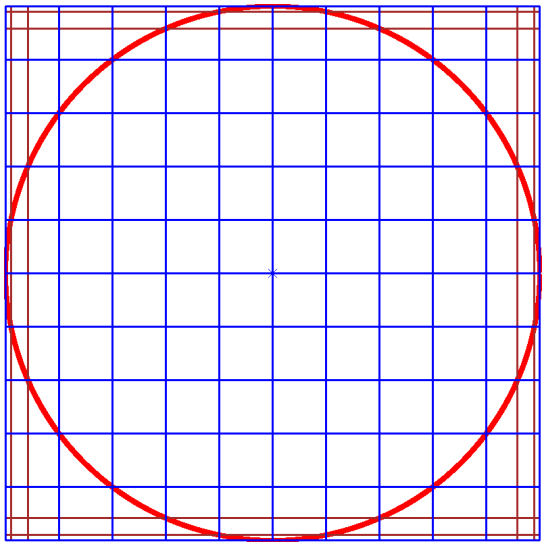

Figure 55: Non uniform grids are employed to mesh the cylindrical geometry so that the cylinder boundary does not cross any side of any control volume. To improve accuracy, more lines can be added to subdivide the control volumes shown in this figure to get a finer mesh.

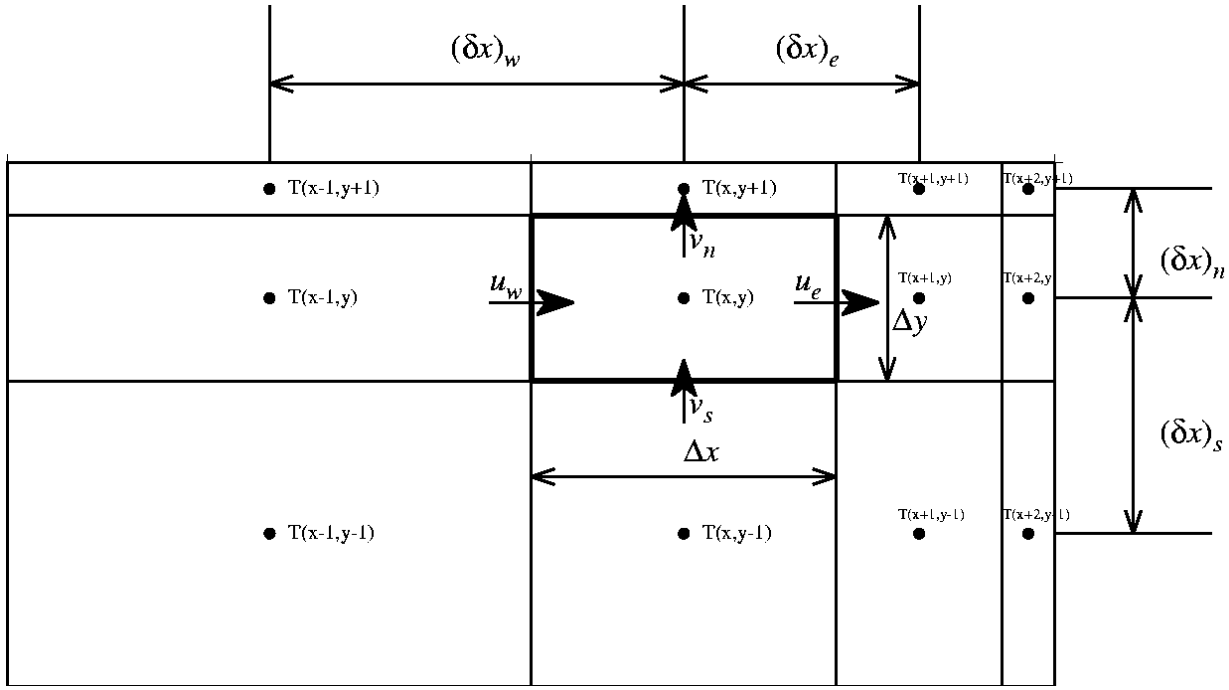

Figure 56: Non uniform grids calculation. Because δx and Δx are different for individual control volume, their exact values have to be used in the modeling. The nodes for the temperature are still in the center of each control volume, and the velocity nodes are still in the middle of each face.

Thus, the mass flow rates and the conductances through the faces of the control volume can be expressed as:

$$G_w = (\epsilon\rho u)_w \Delta y \Delta z \quad D_w = \frac{(\epsilon k_f)_w \Delta y \Delta z}{(\delta x)_w}$$
$$G_e = (\epsilon\rho u)_e \Delta y \Delta z \quad D_e = \frac{(\epsilon k_f)_e \Delta y \Delta z}{(\delta x)_e}$$
$$G_n = (\epsilon\rho v)_n \Delta x \Delta z \quad D_n = \frac{(\epsilon k_f)_n \Delta x \Delta z}{(\delta y)_n}$$
$$G_s = (\epsilon\rho v)_s \Delta x \Delta z \quad D_s = \frac{(\epsilon k_f)_s \Delta x \Delta z}{(\delta y)_s}$$
$$G_t = (\epsilon\rho w)_t \Delta x \Delta y \quad D_t = \frac{(\epsilon k_f)_t \Delta x \Delta y}{(\delta z)_t}$$
$$G_b = (\epsilon\rho w)_b \Delta x \Delta y \quad D_b = \frac{(\epsilon k_f)_b \Delta x \Delta y}{(\delta z)_b}$$

The nodes of pressure and void fraction are at the same places as the nodes of temperature. The nodes of velocity lie on the faces of each control volume. The distances between the velocity node and its neighbors may or may not be the same as a temperature node. The exact values have to be calculated based on the actual grid spacing.

5.1.2 Heat Transfer

There are three mechanisms for heat transfer from the boundary of a heated rotary drum to the inside particles [106]: (i) direct heat transfer from the wall to particles, (ii) heat transfer from the wall to the gas phase, (iii) heat transfer between the gas and solid phase. Besides these three mechanisms, contact heat transfer plays a role among solid particles, while conductive and convective heat transfer contribute to the gas phase heat transfer.

5.1.2.1 Heat Transfer to the Particle The heat transferred to a particle can be expressed as:

$$Q_p = \Sigma Q_c + Q_f + Q_o, \tag{5.1}$$

where Q_c is the heat flux from the neighboring particles due to collision, Q_f is from the gas phase and Q_o is from other sources.

Thus the particle temperature can be updated during each time step using

$$\frac{dT_p}{dt} = \frac{Q_p}{c_p m_p}, \tag{5.2}$$

where c_p is the particle heat capacity and m_p is the particle mass.

The heat flux between two contacting particles with temperature difference ΔT is[107]

$$Q_c = H\Delta T. \tag{5.3}$$

The contact conductance H is the amount of heat transferred per unit temperature per unit time and can be obtained for smooth elastic spheres from

$$H = 2.0 R_c k_s, \tag{5.4}$$

where R_c is the contact radius and k_s is the particle thermal conductivity [107, 108, 109, 110].

Assuming that each cell in the bed is well mixed and that the bulk solids temperature in the bed is the same as the gas temperature, the heat flux from the gas phase to individual particle is given as [17]

$$Q_f = h_{gp} S_p (T_b - T_p), \tag{5.5}$$

where h_{gp} is the local particle-to-gas heat transfer coefficient, S_p is the surface area, T_p is the particle temperature and T_b is the bulk temperature of the neighboring gas phase. The heat transfer coefficient h_{gp} can be obtained from Nu as shown below.

Under high Reynolds number ($Re_{pf} > 100$) conditions

$$Nu = \frac{h_{gp} d_p}{k_g} \approx 2 + (0.6 \sim 1.8) Re_{pf}^{1/2} Pr^{1/3}, \tag{5.6}$$

where k_g is the thermal conductivity of the gas, $Pr = \frac{c_p \mu}{K}$, $Re_{pf} = \frac{\epsilon d_p U \rho}{\mu}$ is calculated per cell unit and U is the superficial gas velocity. This expression is designed such that the values of the particle-to-gas heat transfer coefficient in a fluidized bed lie between those for a fixed bed with large isometric particles (with a factor of 1.8 in the second term [111]) and those for the single particle (with a factor of 0.6 in the second term).

Under low Reynolds numbers ($Re_{pf} < 100$) conditions

$$Nu = \frac{h_{gp} d_p}{k_g} = 0.03 Re_{pf}^{1.3}. \tag{5.7}$$

The heat source in the simulation is the wall, which is treated as a smooth mathematical curve. For the purpose of collision and heat transfer calculations, it is considered as an infinitely large particle. Radiation heat transfer is not included in the current study.

5.1.2.2 Heat Transfer to the Gas For the gas phase, the heat flux from the particles is considered as an added heat source term, thus, the energy equation can be expressed as:

$$\frac{\partial(\epsilon \rho_g c_g T)}{\partial t} + \nabla \cdot \epsilon \rho_g c_g T u = k_g \nabla^2 (\epsilon T) + \Sigma h_{gp} S_p (T_p - T) + Q_{og} \tag{5.8}$$

where ρ_g is the gas density, c_g is the gas heat capacity, k_g is the gas conductivity, $\Sigma h_{gp} S_p (T_p - T_b)$ is the sum of all particles' heat flux to the gas per unit volume, and Q_{og} is the heat flux from other sources to the gas phase per unit volume.

5.1.3 Biot Number

Using the equations outlined above, it is clear that we treat the particles as having a spatially uniform temperature within each particle. This assumption is valid provided that the Biot Number, incorporating all modes of external transport, is much less than unity.

5.1.3.1 Convective and Conductive Heat Transfer Here we estimate the largest rate of external transport due to convection. If the kiln rotation speed is 10RPM, the maximum superficial gas velocity inside the kiln is

$$U = \omega R_{kiln} = 10\text{RPM} \times R_{kiln} = 0.07 m/s. \tag{5.9}$$

Thus, we get a Reynolds number of

$$Re_{pf} = \frac{d_p U \rho_g}{\mu_g} = \frac{3 \times 10^{-3} \times 0.07 \times 1.23}{1.8 \times 10^{-5}} = 14.35 \quad < 100.0 \tag{5.10}$$

therefore the heat transfer coefficient is given as

$$Nu = \frac{h_{gp} d_p}{K} = 0.03 Re_{pf}^{1.3} = 0.957 \tag{5.11}$$

$$h_{gp} = 0.957 \frac{K}{d_p} = 0.957 \frac{0.0261}{3 \times 10^{-3}} = 8.3259 W/(m^2 \cdot K) \tag{5.12}$$

For aluminum, this yields a Bi of

$$Bi = \frac{h_{gp} R}{k_s} = \frac{8.3259 \times 1.5 \times 10^{-3}}{180.0} = 6.938 \times 10^{-5} \ll 1 \tag{5.13}$$

where k_s is the thermal conductivity of solid particle. For aluminum, the value is $180 W/(m \cdot K)$.

Similarly, for glass, we get

$$Bi = \frac{h_{gp} R}{k_s} = \frac{8.3259 \times 1.5 \times 10^{-3}}{1.7} = 7.346 \times 10^{-3} \ll 1 \tag{5.14}$$

For glass, the thermal conductivity k_s is $1.7 W/(m \cdot K)$.

These results show that the heat transfer from convection is significantly smaller than that from conduction, so convective heat transfer is the limiting step.

5.1.3.2 Conductive Heat Transfer on the Surface and Inside of the Particles In order to assure that the temperature does not vary significantly from one contact point to another (that is, that each particle "not sees" the same temperature for particle i), we must assume that the resistance to heat transfer inside the particle is significantly smaller than the resistance between the particles, that is

$$Bi = \frac{HR}{k_s A} = \frac{2 R_c k_s R}{k_s A} = \frac{2 R_c R}{\pi R^2} = \frac{2}{\pi} \sqrt{\frac{\alpha}{R}} \tag{5.15}$$

where $R_c = \sqrt{R\alpha}$ is the contact radius, α is the overlap. Because $\alpha \ll R$, we can conclude $B_i \ll 1$. This suggests that the resistance to heat transfer inside a particle is significantly smaller than the resistance between interacting particles. Moreover, the sum of the external transport contributions (Section 5.1.3.1 and Section 5.1.3.2) would still yield $Bi \ll 1$.

5.2 RESULTS AND DISCUSSIONS

The rotary kiln considered here is 136 mm in diameter. A mathematical wall with constant temperature is used as the boundary. Since the pressure has relative value, the reference pressure 0 is designated on top of the kiln. Periodic boundary conditions are employed on the front and back of the kiln. Physical parameters of both the particles and fluids used in the simulations can be found in Table 7. The initial condition is created by loading the particles in a rectangular lattice and then allowing them to fall under gravity to form a packed bed. With the rotation of the kiln, the particles will move due to friction between the wall and particles. At the same time, heat will be transferred from the higher temperature wall to the lower temperature particles and gas. Furthermore, the gas will exchange heat with the particles. Thus, both conductive and gas-to-solid convective modes of heat transfer exist inside the kiln.

5.2.1 2D Simulation

Since 2D simulations run much faster than 3D simulations, we first tested our model in 2D. Two-dimensional simulations are run in a 10 cm radius kiln rotating at 10 RPM, with the thickness of the kiln equal to the diameter of a single particle [18]. Typical snapshots can be seen in Figure 57 and Figure 58 for glass and aluminum particles, respectively. The different colors corresponds to different temperatures as shown by the color bar. The aluminum particles increase their temperature much faster than glass particles, as is expected due to the higher conductivity of the aluminum (180W/mK versus 1.7W/mK).

Interestingly, for aluminum particles, the color change first happens along the boundary of the kiln which can be attributed to heat conduction from the wall, while for glass particles, the color change first appears in the center of the kiln which may be attributed to convective heat transfer from the gas. This suggests that convective heat transfer is more important for the smaller conductivity glass particles than for aluminum (the larger conductivity particles). This transition will be explored in detail in Section 5.2.4.

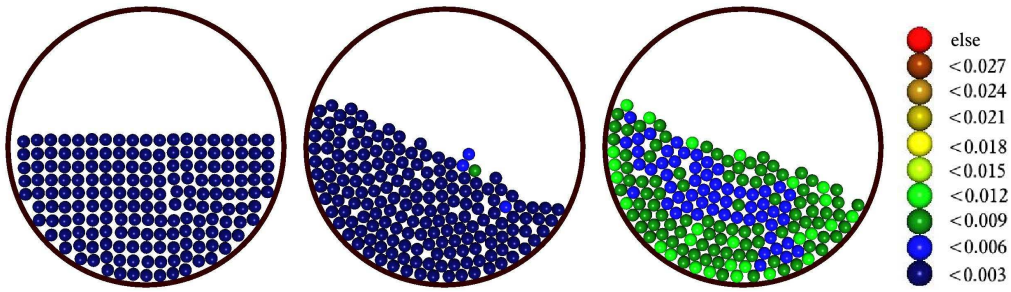

Figure 57: 2D glass particles 0 s, 1.1 s, 18 s. The color bar in the right shows the dimensionless temperature values from the simulation. Red represents high temperature and blue represents low temperature.

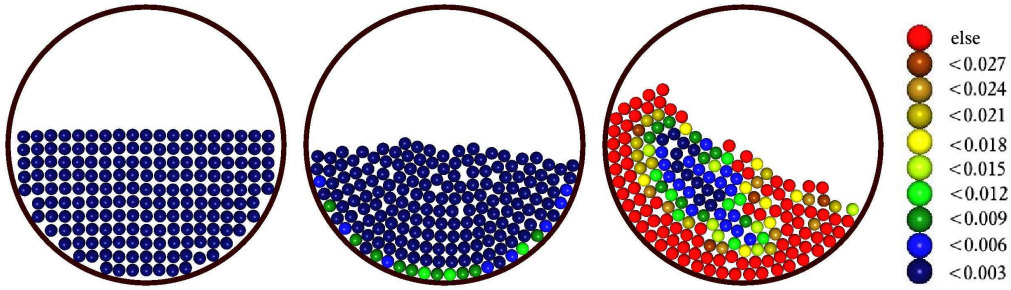

Figure 58: 2D aluminum particles 0 s, 0.03 s, 5 s. The color bar in the right shows the dimensionless temperature values from the simulation. Red represents high temperature and blue represents low temperature.

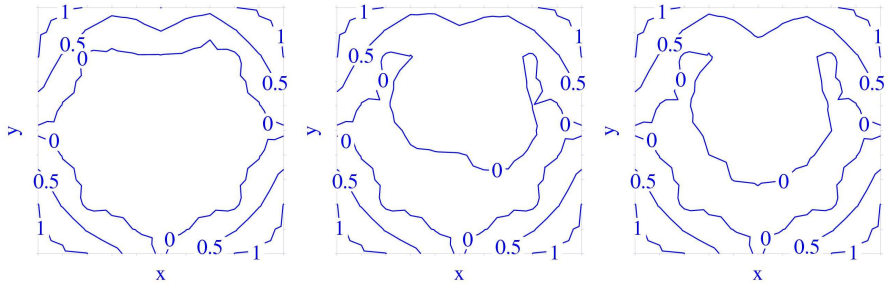

Figure 59: 2D glass gas temperature contour 0 s, 1.1 s, 18 s

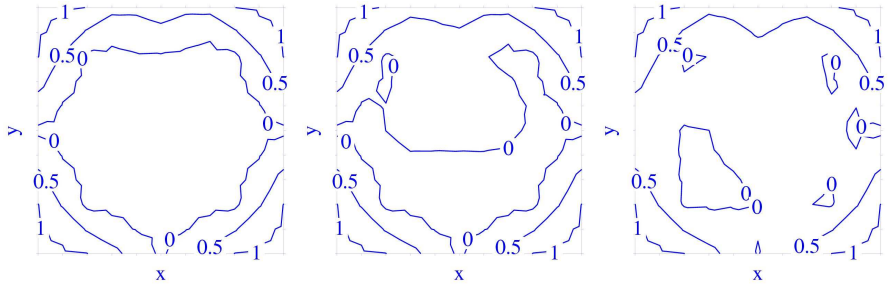

Figure 60: 2D aluminum gas temperature contour 0 s, 0.03 s, 5 s

Figure 59 and Figure 60 show a contour plot of the gas temperatures that correspond to Figure 57 and Figure 58. It is apparent that the low temperature contour line shrinks as time progresses, such that it only contains a small area at 5s for aluminum particles, as shown in Figure 60.

The 2D simulation results in a slightly larger void fraction than a 3D simulation because only one layer of particles is employed. This is illustrated in Figure 61, where the side length of the square region is equal to the diameter of the particles. Figure 61(a) is the schematic for 2D and only one layer of particles appear in the diagram, as only parts of two particles can be inside a square region that has side length equal to particle diameter. In Figure 61(b), which corresponds to a 3D simulation, the square region can have two more parts of particles from different layers. Calculating the 2D void fraction based on volume, we can get the cubic volume having void fraction 0.476. In contrast, the cubic volume in 3D yields a void fraction 0.451, which has only 2.5% difference from the 2D situation. Thus, both 2D and 3D simulation will result in similar void fraction, however, the 2D simulation has an disadvantage when simulating heat transfer. Conductive heat is transfered through the inter-particle contact points. The number of contact points in 2D is much less than that in 3D. As a result, less heat will be conducted than in an actual 3D situation. At the same time, there are fewer particles in the control volume so that the particles will be surrounded by more gas than in a 3D situation, which results in larger convective heat transfer than in 3D situation. Both situations combined together will lead to a disproportionately larger convection in 2D than in 3D situations. In order to overcome these drawbacks, 3D simulation is necessary for heat transfer related gas-solid flows, which is shown in the following part.

5.2.2 Particle Temperature Evolution in 3D Simulation

Figure 62 and Figure 63 are 3D simulation snapshots of the temperature evolution in a 15RPM rotating kiln for glass and aluminum particles respectively. The different colors correspond to different temperatures with red representing the highest temperature and blue representing the lowest temperature. In vacuum, glass hardly has any temperature (color) change, however, in air, there are a lot of particles changing temperature (color) in

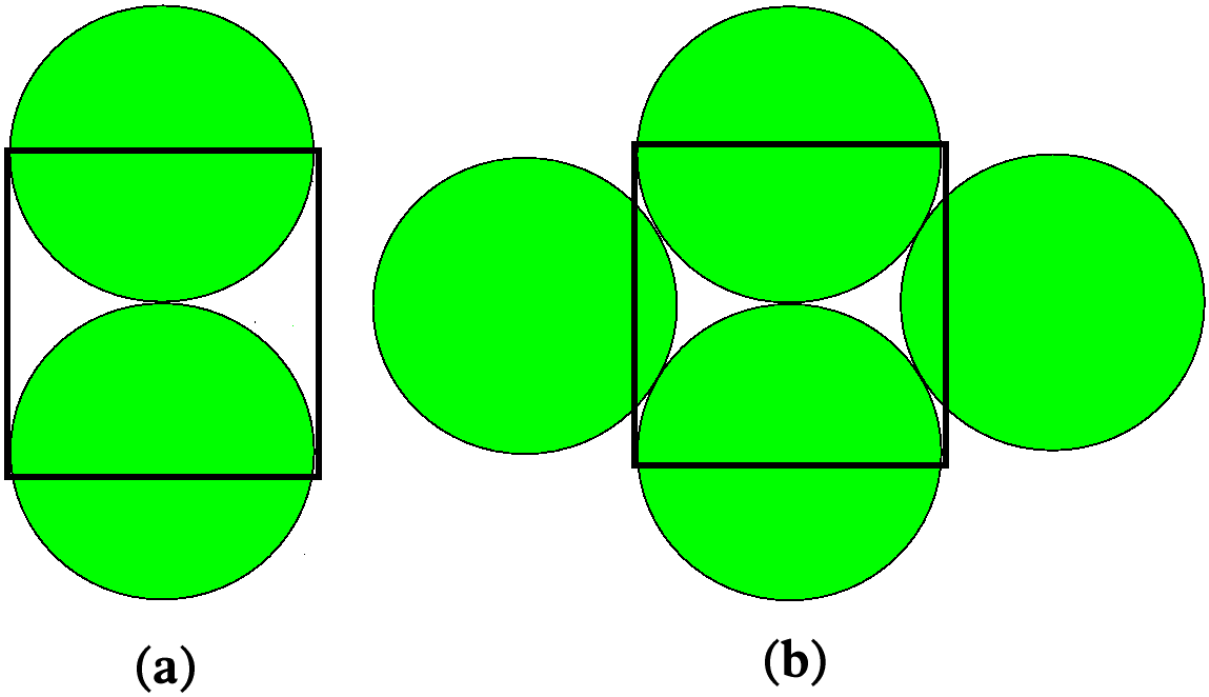

Figure 61: Schematic for void fraction calculation.

30 seconds. It means convective heat transfer plays a significant role in glass beds. For aluminum particle, there are more red particles in air than in vacuum. Convective heat transfer contributes to at least a part of the heat transfer in aluminum beds. The aluminum particles increase their temperature much faster than glass particles, as is expected due to the higher conductivity of the aluminum (180 $\mathrm{W/(m \cdot K)}$ versus 1.7 $\mathrm{W/(m \cdot K)}$).

As was seen in the 2D cases, Figure 64 shows that aluminum particles again change color first along the boundary of the kiln, while glass particles still change color in the center of the kiln. Clearly the same regime transition, from conduction to convection-dominated transport, occurs in 3D as well.

Figure 65 illustrates the temperature evolution for two particles, one starting close to the wall and one starting in the bulk, under vacuum conditions. The longer the particles stay in contact with the wall, the closer the temperature approaches that of the wall with the consequent reduction in the local heat transfer rate. Figure 66 shows the particle temperature evolution in the air system. As shown in the left pictures of Figure 65 (a) and Figure 66 (a), the particle moves from the wall to the shear layer and goes inside the particle bed after many rotations. The middle pictures show the relative radial position of the particles inside the kiln. Similar complicated particle paths can be seen in both Figure 65 (b) and Figure 66 (b) for the particles that originate in the interior. This kind of complicated path has contributed to the fluctuating temperature evolution of individual particles as shown in the rightmost pictures; however, as shown in Figure 67, the bulk temperature of the bed follows a logarithmic functionality. We will discuss this further in Section 5.2.4.

5.2.3 Gas Temperature Evolution

Figure 68 shows the gas temperatures at each simulation node. All the nodes have low temperature at 0s as the blue color indicates. With the rotation of the kiln, more and more nodes become red color (high temperature). The gas temperature coincides with the particle temperature in the lower left part of the kiln as the 30s picture shows and has a much higher temperature in the upper right part when no particles are present.

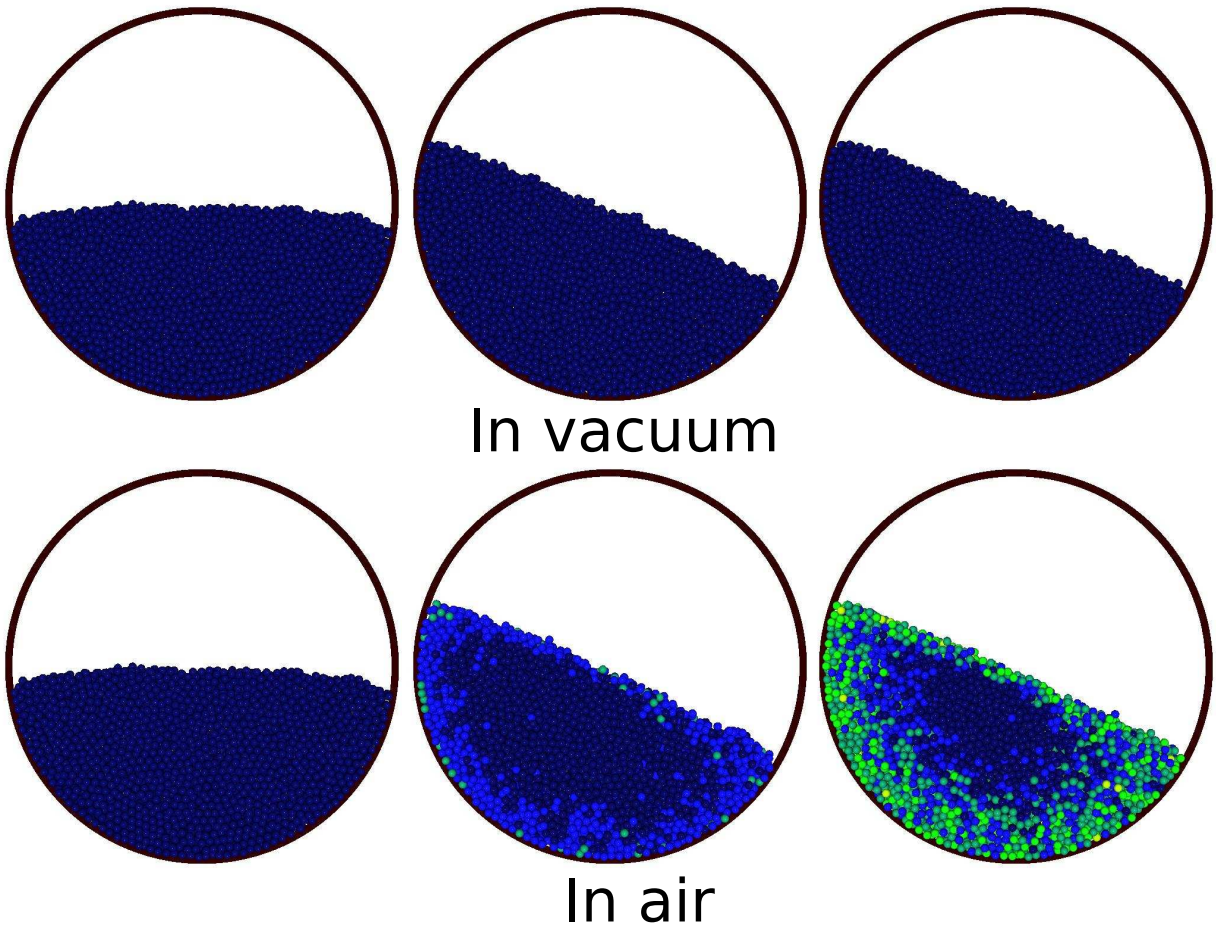

Figure 62: Glass particles 0 s, 15 s, 30 s. In vacuum, glass hardly has any temperature (color) change, however, in air, there are a lot of particles changing temperature (color) in 30 seconds.

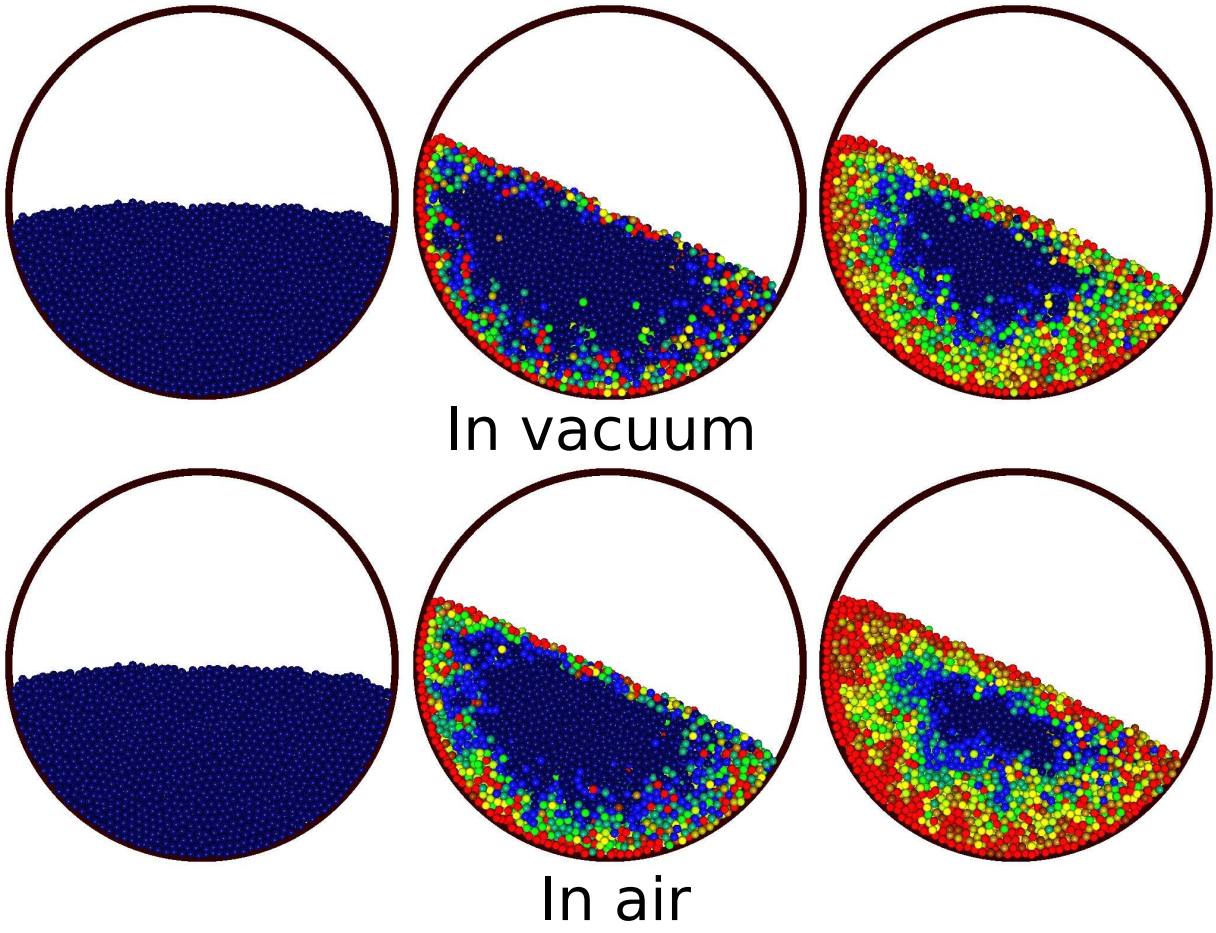

Figure 63: Aluminum particles 0 s, 15 s, 30 s. There are more high temperature (red) particles in air than in vacuum.

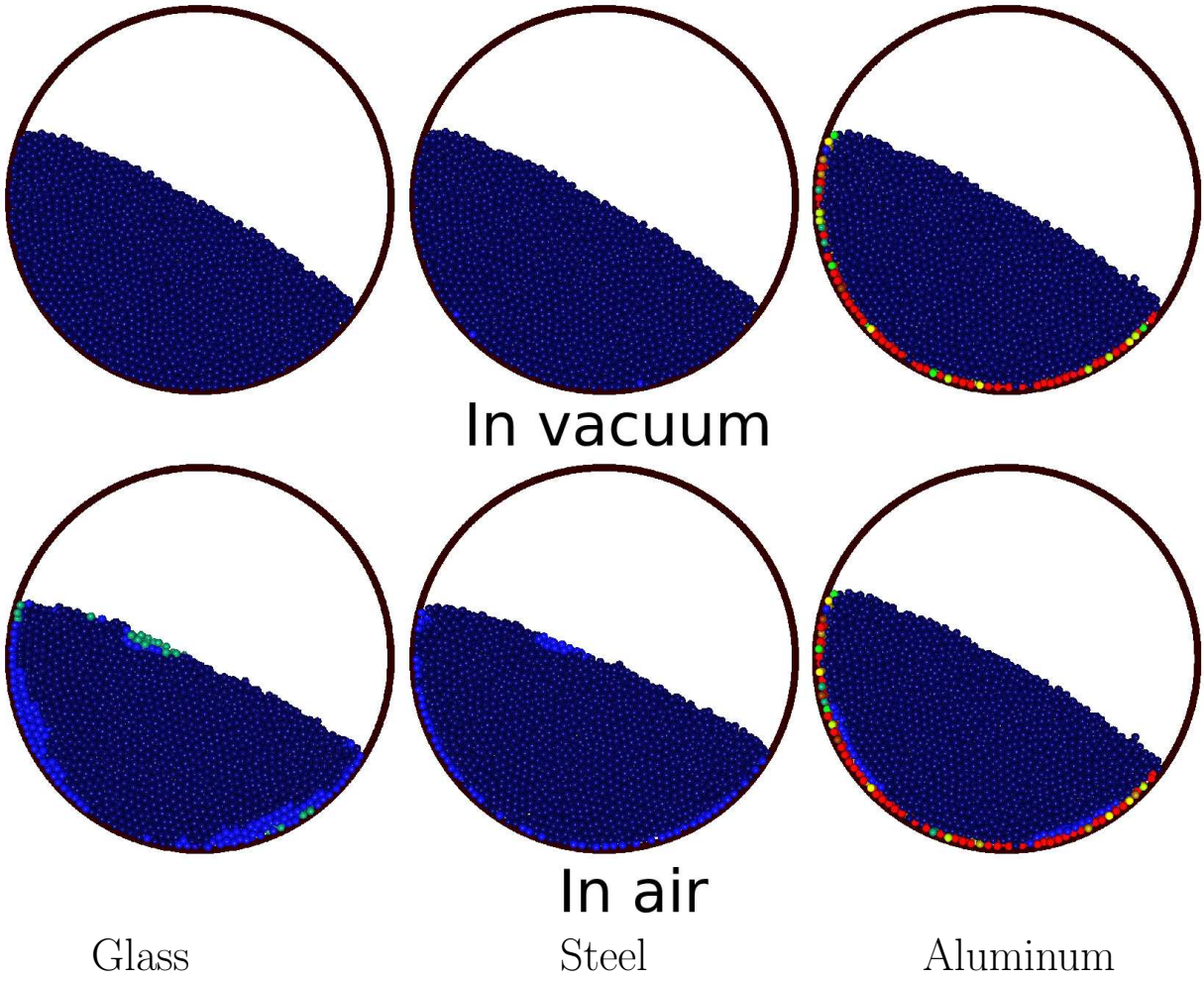

Figure 64: Glass, steel and aluminum at 0.33s in 15RPM kiln. There are some green particles in the glass beds in air, which can only be attributed to the convective heat transfer inside the kiln, which is from air. Steel particles inside the kiln and along the wall change temperature in the same degree. Aluminum particles always change temperature along the wall in both vacuum and air.

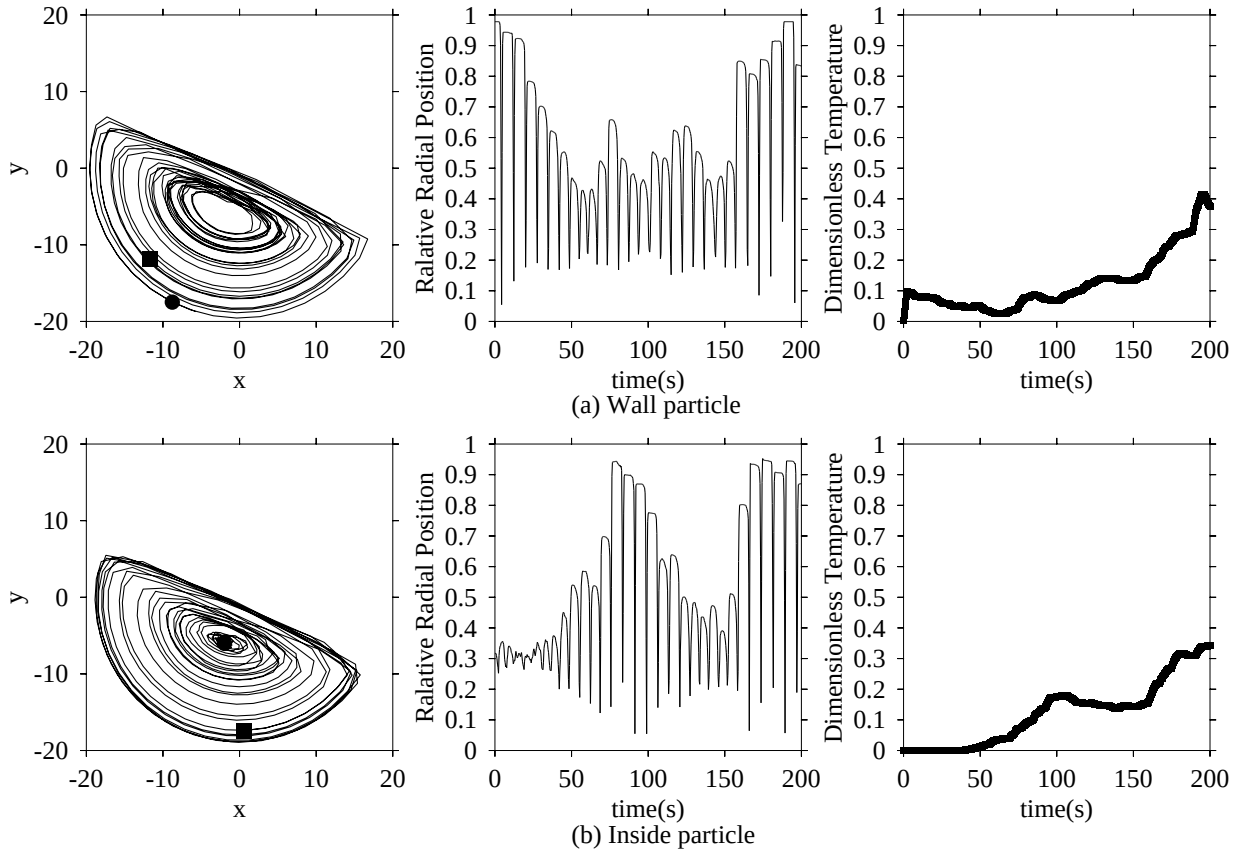

Figure 65: Particle path, relative radial position and temperature evolution in vacuum. Temperature evolution of an aluminum particle (a) close to the wall (b) in the bulk. The left figures illustrate the particle path (circle is the start position and square is the final position). The middle figures show the evolution of the relative radial position. The right figures show the evolution of temperature for individual particles is fluctuating, regardless of the position within the bed.

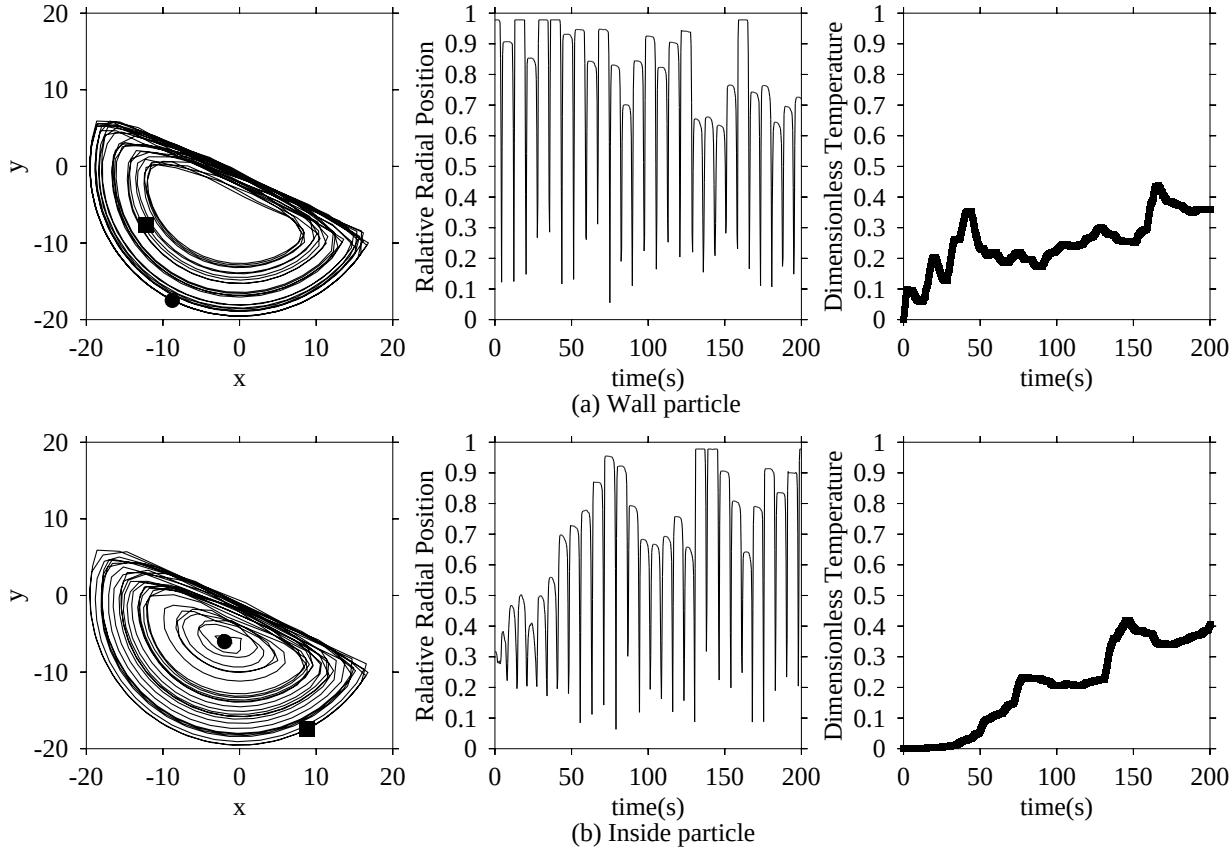

Figure 66: Particle path, relative radial position and temperature evolution in air. Temperature evolution of an aluminum particle (a) close to the wall (b) in the bulk. The left figures illustrate the particle path (circle is the start position and square is the final position). The middle figures show the evolution of the relative radial position. The right figures show the evolution of temperature for individual particles is fluctuating, regardless of the position within the bed.

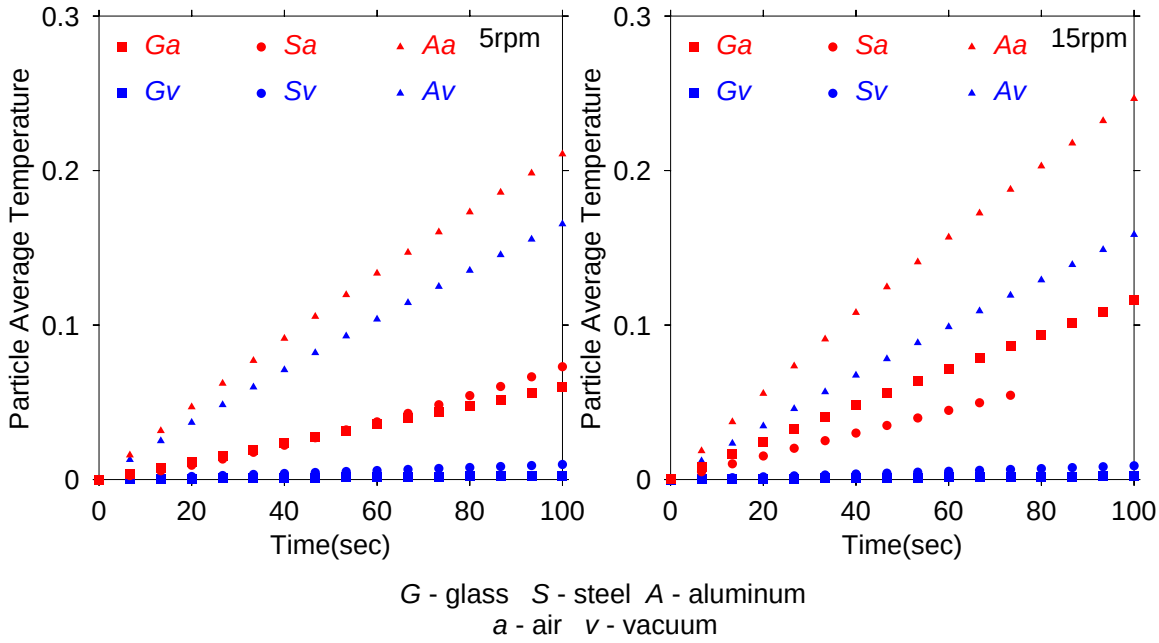

Figure 67: Variation of the bulk temperature in a rotating kiln with two different rotating speeds. The bulk temperature within the drum varies in a logarithmic fashion, although the local temperature evolution of individual particles is fluctuating.

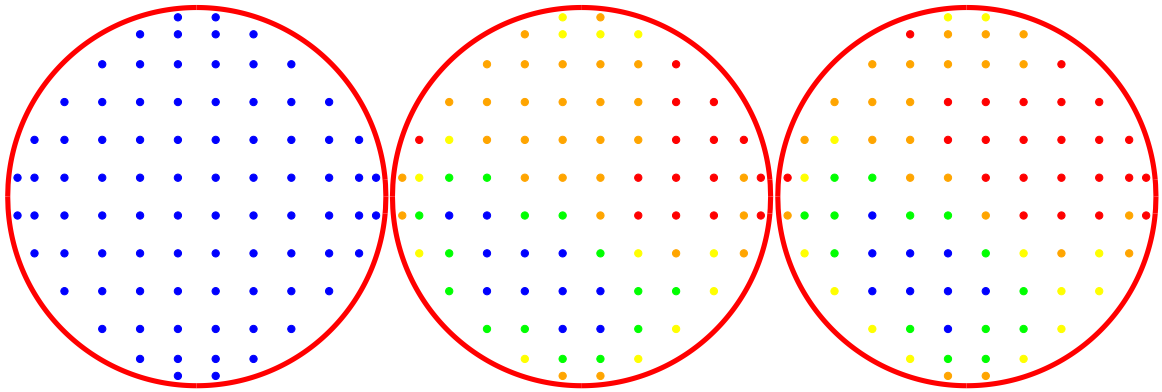

Figure 68: Gas nodes temperature 0 s, 15 s, 30 s for aluminum at 5RPM. There are more and more red nodes above the particle bed. The blue nodes in the lower left part of the kiln coincides with the contour of low temperature particles.

5.2.4 Analysis of Heat Transfer Coefficient

Traditionally, heat transfer in rotating drums has been modeled by means of a heat transfer coefficient (h_w) between the wall of the drum and the bed of particles. The heat transfer coefficient (h_w) is usually determined based on penetration theory arguments – a continuous approach – which are outlined below.

When particles at temperature T_o move into contact with the wall at a temperature T_w and gain heat by unsteady heat conduction, the rate of heat transfer at the wall q_w, is given by

$$q_w = h_w A_w (T_w - T_o) \tag{5.16}$$

where A_w is the area of particles in contact with the wall. The heat transfer coefficient h_w from the wall to the particle bed is then given by [106, 112]

$$h_w = 2\sqrt{\frac{k_{eff}(\rho C_p)_b}{\pi t_c}} \tag{5.17}$$

where k_{eff} is the effective thermal conductivity of the bed of particles, $(\rho C_p)_b$ is the heat capacity of the bulk, and t_c is the contact time between the wall and the particles, which can be linked to the rotational rate of the drum (Ω) by

$$t_c = \frac{l_{arc}}{2\pi\Omega} \tag{5.18}$$

where l_{arc} defines the arc length of material in contact with the wall. This analysis has inspired several experimental methodologies for evaluation of h_w from temperature measurements. One of these methods, proposed by Ito *et al.* [113], relates the transient change of the temperature in the shear layer to the heat transfer coefficient at the wall using the theoretically derived expression

$$\ln \frac{T_w - < T_c(t) >}{T_w - T_o} = \frac{t}{t_c} \ln \left(1 - \frac{h_w A t_c}{c_p w}\right) \tag{5.19}$$

where w is the weight of the particles in the bed and $< T_c(t) >$ is an average temperature far from the wall. According to Eq. 5.20, h_w can be estimated from the plots of $(T_w - < T_c(t) >)/(T_w - T_o)$ vs t as determined from simulations. A simplified correlation for estimating h_w has been derived by Wes et al. [106] based on penetration theory grounds as:

$$\ln \frac{T_w - < T_c(t) >}{T_w - T_o} = -\frac{h_w A}{c_p w} t. \tag{5.20}$$

Note that the expression derived by Wes *et al.* is a first order approximation to that obtained by Ito.

In evaluating the wall to particle heat transfer coefficient, it is important to select the relevant driving force, i.e. the core region, on calculating $< T_c(t) >$. Figure 69 compares profiles of temperature as a function of time used in the estimation of h_w, using different core regions. In this Figure, the linearity is quite good and can be used to estimate the heat transfer coefficients from the slope of the plots as

$$h_w = \frac{(c_p w)\left[1 - e^{slope \cdot t_c}\right]}{A t_c}, \tag{5.21}$$

It should be noted that different values of the slope, and therefore the average heat transfer coefficient, can be obtained for each of the cases considered.

Figure 70 shows the simulation results of plotting $\ln \frac{T_w - < T_c(t) >}{T_w - T_o}$ versus t based on the small core regions. All these data show a linear relationship, as expected. It is interesting to note that steel has a larger slope than glass in vacuum, but a smaller slope in air, especially in the 15RPM simulations. While this observation seems counter-intuitive, the following theoretical argument supports the data (and establishes a testable predictive argument for the bounds on this phenomenon). Taking an approach similar to Ito and Wes et al., we can write the differential equation governing the heat in the small core region as

$$\rho c V \frac{dT_c}{dt} = -H_b (T_c - T_w), \tag{5.22}$$

where H_b is the conductance of the bed. Solving this equation yields

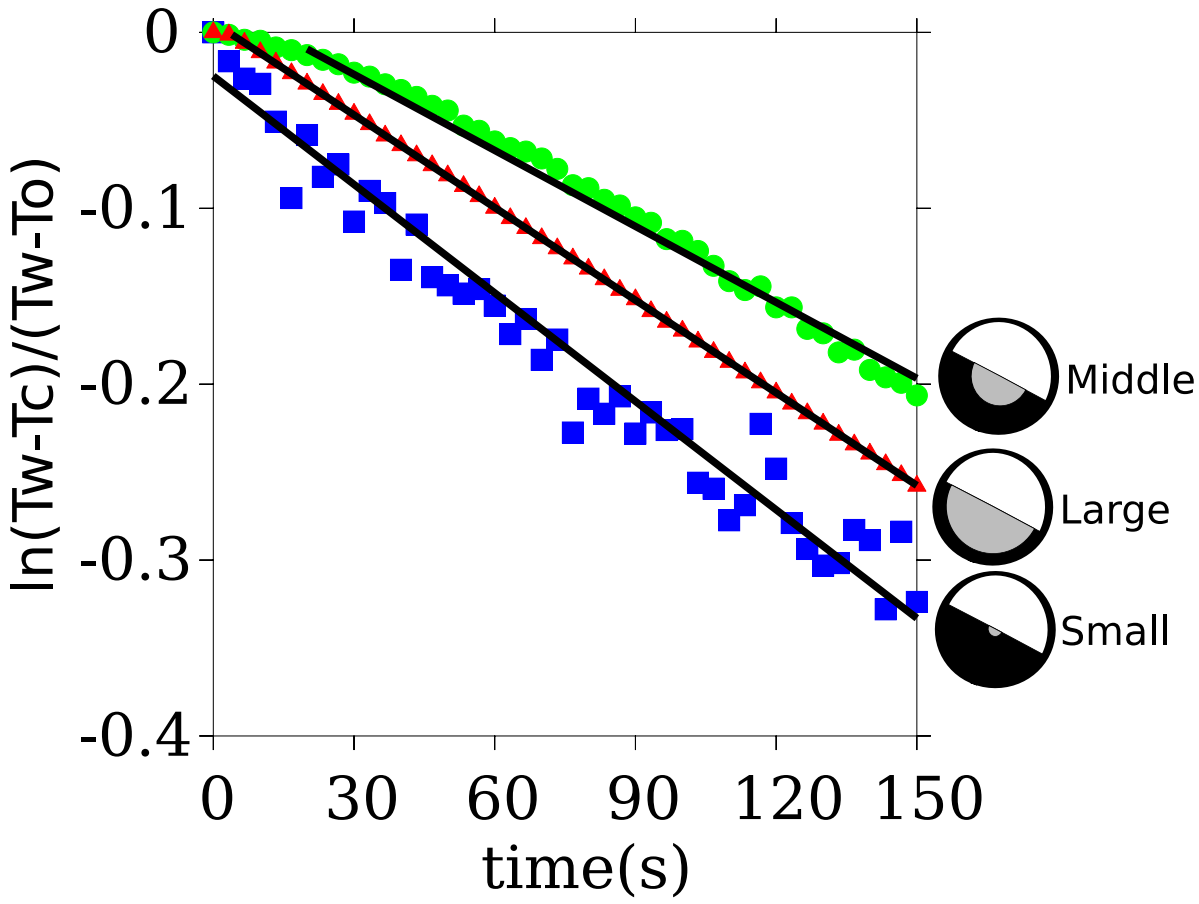

Figure 69: Profiles of temperature used in the estimation of the heat transfer coefficient. Using different regions as the core will result in different results.

$$\frac{T_c(t) - T_w}{T_o - T_w} = exp\left[-\frac{H_b}{\rho c V}t\right], \tag{5.23}$$

so that the rate of change of the scaled temperature (the slopes in Figure 69) is determined by the ratio of the bed conductance to the quantity $(\rho c V)$. As all particles are the same radius, we will ignore the volume in the remainder of the argument. In the case of vacuum conditions, the bed conductance is wholly determined by the transport by conduction through the solid phase. While a rigorous expression for H_b in this case is quite complicated, it is reasonable to expect that it should scale with the particle-to-particle conductance, H, so that it is proportional to the conductivity of the solid times the contact radius, $2.0R_c k_s$ (see Eq. 5.4). Therefore, under vacuum conditions, we expect that the slopes should be determined solely by the ratio of $k_s R_c$ to ρc, the bed equivalent of the thermal diffusivity times the (average) radius of contact (for simplicity we will assume that the R_c values are comparable in all cases). Not surprisingly, the slopes follow the particle thermal diffusivity trends with $\text{slope}_A > \text{slope}_S > \text{slope}_G$. In the case where an interstitial fluid is present, however, H_b includes a second term that accounts for the gas-to-particle transport so that the slopes not only depend on the bed-equivalent of the thermal diffusivity (times R_c) but also on the ratio of $h_{fluid}A$ to ρc. As with the volume, the exposed surface areas of the particles are also the same in all cases and can be ignored. In order to understand the change in slope hierarchy, we must clearly conclude that

$$\left[\frac{k_s R_c}{\rho c} + \frac{h_{fluid}A}{\rho c}\right]_{glass} > \left[\frac{k_s R_c}{\rho c} + \frac{h_{fluid}A}{\rho c}\right]_{steel}, \tag{5.24}$$

despite the fact that $\left[\frac{k_s R_c}{\rho c}\right]_{steel} > \left[\frac{k_s R_c}{\rho c}\right]_{glass}$. This leads to the conclusion that there is a critical value of the convective heat transfer coefficient that would lead to this transition, which is given roughly as

$$h_{fluid}A > \frac{\left(\frac{k_s R_c}{\rho c}\right)_{steel} - \left(\frac{k_s R_c}{\rho c}\right)_{glass}}{\left(\frac{1}{\rho c}\right)_{glass} - \left(\frac{1}{\rho c}\right)_{steel}}. \tag{5.25}$$

Using the properties of steel, aluminum, and glass and this inequality we estimate that the critical fluid heat transfer coefficient for glass to heat more rapidly than aluminum is about 100 times larger than that for glass to heat more rapidly than steel. Moreover, performing a similar analysis shows that there is no value of h_{fluid} that would allow steel to heat more rapidly than aluminum. Both of these conclusions are consistent with our current results and, in fact, lead to an easily testable prediction that replacing air with, for example, water should cause a glass-aluminum transition to be attainable.

Figure 71 shows the calculated average heat transfer coefficient of different materials and different rotation speeds from all the simulations. It is obvious the aluminum has the largest heat transfer coefficients and it is followed by steel, then by glass. In vacuum, increasing the rotation speed from 5RPM to 15RPM will not change the heat transfer coefficients significantly, yet, rotation rate change in air make a noticeable difference in all cases. This can be understood as follows. In a vacuum, conductive heat transfer plays the main role. At any time, there are always almost the same number of particles in contact with the wall whether it is 5 RPM or 15 RPM. In air, increasing the rotation speed will increase the heat transfer coefficients. This is due to the fact that the convective heat transfer coefficient (h_{gp}) increases with velocity as shown in Eq.. 5.6 and 5.7.

Subtracting the heat transfer coefficient in vacuum, (i.e. the conductive heat transfer coefficient) from that in air, we get the effective convective heat transfer coefficient. Figure 72 shows the ratio of convective and conductive heat transfer coefficients. At both 5RPM and 15RPM, the glass has a ratio over 18. This implies that convection contributes to over 90% of the heat transferred. In contrast, the aluminum always has a ratio below 0.6. Thus, the convective heat transfer has a much smaller effect on aluminum particles than on glass and steel particles in both 5RPM and 15RPM cases.

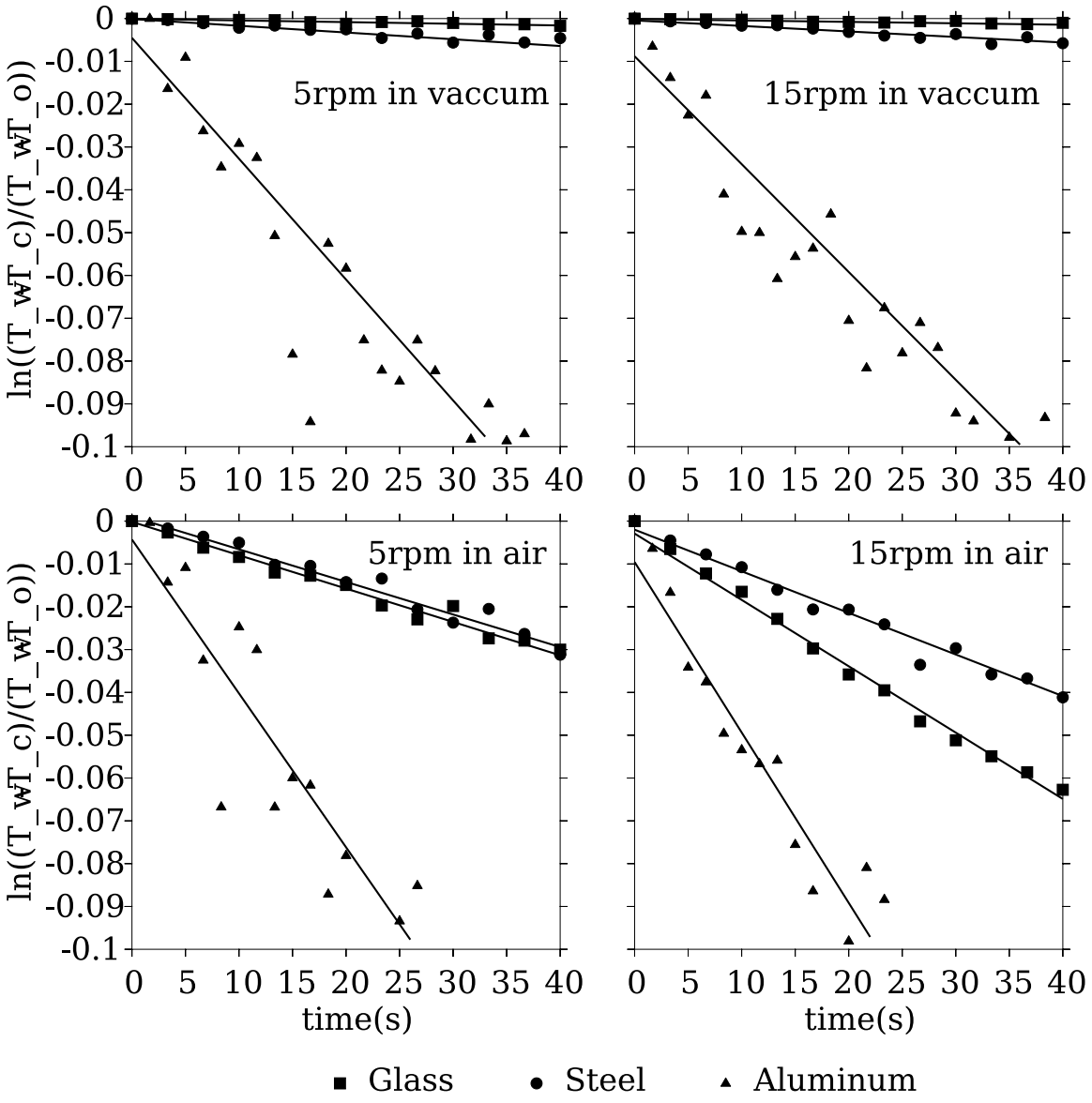

Figure 70: Profiles of temperature used in the calculation of h_w. All the data fall into a linear relationship. Aluminum has always the largest slopes. Steel has larger slopes than glass in vacuum but smaller slopes in air.

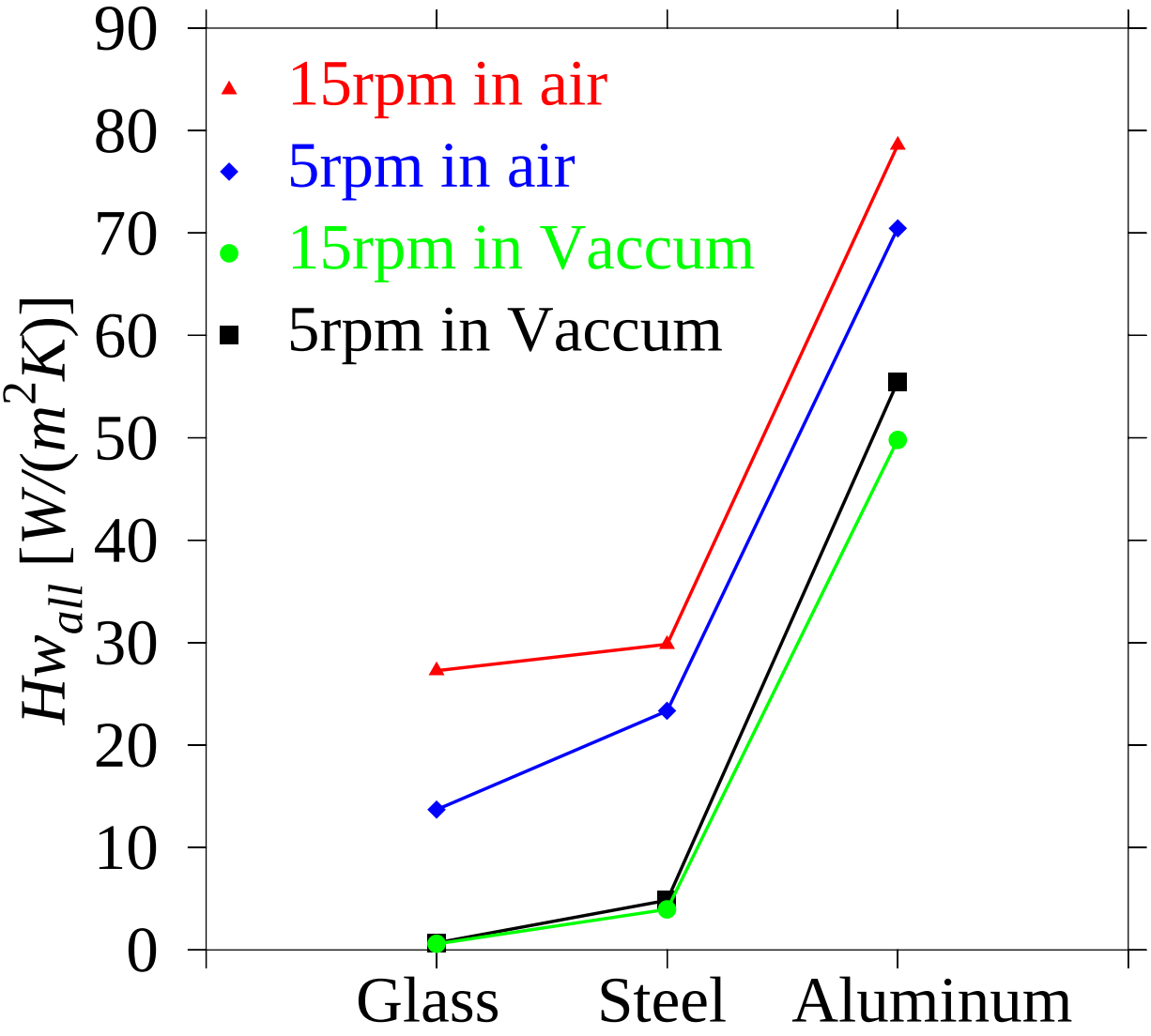

Figure 71: Overall heat transfer coefficient. Aluminum has the largest heat transfer coefficients and glass has the smallest ones. In vacuum, changing the kiln rotation speed will not cause the heat transfer changing significantly. In air, increasing the RPM will increase the heat transfer.

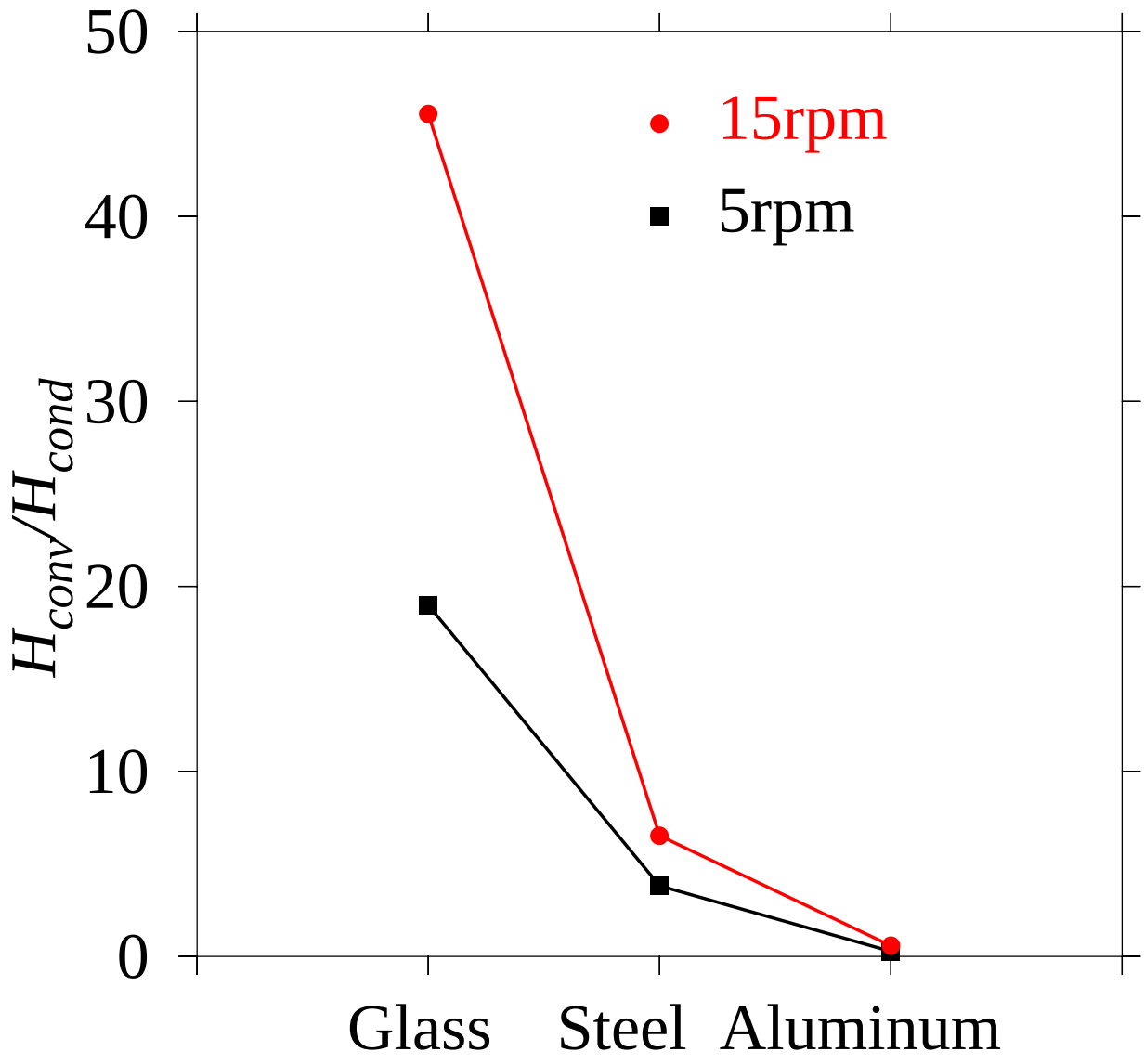

Figure 72: The ratio of convective and conductive heat transfer coefficients. For glass, the convective heat transfer coefficient is over 18 times larger than conductive heat transfer coefficient. For steel and aluminum, it has a much smaller ratio.

5.3 CONCLUSIONS

We use a coupled PD-CFD technique to simulate simultaneous conductive and convective heat transfer in a rotary kiln. Three different materials, "glass, steel and aluminum" are compared in the work. Steel has a larger thermal conductivity and also a larger volumetric heat capacity than glass, thus steel has a relatively faster temperature change in vacuum but a relatively slower one in air. Aluminum has a similar heat capacity to glass but a much larger thermal conductivity, thus conductive heating plays a significant role for aluminum in either vacuum or in air, and aluminum heats faster in both media. We predict, however, that if the conductive transport coefficient were to increase 100 fold (for example, by using a liquid medium), a transition similar to that observed in the glass-steel comparison would be possible.

From the temperature evolution, the effective heat transfer coefficients are extracted. Subtracting the overall heat transfer coefficient in vacuum from that in air, we estimated the heat transfer coefficients between the gas and particles. In this way, we quantify the effects of conductive and convective heat transfer. Overall, our results suggest a transition in heat transfer regime as the conductivities and heat capacities of the particles change. At low particle conductivities, the heat transfer is dominated by gas-solid conduction; however, at higher particle conductivities solid-solid conduction plays the dominant role.

6.0 LIQUID TRANSFER

Liquid spraying, as shown in Figure 73, is of importance in flotation, coating, flocculation, granulation and drying. In these operations, liquid transfer between particles plays the central role, whereby wetting, dewetting and mixing all take place simultaneously. A better understanding of liquid transfer between particles during flow can aid in the control of these processes. Recently, a number of researchers have computationally examined the impact of interstitial moisture on particle flow behavior, as reviewed below.

When liquid exists between two contacting particles, a liquid bridge will be formed and a liquid-induced cohesive force will be introduced [14, 35, 38, 114, 115], ultimately impacting the flow behavior of the particles. Mikami [15] simulated the behavior of a cohesive powder in a fluidized bed. Xu *et al.* [116] studied the impact of different liquid volumes in the fluidized bed system. Goldschmidt [117] simulated fluidized bed spray granulation and accounted for moisture distribution by explicitly simulating the droplets as discrete entities. This hard particle-based method accurately modeled the distributing action of the spray, but neglected liquid-induced interparticle forces (instead incorporating a finite agglomeration probability for wet particles) and did not allow for transfer of moisture from one particle to another. To the best of our knowledge, no studies have computationally explored the impact of varying moisture distribution, interparticle cohesion, and liquid transfer between particles during the flow process. This can likely be attributed to the fact that critical theoretical issues remain to be addressed before an explicit simulation is possible. The specific problems to be solved include how to determine the liquid bridge volume upon heterogeneous particle-particle impact and how to deal with liquid redistribution upon bridge rupture. We propose a solution to both of these issues, based on existing first principles computational results

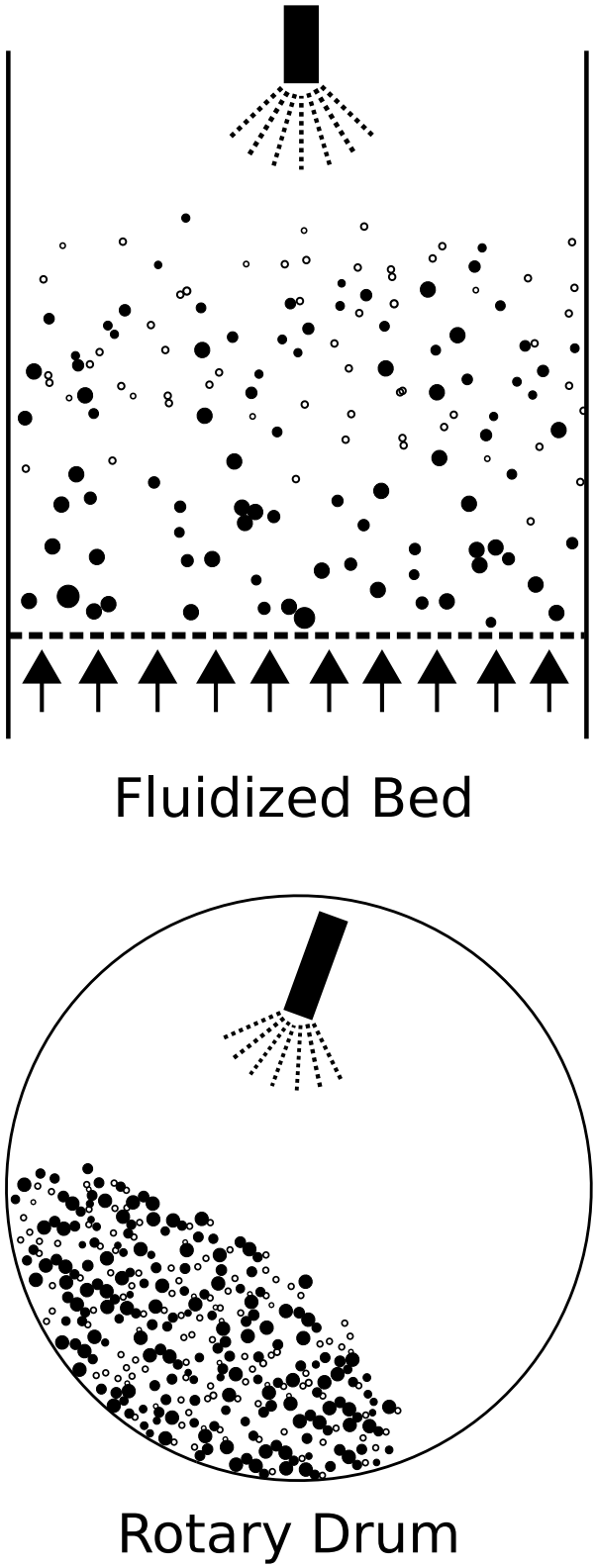

Figure 73: Spraying process in the fluidized bed and rotary drum where the particles have different size and contact angle. Open circle represents dry particle and closed circle represents wet particle. Wetting, dewetting and mixing all take place simultaneously.

[118, 119, 120], and develop an inter-particle liquid transfer model. The model is incorporated into a particle dynamics code to simulate a spraying process.

6.1 MODEL DEVELOPMENT

Here we introduce the theory and model modifications necessary to incorporate moisture tracking and transport. The interparticle cohesive forces from the liquid bridge interactions are discussed and incorporated into the Particle Dynamics simulation technique.

6.2 LIQUID TRANSFER AND FORCE MODELING

The contact angle of a particle will affect the liquid spreading on the solid surface [121]. If the contact angle is greater than 90 degrees, the liquid tends to bead up. Liquids having contact angles less than 90 degrees tend to wet the surface. A contact angle of 0 degrees indicates a liquid will completely cover a surface, while a contact angle of 180 degrees indicates the liquid completely beads up on a surface. Figure 74 shows the cases having contact angle less than 90 degree, 90 degree and greater than 90 degree. When moisture exists at an inter-particle contact, the tendency of the liquid to spread will affect the shape of the liquid bridge.

When two particles – at least one of which is wet – contact each other, the liquid on their surface will form a liquid bridge, generating a liquid-induced cohesive and viscous force. Subsequent breaking of that bridge not only causes the cessation of the liquid-induced force, but also may result in redistribution of the moisture content within the bed. For simplicity, in our simulations, we assume that liquid is evenly distributed on the surface of individual particles, but that individual particles may hold different amounts of liquid. This makes the present work strictly accurate only for particles with relatively hydrophilic (or more generally moisture-philic) surfaces. Relaxing this assumption would require particle

orientation tracking which, while not particularly difficult, is beyond the scope of the current work, although it is outlined in Chapter 8.

6.2.1 Liquid Bridge Volume

The liquid bridge volume is required in most models for calculating the capillary force [122, 123, 124, 125, 126]. We determine the liquid bridge volume for contact between particles of differing liquid content as follows. Each liquid bridge is composed of liquid from both contacting particles. The liquid on the surface of each particle that is within the area of the spherical cap neighboring the contact spot will contribute to the liquid bridge. In other words, the bridge will "harvest" liquid from the particle surfaces near the contact spot. With two particles contacting each other, the spherical cap is bounded by tangential lines from the center of one particle to the surface of the other particle as shown in Figure 75(a). Figure 75(b) shows the spherical caps that contribute to the liquid bridges in several contacting particles.

For mono-dispersed systems, this approach guarantees that any liquid on the surface of a particle can only contribute to one liquid bridge, i.e. no liquid bridge will overlap, which is the characteristic of pendular liquid bridges. For multiple-sized systems, as long as the size difference is not very large, this assumption will yield very small "harvest area" overlap (overlap angle is less than 1.3° for particle size ratio 2.0 system, see Appendix).

Based on the above assumption, the height, h, of the spherical cap can be easily calculated from the particle radii as

$$h_i = R_i - \sqrt{R_i^2 - \left(\frac{R_i R_j}{R_i + R_j}\right)^2}. \tag{6.1}$$

The liquid volume, V, for the liquid bridge contributed from particle i is then given as

$$V_i = \frac{L_i}{4\pi R_i^2} \times 2\pi R_i h_i = \frac{L_i}{2} \times \left(1 - \sqrt{1 - \frac{R_j^2}{(R_i + R_j)^2}}\right). \tag{6.2}$$

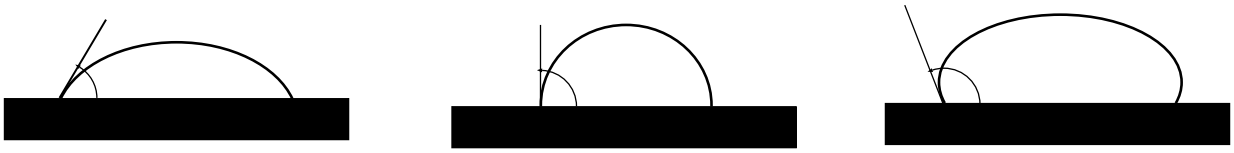

Figure 74: Wetting and contact angle

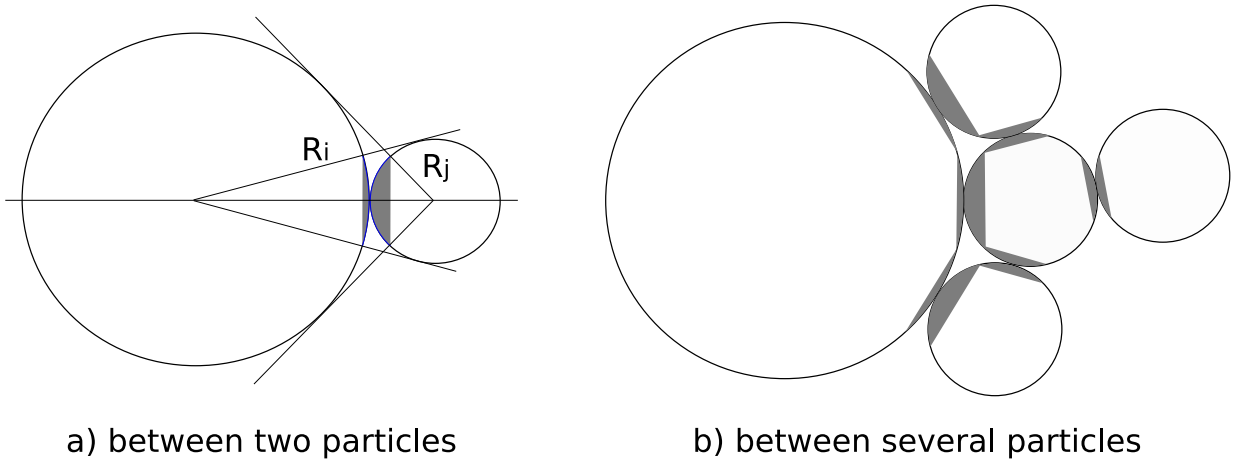

Figure 75: Schematic of the liquid bridge spherical caps between particles.

where L_i is the total liquid volume present on particle i. Similarly, we can get the liquid volume from particle j as

$$V_j = \frac{L_j}{2} \times \left(1 - \sqrt{1 - \frac{R_i^2}{(R_i + R_j)^2}}\right). \tag{6.3}$$

Thus the total liquid bridge volume is

$$V = V_i + V_j. \tag{6.4}$$

For the sake of calculation, we will assume the liquid bridge volume remains constant until the bridge is broken, and we will use this volume to get other parameters.

6.2.2 Liquid Bridge Force

In order to allow generality of particle properties in our model, it is important to develop a liquid-bridge force model that is robust to differing particle sizes and wetting characteristics, as well as bridge volumes and separation distances. In this case, the total capillary force – accounting for both surface tension and pressure effects, but neglecting buoyancy – may be expressed as

$$F_c = 2\pi R_1 \gamma sin\beta_1 sin(\beta_1 + \theta_1) + \pi R_1^2 \Delta p sin^2\beta_1, \tag{6.5}$$

$$= 2\pi R_2 \gamma sin\beta_2 sin(\beta_2 + \theta_2) + \pi R_2^2 \Delta p sin^2\beta_2, \tag{6.6}$$

where Δp is the pressure difference across the curved interface, which can be obtained from solving the Young-Laplace equation [127]

$$\Delta p = \left[\frac{\ddot{Y}}{(1 + \dot{Y})^{3/2}} - \frac{1}{Y(1 + \dot{Y})^{1/2}}\right] \frac{\gamma}{R}, \tag{6.7}$$

where γ is the liquid surface tension, Y is the bridge neck height function y made dimensionless with the particle radius (R).

Substituting $Q = \dot{Y}^2 + 1$, Eq. 6.7 converts into

$$\frac{dQ}{dY} - \frac{2Q}{Y} = \frac{2R\Delta p}{\gamma} Q^{3/2}, \tag{6.8}$$

which may be integrated to give

$$\frac{Y}{(1+\dot{Y}^2)^{1/2}} + \frac{R\Delta p}{2\gamma}Y^2 = C, \tag{6.9}$$

where C is a constant of integration.

Above equations are valid for both "halves" of the bridge. We then simplify this expression with the matching criterion that the neck height must match at the thinnest location ($x = 0,\ Y = Y_0$).

First looking at the rightmost particle (O_1), as shown in Figure 6.2.2, the boundary conditions at $x = xc1$ are

$$Y_1 = sin\beta_1 \tag{6.10}$$

$$\dot{Y}_1 = cot(\beta_1 + \theta_1) \tag{6.11}$$

where β denotes the so-called "half-filling" angle, and θ is the contact (wetting) angle, so we can get (from Eq. 6.9)

$$C = sin\beta_1 sin(\beta_1 + \theta_1) + \frac{R_1\Delta p}{2\gamma}sin^2\beta_1. \tag{6.12}$$

From Eq. 6.12, the force in Eq. 6.5 can be expressed as

$$F_c = 2\pi R_1\gamma C \tag{6.13}$$

The boundary conditions at the thinnest point of the liquid bridge are

$$Y_1 = Y_0 \tag{6.14}$$

$$\dot{Y}_1 = 0, \tag{6.15}$$

We can further get (again using Eq. 6.9)

$$C = Y_0 + \frac{R_1\Delta p}{2\gamma}Y_0^2. \tag{6.16}$$

Thus, the capillary force can be expressed as

$$F_c = 2\pi R_1\gamma Y_0\left(1 + \frac{R_1\Delta p}{2\gamma}Y_0\right). \tag{6.17}$$

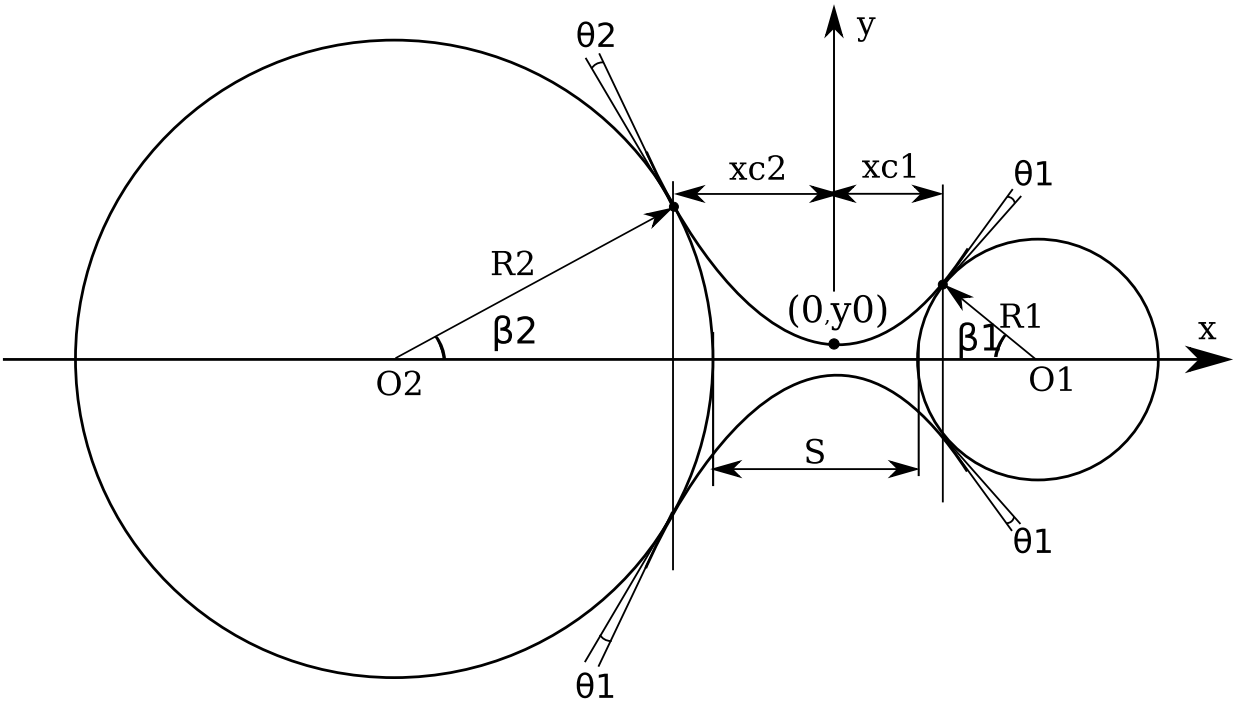

Figure 76: Capillary force calculation between different radius and contact angle particles

Rearranging Eq.6.9, we can get

$$\dot{Y}_1 = \sqrt{\left(\frac{Y_1}{C - \frac{R_1\Delta p}{2\gamma}Y_1^2}\right)^2 - 1} \tag{6.18}$$

Substituting Eq. 6.18 into Eq.6.7, we have

$$\ddot{Y}_1 = \frac{1+\dot{Y}_1^2}{Y_1} + \frac{R_1\Delta p}{\gamma}(1+\dot{Y}_1^2)^{3/2}. \tag{6.19}$$

An approximation of Y_1 can then be obtained from the Taylor series

$$Y_{1,i+1} \approx Y_{1,i} + \dot{Y}_{1,i}\Delta x + 0.5\ddot{Y}_{1,i}(\Delta x)^2. \tag{6.20}$$

Similarly, for particle O_2, we have

$$sin\beta_2 sin(\beta_2+\theta_2) + \frac{R_2\Delta p}{2\gamma}sin^2\beta_2 = Y_0/R_2 + \frac{\Delta p}{2R_2\gamma}Y_0^2 = C \tag{6.21}$$

$$\dot{Y}_2 = \sqrt{\left(\frac{Y_2}{C - \frac{R_2\Delta p}{2\gamma}Y_2^2}\right)^2 - 1} \tag{6.22}$$

$$\ddot{Y}_2 = \frac{1+\dot{Y}_2^2}{Y_2} + \frac{R_2\Delta p}{\gamma}(1+\dot{Y}_2^2)^{3/2} \tag{6.23}$$

and the Taylor series for Y_2

$$Y_{2,i+1} \approx Y_{2,i} + \dot{Y}_{2,i}\Delta x + 0.5\ddot{Y}_{2,i}(\Delta x)^2. \tag{6.24}$$

Numerically solving these equations (as described in Ref. [23] with the added stipulation of matching the dimensional value of Y_0), we can calculate the capillary force, F_c, between different radius and contact angle particles, using Eq. 6.17.

In practice, the implementation in a Particle Dynamics simulation is achieved via a look-up table which allows us to calculate the solution for a range of relevant particles sizes, contact angles, separation distances, and bridge volumes and then rapidly assess the resultant capillary force from the previously calculated data.

The half liquid bridge volume on the particle O_1 side of the bridge is

$$V_1 = \pi\int_0^{x_{c1}} Y_1^2 dx - \frac{\pi}{3}(1-cos\beta_1)^2(2+cos\beta_1), \tag{6.25}$$

while the half liquid bridge volume on the particle 2 side is given as

$$V_2 = \pi \int_0^{x_{c2}} Y_2^2 dx - \frac{\pi}{3}(1 - cos\beta_2)^2(2 + cos\beta_2). \tag{6.26}$$

Thus, the whole liquid bridge volume is

$$V = V_1 + V_2. \tag{6.27}$$

The separation distance is

$$S = x_{c1} - R_1(1 - cos\beta_1) + x_{c2} - R_2(1 - cos\beta_2) \tag{6.28}$$

We have the known variables R_1, R_2, θ_1, θ_2. If the liquid bridge volume V and the separation distance S are also known, we can get the other unknowns β_1, β_2, Y_0, Δp etc., by solving the Equations from Eq.6.7 to Eq.6.28. Thus, we can calculate the capillary force between different radius and contact angle particles in the pendular regime.

6.2.3 Rupture Distance

In our simulations, the moisture content is assumed to be sufficiently low so that bridges only form upon contact of the solid surfaces. These bridges remain in place, however, after solid contact has ceased, until the particles reach a rupture (critical separation) distance (h_c). The half critical separation distance is described by Lian et al. [127] as

$$\frac{h_c}{2} = 0.5R(1 + 0.5\theta)\sqrt[3]{V}. \tag{6.29}$$

Using this expression, we can derive the rupture distance between two different radius and contact angle particles.

The half rupture distance on the particle 1 side is

$$h_{c1} = 0.5R_1(1 + 0.5\theta_1)\sqrt[3]{V_1}. \tag{6.30}$$

The half rupture distance on the particle 2 side is

$$h_{c2} = 0.5R_2(1 + 0.5\theta_2)\sqrt[3]{V_2}. \tag{6.31}$$

Thus, the rupture distance for the whole liquid bridge is

$$h_c = h_{c1} + h_{c2} = 0.5R_1(1 + 0.5\theta_1)\sqrt[3]{V_1} + 0.5R_2(1 + 0.5\theta_2)\sqrt[3]{V_2}. \tag{6.32}$$

6.2.4 Liquid Bridge Rupture and Redistribution

When the separation distance between particle surfaces is larger than some critical distance (the "rupture distance"), the liquid bridge will break. Rossetti *et al.* [128] studied the rupture energy and wetting behavior of pendular liquid bridges in relation to the spherical agglomeration process. Using a first principles approach, Darhuber *et al.* [118, 119] performed quasi-static finite element simulations of the equilibrium shapes of liquid bridges between two parallel plates. In their work, the surface properties of the plates were varied so that the top plate has $\theta = 45°$, while the bottom plate has $\theta = 60°$, as shown in Figure 77(a). With the increment of the separation distance, the neck radius of the liquid bridge becomes smaller and at a critical separation distance, the liquid bridge breaks into two separated droplets and the surface with the smaller contact angle retains the bulk of the liquid bridge volume (as depicted schematically in Figure 77).

Similar results are expected between two wet spherical particles. When the particles reach the critical separation distance S_c, the liquid bridge will break at the thinnest part and the liquid on either "half" of this broken bridge should remain with the individual particles. For particles of the same size and contact angle, the liquid bridge will break in the middle of the two particles due to symmetry. For particles of the same size but different contact angles, the particle having the smaller contact angle should retain the bulk of the liquid from the bridge. For this reason, we expect that during the rupture process liquid can be exchanged between different particles (provided the interaction time of the contact is sufficiently large to allow bridge formation). For different size and/or contact angle particles, we assume that the bridge will rupture at its thinnest point prior to rupture so that, by obtaining an expression for the liquid bridge profile [15], we can calculate the amount of liquid retained by each particle after the rupture event.

An exact liquid profile description becomes complex even for the simple case of equal size spheres. Thus, the approximate treatment of the profile by simplified shapes, such as a circle or parabola has gained attention [114] over the years. Mehrotra [114] obtained the volume of a half liquid bridge by assuming that the liquid bridge has a toroidal profile as shown in

Figure 78. The half liquid volume can be calculated by integrating the liquid profile,

$$x^2 + (y - r_1 - r_2)^2 = r_1^2, \tag{6.33}$$

then subtracting the volumes of the spherical cap. This method is easily extensible to particles of different size but is restricted to particles which have the same contact angle.

Alternatively, Pepin [129, 130] used a parabolic profile approximation to model the liquid bridge, and this method has the advantage of being easily applicable for different contact angle particles as well as varying size particles. In addition, he compared his results with those from the toroidal assumption and concluded that the parabolic profile was slightly more accurate than the toroidal one. For these reasons, we will use the parabolic profile approximation to determine the liquid bridge "half" volumes upon rupture.

Right before rupture, we assume the profile is a second-order polynomial equation in the form

$$y = ax^2 + bx + c. \tag{6.34}$$

The liquid to solid contact points are on the two spheres with coordinates of (0, $y(0)$) and (d, $y(d)$) respectively as shown in Figure 79. The coordinates are related to the cap heights, h, and particle radii, R, by

$$y(0) = \sqrt{R_i^2 - (R_i - h_i)^2}, \tag{6.35}$$

$$y(d) = \sqrt{R_j^2 - (R_j - h_j)^2}, \tag{6.36}$$

where

$$d = h_i + h_j + S_c. \tag{6.37}$$

The solid-liquid contact angles can be calculated from the other parameters as shown below

$$\theta_i = \frac{\pi}{2} + arctan(y^{'}(0)) - arcsin(\frac{y(0)}{R_i}) \tag{6.38}$$

$$\theta_j = \frac{\pi}{2} - arctan(y^{'}(d)) - arcsin(\frac{y(d)}{R_j}). \tag{6.39}$$

The liquid bridge volume is

$$V = \pi \int_0^d y^2(x)dx - \frac{\pi}{6}[3y^2(0)h_i + h_i^3 + 3y^2(d)h_j + h_j^3]. \tag{6.40}$$

Since we have 6 unknown variables (a, b, c, d, h_i, h_j) and 6 equations (Eq.6.35-6.40), we can solve these equations numerically (the possibility of multiple solutions can be effectively decreased by considering the physical meanings of these variables) and can determine the thinnest part of the liquid bridge right before its rupture. Denoting this point as the coordinate (x_{min}, y_{min}), we assume that this is the most probable rupture position for the liquid bridge. Based on this assumption, the liquid volume remaining with each individual particle after rupture (V'), as shown in Figure 80, can be calculated as

$$V_i' = \pi \int_0^{x_{min}} y^2(x)dx - \frac{\pi}{6}[3y^2(0)h_i + h_i^3] \tag{6.41}$$

$$V_j' = \pi \int_{x_{min}}^d y^2(x)dx - \frac{\pi}{6}[3y^2(d)h_j + h_j^3], \tag{6.42}$$

where we have $V_i' + V_j' = V_i + V_j = V$ by conservation of mass.

The liquid transfer ratio between two particles is then defined as the volume fraction of liquid transferred from one particle (source) to another particle (target), and is written as $\frac{|\Delta V_i|}{V}$, where $\Delta V_i, \Delta V_j$ can be calculated as

$$\Delta V_i = V_i' - V_i, \tag{6.43}$$

$$\Delta V_j = V_j' - V_j. \tag{6.44}$$

Figure 81(a) shows the liquid transfer ratio between two equal size particles. If the two particles have the same contact angle, the liquid is evenly split between the two particles after rupture; thus, the 0° line maintains a constant value of 0.5. With an increase in the

contact angle of particle i, the liquid transfer ratio becomes larger and larger. Figure 81(b) shows the ratio between two different size particles. Compared to Figure 81(a), particle i retains less liquid in Figure 81(b) due to its smaller size ($R_i = 0.4$). Figure 81(c) shows the liquid transfer ratio between two different size particles, where $\theta_j = 30°$. Compared to Figure 81(b), particle i retains more liquid due to particle j is more hydrophobic.

As in the case of the liquid bridge cohesive force, a look-up table is generated from the numerical solutions discussed here so that they may be incorporated with minimal computational penalty into a PD simulation.

Darhuber [118] and Chadov [120] calculated the liquid transfer ratio between two plates, as the two solid lines shown in Figure 82. The two solid lines represent the results with source plates $\theta = 30°$ and $\theta = 60°$, respectively. The other lines in this figure represent the liquid transfer ratio between two particles achieved from our model. For the sake of comparison to plates, small liquid bridge volumes are used with dimensionless volumes (made by R^3) of $V = 0.001, 0.0001$, and 0.00001. As shown in the figure, when the contact angles on both particles are equal, the transfer ratio is always 0.5 as dictated by symmetry. When the two contact angles are different, the particle having smaller contact angle retains more liquid. Also, we find that as the liquid bridge content V decreases, our results approach that of two plates.

6.3 RESULTS AND DISCUSSION

6.3.1 Liquid Transfer between Two Particles

Computer simulations are run for the liquid transfer during 100 collisions between two same sized but different contact angle particles, as shown in Figure 83. Initially, particle i has liquid and particle j has no liquid. If they collide with each other with sufficient velocity [131], the particles will meet, form a bridge, then separate. Upon separation, a portion of liquid will transfer from particle i to particle j. If the two particles have the same contact angle, they will hold the same amount of liquid after many collisions as shown in Figure 83

(a) and (b). In the case that they have differing contact angles, the particle having the smaller contact angle (i.e., which is more hydrophilic) will hold more liquid than the particle having larger contact angle (i.e., which is more hydrophobic). Figure 83 (c) shows that particle i holds 89.3% of the total liquid volume after 100 collisions when particle i has a contact angle 30° and particle j has a contact angle 60°. Figure 83 (d) shows the result for particle i having a contact angle 60° and particle j having a contact angle 30°.

6.3.2 Spraying on Top Layer of the Particles in a Rotation Drum

Six spray coating simulations are performed in rotating drums. Three of these are less cohesive with $Bo_g < 1.0$ (See Chapter 4 for the definition of Bo_g) and three with $Bo_g > 1.0$, where the particle behavior is more cohesive in nature. Table 5 shows the particle parameters used in the simulations. Particles in Simulation 1 are uniform in size, density, and wetting characteristics. Simulation 2 contains particles of different contact angles, but otherwise identical mechanical properties. Simulation 3 has particles different in all respects: radius, density and contact angle. Simulations 4, 5 and 6 are similar to Simulation 3 in that they employ particles that vary in all respects, however, in these simulations we explore differing drum fill-levels (and more strongly cohesive materials).

In order to approximate the impact of liquid being sprayed on the top layer of particles, at each time-step we determine which particles are at the surface of the particle bed and then increase their individual moisture content up to the maximum moisture value (here taken to be a dimensionless volume of $V = 0.02$). With the rotation of the drum, more and more particles will be "sprayed" and this wet outer layer of particles will transfer liquid to the inside particles, both through contact redistribution and mixing. As shown in Figure 84, red particles hold more liquid than the blue particles, and other colors such as yellow and green lie between them. We find that some interior particles hold no liquid even after a long time (70s). The pictures in the right column show that there are two kinds of particles, which are labelled in different colors (in order to aid mixing visualization).

The mass coating variability (CV_m) between particles is of special interest to the pharmaceutical industry, and can be calculated by

$$CV_m = \frac{\sigma_m}{\mu_m}, \tag{6.45}$$

where σ_m is the standard deviation of the coating mass gain distribution and μ_m is the average of the coating mass gain distribution.

Figure 85 shows the evolution of CV_m with increasing coating time for simulations with $Bo_g < 1.0$. The left plots in Figure 85 show that CV_m decreases with time. The right plots show that CV_m increases with $\frac{1}{\sqrt{t}}$, and all data achieved over 1 second show a linear correlation. Thus, we can conclude that CV_m is inversely proportional to the square root of coating time in our simulations. This result is consistent with experimental observations from the literature [132, 133, 134, 135, 136, 137] as shown in Eq. 6.46

$$CV_m \propto \frac{1}{\sqrt{t}}. \tag{6.46}$$

Interestingly, Figure 86 shows the effect of CV_m with increasing coating time for simulations with $Bo_g > 1.0$ and while linear, we find these results to display a positive intercept. We attribute this positive intercept to the fact that a large Bo_g decreases the particle mixing, thus it negatively affects the liquid transfer between particles, so that CV_m approaches zero increasingly slowly with time (as the outer layer of particles becomes more cohesive).

6.4 CONCLUSIONS

Here we described a general model for liquid transfer between different size and contact angle particles. When two particles contact each other, the liquid between the particles will form a liquid bridge which, upon rupture, allows liquid to be redistributed between particles. Repeating the formation and rupture of liquid bridges, therefore, forms one mechanism for moisture transport in particle processing devices.

Our model relies on two plausible assumptions that tend to agree with existing first principles modeling of quasi-static liquid bridges. First, that the volume of liquid included in the formation of a liquid bridge is "harvested" from the surface of a spherical cap near the contact spots of both particles. Using this calculated liquid bridge volume, we can get other important parameters such as the critical separation distance and cohesive forces. Second, by numerically solving the parabola profile equations, we take the liquid bridge rupture at the critical separation distance to occur at the thinnest portion of the profile. The two "halves" of the bridge then determine the redistribution of the liquid amount for each particle upon rupture.

Coupling this model with a PD simulation, we simulate liquid spraying in a rotating drum. It is found that this model produces the result that CV_m is inversely proportional to the square root of coating time when $Bo_g < 1$, which is consistent with the literature. We also predict that CV_m linearly increases with the square root of coating time, yet has a positive intercept when $Bo_g > 1$.

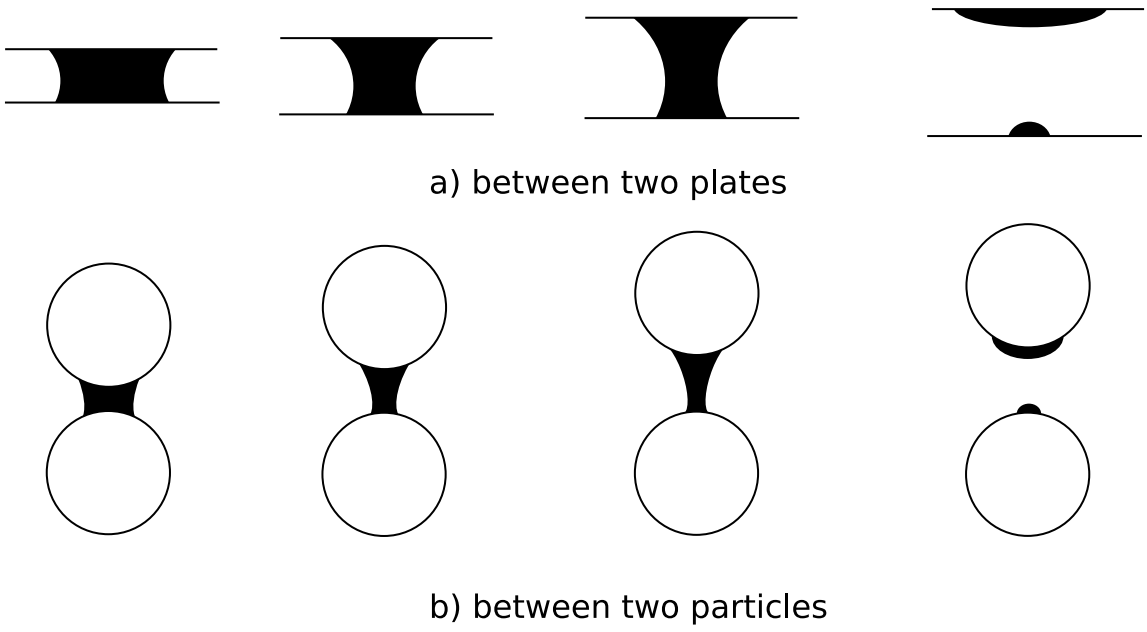

Figure 77: Schematic of liquid redistribution upon liquid bridge rupture

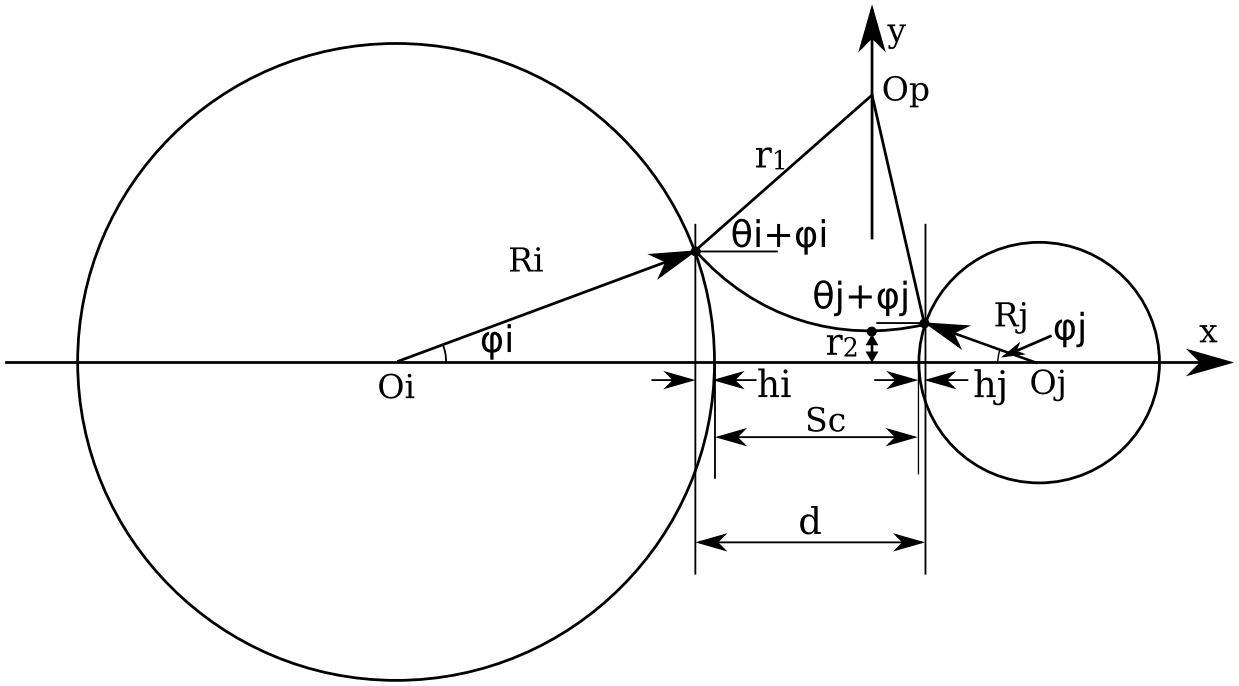

Figure 78: Schematic of the liquid bridge toroidal profile approximation

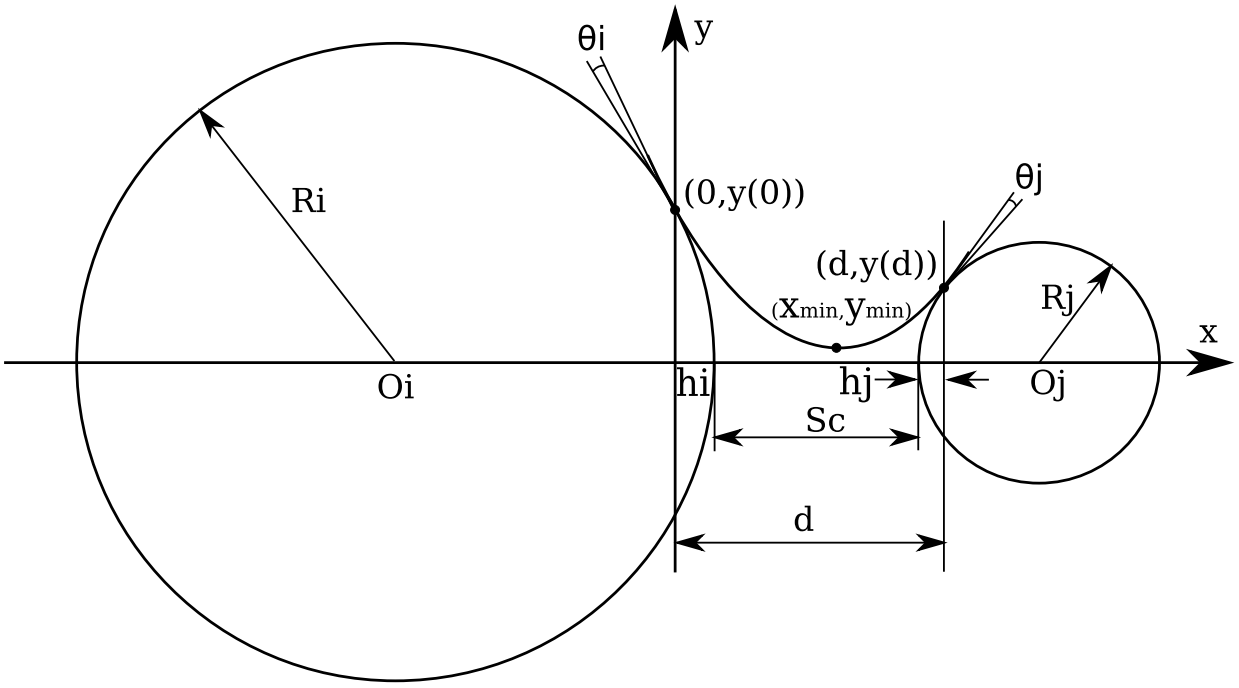

Figure 79: Schematic of the liquid bridge parabola profile approximation

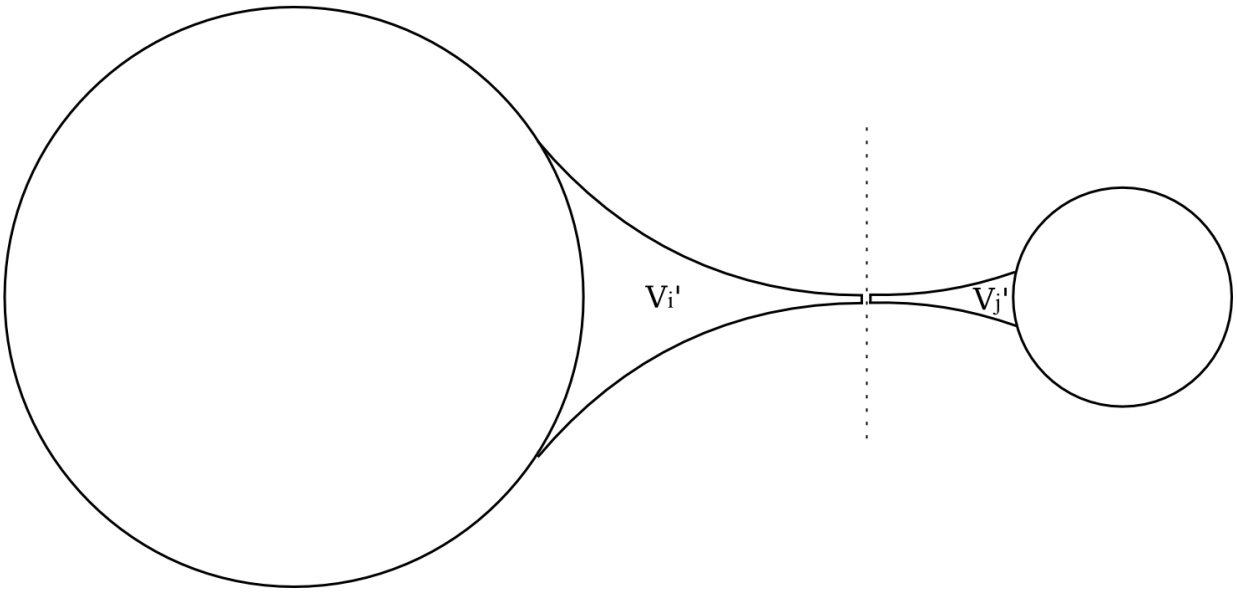

Figure 80: Schematic of the liquid bridge rupture calculation

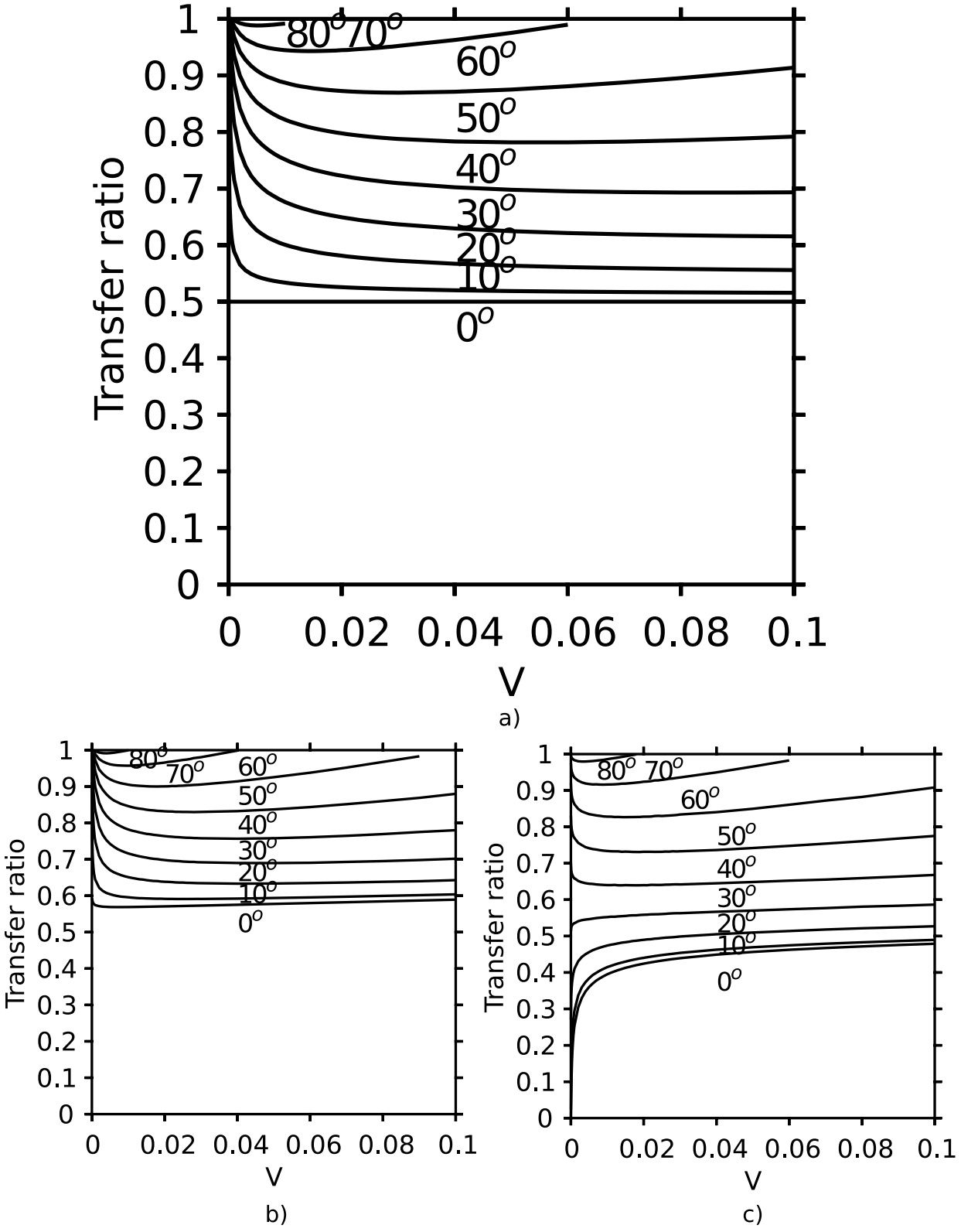

Figure 81: (a)Liquid transfer ratio between two equal-sized particles. $R_i = R_j = 0.5$, $\theta_i = 0° \sim 80°$ and $\theta_j = 0°$. (b)Liquid transfer ratio between two different size particles. $R_i = 0.4$, $R_j = 0.5$, $\theta_i = 0° \sim 80°$ and $\theta_j = 0°$. (c)Liquid transfer ratio between two different size particles. $R_i = 0.4$, $R_j = 0.5$, $\theta_i = 0° \sim 80°$ and $\theta_j = 30°$.

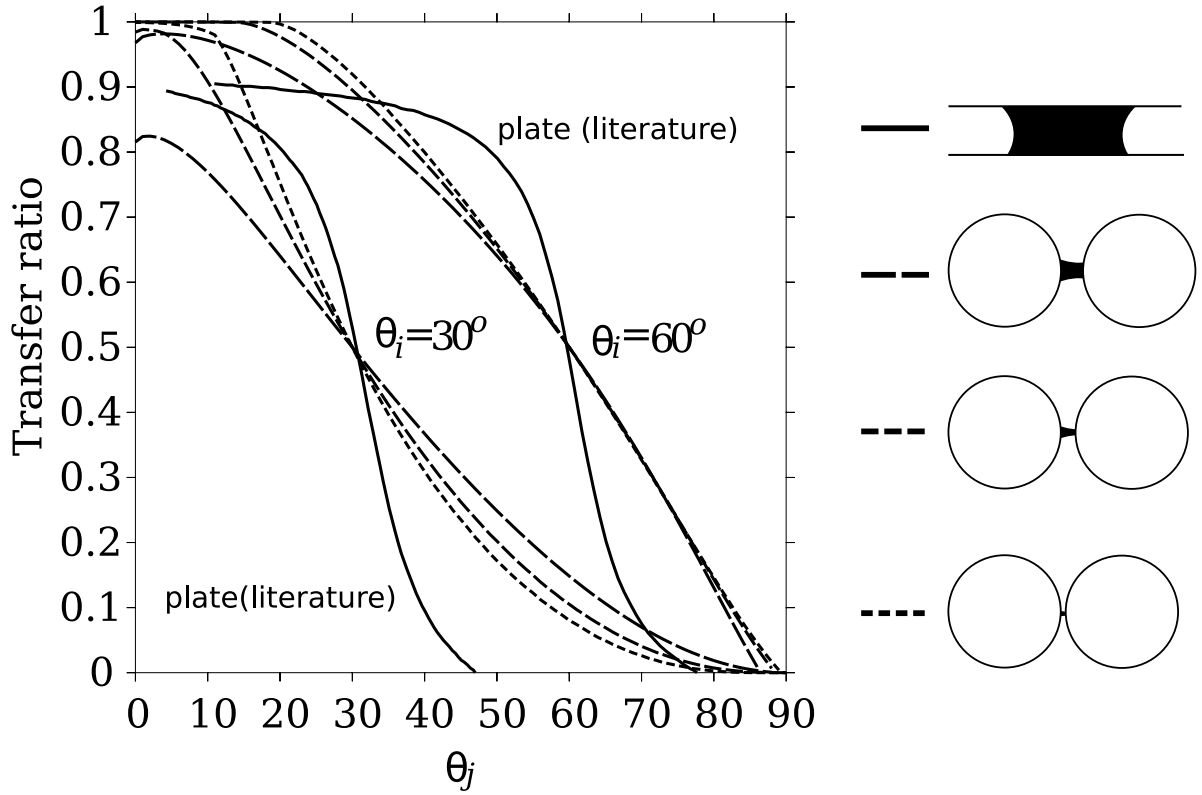

Figure 82: Liquid bridge transfer ratios. Solid lines are between two plates; other lines have $V = 0.001$, $V = 0.0001$ and $V = 0.00001$, respectively.

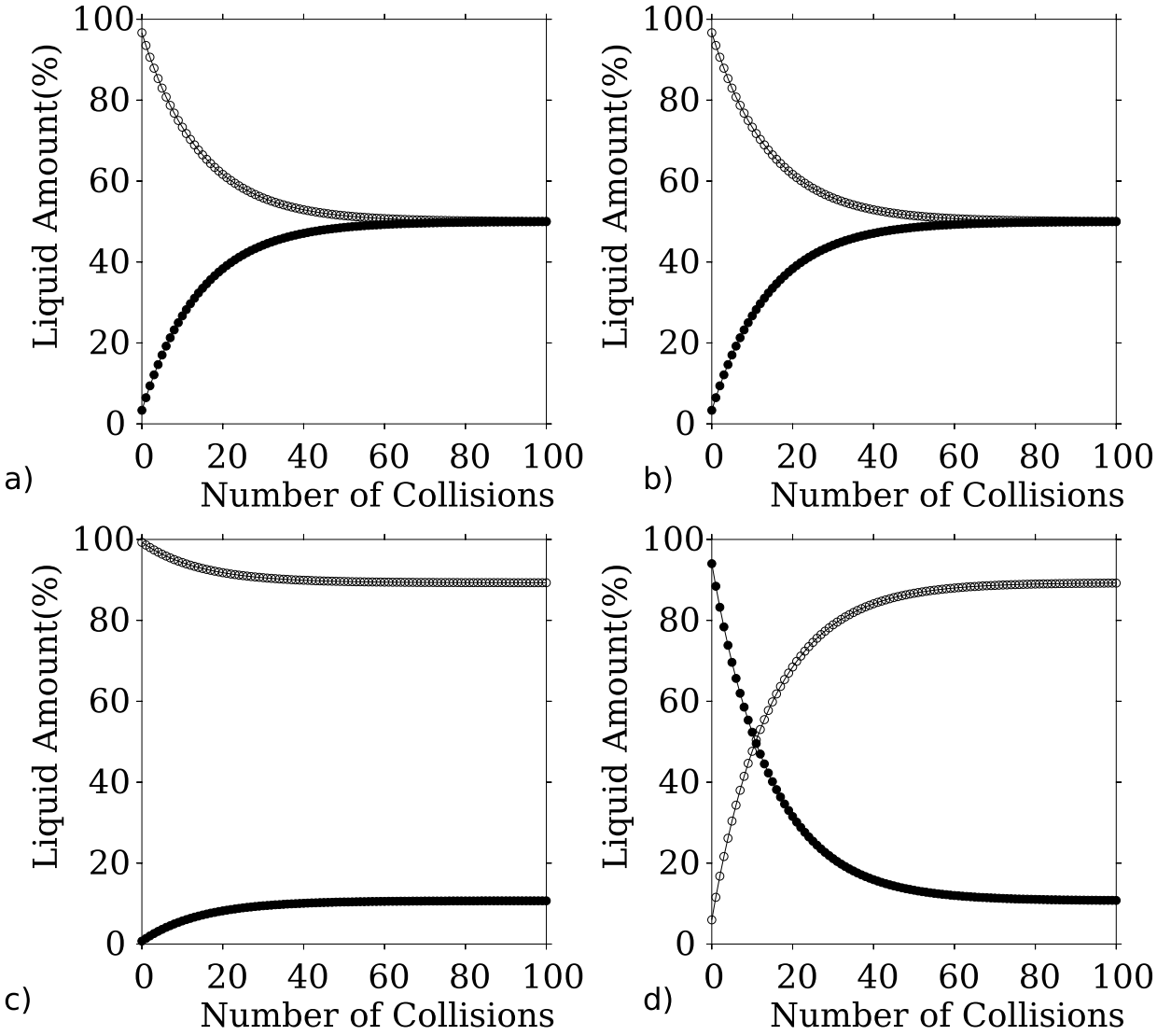

Figure 83: Liquid transfer between two equal size but different contact angle particles (a)$\theta_i = 0°$,$\theta_j = 0°$ (b)$\theta_i = 50°$,$\theta_j = 50°$ (c)$\theta_i = 30°$, $\theta_j = 60°$ (d)$\theta_i = 60°$, $\theta_j = 30°$.

Table 5: PARTICLE PARAMETERS IN LIQUID TRANSFER SIMULATIONS.

	R_i	R_j	ρ_i	ρ_j	θ_i	θ_j
Simulation1	$1.0mm$	$1.0mm$	$1000.0kg/m^3$	$1000.0kg/m^3$	$0°$	$0°$
Simulation2	$1.0mm$	$1.0mm$	$1000.0kg/m^3$	$1000.0kg/m^3$	$0°$	$30°$
Simulation3	$1.0mm$	$0.8mm$	$1000.0kg/m^3$	$560.0kg/m^3$	$0°$	$30°$
Simulation4	$1.0mm$	$0.8mm$	$560.0kg/m^3$	$1000.0kg/m^3$	$0°$	$10°$
Simulation5	$1.0mm$	$0.8mm$	$560.0kg/m^3$	$1000.0kg/m^3$	$0°$	$10°$
Simulation6	$1.0mm$	$0.8mm$	$560.0kg/m^3$	$1000.0kg/m^3$	$0°$	$10°$

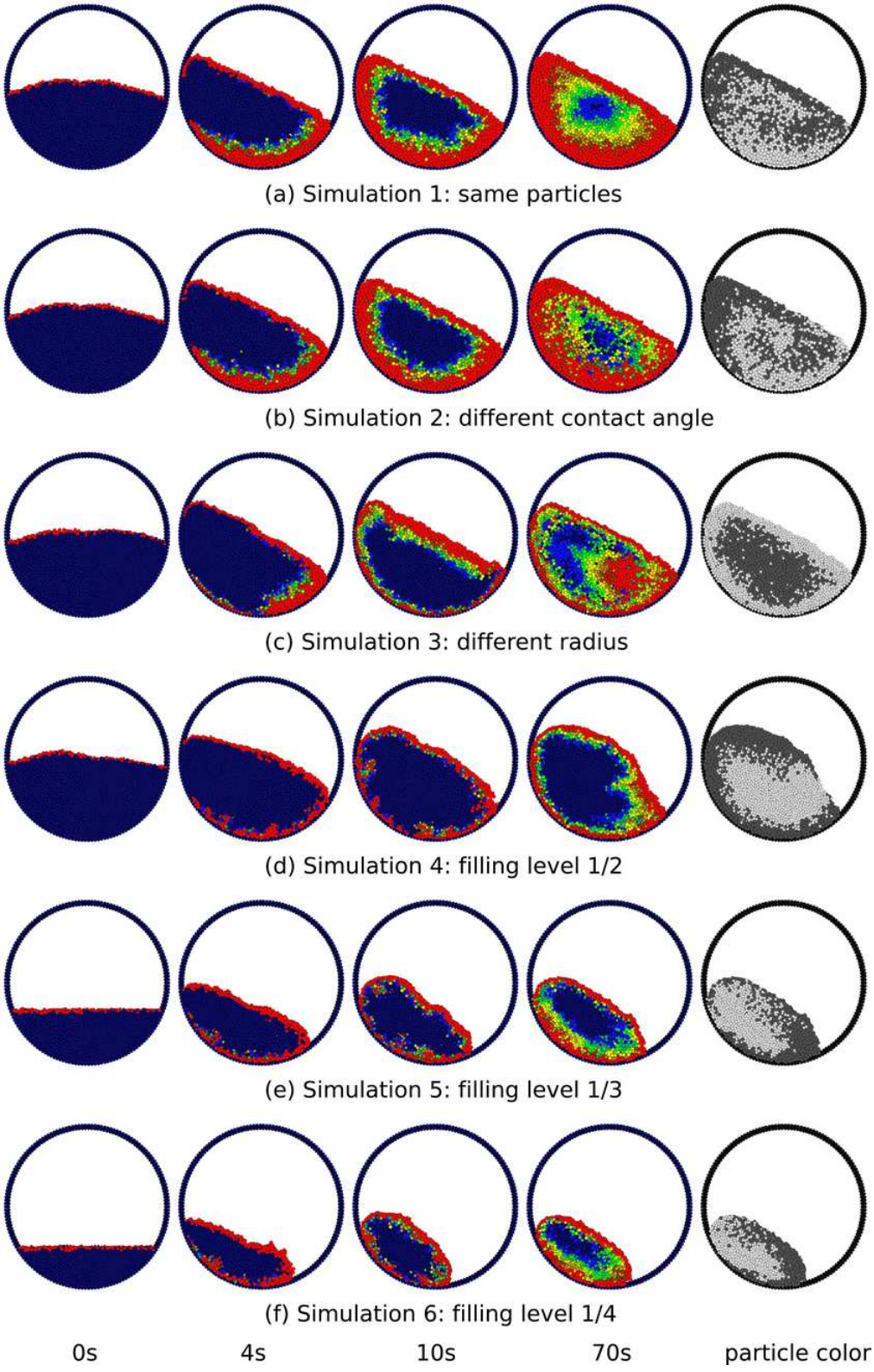

Figure 84: Liquid spraying on rotary drums. The particles are sprayed from the top of the bed. Red color means the particles hold maximum moisture and the blue color means the particles are dry. The other colors are in the middle. Simulation 1-3 have $Bo_g < 1$ and Simulation 4-6 have $Bo_g > 1$.

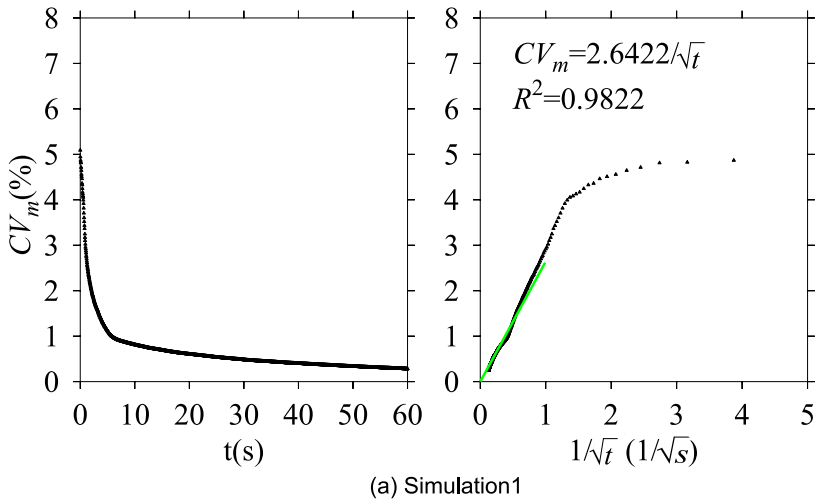

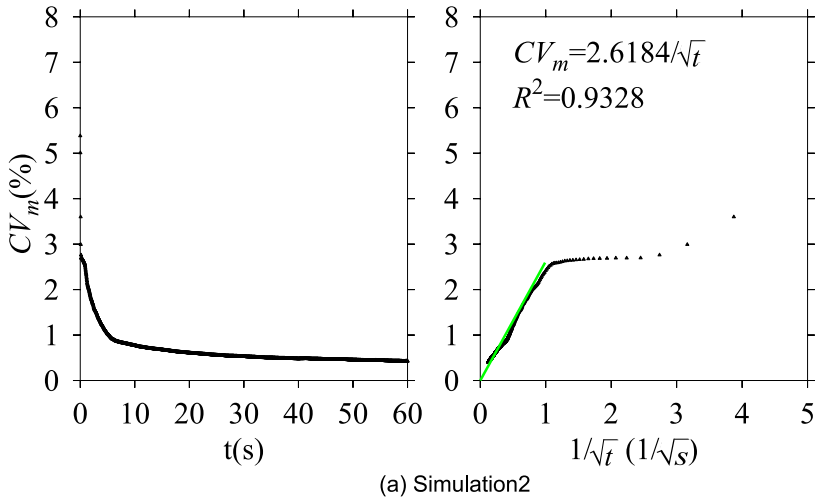

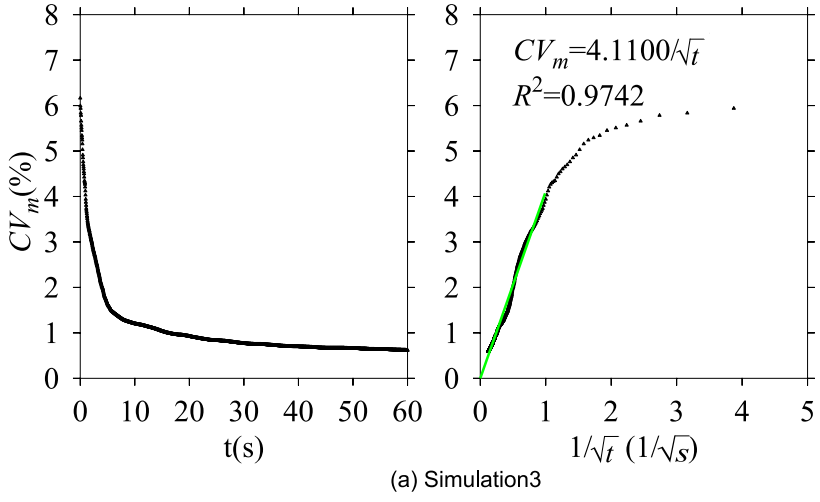

Mass Coating Variability is inversely proportional to the square root of coating time

Figure 85: Mass Coating Variability with $Bo_g < 1$

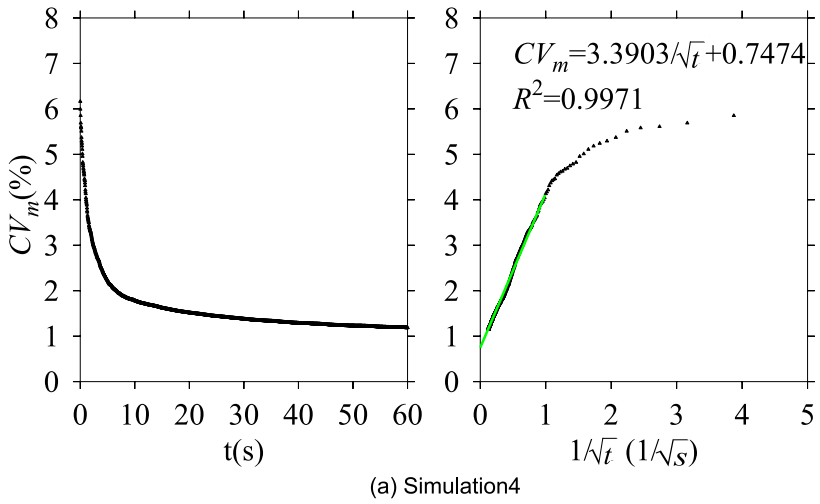

(a) Simulation4

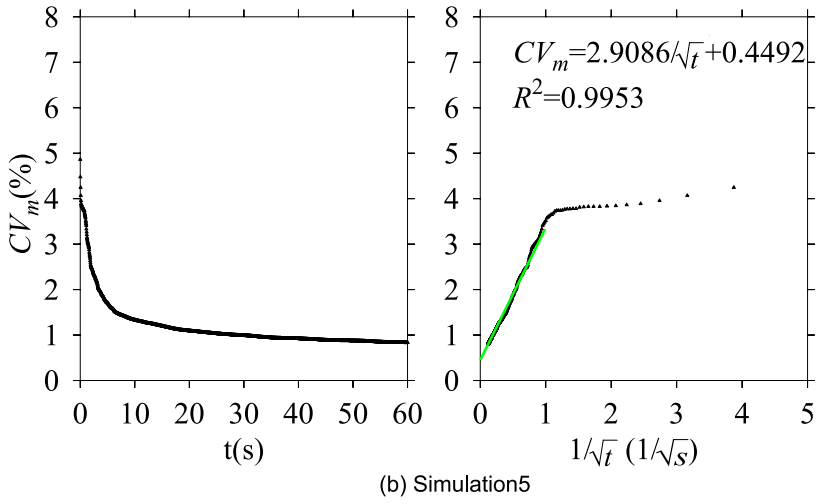

(b) Simulation5

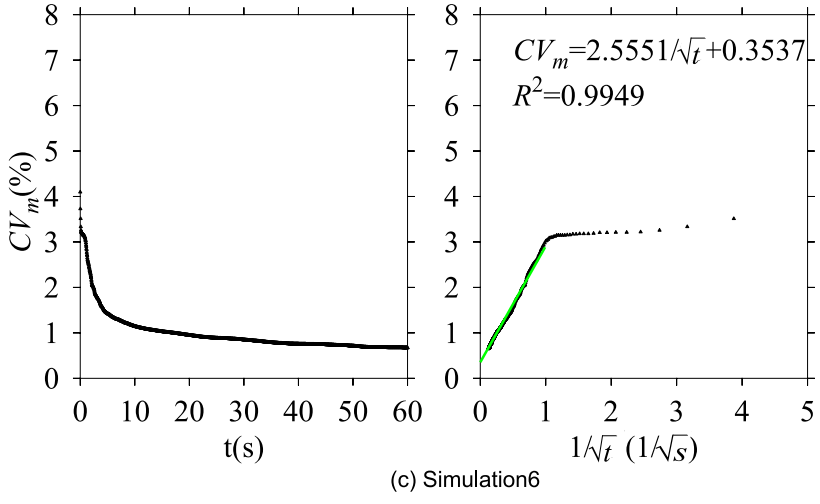

(c) Simulation6

Mass Coating Variability is inversely proportional to the square root of coating time

Figure 86: Mass Coating Variability with $Bo_g > 1$

7.0 DRYING PROCESS

Drying is a widely used unit operation in the food, pharmaceutical, chemical and mineral industries, among others [19, 21, 138, 139, 140, 141, 142]. In many operations, such as granulation or crystallization, it is necessary to get desired products in a wet form first, then use a drying operation to remove the moisture. Drying is the process that employs heat to remove the moisture content between and inside particles by evaporation. The heat transfer rate is related to a variety of process variables which include the kiln rotation speed, the particle sizes and other particle properties. By controlling these variables, we can optimize the efficiency of the drying process. In many industrial operations, the drying stage limits the rate of the overall process [143]. The drying process in gas-solid flows involves complex mass (liquid transfer between particles, liquid evaporation to the gas phase and mass transfer in the gas phase), momentum (solid contacts, gas flow, inter-phase momentum transfer) and heat (heat transfer on solid contacts, convective heat transfer in gas phase, inter-phase heat transfer) transfer. For the most part, these transport mechanisms are coupled and make the overall process more complicated. To the best of our knowledge, no previous studies have been done to simulate the particulate drying process in a gas-solid flow system using PD, a very important tool in solid flow, and CFD, the main tool in fluid flow.

Assuming non-porous particles, moisture in the particle bed will form liquid bridges, which not only give rise to a cohesive force affecting the momentum transfer, but create a complicated three-phase heat transfer problem. The condensed liquid film decreases the area available for gas-solid heat transfer, while it increases the effective contact radius between particles. The evaporated liquid is regarded as a source term in the gas phase. In most drying operations, water is the moisture and air is the drying medium [144].

Here we introduce a drying model that employs particle dynamics to track the solid phase and computational fluid dynamics to simulate the gas phase. First, we outline the inter-phase mass transfer model. Then, we discuss the heat transfer through the liquid bridge between two arbitrary particles, which can have different size and contact angle. As a test of this new model we present results from the simulation of a rotary drum drying system. Specifically, the drying curve and drying rate curve are presented for both a mono-disperse and bi-disperse system.

7.1 MASS TRANSFER

The mass flow rate to (a negative value means from) a particle can be expressed as:

$$\Delta \dot{m}_p = \Sigma \dot{m}_c + \dot{m}_f + \dot{m}_o, \tag{7.1}$$

where $\dot{m}_c$ is the mass transferred from neighboring particles by contact formation and breakage, $\dot{m}_f$ is the liquid mass condensed from (evaporated to) the vapor, and $\dot{m}_o$ represents other mass sources such as chemical reaction etc.

7.1.1 Inter-Phase Mass Transfer

The mass loss caused by evaporation can be calculated as [145]

$$\dot{m}_f = -\alpha \pi d^2 (p_{sat} - p) \sqrt{\frac{Mw}{2\pi RT}} \tag{7.2}$$

$$\tag{7.3}$$

where α is the evaporation coefficient, Mw is the molecular weight ($0.018 kg/mol$ for water), R is the universal gas constant ($8.3145 J/molK$), T is the particle temperature (K) and p_{sat} is the saturation pressure at T, which can be expressed for water as [36]:

$$p_{sat} = 133.322 \times 10^{0.6715 + 0.030(T-273.15) - 0.0000798(T-273.15)^2}. \tag{7.4}$$

7.1.2 Gas Phase Mass Transfer

In the gas phase, the mass flux from the particles is considered as an added mass source term, thus, the mass transfer can be expressed as:

$$\frac{\partial(\epsilon c_w)}{\partial t} + \nabla \cdot \epsilon u c_w = D_g \nabla^2(\epsilon c_w) + \alpha \pi d^2 (p_{sat} - p)\sqrt{\frac{Mw}{2\pi RT}}\frac{1}{\Delta V_{cont}} + \dot{R}_o \tag{7.5}$$

where c_w is the water mass fraction in the gas phase, ΔV_{cont} is the control volume, and $\dot{R}_o$ includes other mass sources in the gas phase per unit volume. D_g is the water in air diffusion coefficient, which can be expressed as [146]

$$D_g = 1.87\times10^{-10} T^{2.072}\frac{p_0}{p} \tag{7.6}$$

at absolute temperature T and pressure p, where p_0 is one normal atmosphere.

7.2 HEAT TRANSFER

Besides the heat sources listed in Section 5.1.2.1, the heat transferred to a particle during the drying process should also include the heat flux through the liquid bridge Q_l and the latent heat due to liquid evaporation Q_e. Thus, the heat transferred to a particle can be expressed as:

$$Q_p = \Sigma Q_c + \Sigma Q_l + Q_e + Q_f + Q_o, \tag{7.7}$$

7.2.1 Heat Transfer through Interstitial Liquid

If liquid bridges are present between the particles, as shown in Figure 87, the heat flux through the liquid bridge can be expressed as [147]

$$\frac{dQ_l}{dt} = H_l \Delta T. \tag{7.8}$$

H_l is the amount of heat transferred through the liquid bridge per unit temperature per unit time and can be approximated by

$$H_l = k_l \frac{< A_l >}{d}, \tag{7.9}$$

where k_l is liquid thermal conductivity, d is the length of the liquid bridge and $< A_l >$ is the average cross area of the liquid bridge.

Since $V =< A_l > d$, we can get

$$H_l = k_l \frac{V}{d^2}. \tag{7.10}$$

In order to extend the model in Ref. [147] (outlined above), which deals with monodisperse particles, to general applications we must determine the bridge profile. As in Chapter 6, we assume the liquid bridge is described by a parabolic equation. In contrast to Ref. [27], we now require the full profile history, rather than simply that at rupture. Figure 88 shows the calculation results for three different separation distances, S, using this assumption. The particles used have different diameter and contact angles. The value of d can be calculated by

$$d = h_i + h_j + S. \tag{7.11}$$

7.2.2 Heat Transfer due to Liquid Evaporation

The liquid evaporation will absorb the latent heat of vaporization from the particles, which can be expressed as

$$Q_e = \dot{m}_f \cdot H_{latent}. \tag{7.12}$$

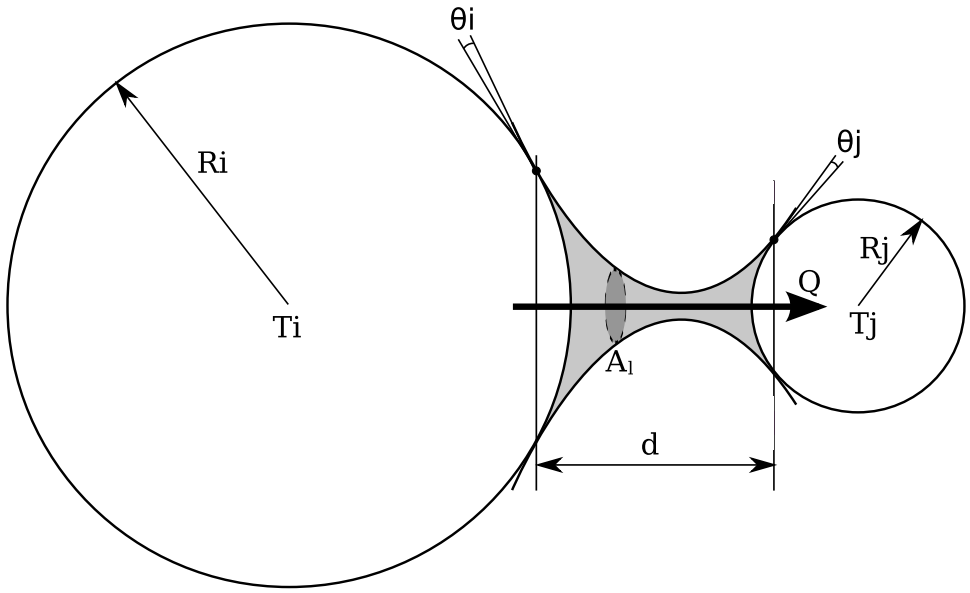

Figure 87: Schematic of heat transfer through liquid bridge

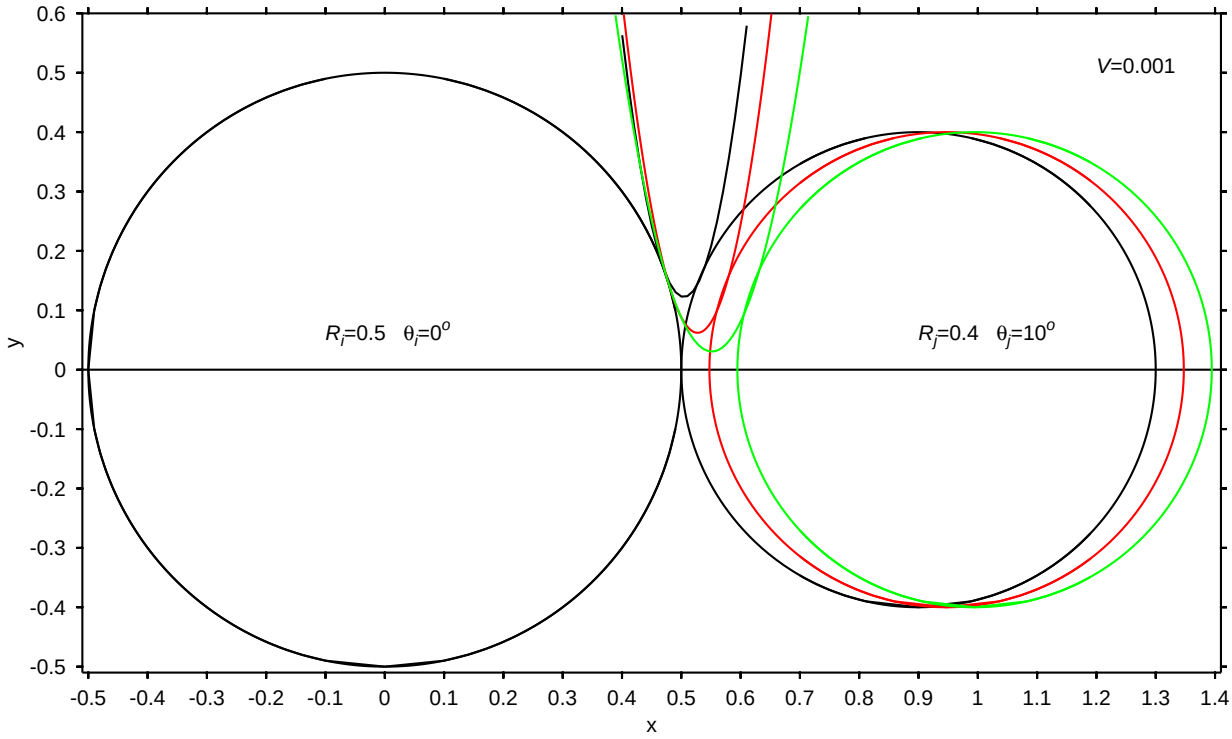

Figure 88: The liquid bridge profile will change with separation distance. Using a parabolic equation assumption, the liquid bridge shape can be predicted based on the liquid bridge volume, V, particle separation distance, S, and the particle properties. Thus we can get the liquid bridge length, d. Three different separation distances are shown in this figure. It should be noted that the liquid bridge is asymmetric due to the two particles having different radius and contact angle.

7.3 RESULTS AND DISCUSSIONS

The simulations are performed in a rotating drum, which has a high temperature of 100°C. Initially, the gas is dry and has low temperature 25°C. The initial condition for the solid is created by loading wet, low temperature (25°C) particles in a rectangular lattice and allowing the particles to fall under gravity to form a packed bed. As the drum is rotated, momentum and heat will be exchanged between the wall, particles and the inside air. At the same time, mass transfer will happen between the solid particles due to liquid bridge formation and rupture, between the solid and gas phase due to evaporation, and in the gas phase due to gas movement and mass diffusion.

Table 6: PARTICLE PARAMETERS IN DRYING SIMULATIONS.

($\rho = 2600.0 kg/m^3$)

	R_i	R_j	θ_i	θ_j
Mono-disperse	$1.5mm$	$1.5mm$	$0°$	$0°$
Heterogeneous	$1.5mm$	$1.2mm$	$0°$	$10°$

Two simulations are run. One is for a mono-disperse system and the other is for a heterogeneous system. The particle parameters used in the simulations are shown in Table 6. Figure 89 shows the drying simulation results for mono-disperse particles in a rotary kiln. Figure 89a shows the mixing evolution of initially segregated particles (as indicated by differing colors). In Figure 89b-e, red represents high values and blue means low values, and other colors such as yellow and green lie between them. Initially, all particles have the largest possible moisture content as evidenced by red colors (red represents 100% of the initial value and blue represents 75%) in Figure 89b. At 1s, some particles at the periphery have changed colors due to evaporation. Due to strong cohesive forces between particles, the top left corner of the particle bed initially has a rounded shape. At 30s, one notes that a high moisture core is surrounded by low moisture particles. Moreover, the round shape has been flattened in the top left corner of the particle bed. Figure 89c shows the temperature evolution of the same simulation. Due to the fact that we use initially completely dry air (i.e., the relative

moisture humidity starts at zero), the moisture on the surface of the particles evaporates rapidly and absorbs latent heat from the particles. Coupled with the fact that heating the air maintains a low relative humidity, this causes the particles to initial drop in temperature despite the fact that we input heat at the wall. Interestingly, the topology of the contour plots are remarkably similar in both the moisture and temperature figures, i.e. the high temperature is located at the same point of the drum as the high moisture content and vice versa. At 30s, the high temperature core is surrounded by low temperature particles. Figure 89d shows the moisture concentration evolution in the gas phase. Figure 89e shows the gas phase temperature. At 30s, corresponding to the low temperature particle core, there is a low temperature air region.

Figure 90 shows the drying curve, which is the relationship between the particle average moisture content and the drying time for the mono-disperse simulation. Figure 91 shows the drying rate curve, where the drying rate is calculated as the time derivative of the moisture content. Initially the particle bed has a high drying rate, caused, in part, by our method of generating the initial condition (as the particles settle via gravity, they are more exposed to the surrounding air). As time progresses, the drying rate decreases and begins to level off, which is similar to the experimentally-observed constant-rate period, caused by liquid evaporation on the particle surface, in a typical drying rate curve [148]. Since we use non-porous particles, we don't consider liquid diffusion inside the particles, so there is no falling-rate period in our simulation, as is also observed in the literature [143, 149, 150, 151, 152, 153, 154, 155].

Figures 92, 93, 94 show the drying simulation results for a heterogeneous particle system in a rotary kiln. As can be seen, the drying rate and bed moisture distribution is dramatically impacted by the particle heterogeneities. In contrast, the bed temperature profile is not substantially different. Surprisingly, the smaller more hydrophobic particles maintain moisture longer, lowering the drying rate.

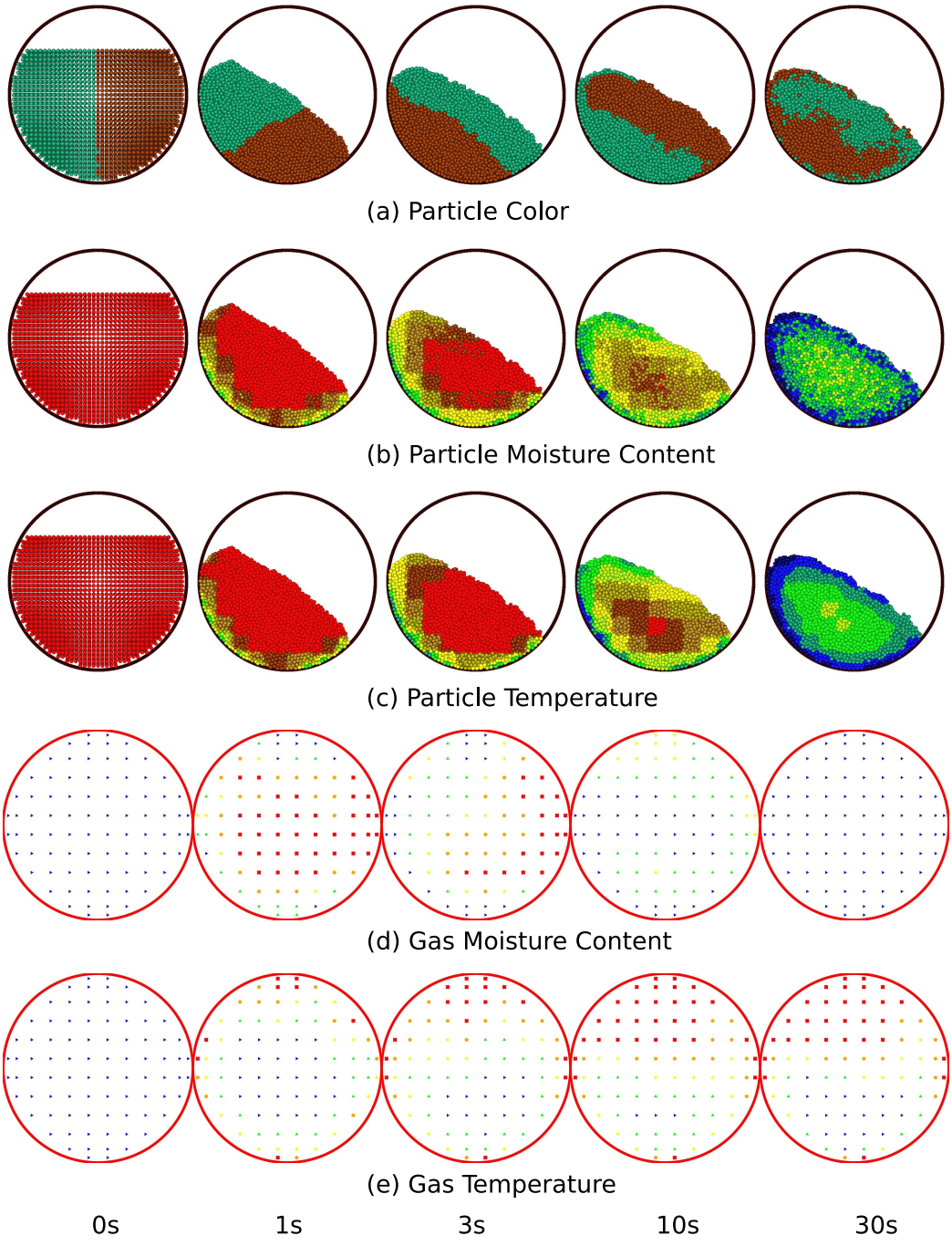

Figure 89: The simulation of the drying process for mono-disperse particles in a rotary kiln. (a) shows the two kinds of particles having different colors (b) shows the moisture content evolution and (c) shows the particle temperature evolution. (d) and (e) are the moisture content and temperature evolutions in the gas phase, respectively.

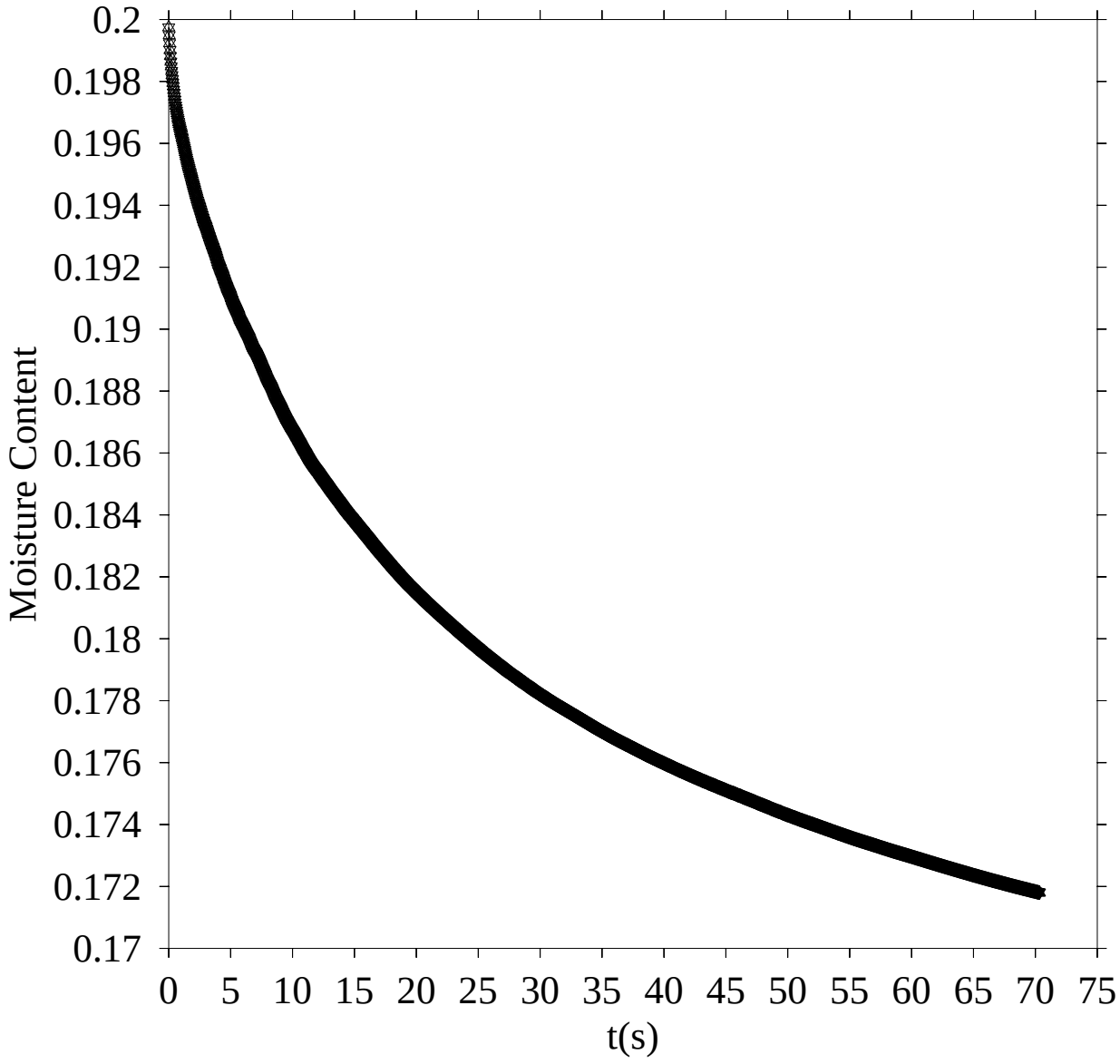

Figure 90: Drying curve for mono-disperse particles drying process. Particle moisture content decreases with time.

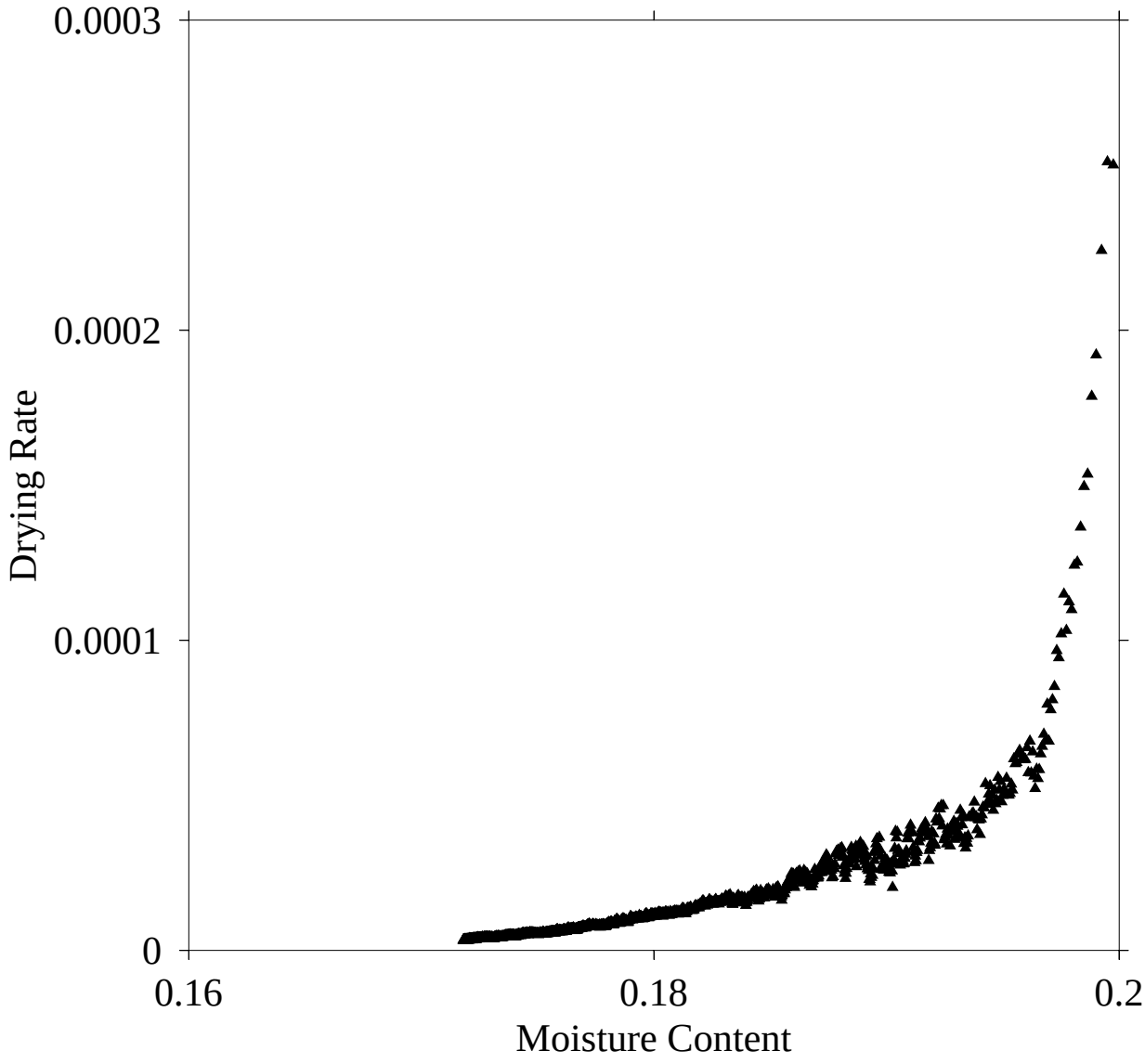

Figure 91: Drying rate curve for mono-disperse particles drying process.

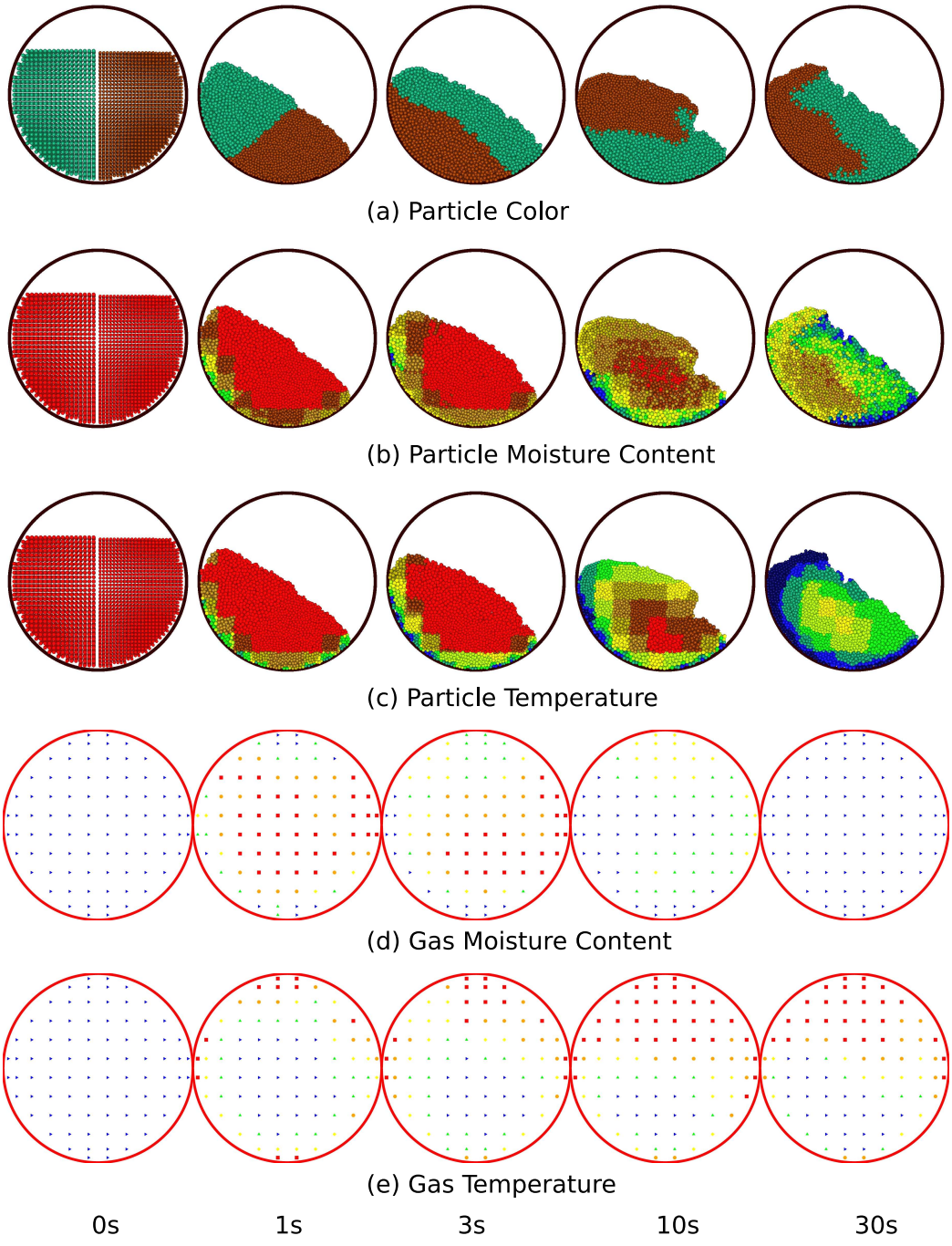

Figure 92: The simulation of heterogeneous particles drying process in a rotary kiln. (a) shows the two kinds of particles having different colors (b) shows the moisture content evolution and (c) shows the particle temperature evolution. (d) and (e) are the moisture content and temperature evolutions in the gas phase, respectively.

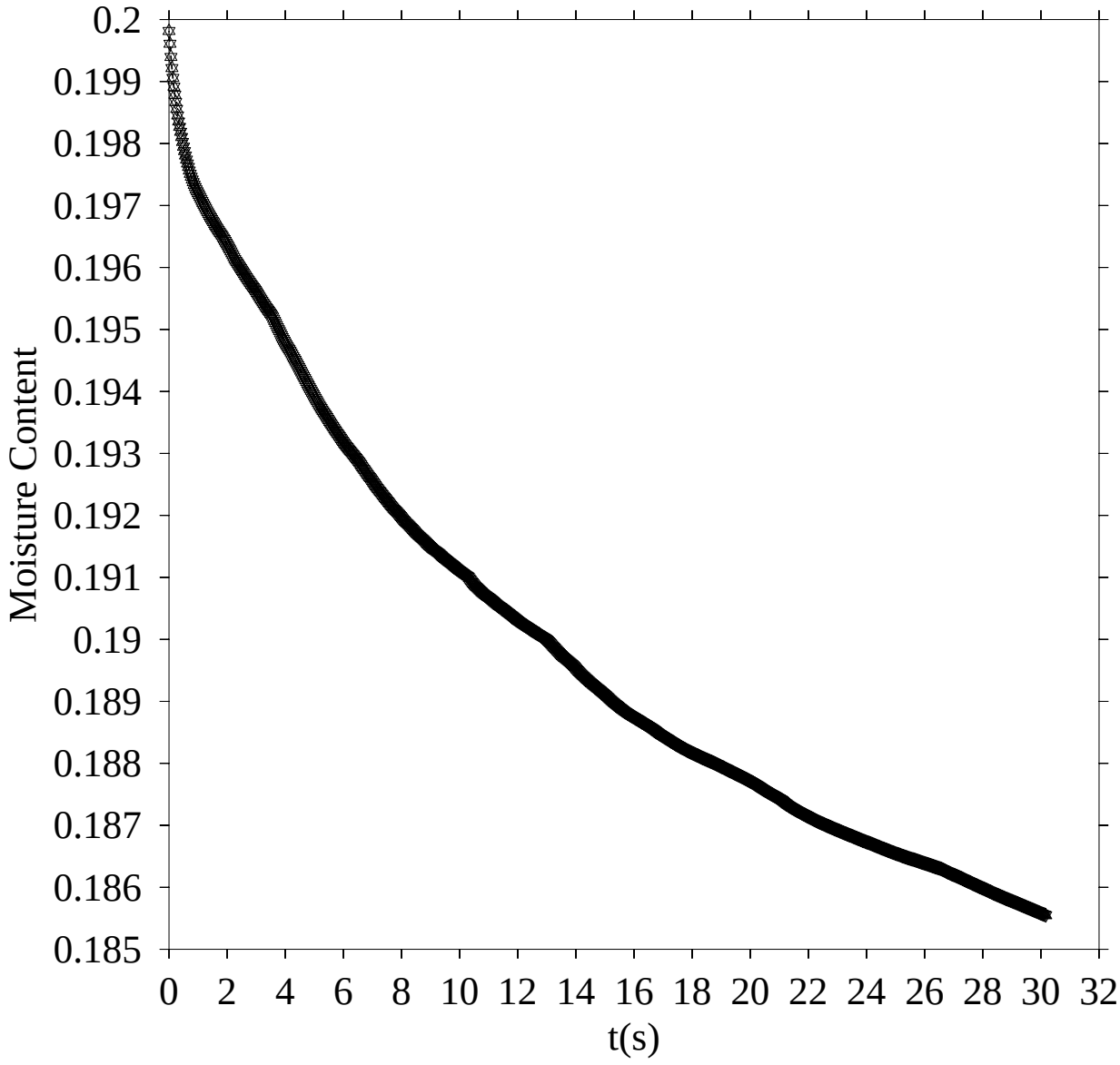

Figure 93: Drying curve for heterogeneous particles drying process. Particle moisture content decreases with time.

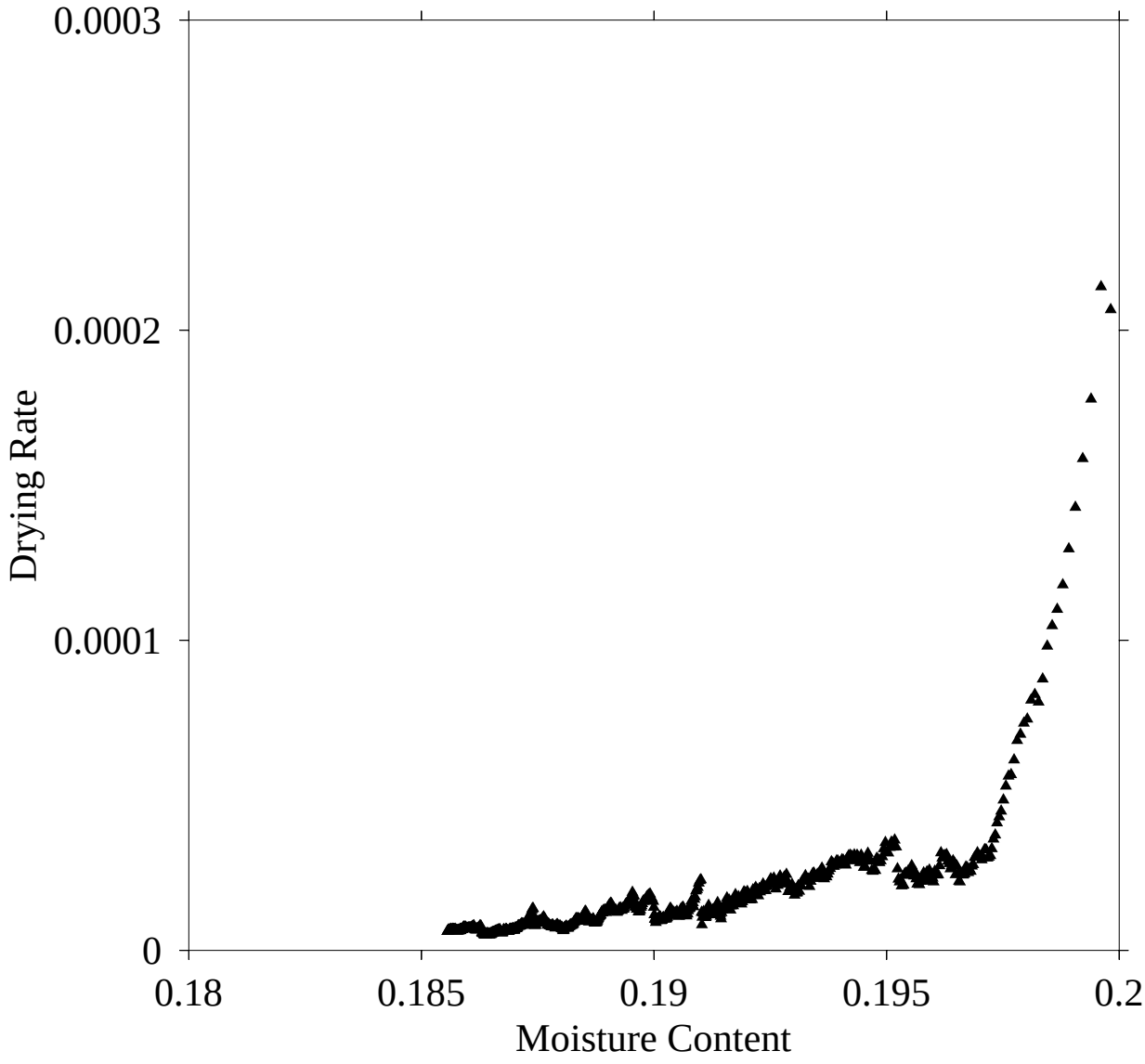

Figure 94: Drying rate curve for heterogeneous particles drying process.

7.4 CONCLUSIONS

Here we describe a comprehensive model for the particulate drying process in gas-solid flows. The momentum transfer is handled using PD for the solid phase, while CFD in used in the gas phase. The mass transfer model includes liquid transfer between particles, liquid evaporation from the solid phase to the gas phase, and convective and diffusive mass transfer in the gas phase. The heat transfer model includes conductive heat transfer from wall to particle, through particle contacts/collisions and liquid bridges, and the convective heat transfer relating to gas movement. We should point out that all the models involving particles are robust to changes in particle properties, i.e. the particles can have different density, size and contact angle.

Using the above models, we simulate the particle drying process in a rotary kiln, which shows the transition of the particle system from a highly cohesive one to a dry one. The drying curve and drying rate curve are obtained from the simulation. The constant-rate drying period is observed, as expected.

8.0 OUTLOOK

8.1 ANISOTROPIC PARTICLE

All the former simulations handle particles having uniform and evenly distributed parameters. In reality, it is necessary to consider different parts of the particle to be different. Here we developed a model for handling amphiphilic particles, which are spheres composed of at least two distinct zones as shown in Figure 95. By allowing each zone to have different physical and/or process parameters, we establish the ability to simulate non-uniform particles. Of course, this method can be extended by dividing the particle into more zones as shown in Figure 96. Theoretically, the method employed here can be used to handle arbitrary geometry particles, such as a square or triangle, etc. [156].

In order to recognize each part of the particle in our simulation, the dynamics for particle rotation is incorporated into the code. Quaternions can provide an elegant and straightforward solution to the rotation direction and angles of rigid bodies[157]. The quaternion Q is composed of four scalar quantities

$$Q = (q_0, q_1, q_2, q_3). \tag{8.1}$$

Any three of them, such as the last three (q_1, q_2, q_3), can constitute a vector. The quaternions satisfy the constraint

$$q_0^2 + q_1^2 + q_2^2 + q_3^2 = 1. \tag{8.2}$$

Dziugys described the use of quaternions to model the orientation of particles undergoing 3D rotations in particle dynamics [158]. Langston used quaternions to model non-spherical

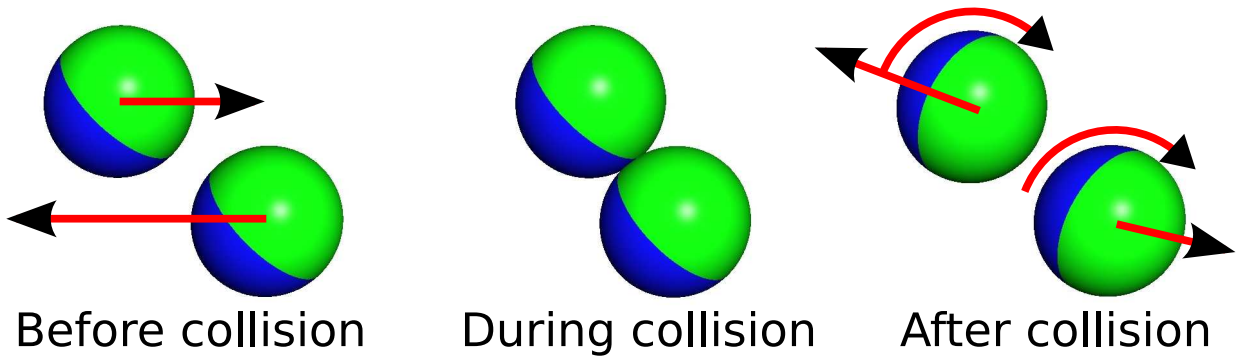

Figure 95: Simulation of amphiphilic particles collision, where each particle is composed of two parts. After collision, the particle rotations are clearly shown in the figure.

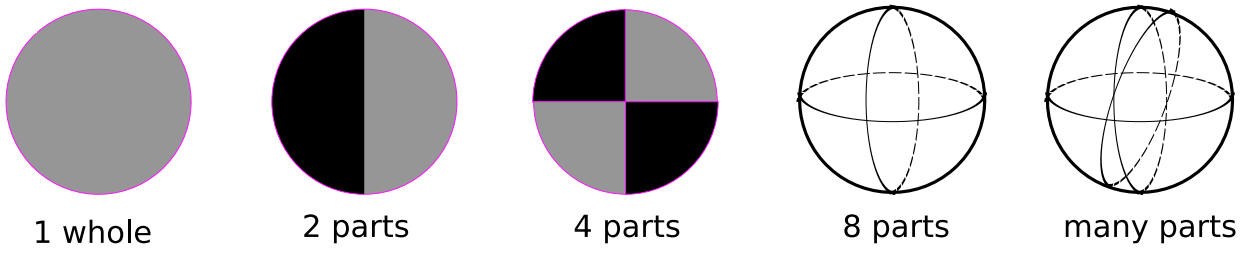

Figure 96: The particles are composed of 1, 2, 4, 8 or more part(s).

frictionless particle flow [156]. Meister has stated that the quaternion method can be used to handle rotations of spherical objects in three-dimensional space [159]. We will use quaternions to handle 3D particle rotation so as to simulate amphiphilic particles.

The orientation of a rigid body can be specified by a vector, which can be expressed in terms of components in both the body-fixed ($\mathbf{x}'$) and space-fixed frames ($\mathbf{x}$) [157]. The components in different frames can be related by the rotation matrix A

$$\mathbf{x}' = A \cdot \mathbf{x}. \tag{8.3}$$

The transformation from one Cartesian coordinate system to another can be achieved by three successive rotations performed in a specific sequence [160]. The Euler angles are defined as the three successive angles of rotation. Depending on the rotation sequences of the axes, there are several conventions, such as the x-convention, y-convention, and xyz-convention for the Euler angles.

Here the x-convention is described. First, the original xyz axes are rotated counterclockwise about the z axis by an angle ϕ to become x_1y_1z axes as Figure 97a shows. Then x_1y_1z is rotated counterclockwise about the x_1 axis by an angle θ into x_1y_2z' as Figure 97b shows. Finally, x_1y_2z' is rotated counterclockwise about the z' axis by an angle ψ into $x'y'z'$ as Figure 97c shows.

Mathematically [161] , the first rotation can be expressed as

$$\begin{bmatrix} x_1 \\ y_1 \\ z \end{bmatrix} = \begin{bmatrix} cos\phi & sin\phi & 0 \\ -sin\phi & cos\phi & 0 \\ 0 & 0 & 1 \end{bmatrix} \begin{bmatrix} x \\ y \\ z \end{bmatrix}.$$

The second rotation is

$$\begin{bmatrix} x_1 \\ y_2 \\ z' \end{bmatrix} = \begin{bmatrix} 1 & 0 & 0 \\ 0 & cos\theta & sin\theta \\ 0 & -sin\theta & cos\theta \end{bmatrix} \begin{bmatrix} x_1 \\ y_1 \\ z \end{bmatrix}.$$

The third rotation is

$$\begin{bmatrix} x' \\ y' \\ z' \end{bmatrix} = \begin{bmatrix} cos\psi & sin\psi & 0 \\ -sin\psi & cos\psi & 0 \\ 0 & 0 & 1 \end{bmatrix} \begin{bmatrix} x_1 \\ y_2 \\ z' \end{bmatrix}.$$

Thus, we have

$$\begin{bmatrix} x' \\ y' \\ z' \end{bmatrix} = \begin{bmatrix} cos\psi & sin\psi & 0 \\ -sin\psi & cos\psi & 0 \\ 0 & 0 & 1 \end{bmatrix} \begin{bmatrix} 1 & 0 & 0 \\ 0 & cos\theta & sin\theta \\ 0 & -sin\theta & cos\theta \end{bmatrix} \begin{bmatrix} cos\phi & sin\phi & 0 \\ -sin\phi & cos\phi & 0 \\ 0 & 0 & 1 \end{bmatrix} \begin{bmatrix} x \\ y \\ z \end{bmatrix}.$$

We get the rotation matrix as

$$A = \begin{bmatrix} cos\phi cos\psi - sin\phi cos\theta sin\psi & sin\phi cos\psi + cos\phi cos\theta sin\psi & sin\theta sin\psi \\ -cos\phi cos\psi - sin\phi cos\theta cos\psi & -sin\phi sin\psi + cos\phi cos\theta cos\psi & sin\theta cos\psi \\ sin\phi sin\theta & -cos\phi sin\theta & cos\theta \end{bmatrix}.$$

The quaternions are related to Euler angles by

$$q_0 = cos\frac{1}{2}\theta cos\frac{1}{2}(\phi + \psi) \tag{8.4}$$

$$q_1 = sin\frac{1}{2}\theta cos\frac{1}{2}(\phi - \psi) \tag{8.5}$$

$$q_2 = sin\frac{1}{2}\theta sin\frac{1}{2}(\phi - \psi) \tag{8.6}$$

$$q_3 = cos\frac{1}{2}\theta sin\frac{1}{2}(\phi + \psi) \tag{8.7}$$

so the rotation matrix becomes

$$A = \begin{bmatrix} q_0^2 + q_1^2 - q_2^2 - q_3^2 & 2(q_1q_2 + q_0q_3) & 2(q_1q_3 - q_0q_2) \\ 2(q_1q_2 - q_0q_3) & q_0^2 - q_1^2 + q_2^2 - q_3^2 & 2(q_2q_3 + q_0q_1) \\ 2(q_1q_3 + q_0q_2) & 2(q_2q_3 - q_0q_1) & q_0^2 - q_1^2 - q_2^2 + q_3^2 \end{bmatrix}.$$

The rotation of the body system will result in the change of Euler angles ϕ,θ and ψ. Using quaternions, the relationship can be expressed as [157]

$$\begin{bmatrix} \dot{q_0} \\ \dot{q_1} \\ \dot{q_2} \\ \dot{q_3} \end{bmatrix} = \frac{1}{2} \begin{bmatrix} q_0 & -q_1 & -q_2 & -q_3 \\ q_1 & q_0 & -q_3 & q_2 \\ q_2 & q_3 & q_0 & -q_1 \\ q_3 & -q_2 & q_1 & q_0 \end{bmatrix} \begin{bmatrix} 0 \\ \omega_x^b \\ \omega_y^b \\ \omega_z^b \end{bmatrix},$$

where ω_x^b, ω_y^b, ω_z^b are the angular velocities of the body system.

8.2 POSSIBLE APPLICATION OF ANISOTROPIC PARTICLE 1 : HEAT TRANSFER IN ANISOTROPIC PARTICLE

In the heat transfer model, we assumed each particle has a uniform temperature and conductivity (Section 5.2.4). This assumption can be removed by assigning different conductivities to each part of the anisotropic particles as shown in Figure 98. Alternatively, we could use this technique to track the temperature profile inside particles for cases where $Bi \geq 1$.

8.3 POSSIBLE APPLICATION OF ANISOTROPIC PARTICLE 2 : UNEVENLY DISTRIBUTED LIQUID IN LIQUID TRANSFER MODEL

In our liquid transfer model, we assumed that liquid is evenly distributed on the surface of individual particles (Section 6.2). If, however, the wetting angles were too large to assume rapid liquid spreading, we need instead to explicitly track moisture on the surface. This could be accomplished by using anisotropic particles as shown in Figure 99. Figure 100 shows the simulation of amphiphilic particles in a fluidized bed (such as would be used in a fluidized spray coater).

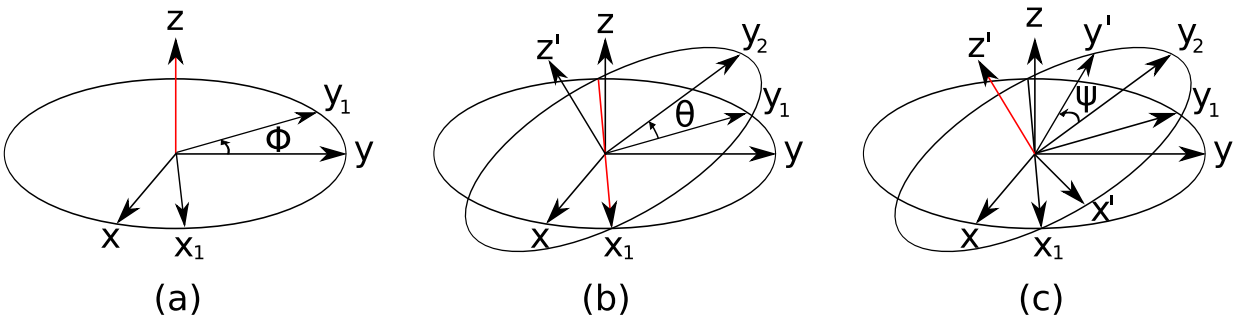

Figure 97: The rotations using Euler angles.

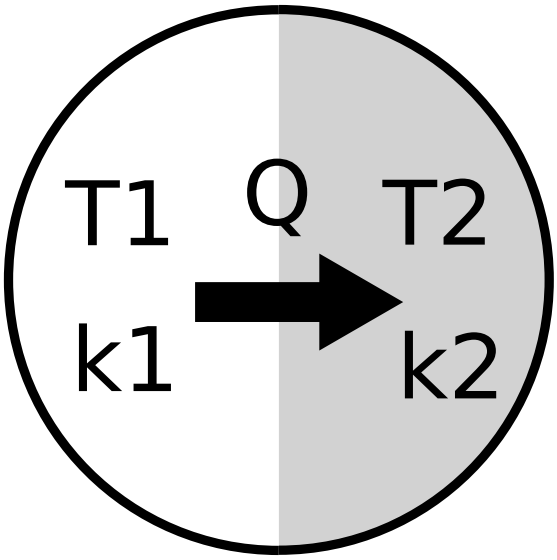

heat transfer inside particle

Figure 98: Different parts of the particle have different temperature and conductivity. Thus, heat exchange exists inside the particle.

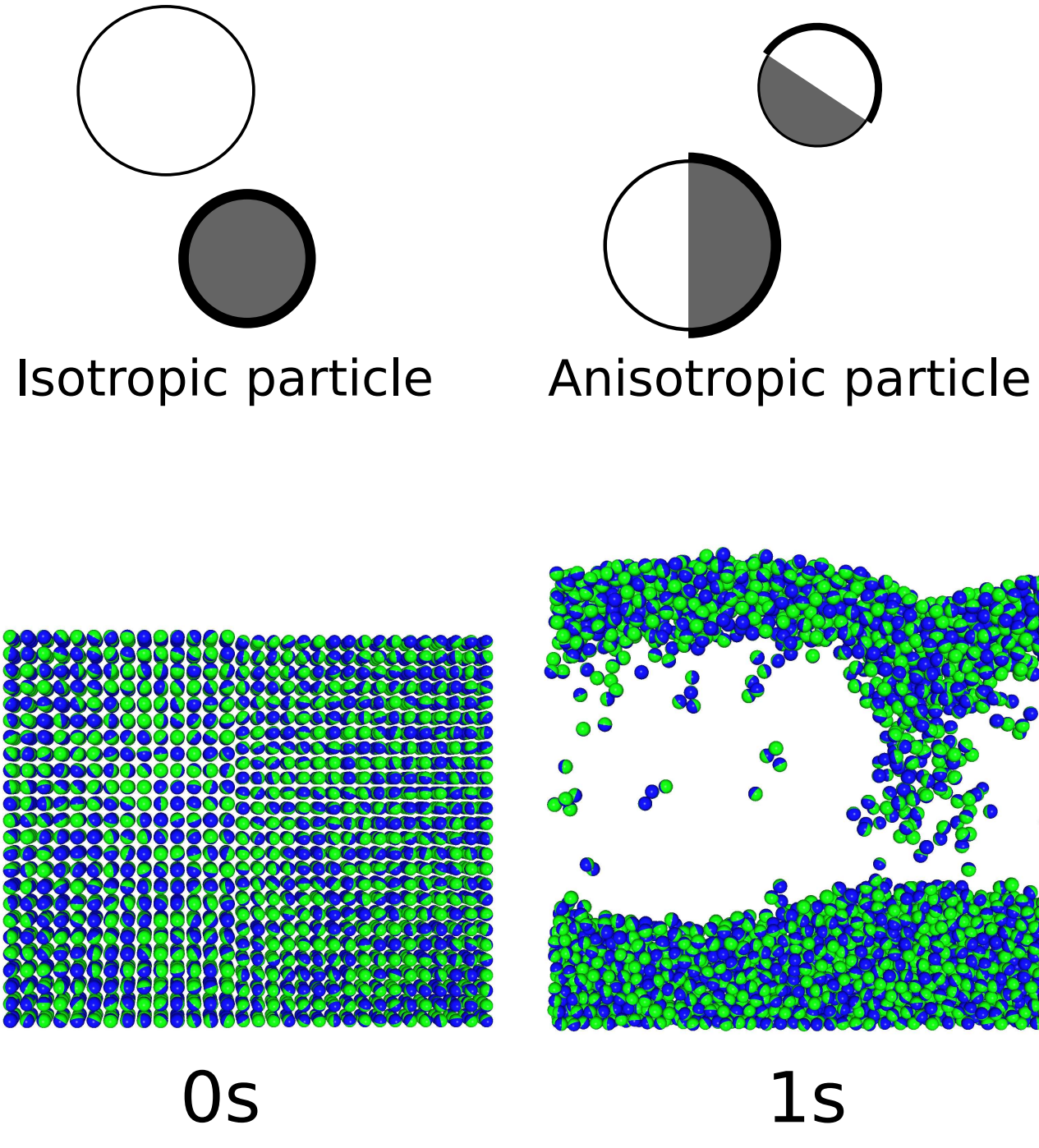

Figure 100: The fluidization of amphiphilic particles in a fluidized bed.

8.4 POSSIBLE APPLICATION OF ANISOTROPIC PARTICLE 3 : ANISOTROPIC PARTICLE AID ON PARTICLE MIXING

In analogy to the use of a surfactant in immiscible liquid mixing, we can also explore the use of amphiphilic particles to aid mixing of two kinds of particles, which otherwise are hard to mix by conventional methods. A potential strategy to achieve this may be as follows. An amphiphilic particle has two faces. Each face has unique surface properties, which make it favor only one kind of particle. Therefore, the "surfactant" particle can be used to connect the two different kinds of particles, as shown in Figure 101. Ultimately, a higher mixing extent can be achieved if the different particles interact in this way.

In order to employ our theory, appropriate particle properties should be selected for the amphiphilic particle faces, so that each face of this kind of particle can form strong cohesive bonds with the corresponding particles. Some preliminary tests of this idea are shown in Figure 102.

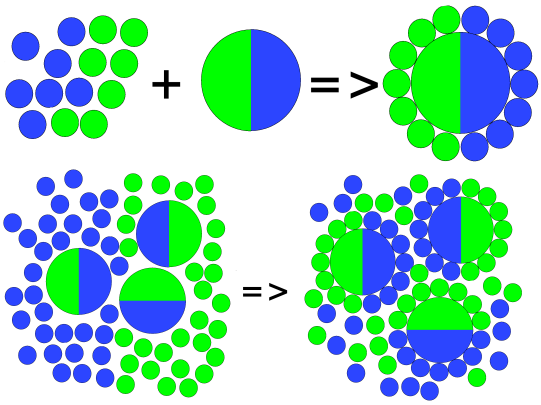

Figure 101: Amphiphilic particles will help mix the particles

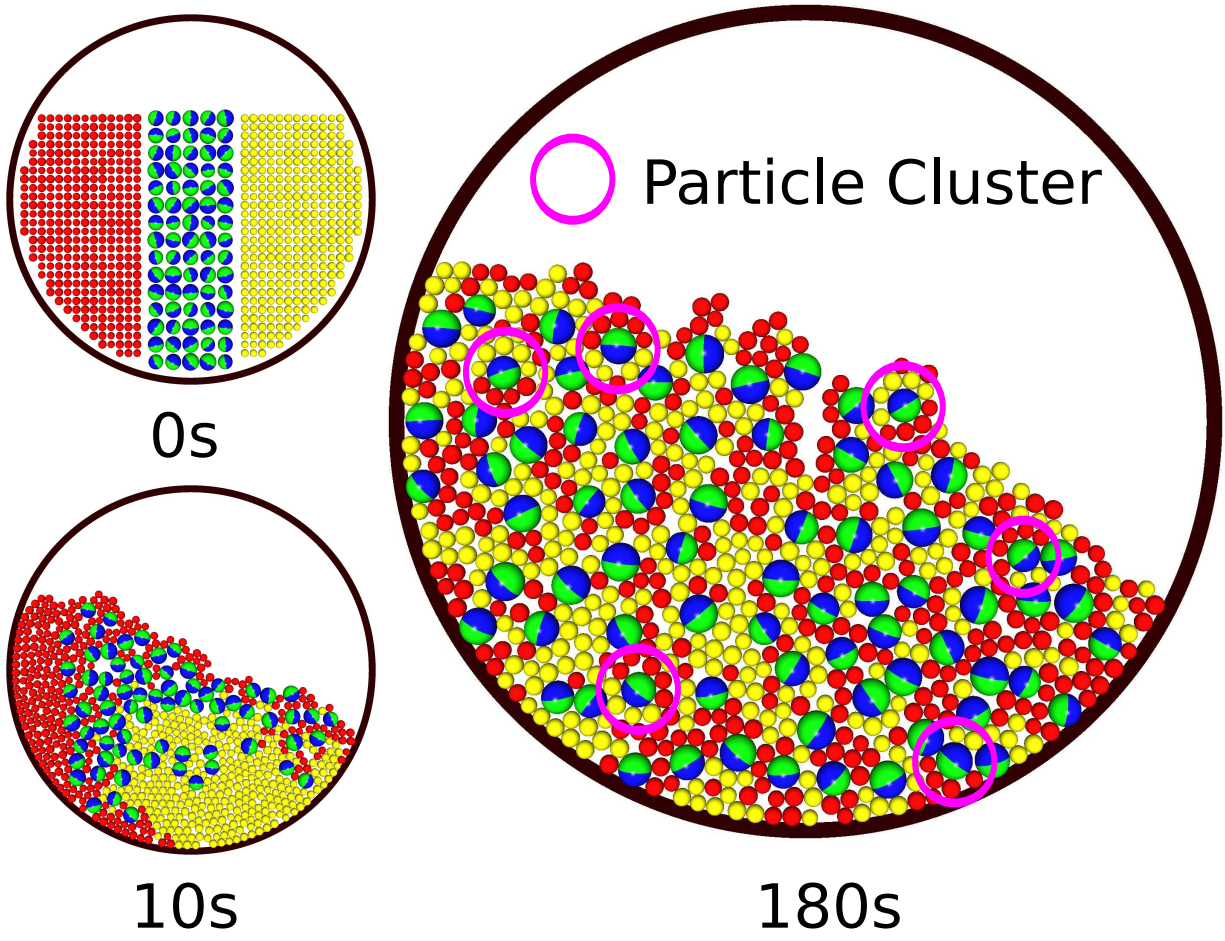

Figure 102: One side of the amphiphilic particle is surrounded by one kind of particle, and the other side is surrounded by another kind of particle, which is clearly shown in the particle cluster.

9.0 NOMENCLATURE

Table 7: PARAMETERS USED IN THE SIMULATIONS.

Particle	**Glass**	**steel**	**Aluminum**
Density	2700 kg/m^3	7900 kg/m^3	2700 kg/m^3
Diameter	$3.0 \times 10^{-3} m$	$3.0 \times 10^{-3} m$	$3.0 \times 10^{-3} m$
Poisson Ratio	0.33	0.29	0.33
Young's Modulus	69 GPa	193 GPa	110 GPa
Friction Coefficient	0.3	0.3	0.3
Thermal Conductivity	1.7 $W/(m \cdot K)$	15 $W/(m \cdot K)$	180 $W/(m \cdot K)$
Heat Capacity	800.0 $J/(kg \cdot K)$	477.0 $J/(kg \cdot K)$	900.0 $J/(kg \cdot K)$
Air			
Density	1.23 kg/m^3		
Viscosity	1.80×10^{-5} $kg/(m \cdot s)$		
Thermal Conductivity	0.0261 $W/(m \cdot K)$		
Heat Capacity	1000.7 $J/(kg \cdot K)$		

Table 8: SYMBOLS USED IN THE DISSERTATION.

SYMBOLS	
A, B, C	constants in the numerical solution of the Laplace-Young equations
A_w	area of particles in contact with the wall m^2
Bo_g	Granular Bond Number
c	heat capacity $J/(kg \cdot K)$
C_d	drag coefficient
Ca_g	Granular Capillary Number
d_p	particle diameter m
$D_w, D_e, D_n, D_s, D_t, D_b$	mass conductances through the control volume kg/s
F	interparticle force N
F_c	capillary force N
$F_{c_{max}}$	maximum capillary force N
F_d	drag force N
F_n	normal interparticle force N
F_t	tangential interparticle force N
F_v	viscous force N
$G_w, G_e, G_n, G_s, G_t, G_b$	mass flow rates through the control volume kg/s
$\hat{F}$	normalized capillary force
g	gravity acceleration m/s^2
h	half separation distance between particles m
$\hat{h}$	dimensionless half separation distance between particles
$\hat{h_c}$	dimensionless critical rupture distance
h_w	heat transfer coefficient from wall to particle $W/(K \cdot m^2)$
h_{gp}	local particle-to-gas heat transfer coefficient $W/(K \cdot m^2)$
H	contact conductance W/K
I_p	particle rotary inertia $kg \cdot m^2/s$
k_g	thermal conductivity of gas $W/(m \cdot K)$
k_s	thermal conductivity of solid $W/(m \cdot K)$
k_{eff}	effective thermal conductivity of the bed of particles $W/(m \cdot K)$
m_p	particle mass kg
p	gas pressure Pa
ΔP	pressure difference across the air-liquid interface Pa

Table 8 (continued).

q_w	heat flux at the wall W
Q_p	heat transferred to a particle J
Q_c	contact heat transferred from neighboring particles J
Q_f	heat transferred from fluid to the particle J
Q_o	heat transferred from other sources J
$\dot{Q}_{og}$	heat flux from other sources per unit volume in gas phase W/m^3
r_1	bridge meridional radius of curvature m
r_2	bridge neck radius m
R	particle radius m
R_c	contact radius m
Re_{pf}	particle Reynolds number based on superficial gas velocity
S_p	particle surface area m^2
t_c	contact time between the wall and the particles K
T_p	particle temperature K
T_w	wall temperature K
T_o	particle initial temperature K
T_b	bulk temperature K
u	gas velocity m/s
U	superficial gas velocity m/s
v	relative velocity of the spheres m/s
v_p	particle velocity m/s
$\hat{V}$	dimensionless bridge volume
w	weight of the particles in the bed kg
Greek Letters	
β	half filling angle
γ	surface tension kg/s^2
δ	characteristic length m
ϵ	void fraction
θ	contact angle
μ	liquid viscosity kg/ms
μ_g	gas viscosity kg/ms
ρ_g	gas density kg/m^3
ρ_s	particle density kg/m^3
τ_g	gas viscous stress tensor Pa
$\phi_1, \phi_2, \phi_3, \phi_4, \phi_5$	dimensionless groups
ω_p	particle angular velocity $1/s$
Ω	kiln rotation speed $1/s$
χ	a function of Reynolds Number

APPENDIX

LIQUID BRIDGE OVERLAP ANALYSIS

For a multiple-size system, we can assume R_1 is the largest particle radius and R_2 is the smallest one as shown in Figure 103.

Let α be the angle between O_1O_2 and the tangential line from O_2 to particle O_1. Let β be the angle between O_2O_3 and the tangential line from O_2 to particle O_3 and ϕ be the angle formed by O_1O_2 and O_2O_3. In the case that three particles contact each other, the spherical cap on particle O_2 contacting particle O_1 may overlap with that contacting particle O_3, where δ is used to denote the overlap angle of the these spherical caps.

Based on Figure 103

$$\alpha = arcsin\frac{R_1}{R_1 + R_2} \tag{.1}$$

$$\beta = arcsin\frac{R_2}{R_2 + R_3} \tag{.2}$$

$$\phi = arccos\frac{(R_1 + R_2)^2 + (R_2 + R_3)^2 - (R_1 + R_3)^2}{2(R_1 + R_2)(R_2 + R_3)} \tag{.3}$$

where R_3 the radius of particle O_3.

The angle δ can then be calculated from

$$\delta = \alpha + \beta - \phi \tag{.4}$$

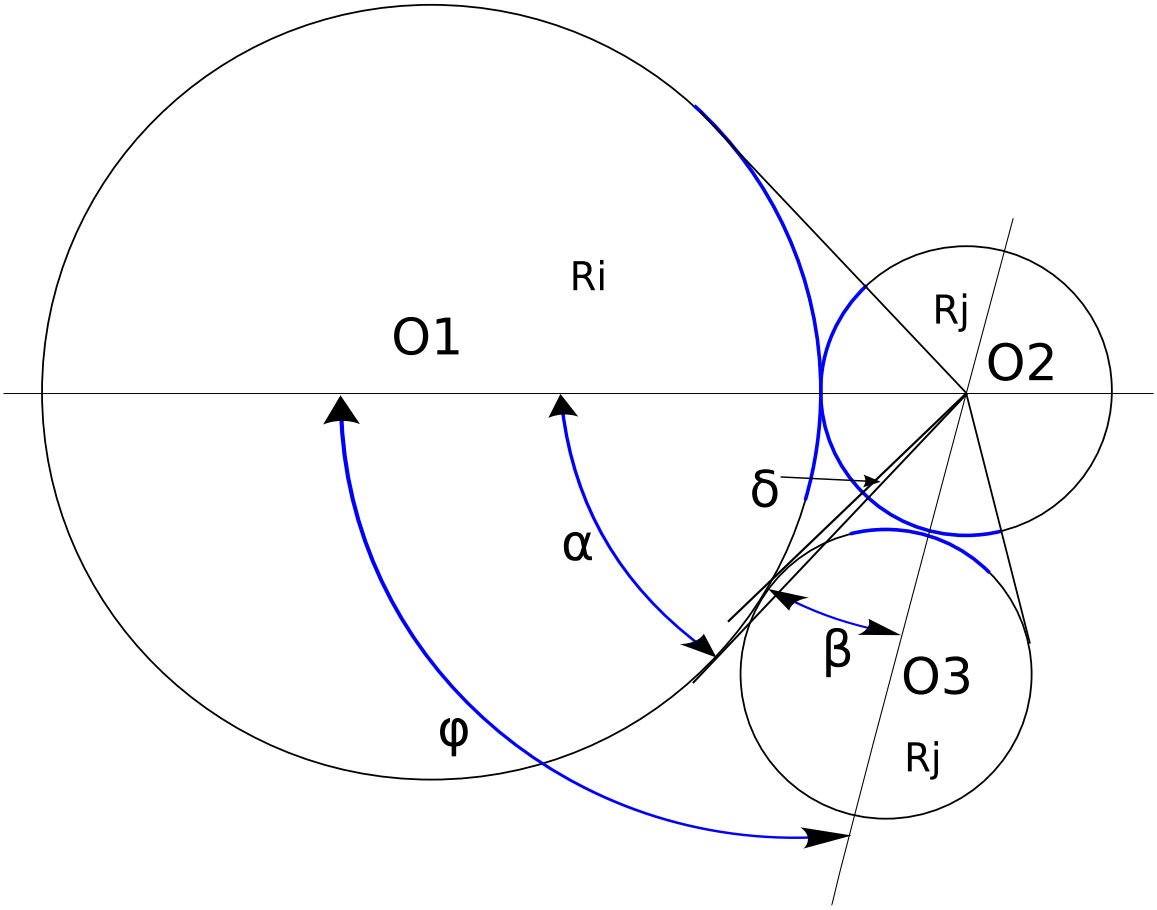

Figure 103: Liquid bridge spherical cap overlap analysis

If R_3 is equal to the largest radius R_1, δ will have value 0. If the value of R_3 decreases, δ will increase. As R_3 decreases to the smallest value R_2, δ will reach its largest value. Thus, we can get the largest overlap angle for a multiple-size system,

$$\delta_{max} = arcsin\frac{R_1}{R_1 + R_2} + arcsin\frac{R_2}{R_2 + R_2} - arccos\frac{R_2}{R_1 + R_2} \tag{.5}$$

Some typical values of δ_{max} are shown in Figure 9.

Table 9: MAXIMUM OVERLAP ANGLE

Radius ratio R_i/R_j	Maximum overlap angle δ_{max}
1.0	0.0°
2.0	1.28°
3.0	3.07°
4.0	4.67°
5.0	6.04°
6.0	7.21°
7.0	8.23°
8.0	9.11°
9.0	9.90°
10.0	10.6°

BIBLIOGRAPHY

[1] Osama S. Sudah, D. Coffin-Beach, and F.J. Muzzio. Quantitative characterization of mixing of free-flowing granular material in tote (bin)-blenders. *Powder Technol.*, 126:191–200, 2002.

[2] Hongming Li and J. J. McCarthy. Controlling cohesive particle mixing and segregation. *Physical Review Letters*, 90 (18):184301, 2003.

[3] Kunal Janin, D. L. Shi, and J. J. McCarthy. Discrete characterization of cohesion in gas-solid flows. *Powder Technol.*, 146:160–167, 2004.

[4] Martin Rhodes. *Introduction to Particle Technology.* John Wiley & Sons, New York, 1998.

[5] Edward L. Paul, Victor A. Atiemo-Obeng, and Suzanne M. Kresta. *Handbook of Industrial Mixing.* Wiley Interscience, New Jersey, 2004.

[6] C.M. Dury and G.H. Ristow. Radial segregation in a two-dimensional rotating drum. *Journal de Physique I*, 7(5):737–745, 1997.

[7] M. A. I. Schutyser, J. T. Padding, F. J. Weber, W. J. Briels, A. Rinzema, and R. Boom. Discrete particle simulations predicting mixing behavior of solid substrate particles in a rotating drum fermenter. *Biotechnol. Bioeng.*, 75(6):666–675, 2001.

[8] M. A. I. Schutyser, F. J. Weber, W. J. Briels, R.M. Boom, and A. Rinzema. Three-dimensional simulation of grain mixing in three different rotating drum designs for solid-state fermentation. *Biotechnol. Bioeng.*, 79(3):284–294, 2002.

[9] C.Y. Wen and L.H. Chen. Flow modeling concepts of fluidized beds. In N.P. Cheremisinoff and R. Gupta, editors, *The Handbook of Fluids in Motion*, pages 665–714. 1983.

[10] D. Geldart. Types of gas fluidization. *Powder Technol.*, 7:285–292, 1973.

[11] J.L.R. Orband and D. Geldart. Direct measurement of powder cohesion using a torsional device. *Powder Technol.*, 92:25–33, 1997.

[12] M.J. Rhodes, X.S. Wang, M. Nguyen, P. Stewart, and K. Liffman. Onset of cohesive behavior in gas fluidized beds: a numerical study using DEM simulation. *Chem. Eng. Sci.*, 56:4433–4438, 2001.

[13] L.J. McLaughlin and M.J. Rhodes. Prediction of fluidized bed behavior in the presence of liquid bridges. *Powder Technol.*, 114:213–223, 2001.

[14] G. Lian, C. Thornton, and M. J. Adams. Discrete particle simulation of agglomerate impact coalescence. *Chem. Eng. Sci.*, 53:3381–3391, 1998.

[15] T. Mikami, H. Kamiya, and M. Horio. Numerical simulation of cohesive powder behavior in a fluidized bed. *Chem. Eng. Sci.*, 53:1927–1940, 1998.

[16] B. P. B. Hoomans, J. A. M. Kuipers, and W. P. M. van Swaaij. Granular dynamics simulation of segregation phenomena in bubbling gas-fluidised beds. *Powder Technol.*, 109 (1):41–48, 2000.

[17] L. S. Fan and C. Zhu. *Principles of Gas-Solid Flows*. Cambridge University Press, New York, 1998.

[18] B.H. Xu and A.B. Yu. Numerical simulation of the gas-solid flow in a fluidized bed by combing disrete particle method with computational fluid dynamics. *Chem. Eng. Sci.*, 52:2785–2809, 1997.

[19] M. Stahl and M. Bentz. High-pressure treatment of wood - combination of mechanical and thermal drying in the "I/D process". *Chemical Engineering and Technology*, 27 (11):1216–1221, 2004.

[20] B. Voglauer and H.P. Jorgl. Dynamic model of a roast process for simulation and control. *Mathematical and Computer Modelling of Dynamcial Systems*, 10 (3-4):217–230, 2004.

[21] Z.F. Sun, C.G. Carrington, J.A. Anderson, and Q. Sun. Air flow patterns in dehumidifier wood drying kilns. *Chemical Engineering Research and Design*, 82 (A10):1344–1352, 2004.

[22] J. J. McCarthy, D. V. Khakhar, and J. M. Ottino. Computational studies of granular mixing. *Pow. Technol.*, 109:72–82, 2000.

[23] S. T. Nase, W. L. Vargas, A. A. Abatan, and J. J. McCarthy. Discrete characterization tools for cohesive granular material. *Powder Technol.*, 116:214–223, 2001.

[24] J.A.M. Kuipers, K.J. van Duin, F.P.H. van Beckum, and W.P.M. van Swaaij. A numerical model for gas-fluidized beds. *Chem. Eng. Sci.*, 47:1913–1924, 1992.

[25] Hernn A. Makse and Jorge Kurchan. Testing the thermodynamic approach to granular matter with a numerical model of a decisive experiment. *Nature*, 415:614–617, 2002.

[26] Deliang Shi, Adetola A. Abatan, Watson L. Vargas, and J. J. McCarthy. Eliminating segregation in free-surface flows of particles. *Phys. Rev. Lett.*, 99:148001, 2007.

[27] Deliang Shi and J. J. McCarthy. Numerical simulation of liquid transfer between particles. *Powder Technol.*, doi:10.1016/j.powtec.2007.08.011, 2007.

[28] H. Hertz. Ueber die berhrungfester elastischer korper. *J. renie ange. Math.*, 92:1–15, 1881.

[29] R. D. Mindlin. Compliance of elastic bodies in contact. *J. Appl. Mech.*, 16:256–270, 1949.

[30] C. Thornton. Coefficient of restitution for collinear collisions of elasti-perfectly plastic spheres. *J. Appl. Mech.*, 64:383–386, 1997.

[31] P. A. Cundall and O. D. L. Strack. A discrete numerical model for granular assemblies. *Geotechnique*, 29:47–65, 1979.

[32] K. L. Johnson. *Contact Mechanics*. Cambridge University Press, Cambridge, 1987.

[33] O. R. Walton and R. L. Braun. Viscosity, granular-temperature, and stress calculations for shearing assemblies of inelastic, frictional disks. *J. Rheol.*, 30:949–980, 1986.

[34] O. R. Walton. Numerical simulation of inclined chute flows of monodisperse, inelastic, frictional spheres. *Mech. Mat.*, 16:239–247, 1993.

[35] R. A. Fisher. On the capillary forces in an ideal soil. *J. Agric. Sci.*, 16:491–505, 1926.

[36] R. B. Bird, W. E. Stewart, and E. N. Lightfoot. *Transport Phenomena*. John Wiley & Sons, New York, 1960.

[37] B.J. Ennis, J. Li, G.I. Tardos, and R. Pfeffer. The influence of viscosity on the strength of an axially strained pendular liquid bridge. *Chem. Eng. Sci.*, 45:3071–3088, 1990.

[38] M.J. Adams and V. Perchard. The cohesive forces between particles with interstitial fluid. *Inst. Chem. Eng. Symp.*, 91:147–160, 1985.

[39] M. J. Adams and B. Edmonson. Forces between particles in continuous and discrete liquid media. In B. J. Briscoe and M. J. Adams, editors, *Tribology in Particulate Technology*, pages 154–172. Adam Hilger Publishers, Philidelphia, 1987.

[40] A. J. Goldman, R. G. Cox, and H. Brenner. Slow viscous motion of a sphere parallel to a plane wall – I. motion through a quiescent fluid. *Chem. Eng. Sci.*, 22:637–651, 1967.

[41] R. B. Bird, W. E. Stewart, and E. N. Lightfoot. *Transport Phenomena, Second Edition*. John Wiley & Sons, New York, 2002.

[42] T. B. Anderson and R. Jackson. A fluid mechanical description of fluidized beds. *Ind. Eng. Chem. Fund.*, 6:527–539, 1967.

[43] H.K. Versteeg and W. Malalasekera. *An introduction to Computational Fluid Dynamics: The Finite Volume Method*. John Wiley & Sons Inc., New York, 1995.

[44] S.V. Patankar. *Numerical Heat Transfer and Fluid Flow*. Hemisphere, New York, 1980.

[45] S. B. Savage. Disorder, diffusion and structure formation in granular flow. In D. Bideau and A. Hansen, editors, *Disorder and Granuar Media*, pages 255–285. Elsevier Science, Amsterdam, 1993.

[46] Z. P. Zhang, A. B. Yu, and R. B. S. Oakeshott. Effects of packing method on the randomness of disc packings. *J. Phys. A: Math. Gen*, 29:2671–2685, 1996.

[47] B.H. Xu and A.B. Yu. Authors reply to the comments of B.P.B. Hoomans, J.A.M. Kuipers, W.J. Briels, and W.P.M. van Swaaij. *Chem. Eng. Sci.*, 53:2646–2647, 1998.

[48] K.D. Kafui, C. Thornton, and M.J. Adams. Discrete particle-continuum fluid modelling for gas-solid fluidised beds. *Chem. Eng. Sci.*, 57:2395–2410, 2002.

[49] S.-C. Liang, T. Hong, and L.-S. Fan. Effects of particle arrangements on the drag force of a particle in the intermediate flow regime. *Int. J. Multiphase Flow*, 22:285–306, 1996.

[50] Sabri Ergun. Fluid flow through packed columns. *Chem. Eng. Prog.*, 48(2):89–94, 1952.

[51] C.Y. Wen and H.Y. Yu. Mechanics of fluidization. *Chem. Engng. Prog. Symp. Ser.*, 62:100, 1966.

[52] Lu Huilin, He Yurong, and Dimitri Gidaspow. Hydrodynamic modelling of binary mixuture in a gas bubbling fluidized bed using the kinetic theory of granular flow. *Chem. Eng. Sci.*, 58:1197–1205, 2003.

[53] Yong Li, Jianping Zhang, and Liang-Shih Fan. Numerical simulation of gas-liquid-solid fluidization systems using a combined CFD-VOF-DPM method: bubble wake behavior. *Chemical Engineering Science*, 54:5101–5107, 1999.

[54] Jianping Zhang, Yong Li, and Liang-Shih Fan. Discrete phase simulation of gas-liquid-solid fluidization systems: single bubble rising behavior. *Powder Technol.*, 113:310–326, 2000.

[55] T. Kawaguchi, T. Tanaka, and Y. Tsuji. Numerical simulation of two-dimensional fiuidized beds using the discrete element method (comparison between the two- and three-dimensional models). *Powder Technol.*, 96:129–138, 1998.

[56] Y. Tsuji, T. Tanaka, and S. Yonemura. Cluster patterns in circulating fluidized beds predicted by numerical simulation(discrete particle method versus two-fluid model). *Powder Technol.*, 95:254–264, 1998.

[57] Jie Li and J.A.M. Kuipers. Gas-particle interactions in dense gas-fluidized beds. *Chem. Eng. Sci.*, 58:711–718, 2003.

[58] J.A.M. Kuipers, K.J. van Duin, F.P.H. van Beckum, and W.P.M. van Swaaij. Computer simulation of the hydrodynamics of a two-dimensional gas-fluidized bed. *Computers Chem. Engng.*, 17(8):839–858, 1993.

[59] M.J.V. Goldschmidt, R. Beetstra, and J.A.M. Kuipers. Hydrodynamic modelling of dense gas-fluidised beds: comparison and validation of 3D discrete particle and continuum models. *Powder Technol.*, 142:23–47, 2004.

[60] R. Di Felice. The voidage function for fluid-particle interaction systems. *Int. J. Multiphas. Flow*, 20:153–159, 1994.

[61] J.C. Williams. The properties of non-random mixtures of solid particles. *Powder Technol.*, 3:189–194, 1969.

[62] P.M.C. Lacey. The mixing of solid particles. *Trans. Inst. Chem. Engrs.*, 21:53–59, 1943.

[63] P.M.C. Lacey. Developments in the theory of particle mixing. *J. Appl. Chem.*, 4:257–268, 1954.

[64] R. L. Brown. The fundamental principles of segregation. *J. Inst. Fuel*, 13:15–19, 1939.

[65] J.C. Williams. The segregation of particulate materials. A review. *Powder Technol.*, 15:245–251, 1976.

[66] Tom Mullin. Granular materials: Mixing and De-mixing. *Science*, 8:1851, 2002.

[67] J. M. Ottino and D. V. Khakhar. Mixing and segregation of granular materials. *Annual Review of Fluid Mechanics*, 32:55–91, 2000.

[68] Stephen L. Conway, Troy Shinbrot, and Benjamin J. Glasser. A taylor vortex analogy in granular flows. *Nature*, 431:433–437, 2004.

[69] K. M. Hill, D. V. Khakhar, J. F. Gilchrist, J. J. McCarthy, and J. M. Ottino. Segregation-driven organization in chaotic granular flows. *PNAS*, 96:11701–11706, 1999.

[70] Hernn A. Makse, Shlomo Havlin, Peter R. King, and H. Eugene Stanley. Spontaneous stratification in granular mixtures. *Nature*, 386:379–382, 1997.

[71] O. Pouliquen, J. Delour, and S. B. Savage. Fingering in granular flows. *Nature*, 386:816–817, 1997.

[72] D. V. Khakhar, J. J. McCarthy, and J. M. Ottino. Radial segregation of granular materials in rotating cylinders. *Phys. Fluids*, 9:3600–3614, 1997.

[73] James B. Knight, H. M. Jaeger, and Sidney R. Nagel. Vibration-induced size separation in granular media: The convection connection. *Phys. Rev. Lett.*, 70:3728–3731, 1993.

[74] N. Burtally, P. J. King, and Michael R. Swift. Spontaneous air-driven separation in vertically vibrated fine granular mixtures. *Science*, 295:1877–1879, 2002.

[75] Azadeh Samadani and A. Kudrolli. Segregation transitions in wet granular matter. *Phys. Rev. Lett.*, 85:5102–5105, 2000.

[76] Nitin Jain, Julio M. Ottino, , and Richard M. Lueptow. Combined size and density segregation and mixing in noncircular tumblers. *Phys. Rev. E*, 71(5):051301, 2005.

[77] G. Flix and N. Thomas. Evidence of two effects in the size segregation process in dry granular media. *Phys. Rev. E*, 70:051307, 2004.

[78] S. B. Savage and C. K. K. Lun. Particle size segregation in inclined chute flow of cohesionless granular solids. *J. Fluid Mech.*, 189:311–335, 1988.

[79] J. T. Jenkins and S. B. Savage. A theory for the rapid flow of identical, smooth, nearly elastic, spherical particles. *J. Fluid Mech.*, 130:187–202, 1983.

[80] C S Campbell. Rapid granular flows. *Annual Review of Fluid Mechanics*, 22:57–90, 1990.

[81] J. M. Ottino. *The kinematics of mixing: stretching, chaos, and transport*. Cambridge Univeristy Press, New York, 1989.

[82] J. J. McCarthy, T. Shinbrot, G. Metcalfe, J. E. Wolf, and J. M. Ottino. Mixing of granular materials in slowly rotated containers. *AIChEJ*, 42:3351–3363, 1996.

[83] C. Wightman, P. R. Mort, F. J. Muzzio, R. E. Riman, and R. K. Gleason. The structure of mixtures of particles generated by time-dependent flows. *Powder Technol.*, 84:231–240, 1995.

[84] SJ Fiedor and JM Ottino. Mixing and segregation of granular matter: multi-lobe formation in time-periodic flows. *J. Fluid Mech.*, 533:223–236, 2005.

[85] D. V. Khakhar, J. J. McCarthy, and J. M. Ottino. Mixing and segregation of granular materials in chute flows. *Chaos*, 9:594–610, 1999.

[86] P. K. Haff. Grain flow as a fluid-mechanical phenomenon. *J. Fluid Mech.*, 134:401–430, 1983.

[87] H.J. Herrmann. On the thermodynamics of granular media. *J. Phys. (France)*, II (3):427–433, 1993.

[88] Irene Ippolito, Chrystle Annic, Luc Oger Jacques Lematre, and Daniel Bideau. Granular temperature: Experimental analysis. *Physical Review E*, 52:2072–2075, 1995.

[89] D. V. Khakhar, J. J. McCarthy, T. Shinbrot, and J. M. Ottino. Transverse flow and mixing of granular materials in a rotating cylinder. *Phys. Fluids*, 9:31–43, 1997.

[90] O. Walton. Application of molecular dynamics to macroscopic particles. *Int. J. Engng. Sci.*, 22:1097–1107, 1984.

[91] Y. Tsuji, T. Kawaguchi, and T. Tanaka. Discrete particle simulation of two-dimensional fluidized bed. *Powder Technol.*, 77:79–87, 1993.

[92] B. P. B. Hoomans, J. A. M. Kuipers, W.J. Briels, and W. P. M. van Swaaij. Discrete particle simulation of bubble and slug formation in a two-dimensional gas-fluidized bed: A hard-sphere approach. *Chem. Eng. Sci.*, 51 (1):99–118, 1996.

[93] B. P. B. Hoomans, J. A. M. Kuipers, W.J. Briels, and W. P. M. van Swaaij. Comments on the paper "numerical simulation of the gas-solid flow in a fluidized bed by combing disrete particle method with computational fluid dynamics" by B.H. Xu and A.B. Yu. *Chem. Eng. Sci.*, 53 (14):2645–2646, 1998.

[94] B. J. Ennis, G. I. Tardos, and R. Pfeffer. A microlevel-based characterization of granulation phenomena. *Powder Technol.*, 65:257–272, 1991.

[95] E. Buckingham. On physically similar systems; illustrations of the use of dimensional equations. *Phys. Rev.*, 4:345–376, 1914.

[96] R. A. Bagnold. Experiments on a gravity-free dispersion of large solid spheres in a newtonian fluid under shear. *Proc. R. Soc. Lond.*, 225:4–63, 1954.

[97] H. M. Li and J. J. McCarthy. Phase diagrams for cohesive particle mixing and segregation. *Phys. Rev. E*, 71 (2):021305, 2005.

[98] Bodhisattwa Chaudhuri, Fernando J. Muzzio, and M. Silvina Tomassone. Modeling of heat transfer in granular flow in rotating vessels. *Chem. Eng. Sci.*, 61:6348–6360, 2006.

[99] Yoshiyuki Shimizu. Three-dimensional simulation using fixed coarse-grid thermal-fluid scheme and conduction heat transfer scheme in distinct element method. *Powder Technol.*, 165:140–152, 2006.

[100] Michel Louge and Jamaludin Mohd. Yusof. Heat transfer in the pneumatic transport of massive particles. *Int. J. Heat Mass Transfer*, 36(2):265–275, 1993.

[101] J. Li and D.J. Mason. A computational investigation of transient heat transfer in pneumatic transport of granular particles. *Powder Technol.*, 112:273–282, 2000.

[102] J. Sun and M. M. Chen. A theoretical analysis of heat transfer due to particle impacts. *Int. J. Heat Mass Transfer*, 31:969–975, 1988.

[103] Haosheng Zhou, Gilles Flamant, and Daniel Gauthier. DEM-LES simulation of coal combustion in a bubbling fluidized bed part ii coal combustion at the particle level. *Chem. Eng. Sci.*, 59:4205–4215, 2004.

[104] E. U. Schlünder. Particle heat transfer. In U. Grigull, E. Hahne, K. Stephan, and J. Straub, editors, *Proc. Seventh Heat Trans. Conf., Munich vol. 1*, pages 195–211. Hemisphere Pub., New York, 1982.

[105] Molerus O. Heat transfer in moving beds with a stagnant interstitial gas. *Int. J. Heat Mass Transfer.*, 40:4151–4159, 1997.

[106] G. W. J. Wes, A. A. H. Drinkenburg, and S. Stemerding. Heat transfer in a horizontal rotary drum reactor. *Powder Technol.*, 13:185–192, 1976.

[107] W. L. Vargas and J. J. McCarthy. Heat conduction in granular materials. *AIChEJ*, 47:1052–1059, 2001.

[108] M. M. Yovanovich. Thermal contact resistance across elastically deformed spheres. *J. Spacecraft Rockets*, 4:119–122, 1967.

[109] R. Holm. *Electrical Contacts: Theory and Application.* Springer-Verlag, New York, 1967.

[110] G. K. Batchelor, F.R.S., and R. W. O'Brien. Thermal or electrical conduction through a granular material. *Proc. R. Soc. Lond.*, 355:313–333, 1977.

[111] W. E. Ranz. Friction and transfer coefficients for single particles and packed beds. *Chem. Eng. Prog.*, 48:247–253, 1952.

[112] Lehmberg J., M. Hehl, and K. Schügerl. Transverse mixing and heat transfer in horizontal rotary drum reactors. *Powder Technol.*, 18:149–163, 1977.

[113] N. Ito, K. Obata, and T. Hakuta. Heat transfer from the wall to a particle bed in a rotary drum. *Kagaku Kogaku Ronbunshu*, 9:628–634, 1983.

[114] V. P. Mehrotra and K. V. S. Sastry. Pendular bond strength between unequal-sized spherical particles. *Powder Technology*, 25:203–214, 1980.

[115] S. J. R. Simons. Modeling of agglomerating systems: From spheres to fractals. *Powder Technol.*, 87:29–41, 1996.

[116] B.H. Xu and A.B. Yu. A study of the effect of liquid-induced forces on gas-solid flow by a combined continuum and discrete model. Second International Conference on CFD in the Minerals and Process Industries, 1999.

[117] M. J. V. Goldschmidt, G. G. C. Weijers, R. Boerefijn, and J. A. M. Kuipers. Discrete element modelling of fluidised bed spray granulation. *Powder Technol.*, 138:39–45, 2003.

[118] A.A. Darhuber, S.M. Miller, S.M. Troian, and S. Wagner. Process simulation for contact print microlithography. *Technical Proceedings of the 2000 International Conference on Modeling and Simulation of Microsystems*, 2000.

[119] Anton A. Darhuber, Sandra M. Troian, and Sigurd Wagner. Physical mechanisms governing pattern fidelity in microscale offset printing. *J. Appl. Phys.*, 90(7):3602–3609, 2001.

[120] A. V. Chadov and E. D. Yakhnin. Investigation of the transfer of a liquid from one solid surface to another I. slow transfer. method of approximation calculation. *Kolloidnyi Zhurnal*, 41(4):817–820, 1979.

[121] Brazing fundamentals. *http://www.asminternational.org*.

[122] Patrick Rynhart, R. McKibbin, R. McLachlan, and J.R. Jones. Mathematical modelling of granulation: Static and dynamic liquid bridges. *Res. Lett. Inf. Math. Sci.*, 3:199–212, 2002.

[123] W. Pietsch and H. Rumpf. Haftkraft, kapillardruck, flussigkeitsvolumen und grenzwinkel einer flussigkeitsbrucke zwischen zwei kugeln. *Chem. Ing. Tech.*, 39:885–893, 1967.

[124] H. Schubert. *Kapillaritat in porosen Feststoffsystemen.1998*. Springer, Berlin Heidelberg New York, 1982.

[125] Tom Weigert and Siegfried Ripperger. Calculation of the liquid bridge volume and bulk saturation from the half-filling angle. *Part. Part. Syst. Charact.*, 16:238–242, 1999.

[126] J. Tomas. *Untersuchungen zum Flieverhalten von feuchten und leichtloslichen Schuttgutern*. Freiberger Forschungsheft A 677, Deutscher Verlag fur Grundstofndustrie, 1983.

[127] G. Lian, C. Thornton, and M. J. Adams. A theoretical study of the liquid bridge forces between two rigid spherical bodies. *Journal of Colloid and Interface Science*, 161:138–147, 1993.

[128] Damiano Rossetti, Xavier Pepin, and Stefaan J.R. Simons. Rupture energy and wetting behavior of pendular liquid bridges in relation to the spherical agglomeration process. *Journal of Colloid and Interface Science*, 261:161–169, 2003.

[129] Xavier Pepin, Damiano Rossetti, Simon M. Iveson, and Stefaan J. R. Simons. Modeling the evolution and rupture of pendular liquid bridges in the presence of large wetting hysteresis. *Journal of Colloid and Interface Science*, 232(2):289–297, 2000.

[130] Xavier Pepin, Damiano Rossetti, and Stefaan J. R. Simons. Modeling pendular liquid bridges with a reducing solid-liquid interface. *Journal of Colloid and Interface Science*, 232(2):298–302, 2000.

[131] Yongxin Song and Richard Turton. Study of the effect of liquid bridges on the dynamic behavior of two colliding tablets using dem. *Powder Technol.*, to appear, 2007.

[132] Hall HS. *Granulation Technology for Bioproducts*. CRC Press, Boca Raton, FL, 1990.

[133] Preetanshu Pandey, Manoj Katakdaunde, and Richard Turton. The prediction of variability occurring in fluidized bed coating equipment part 2: the role of non-uniform particle coverage as particles pass through the spray zone. *Pharm. Dev. Technol.*, 5(3):323–332, 2000.

[134] Pandey P and Turton R. A study to quantify the effects of mixing aids during a coating operation in an industrial scale rotating pan coater. *AAPS Journal*, 6(S1):Abstract W4186, 2004.

[135] Pandey P, Song Y, Kahiyan F, and Turton R. Simulation of particle movement in a pan coating device using discrete element modeling and its comparison with video-imaging experiments. *Powder Technology*, 161(2):79–88, 2005.

[136] Preetanshu Pandey and Richard Turton. Investigation of operating parameters that affect uniformity in pan coating devices. *World Congress on Particle Technology*, 5:April 23–27, 2006.

[137] Preetanshu Pandey, Manoj Katakdaunde, and Richard Turton. Modeling weight variability in a pan coating process using monte carlo simulations. *AAPS PHARMSCITECH*, 7(4):Art. No. 83 2006, 2006.

[138] T.A.G. Langrish and T.K. Kockel. The assessment of a characteristic drying curve for milk powder for use in computational fluid dynamics modelling. *Chem. Eng. J.*, 84:69–74, 2001.

[139] Ian C. Kemp and David E. Oakley. Modelling of particulate drying in theory and practice. *Dry. Technol.*, 20(9):1699–1750, 2002.

[140] Zhaohui Wang and Guohua Chen. Heat and mass transfer in batch fluidized-bed drying of porous particles. *Chem. Eng. Sci.*, 55:1857–1869, 2000.

[141] K. Malhorta. R and D opportunities in drying of advanced electro-ceramics. *Drying Technol.*, 10:715–732, 1992.

[142] T. Scheafer and O. Worts. Control of fluidized bed granulation: III. Effects of inlet air temperature and liquid flow rate on granule size and size distribution. control of moisture content of granules in the drying phase. *Arch. Pharm. Chem. Sci.*, 6:1–13, 1978.

[143] Roman G. Szafran and Andrzej Kmiec. Point-by-point solution procedure for the computational fluid dynamics modeling of long-time batch drying. *Ind. Eng. Chem. Res.*, 44:7892–7898, 2005.

[144] B. Saravanan, N. Balasubramanian, and C. Srinivasakannan. Drying kinetics in a vertical gas-solid system. *Chem. Eng. Technol.*, 30(2):176–183, 2007.

[145] I. W. EAMES, N. J. MARR, and H. SABIR. The evaporation coefficient of water: a review. *Int. J. Heat Mass Transfer*, 40(12):2963–2973, 1997.

[146] Mark W. Denny. *Air and Water: The Biology and Physics of Life's Media*. Princeton University Press, Princeton, NJ, 1993.

[147] W. L. Vargas and J. J. McCarthy. Conductivity of granular media with stagnant interstitial fluids via thermal particle dynamics simulation. *Int. J. Heat Mass Transfer.*, 45:4847–4856, 2002.

[148] Daizo Kunii and Octave Levenspiel. *Fluidization Engineering, 2nd ed*. Butterworth-Heinemann, Stoneham, MA, 1991.

[149] J. Andrieu and A.-A. Stamatopoulos. Moisture and heat transfer modelling during durum wheat pasta drying. *International Drying Symposium 1986*, Boston:U.S.A, 1986.

[150] E. Mitura, S. Michalowski, and W. Kaminski. A mathematical model of convection drying in the falling drying rate period. *Dry. Technol.*, 6:113–137, 1988.

[151] H.G. Wang, T. Dyakowski, P. Senior, R.S. Raghavan, and W.Q. Yang. Modelling of batch fluidised bed drying of pharmaceutical granules. *Chemical Engineering Science*, 62:1524–1535, 2007.

[152] David E. Oakley. Spray dryer modeling in theory and practice. *Dry. Technol.*, 22(6):1371–1402, 2004.

[153] Z. Chen, P.K. Agarwal, and J.B. Agnew. Steam drying of coal. part 2. modeling the operation of a fluidized bed drying unit. *Fuel*, 80:209–223, 2001.

[154] Ebrahim Hajidavalloo and Feridun Hamdullahpur. Thermal analysis of a fluidized bed drying process for crops. part i: Mathematical modeling. *Int. J. Energy Res.*, 24:791–807, 2000.

[155] H Basirat-Tabrizi, M Saffar-Avval, and M R Assarie. Two-dimensional mathematical model of a packed bed dryer and experimentation. *Proceedings of the Institution of Mechanical Engineers, Part A: Journal of Power and Energy*, 216(2):161–168, 2002.

[156] Paul A. Langston, Mohammad A. Al-Awamleh, Feras Y. Fraige, and Basel N. Asmar. Distinct element modelling of non-spherical frictionless particle flow. *Chem. Eng. Sci.*, 59:425–435, 2004.

[157] M. P. Allen and D. J. Tildesley. *Computer Simulation of Liquids*. Clarendon Press, Oxford, 1987.

[158] A. Drescher. An approach to simulate the motion of spherical and non-spherical fuel particles in combustion chambers. *Granul. Matter*, 3:231–265, 2001.

[159] L. Meister and H. Schaeben. A concise quaternion geometry of rotations. *Mathematical Methods in the Applied Science*, 28 (1):101–126, 2005.

[160] Herbert Goldstein, Charles P. Poole, and John L. Safko. *Classical Mechanics*. Addison Wesley, Cambridge, MA, 2002.

[161] Eric W. Weisstein. *CRC Concise Encyclopedia of Mathematics, Second Edition*. CRC Press, Boca Raton, FL, 2002.